

ELECTRON-ELECTRON INTERACTION IN ION-ATOM
COLLISIONS STUDIED BY PROJECTILE
STATE-RESOLVED AUGER ELECTRON SPECTROSCOPY

by

DO-HYUNG LEE

B.S., Seoul National University, 1974

M.S., Seoul National University, 1978

A DOCTOR'S DISSERTATION

submitted in partial fulfillment of the
requirements for the degree

DOCTOR OF PHILOSOPHY

Department of Physics
KANSAS STATE UNIVERSITY
Manhattan, Kansas

1990

Approved:

Major Professor

ELECTRON-ELECTRON INTERACTION IN ION-ATOM

COLLISIONS STUDIED BY PROJECTILE

STATE-RESOLVED AUGER ELECTRON SPECTROSCOPY

DO-HYUNG LEE

B.S., Seoul National University, 1973

M.S., Seoul National University, 1975

A DOCTOR'S DISSERTATION

submitted in partial fulfillment of the

requirements for the degree

DOCTOR OF PHILOSOPHY

Department of Physics

KANSAS STATE UNIVERSITY

Manhattan, Kansas

1978

Approved:

Major Professor

TABLE OF CONTENTS

LIST OF TABLES	iii
LIST OF FIGURES	iv
ACKNOWLEDGEMENTS	viii
I. INTRODUCTION	1
II. ZERO-DEGREE ELECTRON SPECTROMETER SYSTEM	
A. Kinematics of Projectile Auger Electrons	12
B. Zero-Degree Tandem Electron Spectrometer	19
III. EXPERIMENT	
A. Projectile Ions	38
B. Electron Spectrum Acquisition	46
IV. ZERO DEGREE BINARY ENCOUNTER ELECTRONS	
A. Background and Motivation	67
B. Binary Encounter Impulse Approximation	74
C. Spectrometer Efficiency Normalization and Data Analysis	77
D. Results and Discussion with Bare Ions.	81
E. Projectile q -Dependence	93
V. ZERO-DEGREE AUGER CROSS SECTION ANALYSIS	
A. Cross Sections and Solid Angle Calculation	101
B. State-Resolved and Total <i>KLL</i> Auger Cross Sections	124
C. Error Analysis	138
VI. RESONANT TRANSFER EXCITATION	
A. Background	141
B. A Theoretical Description	
1. RTE Impulse Approximation	143

2. RTE Alignment and RTEA Interference	147
C. RTEA with O^{5+} and F^{6+} Ions	154
D. RTEA with F^{7+} Ions	163
VII ELECTRON-ELECTRON EXCITATION AND IONIZATION	
A. Electron-Electron Excitation	
1. $1s2s2p^4P$ State	181
2. Other $1s2s2l$ States	190
B. Electron-Electron Ionization	198
VIII. CONCLUSIONS	212
REFERENCES	221
APPENDIX	230
ABSTRACT	

LIST OF TABLES

Table	Page
1. Electron-electron interactions and electron-ion binary encounter	10
2. Design parameters of the tandem 45° spectrometer	26
3. Ratios of increased chamber pressures to target pressures	33
4. Physical quantities of the tandem 45° spectrometer.	37
5. Measured cusp energies and observed energy shift of the BEe peak	78
6. Lifetimes and Auger yields for various Auger states.	108
7-14. Calculated effective solid angle factors for the various collision systems.	119
15. Three RTE-IA cases	146
16. Auger energies and dominate state production mechanisms for $O^{5+} + H_2/He$ and $F^{6+} + H_2/He$ collisions	158
17. Calculated and Measured RES strengths for O^{4+} and F^{5+} ($1s2s2p^2$) $^3,^1D$ states.	162
18. Auger production mechanism matrix in collisions of F^{7+} ($1s^2, 1s2s^3S$) with He/H_2 targets.	171
19. Calculated and Measured RES strengths for F^{6+} ($1s2l2l'$) ($2S+1$) L states.	177
20. Auger energies measured in O^{4+} ($1s^22s^2, 1s^22s2p^3P$) + He/H_2 collisions	201

LIST OF FIGURES

Figure	Page
1. Velocity addition diagram of a projectile Auger electron	13
2. Observable angle range for a given energy of projectile and projectile electron	15
3. Kinematic (Doppler) broadening of a projectile Auger electron	17
4. Zero-degree tandem electron spectrometer system for projectile electron studies in ion-atom collisions (horizontal view)	20
5. Zero-degree tandem electron spectrometer system for projectile electron studies in ion-atom collisions (side view)	22
6. Electron trajectory diagram for a parallel-plate spectrometer	24
7. Test of spectrometer response function and spectrometer constant	27
8. Spectrometer einzel-lens test for a high-resolution electron spectrum.	30
9. Double differential pumping performance of the target gas cell	34
10. Electron ray trajectory in the tandem spectrometer	36
11. Collision schematic and zero-degree measurement	39
12. Schematic of the 6 MV tandem Van de Graaff accelerator at the J.R. Macdonald Laboratory at Kansas State University	42
13. Beam line R-2 and scattering chamber arrangement	47
14. Schematic diagram of electron analyzing voltages of the tandem electron spectrometer.	49
15. Block diagram of the supporting electronics for spectrum acquisition	51
16. Beam passage diagnosis through the target gas cell and spectrometer. ...	56
17. Comparison between the truly collisionally produced electrons and the beam-induced background electrons in the overall electron spectra	58
18. Magnetic shielding performance test with a pair of Helmholtz coils.	60
19. Sample of high-resolution projectile <i>K</i> or <i>KLL</i> Auger electron spectra for various collision systems.	61
20. Overall electron spectra for two different collision systems	68

21. Test of single collision conditions of the binary encounter electron production	72
22. Electron energy spectrum for collisions of 19 MeV $F^{9+} + H_2$ observed at zero degrees showing the cusp and binary encounter peaks.	73
23. Schematic diagram of the kinematics of a target electron in a binary encounter collision.	75
24. Overall absolute spectrometer efficiency as a function of electron energy	80
25. BEe DDCS (projectile frame) measured at zero degrees for various collision energies of F^{9+} incident on H_2/He	82
26. Comparison of four different calculations to the measured BEe DDCS (projectile frame).	83
27. BEe DDCS (laboratory frame) measured for 1.5 MeV $H^+ + H_2/He$ collisions	86
28. BEe Spectra (projectile frame) for the five bare projectiles.	89
29. Projectile Z_P dependence of BEe single differential cross sections (projectile frame).	91
30. Projectile energy dependence of BEe DDCS (projectile frame) for $F^{9+} + H_2/He$ collisions.	92
31. Measured BEe spectra (projectile frame) for 28.5 MeV $F^{9,7,5} + H_2$ collisions.	95
32. Projectile charge state dependence of BEe production.	97
33. Schematic diagram for the measurement of zero-degree Auger production cross sections.	102
34. Total single capture cross sections for $O^{5+} + He/H_2$ collisions as a function of impact energy	105
35. Variation of the parameters for the effective solid angle calculations for the prompt and metastable $1s2s2p^4P$ states.	110
36. A pair of electron spectra in the non-retarding and state-resolved, high-resolution modes.	125
37. Experimental spectrometer response function for a high resolution spectrum.	128

38.	Separation of the metastable $1s2s2p^4P$ electron yields produced inside and outside the gas cell.	130
39.	<i>KLL</i> Auger production cross sections at 0° in collisions of O^{5+} with H_2 and He targets.	134
40.	<i>KLL</i> Auger production cross sections at 0° in collisions of F^{6+} with H_2 and He targets.	135
41.	<i>KLL</i> Auger production cross sections at 0° in collisions of F^{7+} with H_2 and He targets.	136
42.	<i>KLL</i> Auger production cross sections at 0° in collisions of O^{4+} with H_2 and He targets.	137
43.	RTEA-IA comparison for $2p^2\ ^1D$ state produced in $He^+ + He$ collisions	150
44.	RTEA-IA comparison for $C^{3+} + He$ collisions	151
45.	RTEA-IA comparison for $F^{7+} + He$ collisions	152
46.	RTEA-IA comparison for $Si^{12+} + He$ collisions	153
47.	Normalized zero-degree electron spectra measured for $O^{5+} + He/H_2$ collisions.	155
48.	Normalized zero-degree electron spectra measured for $F^{6+} + He/H_2$ collisions.	157
49.	Absolute TE Auger cross sections for the $(1s2s2p^2)^{3,1}D$ state in $O^{5+} + He/H_2$ collisions versus projectile energy	159
50.	Absolute TE Auger cross sections for $(1s2s2p^2)^{3,1}D$ state in $F^{6+} + He/H_2$ collisions versus projectile energy	161
51.	Normalized zero-degree electron spectra measured for $F^{7+} + He/H_2$ collisions at various projectile energies.	164
52.	State production mechanisms from $F^{7+}(1s^2, 1s2s\ ^3S)$ to $F^{6+}(1s2l2l')$...	166
53.	Auger cross sections for $(1s2p^2)^2D$ and $(1s2s2p)^2P_+$ states in $F^{7+}(1s^2, 1s2s\ ^3S) + He/H_2$ collisions versus projectile energy.	168
54.	Auger cross sections for $(1s2s2p)^2P_-$ and $(1s2s^2)^2S$ states in $F^{7+}(1s^2, 1s2s\ ^3S) + He/H_2$ collisions versus projectile energy.	170
55.	$(1s2s2p)^4P$ state production cross sections by capture to $F^{7+}(1s2s)^3S$	173

56. Various $O^{5+}(1s^2 2s) 1s \rightarrow 2p$ electron excitation mechanisms and excitation cross sections.	183
57. Cross sections for the production of the $(1s2s2p)^4P$ state by $1s \rightarrow 2p$ projectile excitation in F^{6+} and $O^{5+}(1s^2 2s)$ collisions with He/H_2	187
58. Theoretical cross sections of electron impact $1s \rightarrow 2p$ excitation of O^{5+} and F^{6+} ions.	191
59. Cross sections for the production of $(1s2s2l)$ states by $1s \rightarrow 2l$ projectile excitation in $O^{5+}(1s^2 2s) + H_2$ collisions	193
60. Cross sections for the production of $(1s2s2l)$ states by $1s \rightarrow 2l$ projectile excitation in $O^{5+}(1s^2 2s) + He$ collisions	194
61. Cross sections for the production of $(1s2s2l)$ states by $1s \rightarrow 2l$ projectile excitation in $F^{6+}(1s^2 2s) + H_2$ collisions	195
62. Cross sections for the production of $(1s2s2l)$ states by $1s \rightarrow 2l$ projectile excitation in $F^{6+}(1s^2 2s) + He$ collisions	196
63. Comparison of zero-degree $(d\sigma_{eeE}/d\Omega)$ and $(d\sigma_{RTE}/d\Omega)$ for collisions of F^{6+} with H_2 targets.	197
64. Normalized zero-degree electron spectra measured for $O^{4+} + He/H_2$ collisions at various projectile energies.	199
65. State production mechanisms from $O^{4+}(1s^2 2s^2, 1s^2 2s2p^3P)$ to $O^{5+}(1s2l2l')$ and $O^{4+}(1s2l2l'2l')$	202
66. Measured $O^{4+}(1s^2 2s2p)^3P$ metastable beam fractions.	205
67. Extracted $(1s2s2p)^4P$ electron yield factor inside gas cell for $O^{4+} + He/H_2$ collisions	207
68. K -shell ionization cross sections in $O^{4+} + H_2/He$ collisions	208
69. Calculated K -shell ionization cross sections in $C^{2+} + H_2$ collisions	211

58	Various $O^{+}(1s^2 2s)$ $1s-2p$ electron excitation mechanisms and excitation cross sections	183
59	Cross sections for the production of the $(1s^2 2s) 2^1P$ state by $1s-2p$ projectile excitation in F^{+} and $O^{+}(1s^2 2s)$ collisions with $He H_2$	187
60	Theoretical cross sections of electron impact $1s-2p$ excitation of O^{+} and F^{+} ions	191
61	Cross sections for the production of $(1s^2 2s) 2^1P$ states by $1s-2p$ projectile excitation in $O^{+}(1s^2 2s) + H_2$ collisions	193
62	Cross sections for the production of $(1s^2 2s) 2^1P$ states by $1s-2p$ projectile excitation in $O^{+}(1s^2 2s) + He$ collisions	194
63	Cross sections for the production of $(1s^2 2s) 2^1P$ states by $1s-2p$ projectile excitation in $F^{+}(1s^2 2s) + H_2$ collisions	195
64	Cross sections for the production of $(1s^2 2s) 2^1P$ states by $1s-2p$ projectile excitation in $F^{+}(1s^2 2s) + He$ collisions	196
65	Comparison of two different $(1s^2 2s) 2^1P$ and $(1s^2 2s) 2^3P$ for collisions of F^{+} with He targets	197
66	Normalized non-relativistic electron spectra measured for $O^{+} + He/H_2$ collisions at various projectile energies	199
67	State production mechanisms from $O^{+}(1s^2 2s) 2^1P$ to $O^{+}(1s^2 2s) 2^3P$ and $O^{+}(1s^2 2s) 2^1P$	200
68	Measured $O^{+}(1s^2 2s) 2^1P$ metastable beam functions	205
69	Estimated $(1s^2 2s) 2^1P$ electron yield below threshold for $O^{+} + He/H_2$ collisions	207
70	A-shell ionization cross sections in $O^{+} + He/H_2$ collisions	208
71	Calculated A-shell ionization cross sections in $O^{+} + H_2$ collisions	211

ACKNOWLEDGEMENTS

I would like to express my sincere gratitude to many people, without whose support this work would not have been accomplished. First and foremost to my adviser, Professor Patrick Richard, for his insight and guidance throughout the course of this dissertation work. His unfailing encouragement and patience are also greatly appreciated. Secondly, to my advisory committee members, Professors C. Lewis Cocke, Chii-Dong Lin, Siegbert Hagmann, and Willard Parker, for their valuable comments and encouragement concerning my education and research. My appreciation is also extended to my colleagues and friends, to Dr. Theo Zouros for the many invaluable discussions and collaboration in this project and for the development of an electron spectrum acquisition program and the implementation of the spectrum analyzing program DET, to Justin Sanders and Dr. Jeff Shinpaugh for many vital discussions about basic physics problems and for their assistance in various phases of this work, and to Professor Brett DePaola, Dr. Jim Hall, Tracy Tipping, Visiting Professor S.L. Varghese, and Hisham Hidmi, for their help in the laboratory during many stages of this work. I would also like to express my appreciation to Professors Chander Bhalla and James McGuire for many helpful comments concerning my education and for their time to answer my questions. I would also like to thank all other Physics faculty members for teaching and encouraging me to be a physicist.

I would also like to thank the entire KSU Physics Department and the J.R. Macdonald Laboratory staff for their friendly atmosphere of cooperation and support, especially to Mr. Dave Hill and Mr. Bob Geering for their expert craftsmanship in building the electron spectrometer, scattering chamber, and many other necessary parts used during the course of the experiments, to Mr. Mark Ross for his valuable skills in the electronics shop, to Bob Krause and Tracy Tipping for their assistance in the accelerator operation and ion source preparation including my call for help on weekends, to Dr. Kevin Carnes for his generous and expert help in my data taking and analyzing processes with the newly-installed laboratory computers. All other staff members' skills and assistance are greatly appreciated. Without those, any type of basic research in this work would not have

been performed. I also thank my other fellow graduate students, Nabil Malhi, Ramakrishnan C. Parameswaran, Song Cheng, Vicky Frohne, and Rami Ali, for their friendship and help in the laboratory. A special thanks goes to Dea Richard for her expert proofreading and sometimes refining my crude expressions in this dissertation.

I am also grateful to the United States Department of Energy, Office of Basic Energy, Office of Energy Research, Division of Chemical Sciences, for financial support during the course of all my graduate training including this dissertation work, particularly the electron spectrometer development.

Finally, I would like to express my thanks to my wife Mee Hye, for her patient endurance and love and support for a number of years, who has prayed and waited for this accomplishment, and to my son Jaehoon, for his understanding, who has wondered when I will get it done and play with him on weekends. Many thanks go to my own and my wife's parents and brothers in my country for their support, especially to my father who sincerely encouraged my study abroad but passed away suddenly during my stay here in this land.

This dissertation is dedicated to my late father, Jeung-Hee Lee.

I. INTRODUCTION

State-Resolved Studies in Ion-Atom Collisions

The fundamental atomic processes of ionization, electron excitation, and electron capture resulting from highly-charged fast ion-atom collisions are investigated in this dissertation. These subjects have been studied extensively over the last two decades,¹ due to the availability of particle accelerators capable of producing highly charged ions with energies typically in the range of a few tens of thousands of electron volts per atomic mass unit (keV/u) to a few million electron volts per atomic mass unit (MeV/u). Particle accelerators allow one to study individual collision systems over a wide range of charge states of the projectile in addition to a wide range of particle velocities. The projectile charge can be varied typically from singly ionized up to fully stripped ion species and the velocities can be varied from values below to several times above a given bound electron's orbital velocity depending on the system studied.

Atomic processes involving predominantly the interaction of the projectile with the *target* electrons have been explored using the accelerated ion method. For example, inner shell ionization of the *K*-shell of the *target* by a highly charged ion has been extensively studied by measuring the total and differential cross sections for *K* x-ray¹⁻³ and *K* Auger electron^{1,2,4} production. When the resolution of the x-ray or *K* Auger electron spectrometer is sufficiently high to resolve the final states, the study is typically referred to as state-selective or state-resolved spectroscopy. Obtaining completely resolved final states is sometimes impossible because of the high level density of final states in the residual target after collision. In some cases, however, it is possible to separate the final states into groups of states defined by the electron configuration (e.g., a configuration consisting of

one K -shell and 4 L -shell electrons, K^1L^4 , which couple to form many closely spaced final states). Another example is the study of electron capture or ionization by measuring the final charge change of the projectile after the collision. These studies become more powerful when combined with coincidence measurements of the recoils/ion and the projectile ion.

As another important subject using the accelerated ion method, electron capture, excitation, or ionization of the *projectile* ion has been explored by high-resolution (state-resolved) x-ray or Auger spectroscopy measuring their production cross sections.⁵⁻¹⁵ The studies of *projectile* atomic state evolution during and after the collision are particularly useful when the target is atomic hydrogen or helium. Because of ease molecular hydrogen is often used as a target. These studies are of main interests in this dissertation and are performed extensively. In the collision systems of few-electron projectiles incident on a He or H₂ target, the density of final states of the projectile is usually such that individual final states can be resolved. Projectile collisions with these light targets thus allow one to observe and investigate predominantly one- and two-electron processes as a function of the ion charge and/or ion velocity, which typically gives the type of results amenable to comparisons with theory.

Dynamic Electron-Electron Interactions.

In typical ion-atom collisions, the nucleus of the target plays a dominant role in changing the atomic state of the incoming projectiles. However, using a simple target such as He or H₂ and employing few electron projectiles such as O⁵⁺ or F⁷⁺, it has been found that the target electrons give rise to a *unique* and sometimes dominant contribution in projectile state formation in which projectile K -shell excitation is involved, and thus the target electron contribution can be distinguished

from the target nucleus contribution particularly in the case of fast collisions. The electron contribution, originating from the dynamic electron-electron interaction¹⁶ (so-called correlated two-electron processes,¹⁷ scattering correlation,¹⁸ or dynamic correlation¹⁹) has been manifested in the recent observations of resonant transfer-excitation (RTE),²⁰ electron-electron excitation (eeE),²¹ and electron-electron ionization (eeI),^{22,23} which consolidates the strong evidences for the electron-electron interactions during ion-atom collisions. The problems of RTE, single inner-shell excitation, and single inner-shell ionization of the projectile by a target electron are of current interest in heavy ion-atom collision physics and are focused and addressed in this dissertation using high-resolution, state-resolved Auger electron spectroscopy.

The major emphasis in this work is the study of transfer excitation (TE) cross sections. TE is a process in which two electrons are rearranged during the ion-atom collision. One electron is transferred from the target to the projectile and simultaneously one of the projectile electrons is excited (e.g., from the *K*-shell to the *L*-shell). This process can proceed via either a resonant, RTE, or a non-resonant, NTE,²⁴ mode. RTE is a correlated process which occurs when the projectile electron excitation is mediated by the transferred electron.²⁰ NTE is an uncorrelated process in which the projectile electron excitation is mediated by the Coulomb field of the target nucleus. The study of TE, and in particular of RTE, has received considerable attention in the last several years, since it can provide direct information on electron correlation phenomena as a strong and unique electron-electron interaction presently of great interest in atomic physics.

For fast ion-atom collisions, where the orbital velocity of the active target electron is much smaller than the incoming velocity of the projectile, the target gas can be viewed as a composite beam of electrons and nuclei in the projectile-rest

frame as far as their coherent action is negligible for certain collision phenomena. In particular, if the target electron is loosely bound to the target nucleus, it can be treated as an incoming "quasi-free" particle with its orbital momentum distribution (Compton profile). Thus, RTE is related to the dielectronic recombination (DR)²⁵ process which occurs in free-electron-ion collisions,²⁶ and has been successfully described by an Impulse Approximation (IA)²⁷ in which the Compton profile of the target electrons are folded with the DR cross section.²⁸ The RTE process, in particular, RTEA (RTE followed by Auger decay) will be discussed in detail in Chapter VI where our experimental results are compared with the IA calculation. Alignment^{29,30} of the doubly excited state formed by RTE also will be discussed together with the interference^{29,30} effect between the RTE Auger electron and the binary-encounter electrons^{31,32} which are target electrons quasi-elastically scattered by the projectile.

An electron colliding with a highly charged ion is of prime interest in atomic collision processes³³ of high temperature plasmas/in/astrophysical environments or proposed thermonuclear fusion reactors.³⁴ For example, in the case of DR, an impurity ion in the fusion plasmas is frequently doubly-excited by capturing an electron at a high temperature and emitting a photon of radiation through deexcitation. Thus, the thermal energy of the electron is eventually transformed to the radiation, resulting in cooling the plasmas unless the emitted photon is re-absorbed by the plasmas. Therefore, cross section measurements in heavy ion-atom collisions can be used for exploiting and complementing some electron-ion collision processes. This can be one application of fast heavy ion-atom collisions, where the highly charged projectile is used as a "moving laboratory". As another application using this moving laboratory, the collision data from spectroscopic studies, identifying the excited states and their lifetimes and energy levels, are

necessary for the development of the x-ray laser³⁵ where highly charged heavy-ion plasmas can be used in principle.

The motivation for studying inner-shell excitation and ionization is to investigate the effects of so-called screening and antiscreening as a function of projectile charge. The dominant mechanism for these processes is the Coulomb interaction between the target nucleus and the projectile electron which is excited or ionized. In this work I will refer to the processes of excitation and ionization by the nuclear Coulomb field of the target as "enE" and "enI", respectively. Screening is a process where the spectator electrons shield the active electron during the collision and generally reduces the cross section. This effect can be calculated from a screened potential model.³⁶ Antiscreening is a term which refers to an enhancement of the cross section as opposed to a reduction of the cross section as is the case for screening (i.e., screening reduces the charge of the exciting specie which in turn reduces the interaction strength). Antiscreening is in fact the result of electron-electron interactions during the collision which leads to an additional term in the cross section. For example, in the case of projectile excitation or ionization by H_2 , antiscreening refers to the excitation or ionization of one of the projectile electrons by one of the H_2 electrons.

Prior to this work there existed no direct evidence of the effect of antiscreening. In this work I will refer to antiscreening as another kind of electron-electron interaction in ion-atom collisions and will use the abbreviations "eeE" and "eeI" to refer to projectile electron excitation and ionization by a target electron, respectively. The eeE and eeI will have a threshold at a relatively high projectile energy due to the small electron to ion mass ratio. The threshold for an inelastic excitation requiring an energy E will occur at a projectile energy $E_P = \frac{M}{m} E$, where $\frac{M}{m}$ is the projectile to electron mass ratio. For example, $O^{5+} 1s \rightarrow 2p$ excitation, \sim

560 eV, will have a threshold energy of approximately 16 MeV projectile energy assuming the electron moves with the same velocity as the projectile. The processes of eeE and eeI will be discussed in Chapter VII. We will compare the results of the measurements to an IA model which allows one to take into account the distribution of the target electron velocity distribution. This model conveniently casts the theory in terms of the Compton profiles of the target electrons, which are well known quantities, and the cross sections for free-electron-ion collisions, which are also readily calculated. The free-electron-ion process of excitation and ionization will be referred to by the abbreviations "eIE" (electron impact excitation) and "eII" (electron impact ionization), respectively.

Zero-Degree Projectile Auger Electron Spectroscopy

The motivation for the work presented in this dissertation was to obtain improved results on the state-resolved spectroscopy of O^{q+} and F^{q+} incident on H_2 and He targets. Previous measurements using this technique were limited by the kinematic (Doppler) broadening in the projectile Auger electron spectroscopy or by limited efficiency of the high resolution x-ray spectrometer in general.

The kinematic (Doppler) broadening of projectile electrons for large angle observations relative to the projectile beam axis is formidable. However, when projectile Auger electrons are observed at zero degrees with respect to the beam direction, the kinematic broadening is minimized and substantially reduced. Thus, this zero-degree projectile electron spectroscopy³⁷ has been an excellent technique used to investigate the collisionally-produced atomic states in the projectile. For non-zero degree observations such as Auger measurements, for example, using the cylindrical mirror analyzer (CMA) in which the projectile Auger electrons are detected at 42° from the beam direction, high-resolution Auger spectroscopy

practically failed in the case of fast projectiles at velocities larger than about 1 MeV/u due to this strong kinematic broadening.³⁸

The plan was implemented by building a new improved high-resolution Auger electron spectrometer. A tandem 45° parallel-plate electron spectrometer, first used by the Berlin group,³⁹ was designed and constructed⁴⁰ together with a collision gas cell and a scattering chamber. The spectrometer is a double pass geometry which allows one to observe electrons at zero degrees with respect to the beam direction. The kinematic broadening of the projectile *K* Auger electrons was found to be practically negligible for this spectrometer, even for fast projectiles at a velocity of 2 MeV/u. A type of tandem (double) spectrometer was chosen in which the first analyzer serves as a deflector to separate the projectile electrons from the moving projectiles and the second analyzer functions to analyze the energies of the electrons with energy retardation giving rise to a high resolving power required in the final state selection. The spectrometer system is discussed in more detail in Chapter II. The kinematics of the projectile Auger electrons is also described in Chapter II.

Binary Encounter Electrons

In projectile Auger cross section measurements for fast collisions, a strong intensity of binary encounter electrons^{31,32} (BEE) is detected. BEE are the electrons originating from the target ionization by quasi-elastic scattering due to projectile impact on the weakly-bound target electrons. In the case of forward angle observation, BEE produces the strong background with a broad peak structure which represents the orbital momentum distribution of the target electron. Employing the fast, bare projectiles of F, O, N, C, and protons and the simple targets of H₂ and He, the production cross sections of BEE were measured and compared with

a semi-classical calculation which was developed³² in this work. The calculation was done by treating the 0° BEE in the laboratory frame as electrons scattered through 180° in the projectile frame. This quasi-elastic scattering process was effected using the Rutherford formula and the Compton profiles of the He or H_2 target electrons through the IA. An excellent agreement between the measurement and IA calculation was observed and the IA prediction was found to be better than the available PWBA⁴¹ prediction.

A detailed study of the BEE production is very valuable for the following reasons: First, BEE is found to be a strong background for the projectile K -Auger electrons at projectile energies around resonance of the RTE and around threshold of the eeE process. Both BEE and RTE Auger electrons are produced as the result of quasi-elastic scattering with the only difference being the intermediate atomic states, so that these two kinds of electrons are not distinguishable and thus interfere with each other. This presents a good opportunity to study the quantum interference effect between two outgoing waves of the electrons with different phases. In addition, the same treatment of IA can be applied for both binary-encounter scattering and RTEA processes, giving a stringent test of IA. Lastly, the Auger cross sections can be normalized to the BEE production cross sections. This is a very useful technique as described below.

Spectrometer efficiency normalization is one of the most important procedures for absolute cross section measurements. Since the efficiency may vary with laboratory electron energy, a new method was employed in which the BEE production cross sections with "bare" projectiles at various energies was normalized to the corresponding IA calculation to determine the spectrometer efficiency at the BEE peak electron energy. This was also compared to a normalization using known Ne K -Auger production cross sections in collisions of 3 MeV H^+ with Ne. This Ne K

Auger normalization may be only valid around a Ne K Auger electron energy of 800 eV. Considering the simplicity of the collision system of the bare projectiles with quasi-free target electrons and the excellent agreement between the theory and experiment, BEe-IA normalization has been used for absolute Auger cross section measurements in this study.

Impulse Approximation (IA)

Theoretically, atomic collision studies have provided an excellent testing ground for the application of quantum mechanics and semi-classical physics. Since the Coulomb interaction, which governs all the atomic phenomena, is well understood among the four natural forces, atomic collisions are used to investigate the many-body dynamics by systematically controlling various collision parameters such as projectile velocity, projectile charge state, atomic numbers of both projectile and target, and so on. However, approximations are requisite in many cases of the atomic collision and atomic structure calculations due to the unsolvability of the many-body problem. As a semi-classical approach, the dynamic electron-electron interactions such as those involved in RTE have been investigated through the IA, whose treatment was previously mentioned for the theoretical description of RTE, eeE, eeI, and BEe, relating the ion-atom collision cross sections to the ion-electron collision cross sections. In the projectile ion frame, the loosely-bound target electron can be treated as an incoming quasi-free particle moving toward the ion while conserving its momentum distribution until it leaves its parental nucleus or nuclei and then can interact with the collision partner. This could be an assumption to be verified, but, in the spirit of the approximation, can be valid. Besides identifying the contributions due to the electron-electron interaction, the nuclear-electron interaction for a process such as projectile $1s \rightarrow 2p$ excitation by the target nucleus

can be tested by the theory of the plane-wave Born-approximation (PWBA),⁴² as far as both the target electron and the nucleus do not excite or ionize the projectile with a strong coherence.

In this work, the IA treatment will be consistently applied in the same way for the description of the ion-electron binary-encounter interaction (BEe), and for the dynamic electron-electron interactions in RTE, eeE, and eeI. As in the IA treatment in Ref. 28 for RTE, as long as the velocity of the incoming ion projectile is much larger than the orbital velocity of the target electron, any ion-atomic collision cross section originated from an electron-electron interaction, σ_{I-A}^e , can be related to an ion-free-electron collision cross section, σ_{I-e} , as follows:

$$\sigma_{I-A}^e = \sum_i \int \sigma_{I-e} \cdot |\Psi_i(\mathbf{p}_i)|^2 d^3 p_i, \quad (1)$$

where $\Psi_i(\mathbf{p}_i)$ is the momentum wave function of the i -th electron of the target. The BEe is also related to the Rutherford elastic scattering in the same manner. These relationships are summarized as follows, for the physics we are going to deal with:

TABLE 1

σ_{I-A}^e		σ_{I-e}
$\sigma[\text{RTEA}]$	$\leftarrow \text{IA} \rightarrow$	$\sigma[\text{RES}]$
$\sigma[\text{eeE}]$	$\leftarrow \text{IA} \rightarrow$	$\sigma[\text{eIE}]$
$\sigma[\text{eeI}]$	$\leftarrow \text{IA} \rightarrow$	$\sigma[\text{eII}]$
$\sigma[\text{BEe}]$	$\leftarrow \text{IA} \rightarrow$	$\sigma[\text{Rutherford}]$

RES stands for resonant excitation scattering in electron-ion collisions.⁴³ RES is also abbreviated as RE (resonant excitation).^{9,13} For a given channel, the RES cross section is related to the DR cross section as follows:

$$\sigma_{\text{RES}} = \sigma_{\text{DR}} \cdot \frac{\xi}{\omega}, \quad (2)$$

where ξ and ω are the Auger and x-ray yield for a given x-ray and Auger de-excitation channel, respectively. Since the acronym RES has the meaning of the completed sequence of the atomic process (as does DR), I will use RES rather than RE in this dissertation.

Scope of Study.

The scope of this dissertation is to search for and to address the dynamic electron-electron interactions in ion-atom collisions by applying zero-degree projectile *K*-Auger electron spectroscopy and measuring the absolute, state-resolved Auger cross sections to confirm the theoretical calculations predicted with a validated IA calculation. To perform this task, a spectrometer system was designed and constructed. Then, ion-electron binary-encounter interactions were investigated in an extended order, resulting in the relevance of the IA and thus giving rise to a spectrometer efficiency normalization procedure. For zero-degree *KLL* high-resolution Auger spectroscopy, collisions of 0.25–2 MeV/u O^{5+} , F^{6+} , F^{7+} , and O^{4+} with He and H_2 targets were investigated. For zero-degree BEE measurements, various bare and highly-charged, high velocity (mostly 1–2 MeV/u) projectile ions of F, O, N, C and protons were employed in collisions with He and H_2 targets.

For the theoretical description, an improved IA treatment was used for the description of BEE, RTE, eeE, and eeI rather than the model of Brandt given in Ref. 28. The associated electron-ion cross sections for RES, eIE, and eII are adopted or calculated using the available information in the literature. When an estimation of the contribution due to enE or enI is needed, the PWBA model is used.

II. ZERO-DEGREE ELECTRON SPECTROMETER SYSTEM

A. Kinematics of Projectile Auger Electrons

When an Auger electron is emitted from a moving projectile, the measured kinetic energy of the electron in the laboratory frame is varied with the observation angle. Using the geometry of the velocity addition diagram shown in Fig. 1, the laboratory electron energy E is expressed as:

$$E_{\pm} = (\sqrt{t}\cos\theta \pm \sqrt{E' - t\sin^2\theta})^2, \quad (3)$$

where θ is the observation angle with respect to the projectile beam direction and E' is the electron energy in the projectile "rest" frame, i.e., the Auger energy. t is the so-called cusp electron energy (or sometimes called reduced electron energy) which is given by

$$t = \frac{m}{M}E_P = 548.58 \cdot E_P(\text{in MeV/u}) \text{ eV}, \quad (4)$$

where E_P is the projectile energy and m/M is the electron-to-projectile mass ratio. The \pm sign in Eq. (3) refers to high and low branch laboratory electron energy, respectively, for the geometry shown in Fig. 1, where t is larger than E' . If t is smaller than E' , only the high energy branch (+) electrons will be detected. For zero-degree observation, where electrons are observed in the beam direction, the laboratory electron energy is given by

$$E_{\pm} = (\sqrt{t} \pm \sqrt{E'})^2. \quad (5)$$

From the geometry of Fig. 1 or Eq. (3), we see that in order to observe the projectile electron whose Auger energy E' is smaller than t , the observation angle should be smaller than a critical angle which is given by

$$\theta_c = \sin^{-1} \sqrt{\frac{E'}{t}}. \quad (6)$$

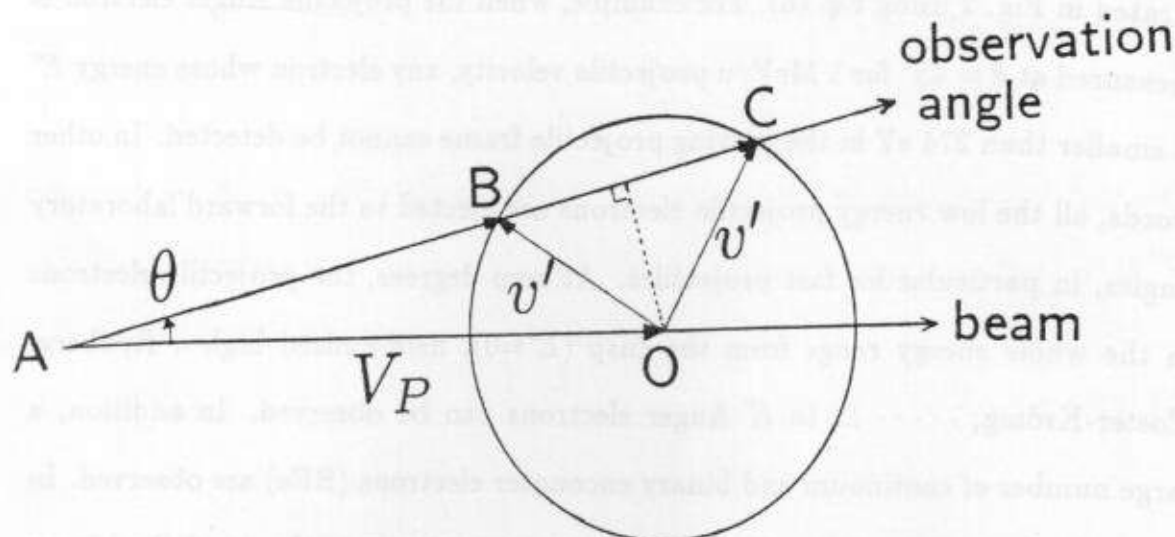


FIGURE 1. Velocity addition diagram of a projectile Auger electron. The radius of the circle is the velocity, v' , of the ejected Auger electron in the projectile frame. In the units of $\sqrt{2/m}$, $v' = \sqrt{E'}$, $AO = V_P = \sqrt{t}$ is the projectile velocity, and $AB = \sqrt{E_-}$ and $AC = \sqrt{E_+}$ are electron velocities measured at θ in the laboratory frame (see text). Using these velocity quantities, Eq. (3) is easily obtained.

Therefore, in order for the projectile Auger electrons to be detected, the observation angle should be smaller than the critical angle θ_c . For large angle observation (e.g., 42° in the case of a cylindrical mirror analyzer), only Auger electrons which fulfill this condition can be detected. This is a crucial limitation for non-zero, large-angle projectile Auger spectroscopy. This limitation is demonstrated in Fig. 2 using Eq. (6). For example, when the projectile Auger electron is measured at $\theta = 45^\circ$ for 1 MeV/u projectile velocity, any electron whose energy E' is smaller than 274 eV in the moving projectile frame cannot be detected. In other words, all the low energy projectile electrons are ejected to the forward laboratory angles, in particular for fast projectiles. At zero degrees, the projectile electrons in the whole energy range from the cusp ($E'=0$), field-ionized high- n Rydberg, Coster-Krönig, $\dots L$, to K Auger electrons can be observed. In addition, a large number of continuum and binary encounter electrons (BEE) are observed. In particular, measuring BEE will be a good opportunity to understand the binary encounter process and to obtain the spectrometer efficiency.

Kinematic (Doppler) broadening is a difficulty in non-zero degree high resolution Auger spectroscopy and can be evaluated through a Taylor expansion:

$$\Delta E(\theta) = \sum_n \frac{1}{n!} \frac{\partial^n E}{\partial \theta^n} (\Delta \theta)^n, \quad (7)$$

where $\Delta \theta$ is the acceptance angle of the electron spectrometer in radians. To first order, $\Delta E(\theta)$ can be given using Eq. (3):

$$\Delta E(\theta) = \frac{2E \sin \theta}{\cos \theta - \sqrt{E/t}} \Delta \theta. \quad (8)$$

For zero-degree observation, this first order term vanishes, so that the second order term of Eq. (7) is dominant and the broadening is given to the second order by:

$$\Delta E(\theta = 0^\circ) = \frac{E}{1 - \sqrt{E/t}} (\Delta \theta)^2. \quad (9)$$

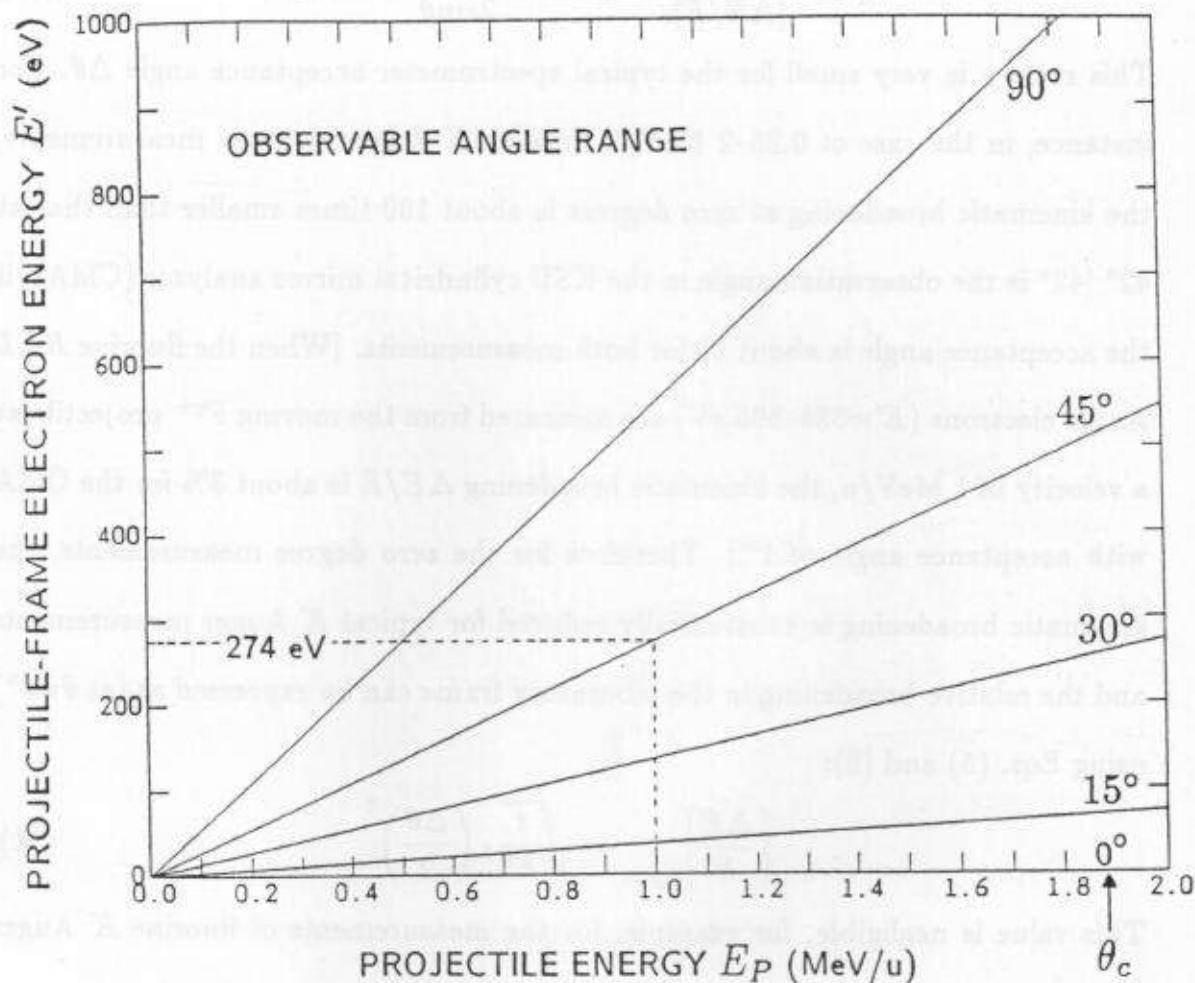


FIGURE 2. Observable angle range for a given energy of the projectile and projectile electron (see text).

In Eqs. (8) and (9), the + branch of the laboratory energy E in Eq. (2) is used.

If we compare $\Delta E(\theta = 0^\circ)$ with $\Delta E(\theta)$ by defining a factor χ as follows:

$$\chi \equiv \frac{[\Delta E/E]_{\theta=0^\circ}}{[\Delta E/E]_\theta} \simeq \frac{\sqrt{1 - (t \sin^2 \theta / E')}}{2 \sin \theta} \Delta \theta. \quad (10)$$

This ratio χ is very small for the typical spectrometer acceptance angle $\Delta \theta$. For instance, in the case of 0.25–2 MeV/u fluorine K Auger electron measurements, the kinematic broadening at zero degrees is about 100 times smaller than that at 42° [42° is the observation angle in the KSU cylindrical mirror analyzer (CMA)] if the acceptance angle is about 1° for both measurements. [When the fluorine KLL Auger electrons ($E' = 525$ – 595 eV) are measured from the moving F^{9+} projectile at a velocity of 1 MeV/u, the kinematic broadening $\Delta E/E$ is about 3% for the CMA with acceptance angle of 1° .] Therefore for the zero degree measurements, the kinematic broadening is substantially reduced for typical K Auger measurements and the relative broadening in the laboratory frame can be expressed as (at $\theta = 0^\circ$) using Eqs. (5) and (9):

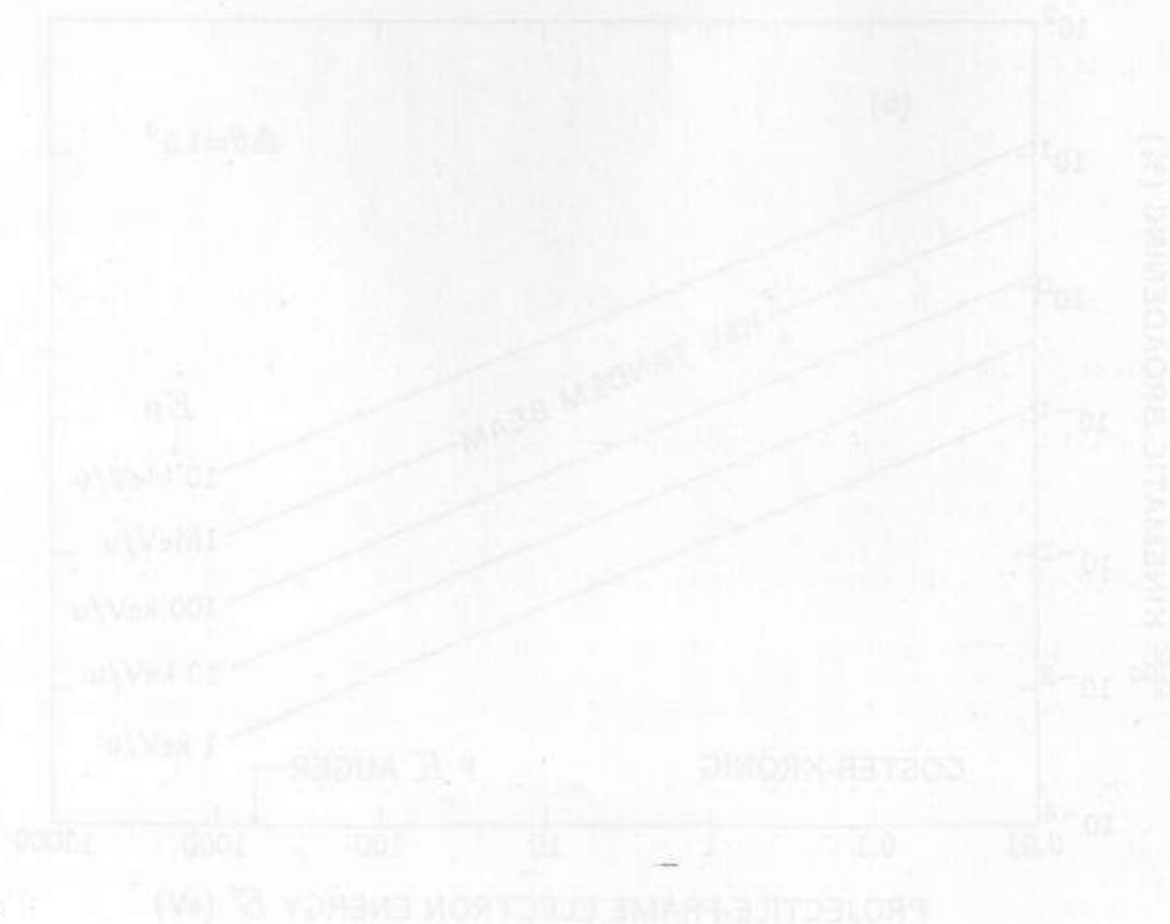
$$\left[\frac{\Delta E}{E} \right]_{\theta=0^\circ} = \sqrt{\frac{t}{E'}} \cdot \left(\frac{\Delta \theta}{2} \right)^2 \quad (11).$$

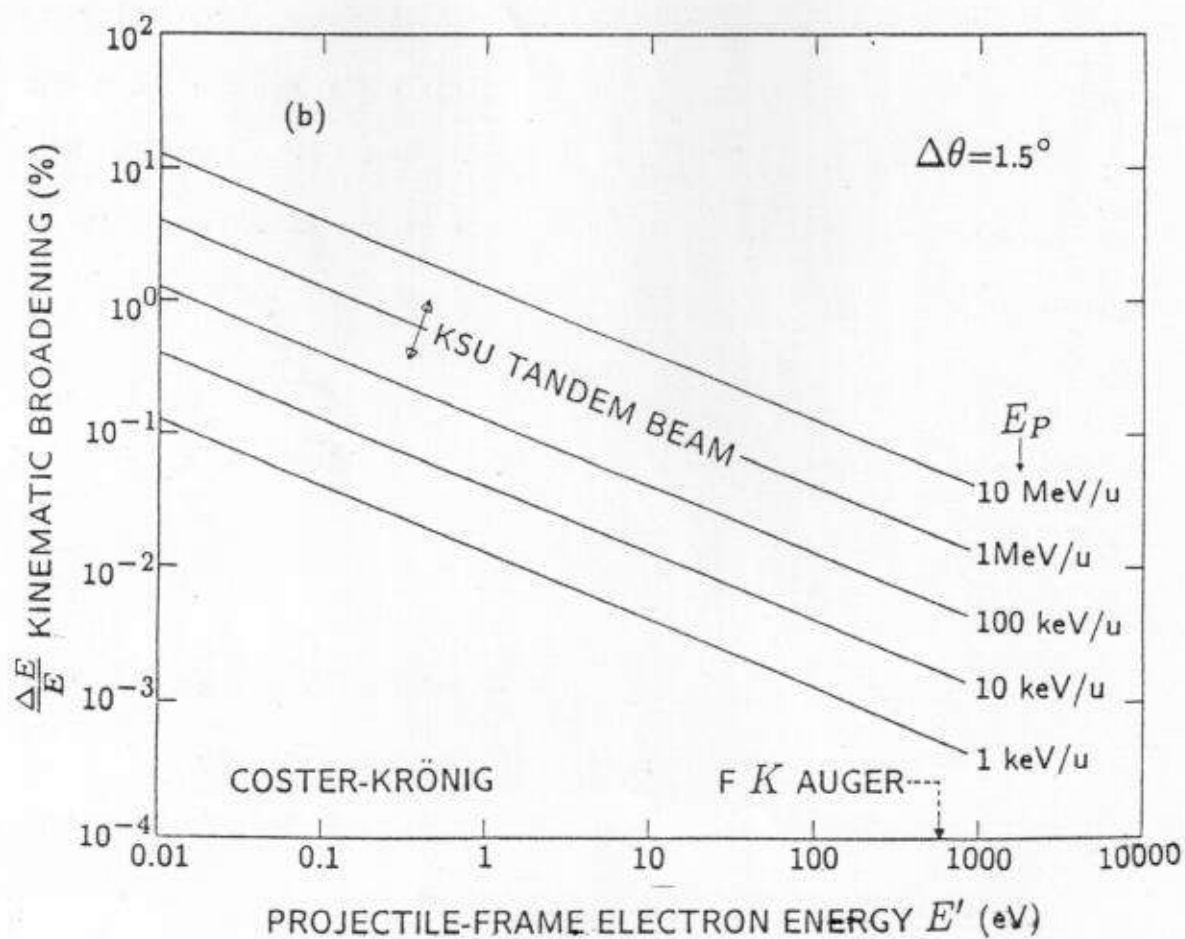
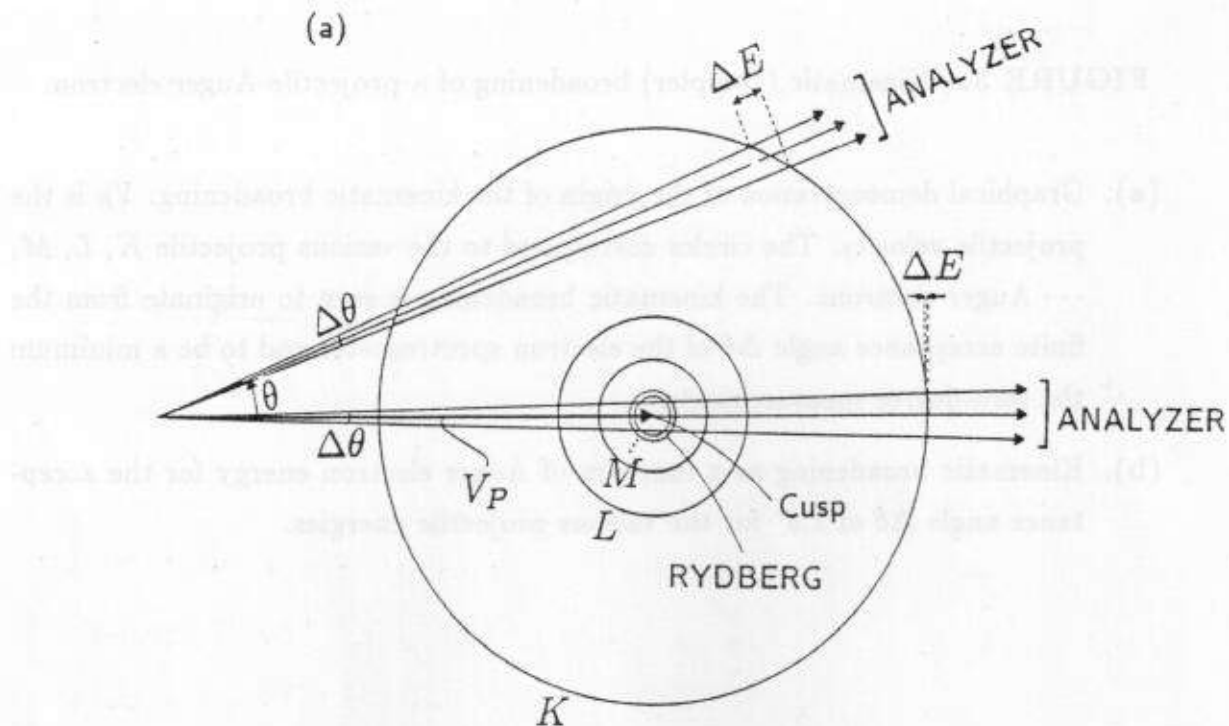
This value is negligible, for example, for the measurements of fluorine K Auger electrons emitted from about 0.25–2 MeV/u projectile for a typical acceptance angle of 1° . However, in the case of Rydberg electrons at small energies (e.g., $E' \sim 0.1$ – 10 eV), the broadening is usually not negligible.

The kinematic broadening is geometrically illustrated in Fig. 3-(a). It is easily understood that the kinematic broadening which originates from the finite acceptance angle in the electron detection, has a minimum at $\theta = 0^\circ$, and increases with decreasing projectile electron energy E' . In Fig. 3-(b), the kinematic broadening is represented with the function of the projectile electron energy E' for various projectile velocities in units of MeV/u or keV/u.

FIGURE 3. Kinematic (Doppler) broadening of a projectile Auger electron.

- (a). Graphical demonstration of the origin of the kinematic broadening. V_P is the projectile velocity. The circles correspond to the various projectile K, L, M, \dots Auger electrons. The kinematic broadening is seen to originate from the finite acceptance angle $\Delta\theta$ of the electron spectrometer and to be a minimum at the zero-degree measurements.
- (b). Kinematic broadening as a function of Auger electron energy for the acceptance angle $\Delta\theta$ of 1.5° for the various projectile energies.





B. Zero-Degree Tandem Electron Spectrometer

An electron spectrometer system consisting of a tandem 45° parallel-plate spectrometer was designed and constructed together with a suitable scattering chamber.⁴⁰ The basic arrangement of the tandem spectrometer was modeled after one built and used by the Berlin group for 0° projectile high-resolution spectroscopy.³⁹ Figs. 4 and 5 show a horizontal view (bottom view from the ground) and a vertical view, respectively, of the overall system including a differentially pumped gas cell. In this section, some design parameters are described together with some results of the system performances.

The general properties of the various electrostatic electron spectrometers (electron energy analyzers) have been reviewed by Sevier.⁴⁴ The principle of the parallel plate spectrometer was described by Yarnold and Bolton⁴⁵ for the first time, by Harrowerm⁴⁶ for the 45° entrance angle, and by Steckelmacher and Lucus⁴⁷ for the 30° entrance angle. Fig. 6 shows a typical electron trajectory through a parallel-plate spectrometer. As shown in Fig. 6, when an electron with energy E enters at an angle ϑ the uniform electric field between the two plates from the source position at $(0, h)$, the x -coordinate (or so-called spectrometer equation) is given by:⁴⁷

$$x = (h + y)\cot\vartheta + \frac{2d\sin 2\vartheta}{f}, \quad (12)$$

where d is the separation of the plates where voltage V is applied, and spectrometer constant f is defined as:

$$f \equiv \frac{Ve}{E} = \frac{2d}{l_0}\sin 2\vartheta, \quad (13)$$

where l_0 is the distance between the entrance and exit slits. Thus, the spectrometer constant can be geometrically determined and is $2d/l_0$ for the $\vartheta=45^\circ$.

Now d must be made greater than y_m , the maximum height of the parabolic

FIGURE 4. Zero-degree tandem electron spectrometer system for projectile electron studies in ion-atom collisions (horizontal bottom view). (A) target gas cell, (B) deflector, (C) Rydberg analyzer, (D) first spectrometer, (E) lens and retarding grids, (F) second spectrometer, (G) electron detector, (H) Faraday cup, and (I) μ -metal shield.

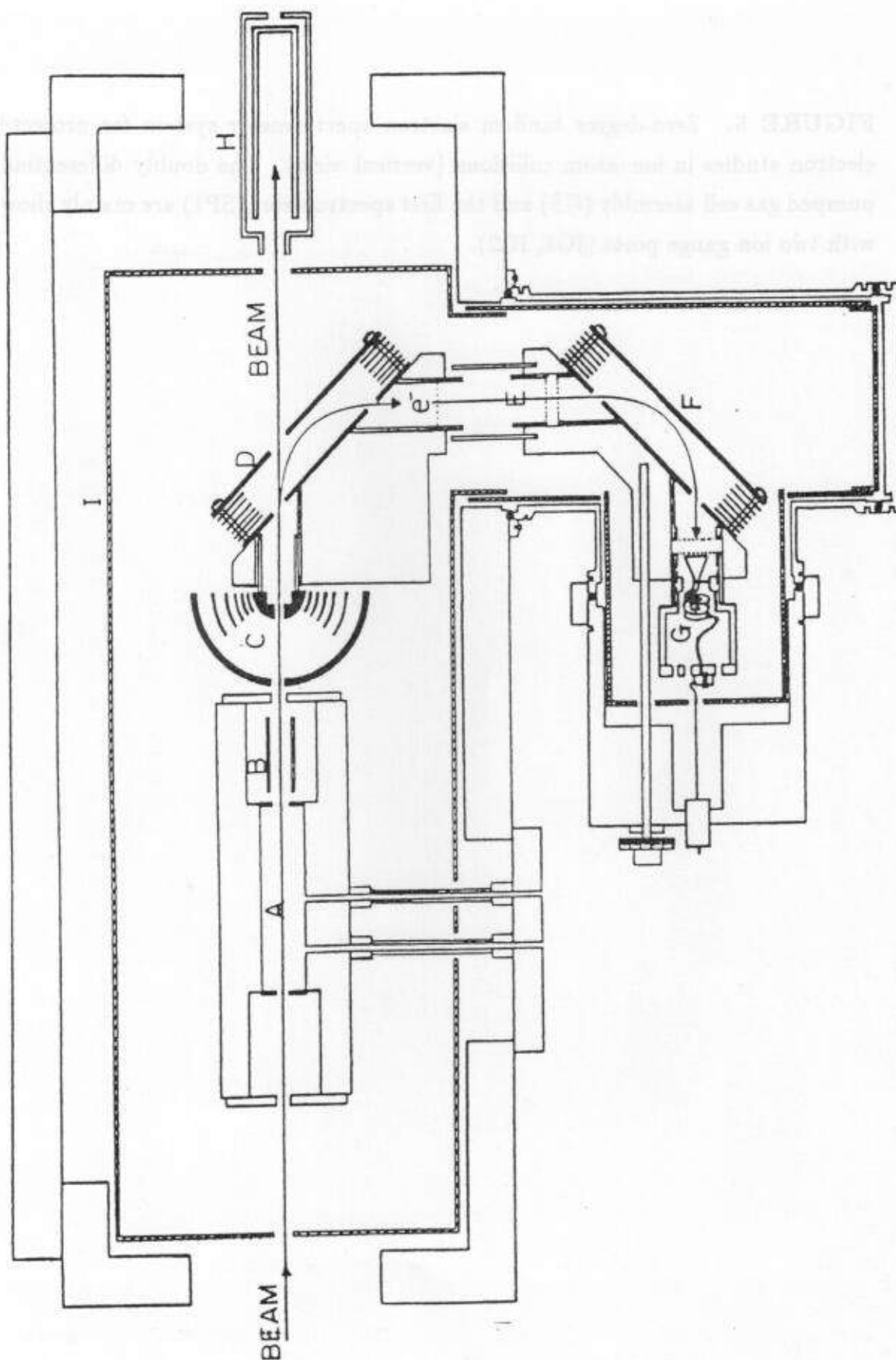
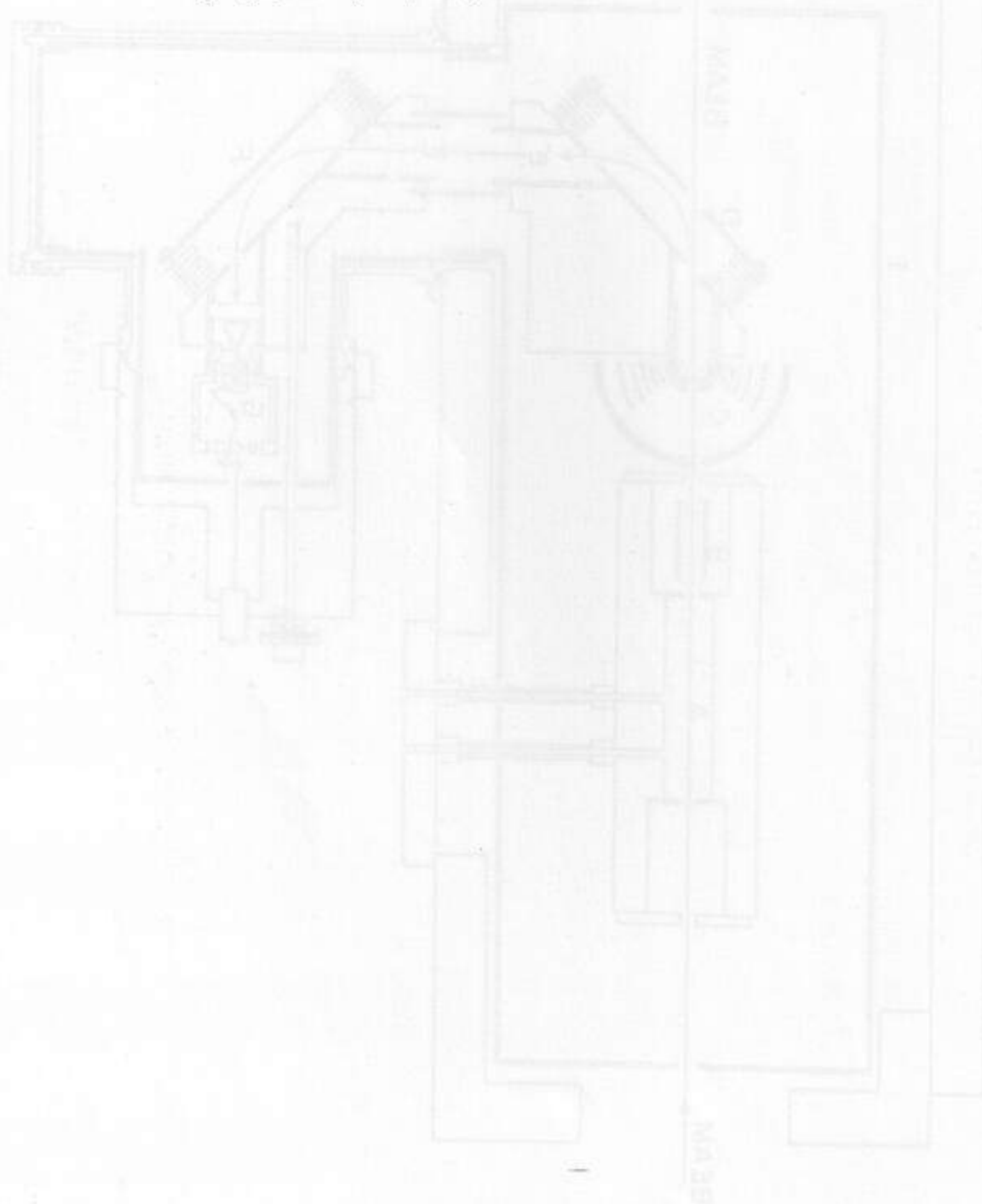
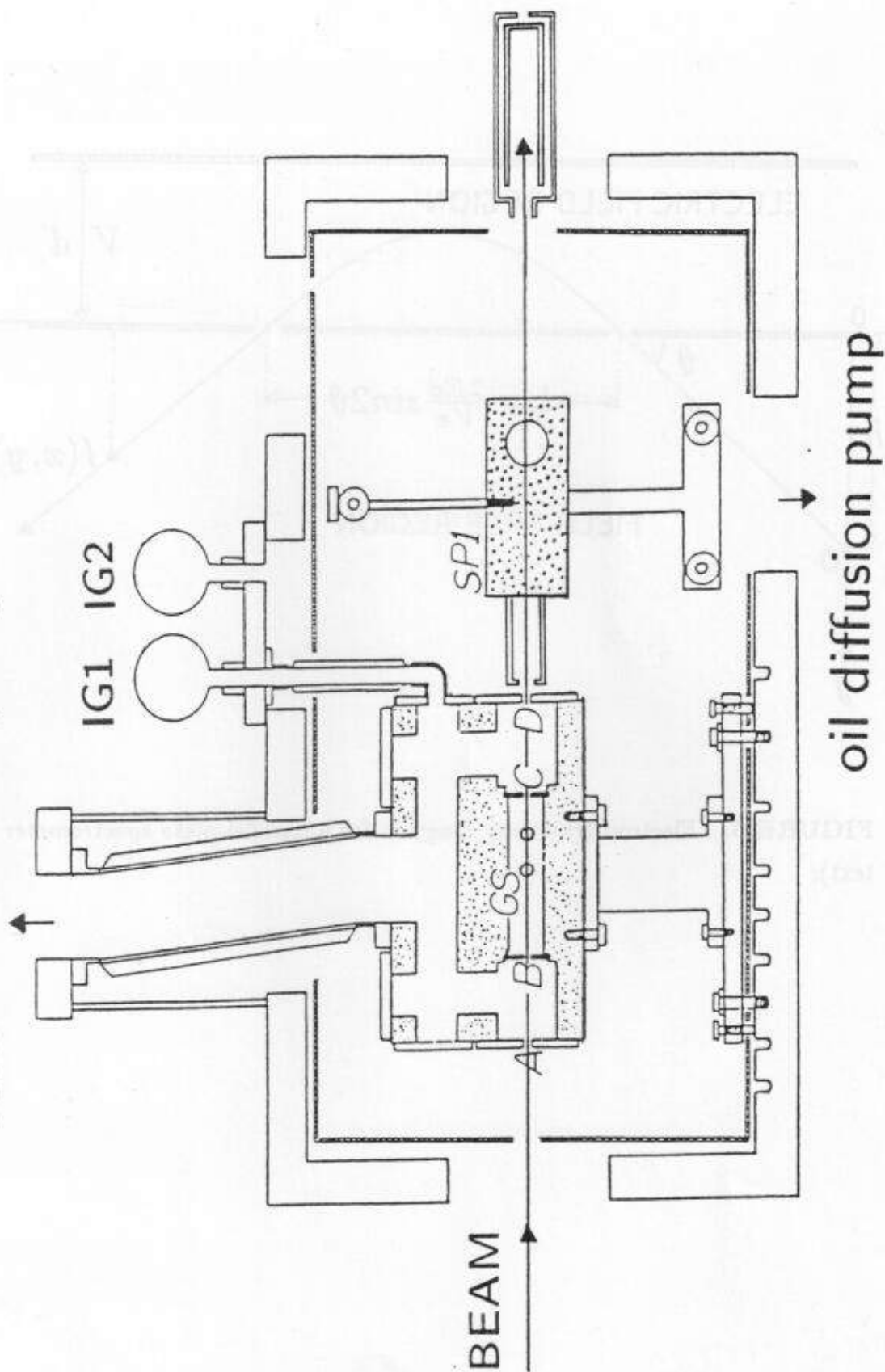


FIGURE 5. Zero-degree tandem electron spectrometer system for projectile electron studies in ion-atom collisions (vertical view). The doubly differentially pumped gas cell assembly (GS) and the first spectrometer (SP1) are mainly shown with two ion gauge ports (IG1, IG2).



turbo-molecular pump



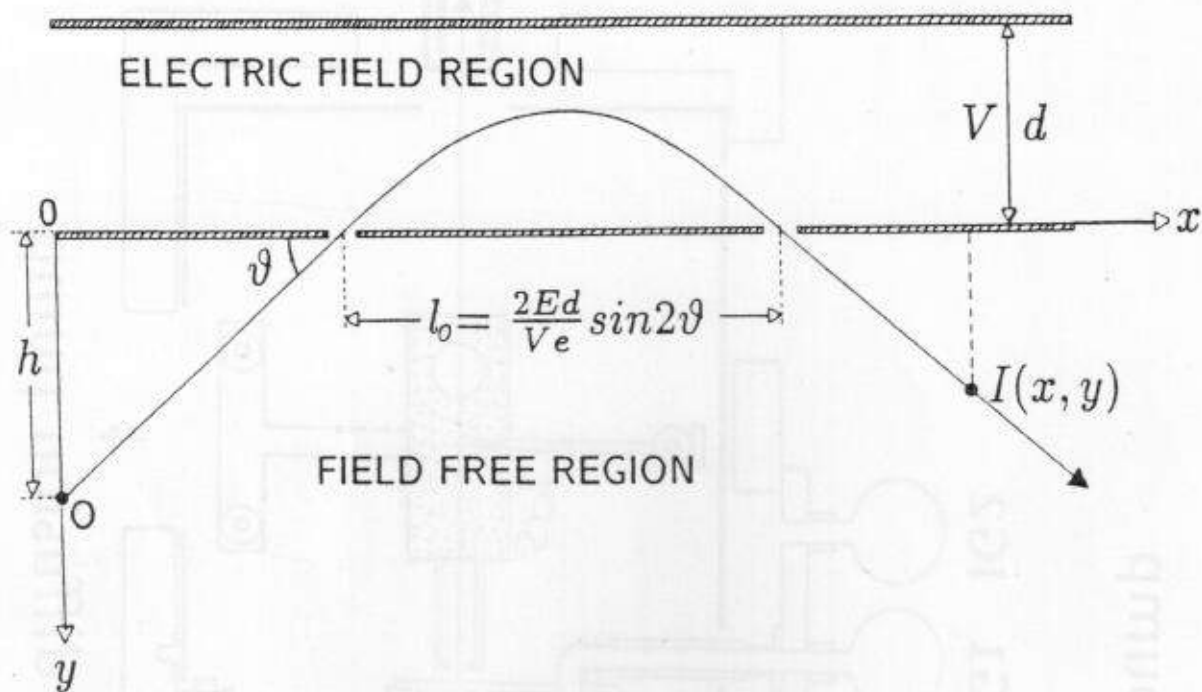


FIGURE 6. Electron trajectory diagram for a parallel-plate spectrometer (see text).

path of the electron trajectory inside the spectrometer (see Fig. 6.), so that the electrons which enter with larger angles than ϑ can be deflected without hitting the top plate. When $\vartheta=45^\circ\pm3^\circ$, $y_m=(0.25\pm0.025)l$. Therefore, the choice of $d=0.3l$ will be adequate for a $\vartheta=45^\circ$ spectrometer.

Focusing conditions can be obtained using Eq. (12). The first order focusing condition is given by:

$$\frac{\partial x}{\partial \vartheta} = \frac{-(h+y)}{\sin^2 \vartheta} + \frac{4d \cos^2 \vartheta}{f} = 0. \quad (14)$$

For the case of a 45° parallel-plate spectrometer, $h+y=0$. In other words, if the object point is located at $h=0$ (entrance slit position), the focal point will be located at $y=0$. However, in the electron spectroscopy in this work, the object point is located at $h>0$ so that the focal point will be inside the spectrometer, which means we will have a "virtual" image at $y=-h$. This concept of the virtual image will be used later when the geometrical solid angle is evaluated with electron trajectory tracing. For the second order focusing, $\partial x/\partial \vartheta = \partial^2 x/\partial \vartheta^2 = 0$. This results in $\vartheta=30^\circ$, and a 30° spectrometer also has been widely used with better focal properties. However, a 45° spectrometer was chosen in this work.

The instrumental resolution, R , of the 45° spectrometer can be given by:⁴⁴

$$R = \frac{\Delta E}{E_0} = \frac{w^i + w^o}{2l_0} + 2(\Delta \vartheta)^2 + (\Delta \phi)^2, \quad (15)$$

where w^i and w^o are the widths of the entrance and exit slits. $\Delta \vartheta$ and $\Delta \phi$ are the spectrometer acceptance angles in the dispersion plane (x - y plane in Fig. 6) and in the plane perpendicular to the dispersion plane, respectively. These values are negligibly small compared to $(w^i + w^o)/2l_0$ so that the instrumental resolution is determined mainly by the first term of Eq. (15).

In order to obtain a uniform analyzing field between the two plates of the spectrometer, fringing field reducers were inserted as partially shown in Fig. 4.

The voltage V is equally divided by connecting 20 mega-Ohm resistances between the fringing field reducers.

In the following table, some important design parameters are listed for the first and second analyzer of the present tandem 45° spectrometer.

TABLE 2

Physical quantity	Symbol	First analyzer	Second analyzer
slit separation	l_0	68.7 mm	68.7 mm
entrance slit width	w^i	3.31 mm	2.52 mm
entrance slit length	t^i	4.73 mm	9.90 mm
exit slit width	w^o	4.72 mm	1.32 mm
exit slit length	t^o	10.0 mm	9.75 mm
field plate separation	d	21.78 mm	21.21 mm
spectrometer constant	f	0.634	0.614
instrumental resolution	R	6.8%	2.8%

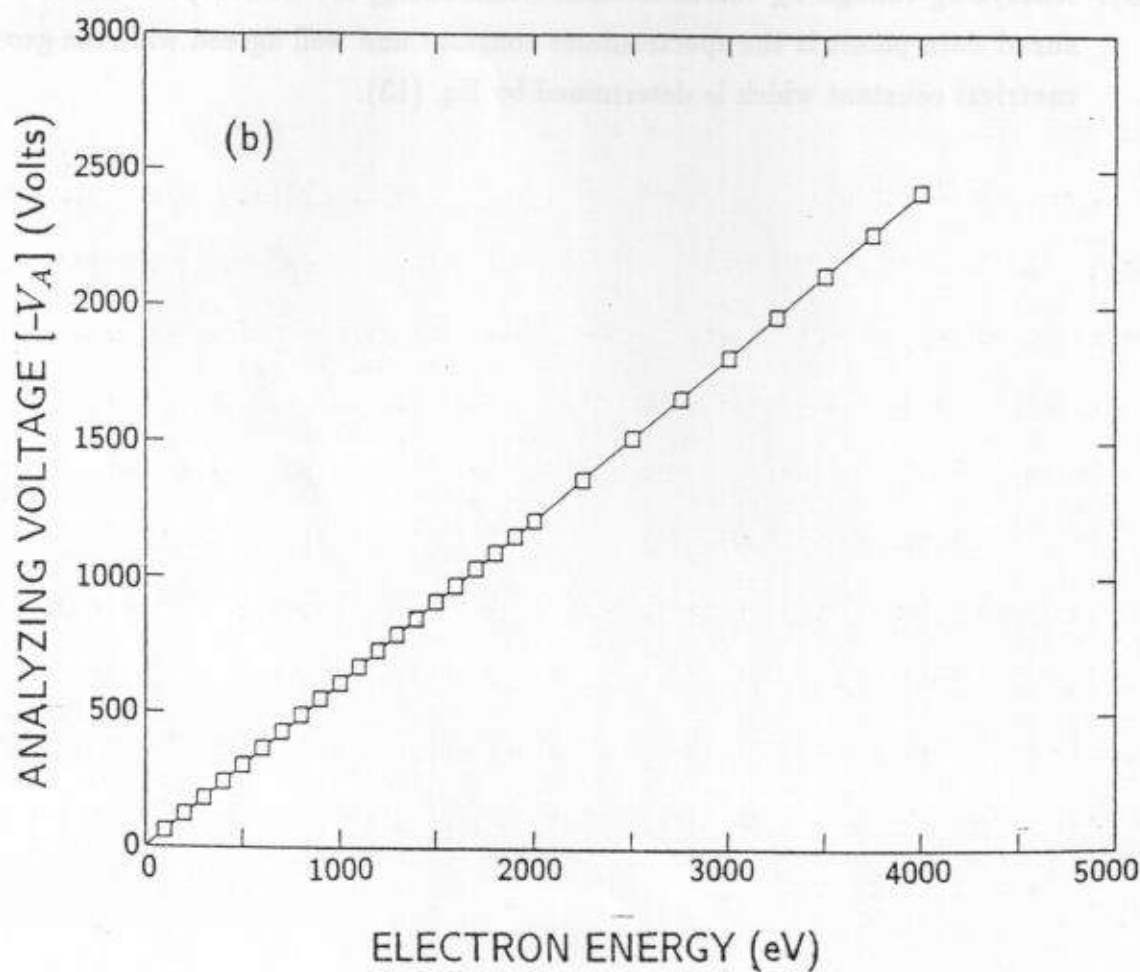
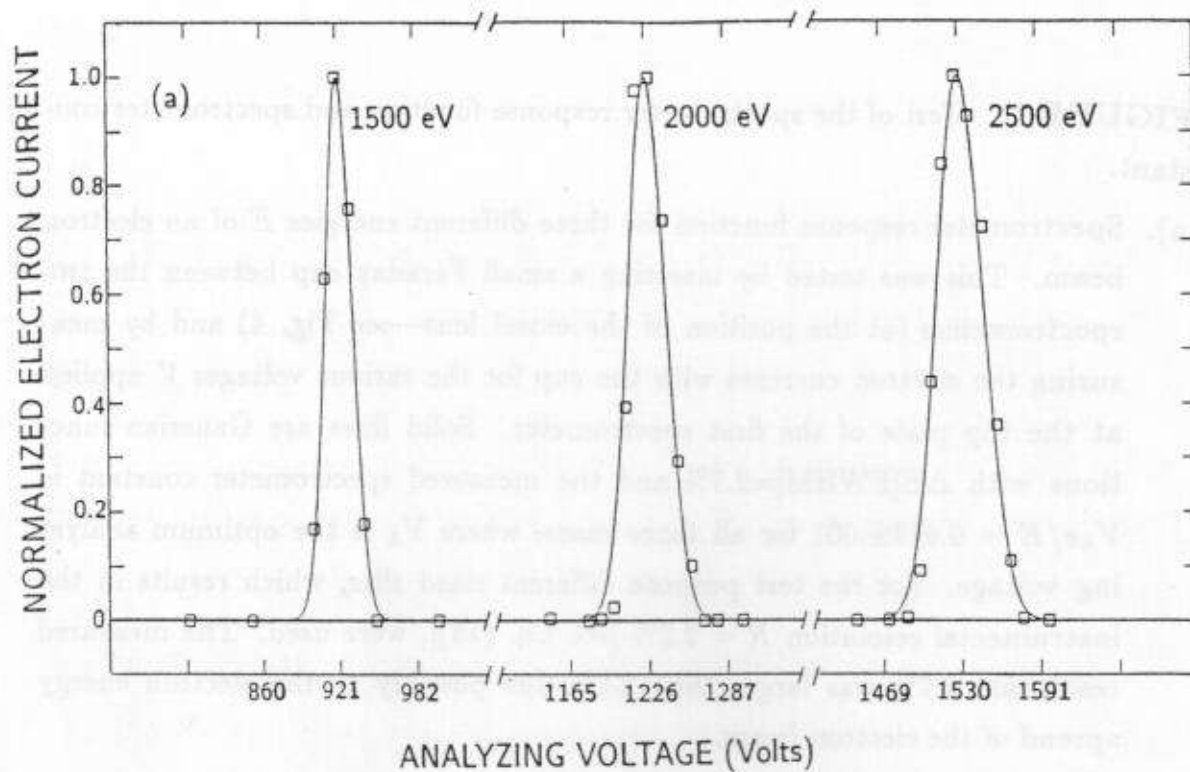
The first and second spectrometers have the same dimensions but different size slits. The geometrical FWHM energy resolution, R , is estimated to be 6.8% and 2.8% using Eq. (15) for the first and second spectrometers, respectively. The resolution R is reasonably confirmed using a 1.5–2.5 keV electron beam obtained from the typical electron gun which was installed before the collision chamber for the testing. This result is shown in Fig. 7-(a), where the spectrometer response function also can be obtained if the electron beam is truly monochromatic.

The geometrical spectrometer constants f , which are obtained by Eq. (13), are 0.634 and 0.614 for the first and second spectrometers, respectively. The "constant" value of 0.614 is well confirmed using electron beams at various energies. This test was done by finding the optimum analyzing voltages for the various electron beam energies which are known by applied voltages to the electron gun.

FIGURE 7. Test of the spectrometer response function and spectrometer constant.

- (a). Spectrometer response function for three different energies E of an electron beam. This was tested by inserting a small Faraday cup between the two spectrometers (at the position of the einzel lens—see Fig. 4) and by measuring the electron currents with the cup for the various voltages V applied at the top plate of the first spectrometer. Solid lines are Gaussian functions with $\Delta E[\text{FWHM}] = 2.7\%$ and the measured spectrometer constant is $V_A e / E = 0.613 \pm .001$ for all three cases, where V_A is the optimum analyzing voltage. For the test purpose different sized slits, which results in the instrumental resolution $R = 2.2\%$ [see Eq. (15)], were used. The measured resolution 2.7% was larger than 2.2% due possibly to the electron energy spread of the electron beam.
- (b). Analyzing voltage V_A versus electron beam energy E . The slope of the measured data points is the spectrometer constant and well agreed with the geometrical constant which is determined by Eq. (13).





This result is given in Fig. 7-(b).

The first and second spectrometers were assembled in the tandem arrangement as shown in Fig. 4. Both spectrometers were installed with several adjustments for easy alignment.

The most important experimental requirement in this study is obtaining high resolution electron spectra, since without this the state-resolved Auger electron studies are not allowed. The technique of the high energy resolution was facilitated by electron energy retardation between the two spectrometers. This energy retardation was effected by inserting two parallel high-transmission grids between the two spectrometers. The overall energy resolution for high resolution spectra is determined by the pass energy, E_{pa} , after the retarding potential between the two grids and R , the energy resolution of the second spectrometer, as follows:

$$\frac{\Delta E}{E} = \frac{E_{pa} \cdot R}{E} = \frac{R}{F}, \quad (16)$$

where we define the retarding factor, $F = E/E_{pa}$.

A simple einzel lens was placed between the two spectrometers to focus the outgoing electrons from the first spectrometer and thus increase the transmission. The optimum einzel lens voltage is determined empirically. With the lens, the transmission (thus the total efficiency) of the system has been observed to increase by a factor of about 2 (for the retarding factor=15) without any change in the structure or shape of the electron spectra. This is illustrated in Fig. 8.

During the early stage of the system development a strong peak due to spectrometer field ionized high- n Rydberg electrons^{48,49} was observed around the continuum cusp peak for 0.5-1.5 MeV/u O^{q+} , $F^{q+} + He$, Ne collisions.⁴⁰ A Rydberg electron analyzer⁵⁰ was also constructed and installed before the first spectrometer to study the production of high- n Rydberg states in ion-atom collisions (see

FIGURE 8. Einzel lens performance for a high-resolution electron spectrum. The pass energy E_{pa} is 150eV and the average laboratory Auger energy is 1600 eV. Thus, the overall retarding factor F is about 10.7. The lens power was observed to be about 2.5 from the measured electron yields, which means an increase of the counting rate by this factor.

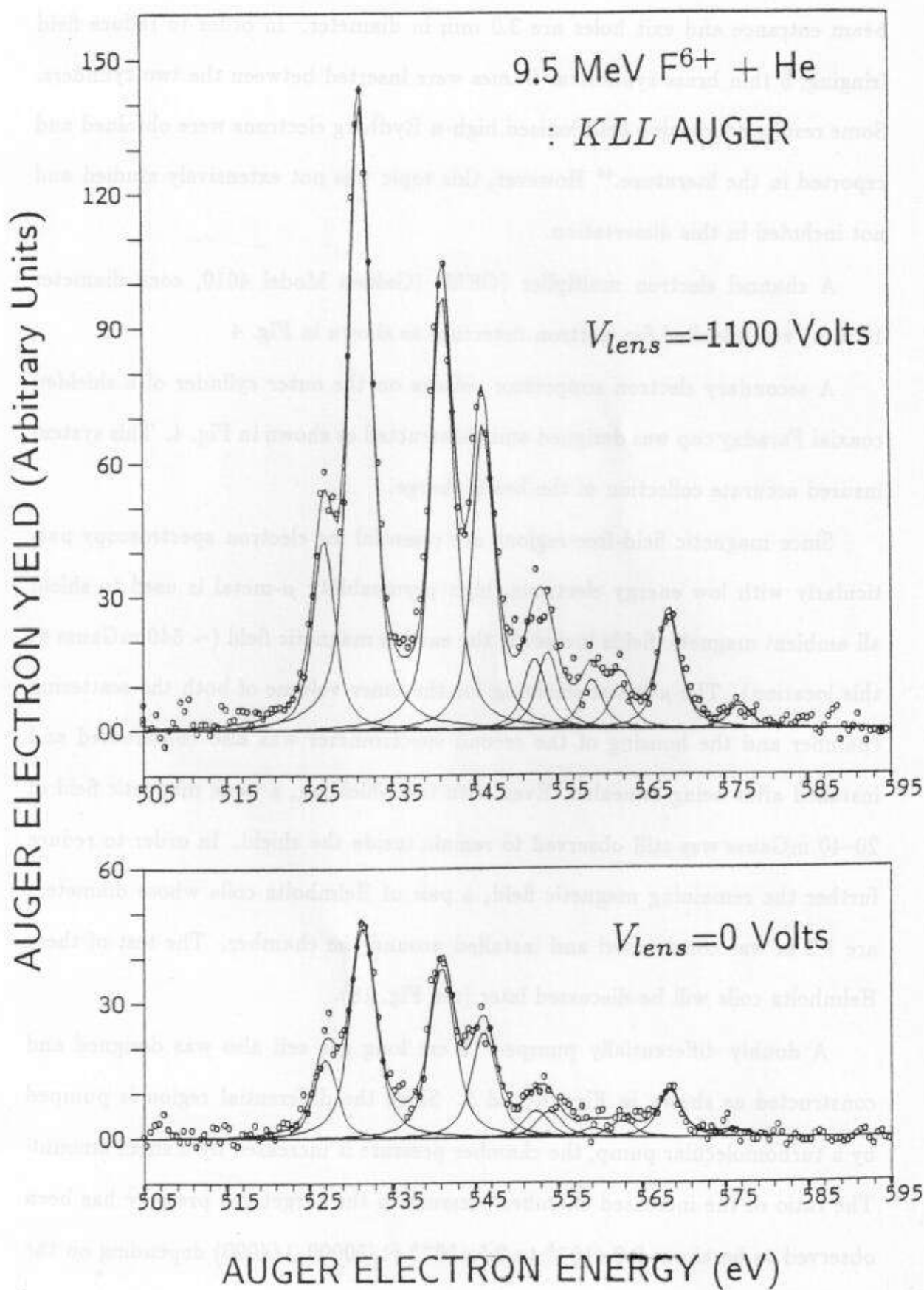


Fig. 4). The radii of inner and outer cylinders are 15 mm and 60 mm and the beam entrance and exit holes are 3.0 mm in diameter. In order to reduce field fringing, 5 thin brass cylindrical frames were inserted between the two cylinders. Some results concerning field-ionized high- n Rydberg electrons were obtained and reported in the literature.⁴⁰ However, this topic was not extensively studied and not included in this dissertation.

A channel electron multiplier (CEM) (Galileo Model 4010, cone diameter 10 mm) was installed for electron detection as shown in Fig. 4

A secondary electron suppressor voltage on the outer cylinder of a shielded coaxial Faraday cup was designed and constructed as shown in Fig. 4. This system insured accurate collection of the beam charge.

Since magnetic field-free regions are essential for electron spectroscopy particularly with low energy electrons, high permeability μ -metal is used to shield all ambient magnetic fields including the earth's magnetic field (~ 540 mGauss at this location). The μ -metal shielding for the inner volume of both the scattering chamber and the housing of the second spectrometer was also constructed and installed after being annealed. Even with this shielding, a weak magnetic field of 20–40 mGauss was still observed to remain inside the shield. In order to reduce further the remaining magnetic field, a pair of Helmholtz coils whose diameters are 1.2 m was constructed and installed around the chamber. The test of these Helmholtz coils will be discussed later (see Fig. 18).

A doubly differentially pumped 10 cm long gas cell also was designed and constructed as shown in Figs. 4 and 5. Since the differential region is pumped by a turbomolecular pump, the chamber pressure is increased by a small amount. The ratio of the increased chamber pressure to the target gas pressure has been observed to be about 2.0×10^{-5} to 2.5×10^{-4} ($1/50000$ – $1/4000$) depending on the

target gas species and on the size of the beam entrance and exit apertures of the gas cell and gas cell differential region. The differential pumping performance of the gas cell is demonstrated in Fig. 9. With 1.6-2.4-2.4-2.5 mm apertures for beam entrance and exit as seen in Fig. 5 (see A, B, C, and D), the gas cell can be run up to 100 mTorr (0.1 mmHg) of neon increasing the chamber pressure by only 2×10^{-6} mmHg. The base (background) pressure of the chamber has been observed to be about 1×10^{-6} mmHg during all the experiments. The chamber pressure was measured with the ion gauge located on the top of the chamber (see Fig. 5). In the following table, the ratio of the increased chamber pressure to the target gas cell pressure is tabulated with a different set of apertures and for different target gases. These results were obtained in all the accelerator beam times in this work. The target pressure range was 2.5 to 50 mTorr insuring single collision conditions. The target gas cell pressure was measured with an MKS Baratron capacitance manometer (type 270B) and was maintained by an MKS pressure controller (type 250B).

TABLE 3

Target gas	Ratio of increased chamber pressure to target pressure	
	1.6-2.4-2.4-2.5 mm apertures	1.6-2.4-2.4-4.0 mm apertures
He	$1.5-3 \times 10^{-5}$	$4-7 \times 10^{-5}$
H ₂	$6-8 \times 10^{-5}$	$20-30 \times 10^{-5}$
Ne	2.0×10^{-5}	$\sim 8 \times 10^{-5}$

The scattering chamber, which is made from a 1-inch thick aluminum plate, was designed and constructed as sketched in Figs. 4 and 5. This chamber is pumped by a 4-inch oil diffusion pump and is installed on a platform making it possible to align the chamber to the beam direction.

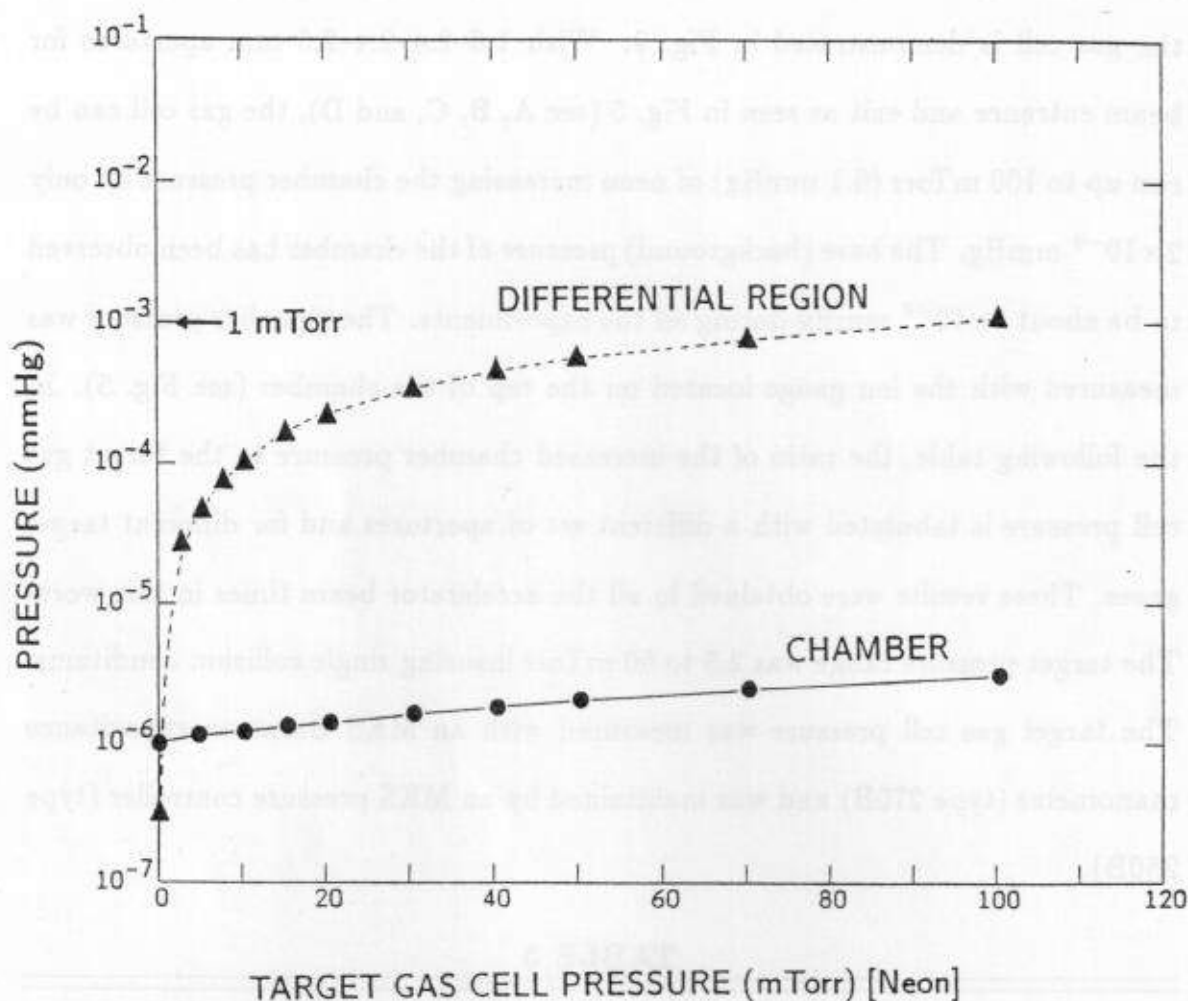


FIGURE 9. Double Differential pumping performance of the target gas cell. For the performance test, the pressures of the chamber and the gas-cell differential region were measured with two ion gauges (see Fig. 5) for the various pressures of Neon gas in the target gas cell.

The geometrical solid angle of the present tandem spectrometer can be evaluated by a simple electron-ray tracing shown in Fig. 10 with the assumption of a uniform analyzing electric field inside each spectrometer. Without any electron energy retarding and any focusing (as discussed later, the absolute cross sections are measured under these conditions.), the detector subtends angles $\Delta\theta$ in the dispersion plane (x - y plane) and $\Delta\phi$ in the plane perpendicular to the dispersion plane. These angles can be calculated using the geometrical factors. For a point source located in the collision region of the gas cell with ion projectiles, $\Delta\theta$ and $\Delta\phi$ are given by:

$$\Delta\theta = \frac{w_2^o/\sqrt{2}}{y + S} \quad (17a)$$

and

$$\Delta\phi = \frac{t_2^o}{y + S + L_1 + L_2}, \quad (17b)$$

where w_2^o and t_2^o (the values listed in Table 2) are the width and length, respectively, of the exit slit of the second spectrometer which has the smallest subtending angles for the channeltron detector among the four slits of the two spectrometers in the present system, y is the distance from the source point to the entrance slit of the first spectrometer, S is the distance between the exit slit of the first spectrometer and the entrance slit of the second spectrometer, and L_1 and L_2 are electron parabolic-path lengths in each spectrometer. In the evaluation of $\Delta\theta$, L_1 and L_2 are not included in the denominator, since electrons are not diverging in the dispersion plane inside the spectrometer as illustrated in the Fig. 10 using the concept of a virtual image. However, in the $\Delta\phi$ direction the electron continuously diverges until it is detected by the channeltron. Therefore, the solid angle of the present tandem spectrometer system can be evaluated by treating the extended

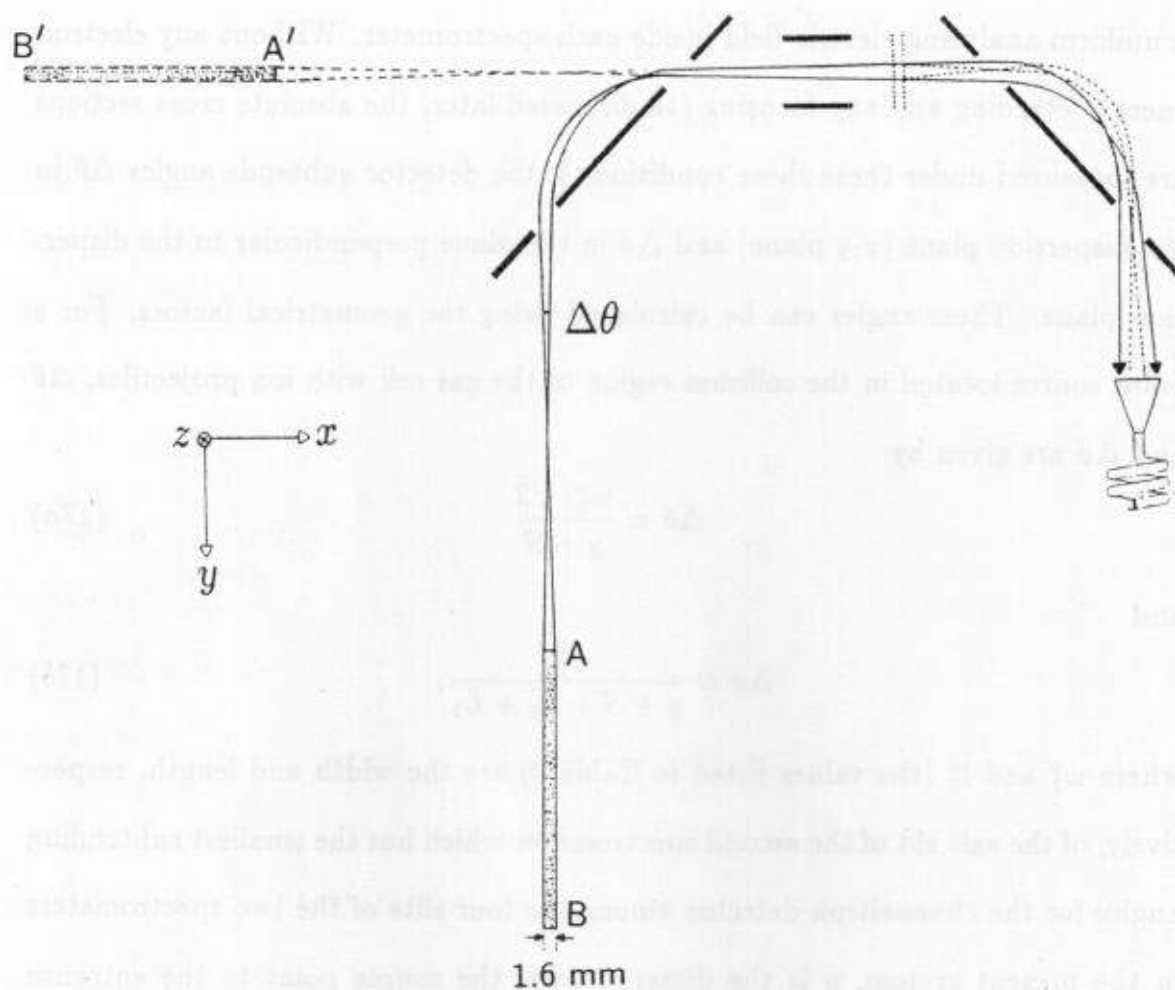


FIGURE 10. Electron ray trajectory in the tandem spectrometer. The trajectory is illustrated in the $x - y$ dispersion plane. In this plane, CD represents a virtual image of the line source AB for the first spectrometer. The projectile beam is collimated by an 1.6mm-diameter collimator. With an ideal lens and retarding grids, the trajectory for the second spectrometer is shown as short-dashed lines.

source as a line source as follows:

$$\Delta\Omega = \frac{1}{l} \cdot \int_{y_c-l/2}^{y_c+l/2} \Delta\theta \cdot \Delta\phi dy, \quad (18)$$

where y_c is the distance from the center of the gas cell to the entrance of the first spectrometer and l is the gas cell length. By this way of estimation, the solid angle is about $5-6 \times 10^{-5}$ sr depending on the position of the gas cell. The solid angle, assuming that all of the source is located at the gas cell center (point source approximation), was calculated to be about 2% smaller than the value above for the gas cell and spectrometer arrangement.

In the following table, some geometrical factors are summarized for the present tandem spectrometer. The geometrical factors (design parameters) for an individual spectrometer were already listed in the Table 3. The physical quantities are explained in the text above.

TABLE 4

Physical quantity	Symbol	Values I	Values II
spectrometer separation	S	120 mm	120 mm
gas cell distance	y_c	228 mm	202 mm
gas cell length	l	100 mm	100 mm
acceptance angle	$\Delta\theta$	$0.18^\circ-0.13^\circ$	$0.20^\circ-0.14^\circ$
acceptance angle	$\Delta\phi$	$1.2^\circ-1.0^\circ$	$1.3^\circ-1.1^\circ$
solid angle	$\Delta\Omega$	5.2×10^{-5}	6.0×10^{-5}

Values I were used in the first half of the experiment of this work. Values II were used in the second half of the experiment after taking out the Rydberg analyzer and the deflector (see Fig. 4) to increase the solid angle $\Delta\Omega$.

III. EXPERIMENT

A. Projectile Ions

Fig. 11 shows a schematic diagram of a fast ion-atom collision of interest in this work. As discussed earlier, studying atomic states formed in highly-charged heavy projectile ions (e.g., He-like F^{7+}) colliding with gas target atoms was accomplished by measuring the electrons emitted from projectile autoionization at 0° with respect to the beam direction. Since I concentrated on inner-shell processes, projectile K Auger electrons were measured. Binary encounter electrons produced from target direct ionization also were observed as a strong background resulting in a good opportunity to understand ion-electron binary encounter process in ion-atom collisions.

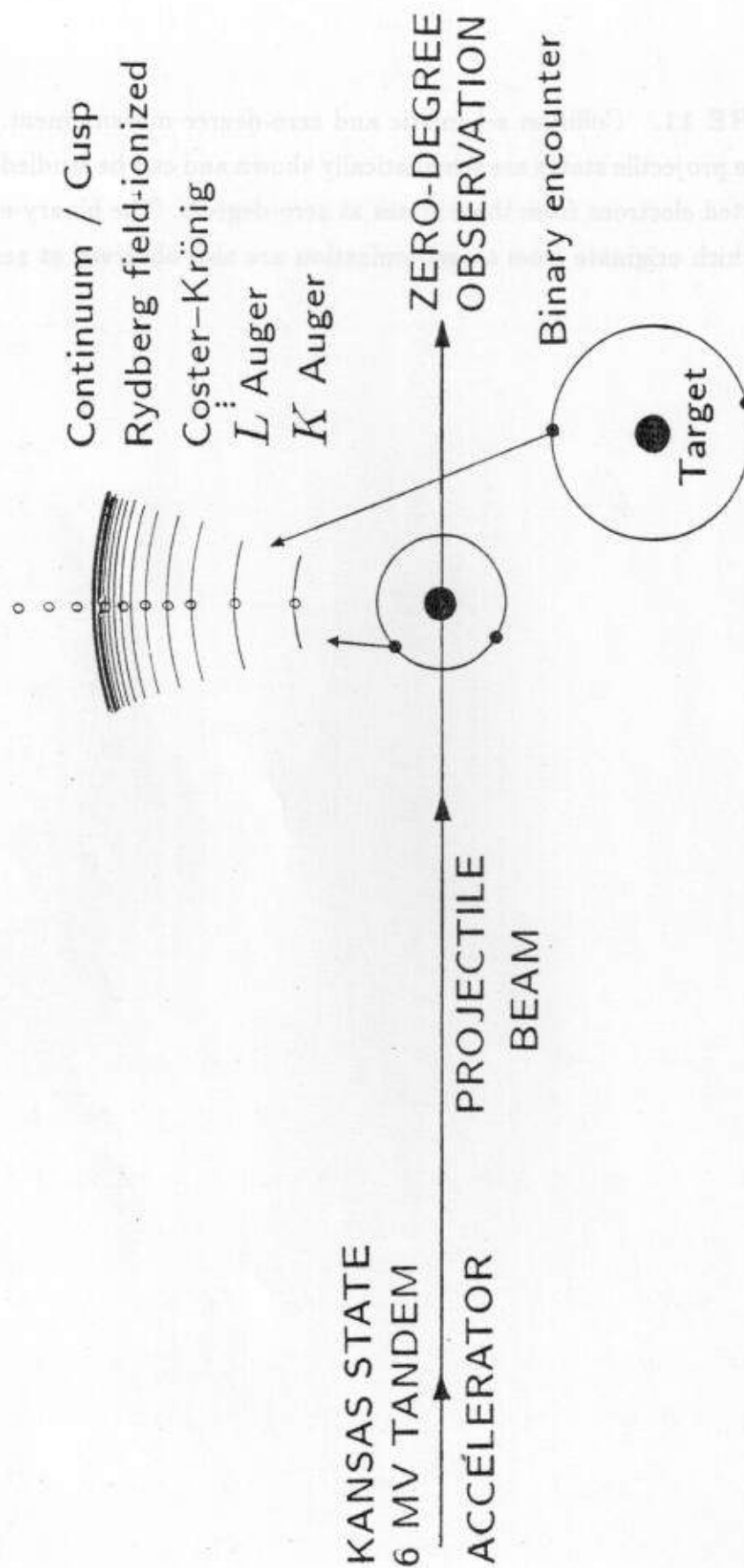
One important aspect in the *fast* ion collisions with the *light* targets of H_2 and He is that the effects from the projectile Rutherford scattering by the target atom or nuclear reaction between the two nuclei is negligible in the present measurements of atomic processes. If some incoming projectiles are scattered out considerably from the original beam direction while passing the gas targets, this scattering probability would result in an erroneous beam integration. As the worst case senario of the projectile scattering in the present study, let us consider 0.25 MeV/u $F^{9+} + He^{2+}$ collisions. The cross section for the projectile scattering to laboratory angle larger than 0.2° , the minimum diverging angle of the present aperture arrangement (see Fig. 10), is estimated to be $\sigma = 2 \times 10^{-19} \text{ cm}^2$ by integrating the Rutherford formula. This gives the probability of $P = n l \sigma = 0.0013$ for 40 mTorr target gas pressure, where $n = 3.22 \times 10^{13} / \text{cm}^3$ is the gas cell number density per 1 mTorr pressure at 300 °K and $l_g = 10 \text{ cm}$ is the gas cell length.

Besides, the projectile momentum change during any collision event of RTE,

FIGURE 11. Collision schematic and zero-degree measurement. All the measurable projectile states are schematically shown and can be studied by measuring the ejected electrons from these states at zero-degrees. The binary-encounter electrons which originate from target ionization are also observed at zero-degrees.



COLLISION SCHEMATIC / ZERO-DEGREE MEASUREMENT



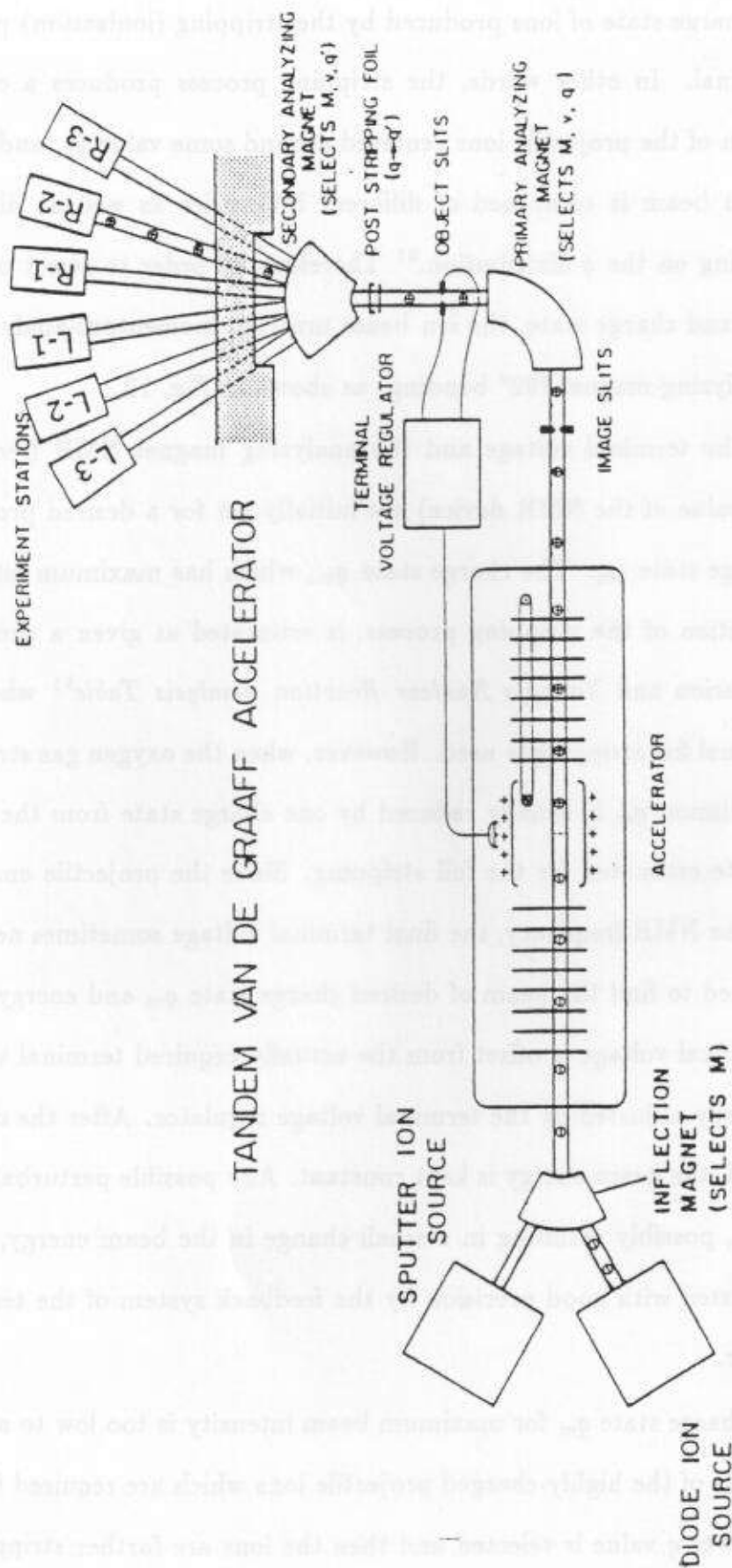
BFe, eeE, and eeI in the present study is not considered either, since any detectable evidence resulting from these phenomena was not observed in the present experimental studies of fast ion-atom collisions. In other words, any change in the projectile energy and its scattering angle during the collision was not accounted for in the measurements of the Auger energy and cross sections.

All measurements were performed at the James R. Macdonald Laboratory at Kansas State University (KSU). The highly charged projectile ions were obtained from the EN tandem Van de Graaff accelerator. The maximum terminal voltage available from the accelerator is 6 MV. A schematic diagram of the main accelerator facilities is shown in Fig. 12. Two ion sources, two analyzing magnets (primary and secondary), and several beam lines of experimental stations are shown schematically in Fig. 12. (This accelerator also will be used as the ion beam injector of a superconducting linear accelerator, which has been under construction for the period of the present work.)

Singly-charged, negative ions, were extracted from either the diode ion source (plasma-arc type) or the sputter ion source (cesium-sputter type) depending on its capability of producing a high intensity of the negative ions. F^- for a F^{q+} beam, CN^- for N^{q+} and C^{q+} beams, and H^- for a proton beam were extracted from the diode ion source, while O^- for a O^{q+} beam was extracted from the sputter ion source. The negative ions of energy, about 50 keV, were then analyzed by the 20° inflection magnet as shown in Fig. 12.

These negative ions were then injected into the accelerator, accelerated to an energy of Ve , where V is the highly positive voltage (1-6 MeV) of the terminal halfway inside the accelerator, stripped to become positive ions of charge state q by a low density oxygen gas or a thin carbon foil ($5\mu\text{g}/\text{cm}^2$), and accelerated again away from the terminal. The final energy of the accelerated ions is $(1 + q)Ve$,

FIGURE 12. Schematic of the 6 MV tandem Van de Graaff accelerator at the J.R. Macdonald Laboratory at Kansas State University.



where q is the charge state of ions produced by the stripping (ionization) process inside the terminal. In other words, the stripping process produces a charge-state distribution of the projectile ions centered around some value q_m and, thus, the resulting ion beam is composed of different intensities as well as different energies depending on the q -distribution.⁵¹ Therefore, in order to select out the desired velocity and charge state, the ion beam must be momentum-analyzed by the primary analyzing-magnet (90° bending) as shown in Fig. 12.

In reality, the terminal voltage and the analyzing magnet NMR frequency (the calibrated value of the NMR device) are initially set for a desired projectile energy and charge state q_m . The charge state q_m , which has maximum intensity in the q -distribution of the stripping process, is estimated at given a projectile energy using Marion and Young's *Nuclear Reaction Analysis Table*⁵¹ when the method of terminal foil stripping is used. However, when the oxygen gas stripping is used, the maximum q_m is usually reduced by one charge state from the maximum charge state estimated for the foil stripping. Since the projectile energy is determined by the NMR frequency, the final terminal voltage sometimes needs to be manually tuned to find the beam of desired charge state q_m and energy when the initially terminal voltage is offset from the actually required terminal voltage to be automatically adjusted by the terminal voltage regulator. After the desired beam is obtained, the beam energy is kept constant. Any possible perturbation of terminal voltage, possibly resulting in a small change in the beam energy, is automatically adjusted with good precision by the feedback system of the terminal voltage regulator.

When the charge state q_m for maximum beam intensity is too low to acquire sufficient amounts of the highly-charged projectile ions which are required for the experiment, a lower q value is selected and then the ions are further stripped by

a post-stripping foil (5 or 10 $\mu\text{g}/\text{cm}^2$ carbon foil) located between the primary and secondary analyzing magnet. Thus, the beam of higher charge states $q' > q$, whose intensity distribution may be centered around some values q'_m , is obtained. Finally, the projectile ion beam with the required charge state is selected by the secondary analyzing (switching) magnet and injected into beam line R-2 toward the scattering chamber. 2026

When the beam was obtained by post-stripping, the beam current measured by the Faraday cup in the collision chamber was usually observed to decrease with time due to the apparent deposition of the carbon-oxide material from the vacuum system. This means the beam centroid energy is slightly decreased. In this case, tuning the switching magnet is not desirable to increase or to retrieve the projectile beam intensity, since this leads to a possibility of injecting the beam at a slightly different energy which shifts the projectile electron spectrum. Instead, the foil position is moved to an unused part of the foil or the foil should be replaced with a new foil of the original thickness. This turned out to be a crucially important step, in particular, for the projectile high resolution electron spectroscopy of main interest in this study. Experience shows that the analyzing fields of the magnets rarely drifted. Maintaining a very constant projectile energy is required when high resolution spectra are obtained by multiple scans of the electron energy. In other words, if the beam energy is changed during a spectrum scan, where the electron energy is multiply swept, the laboratory Auger electron energy will be changed for a given Auger transition and thus the measured Auger lines will be broadened or mixed with the adjacent Auger transition which were recorded for the time of the previous sweeps.

Since the projectile beam is highly collimated by the 1.6 mm diameter collimator before the differential region of the gas cell (see Figs. 4 and 10), a beam

which is well focused with a good para-axial property is necessary in order to obtain as high as possible electron counting rate. This is done by utilizing a pair of quadrupole lens in the beam line shown in Fig. 13. Ion pumps on the beam line were all decommissioned by removing all the permanent magnets, since it was observed that both the high voltage (5 keV) inside the pumps and the strong magnet field outside the pumps deflect and defocus the projectile ion beam, in particular, for low energy and high charge states. In addition, the quadrupole lens were carefully aligned to the beam axis in order to get proper focusing properties during the test experiments for the spectrometer system development and the beam line refinement.

After obtaining a good beam trajectory with a high intensity, the beam is focused by the beam-line quadrupole lens by monitoring the focused beam spot on a quartz located just before the scattering chamber (see Fig. 13). Finally, the projectile beam is retuned by using all the adjustments mentioned above by monitoring the beam current at the Faraday cup after the gas cell. The typical beam charge current used for the experiment was 50–800 nA depending on the charge state and energy of the projectile beam.

B. Electron Spectrum Acquisition

The experimental procedures of obtaining raw electron spectra are described in this section. The purpose of the present electron spectroscopy is to measure electron "energy" and to count the "number" of electrons for each electron energy for a given collision condition, thus extracting the electron production cross sections of interest.

The electrons are first energy-analyzed by the tandem electron spectrometer. Suppose an electron with energy E in eV enters the first spectrometer.

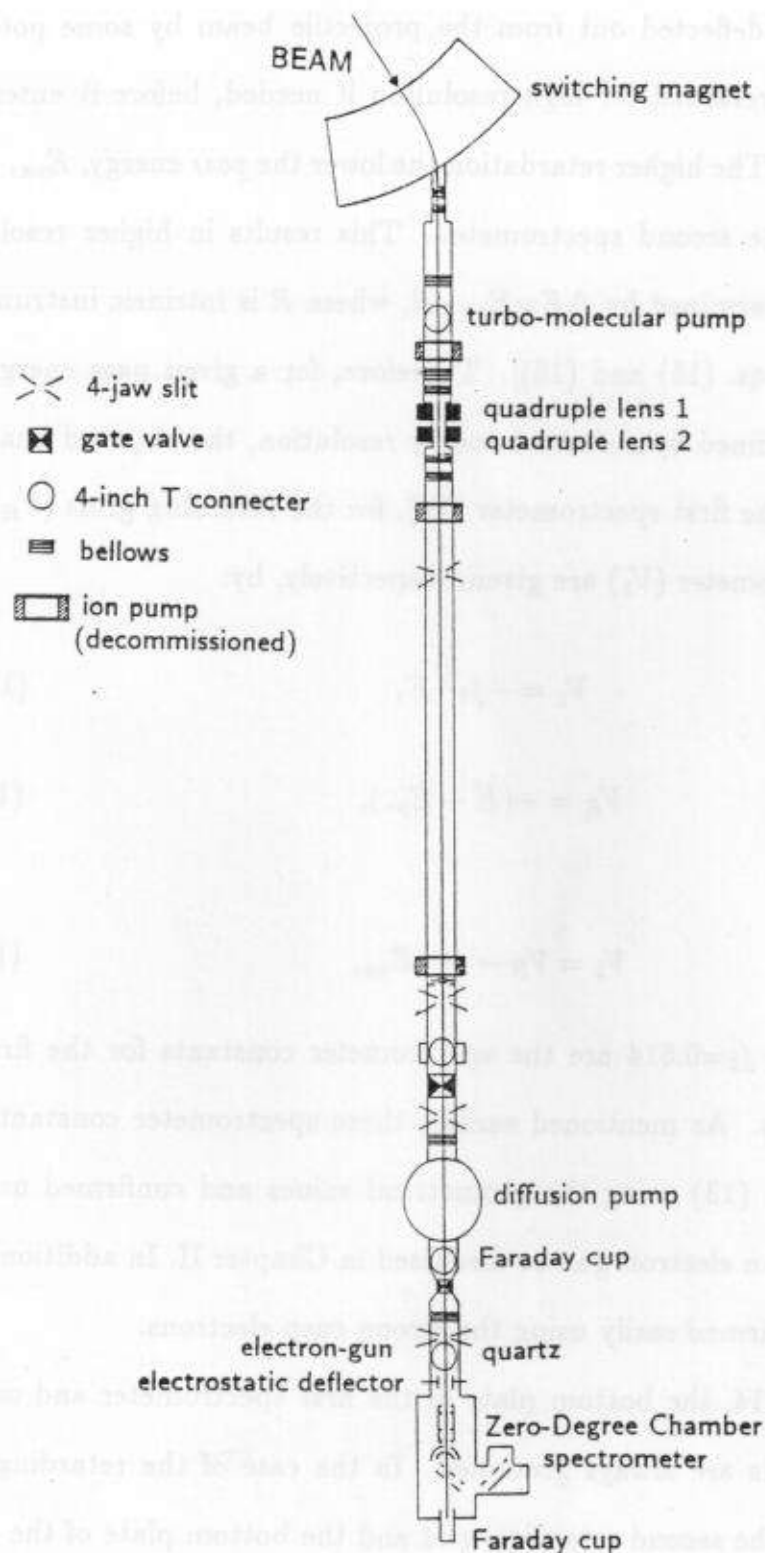


FIGURE 13. Beam line R-2 and scattering chamber arrangement.

The electron is then deflected out from the projectile beam by some potential V_1 and its energy is retarded for high resolution if needed, before it enters the second spectrometer. The higher retardation the lower the *pass* energy, E_{pa} , which is analyzed within the second spectrometer. This results in higher resolution, since resolution is determined by $\Delta E = E_{pa} \cdot R$, where R is intrinsic instrumental resolution [see also Eqs. (15) and (16)]. Therefore, for a given pass energy E_{pa} in eV which is determined by a desired energy resolution, the required analyzing voltages in Volt for the first spectrometer (V_1), for the retarding grids (V_R), and for the second spectrometer (V_2) are given, respectively, by:

$$V_1 = -f_1 \cdot E, \quad (19 - a)$$

$$V_R = -(E - E_{pa}), \quad (19 - b)$$

and

$$V_2 = V_R - f_2 \cdot E_{pa}, \quad (19 - c)$$

where $f_1=0.634$ and $f_2=0.614$ are the spectrometer constants for the first and second spectrometers. As mentioned earlier, these spectrometer constants were determined from Eq. (13) using the geometrical values and confirmed using an electron beam from an electron gun as discussed in Chapter II. In addition, these values also were confirmed easily using the strong cusp electrons.

As seen in Fig. 14, the bottom plate of the first spectrometer and one side of the retarding grids are always grounded. In the case of the retarding mode for high resolution, the second retarding grid and the bottom plate of the second spectrometer are at the retarding potential V_R . In order to increase electron counting efficiency, an optimum einzel lens voltage V_L is empirically determined for a given electron energy by maximizing the electron counting rate.

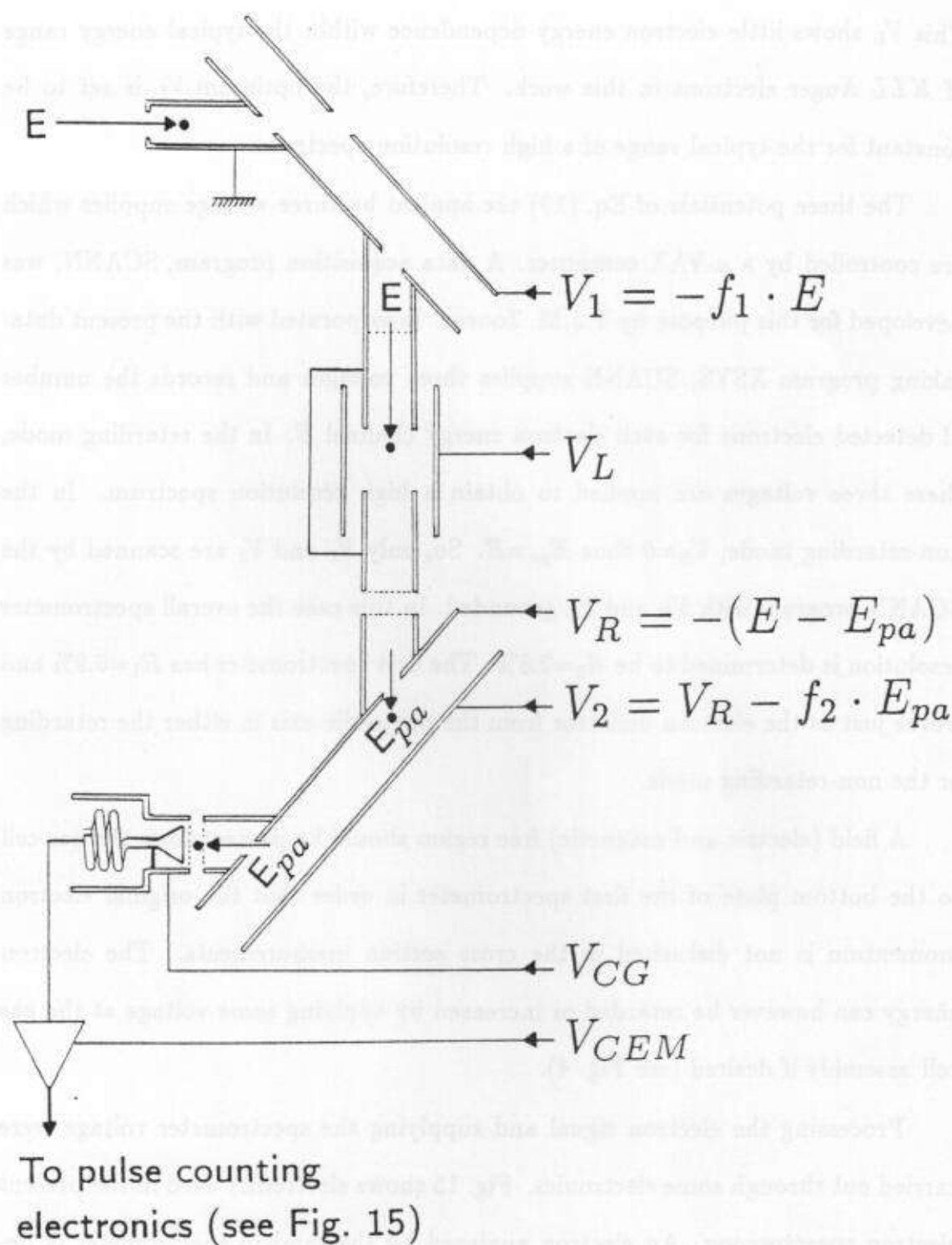


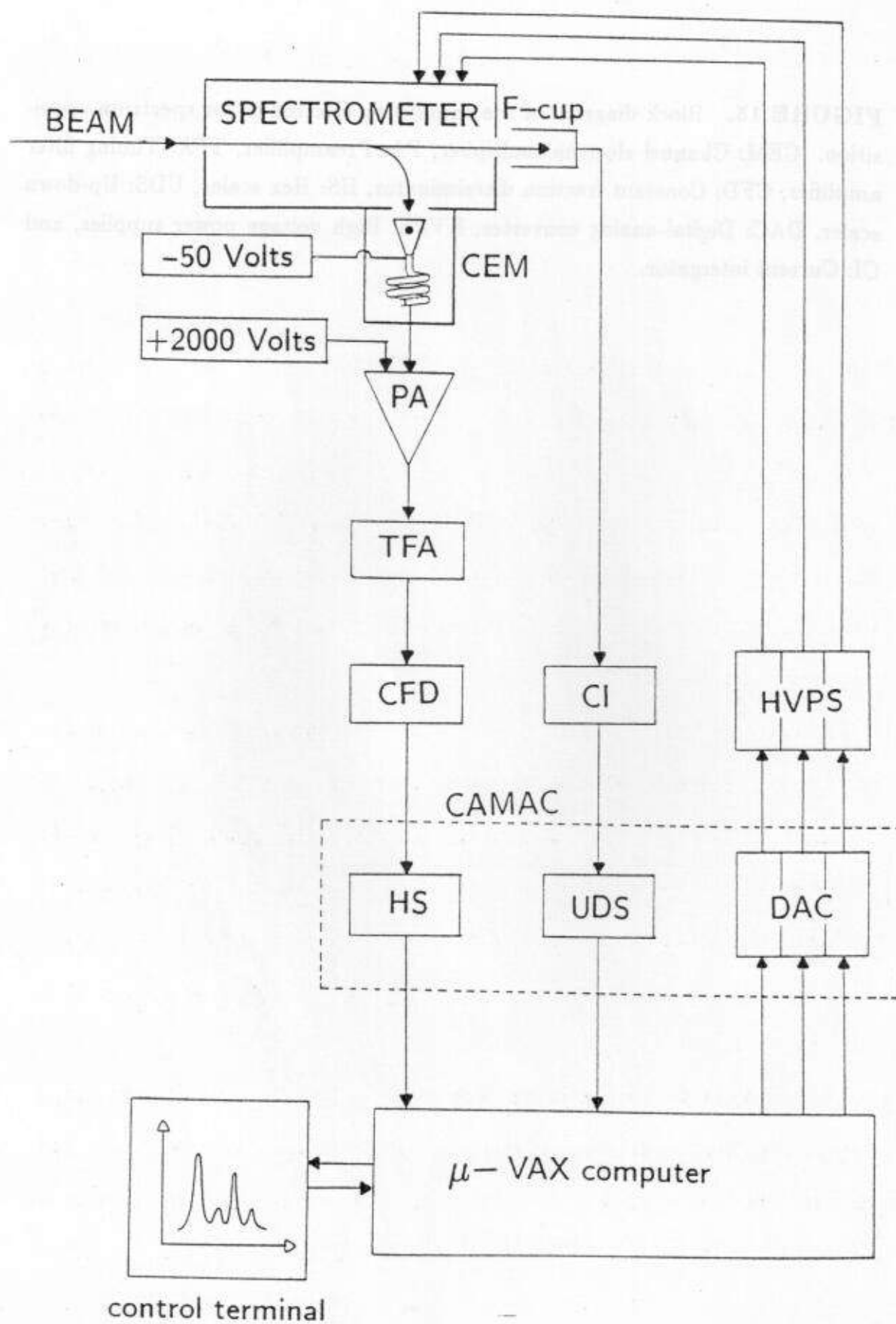
FIGURE 14. Schematic diagram of electron analyzing voltages of the tandem electron spectrometer.

This V_L shows little electron energy dependence within the typical energy range of *KLL* Auger electrons in this work. Therefore, the optimum V_L is set to be constant for the typical range of a high resolution spectrum.

The three potentials of Eq. (19) are applied by three voltage supplies which are controlled by a μ -VAX computer. A data acquisition program, SCANN, was developed for this purpose by T.J.M. Zouros. Incorporated with the present data-taking program XSYS, SCANN supplies three voltages and records the number of detected electrons for each electron energy channel E . In the retarding mode, these three voltages are applied to obtain a high resolution spectrum. In the non-retarding mode, $V_R=0$ thus $E_{pa}=E$. So, only V_1 and V_2 are scanned by the SCANN program with V_R and V_L grounded. In this case the overall spectrometer resolution is determined to be $R_2=2.8\%$. The first spectrometer has $R_1=6.9\%$ and works just as the electron deflector from the projectile axis in either the retarding or the non-retarding mode.

A field (electric and magnetic) free region should be present from the gas cell to the bottom plate of the first spectrometer in order that the original electron momentum is not disturbed in the cross section measurements. The electron energy can however be retarded or increased by applying some voltage at the gas cell assembly if desired (see Fig. 4).

Processing the electron signal and supplying the spectrometer voltage were carried out through some electronics. Fig. 15 shows electronics used in the present electron spectroscopy. An electron analyzed by the tandem spectrometer is detected by a channel electron multiplier⁵² (channeltron) (CEM). Its principle and operation are described in Ref. 52. The channeltron, Galileo model 4039C, was used for all the electron measurements in this work. The diameter of the cone entrance was 10 mm. Some negative voltage (V_{CG} in Fig. 14), usually -50 Volts,



was applied to the CEM entrance cone and CEM housing in order to repel any stray, low energy electrons which may have come from the outside of the gas cell. The V_{CG} cuts off detection of all the low energy electrons smaller than 50 eV. At any rate, these low energy electrons are not of interest and the present residual small magnetic field or unwanted electric field interfere in properly analyzing them.

The channeltron voltage, V_{CEM} , is applied through a preamplifier (e.g., ORTEC 109PC model) as seen Fig. 14. Optimum operation voltage, $V_{CEM} - V_{CG}$ in Fig. 14, started with 1800 Volts and gradually increased to 2200 Volts when it had been used for approximately 15 accelerator beam times (about 600 hours electron collecting time). Dark counts, virtual counts without any true electron detection, have been observed to be smaller than 0.1/sec. This has been frequently checked during the normal operation simply by cutting the projectile beam before the chamber. CEM efficiency will be discussed in detail later in the procedure of the spectrometer efficiency normalization.

The CEM-detected electron signals were then processed by a preamplifier. The preamplified signals were sent through a timing filter amplifier (TFA, e.g., ORTEC model 454) to a constant fraction discriminator (CFD, e.g., ORTEC model 583), where a threshold was set to discriminate all the electronic background signals. These background signals, which originate from the electronics, were easily identified by cutting the projectile beam. It was observed to be very small compared to true electron signals.

The discriminated true electron signals were then sent to a micro-Vax computer system after being processed through a CAMAC interface (Hex scaler, e.g., kinetic systems model 3513). The digital information was then processed using the data analysis program XSYS and recorded by the data acquisition procedure of the SCANN program for each electron energy channel. The period of electron

counting for each electron energy channel was determined by the amount of the projectile charge accumulation which was preset by the program SCANN.

As shown in Fig. 15, the projectile charge was collected by a Faraday cup and sent to the computer through a current integrator (BIC model 1000), where a pulse is generated for each accumulated charge in some units, and a CAMAC interface (up-down scaler, e.g., Bi Ri systems model 2204 DPR), where the pulses are processed into digital numbers. When the accumulated projectile charge for an electron energy channel becomes the preset value by the SCANN program, the electron energy channel proceeds to the next channel and thus the new digital signals for the spectrometer voltages of Eq. (19) for the next electron energy are issued by the program. These digital signals are converted to voltages (0-10 Volts) through 12-bit digital analog converter (DAC, e.g., kinetic systems model 3112) and then amplified by the computer controlled power supplies (TENNELEC model 952) to create the analyzing voltages of Eq. (19).

In this way, the electron energy channels are stepped from a starting value E_S to an ending value E_E by stepping all the spectrometer analyzing voltages and thus completing one scan and making an electron spectrum. When better counting statistics are required, multiple scans were made by repeating the procedure above. All of these are controlled by the program SCANN. Finally, this acquired electron spectrum is stored on a 70 Mega-byte hard disk through the data analysis program XSYS.

Considerable care was taken in reducing the beam-induced background electrons by strongly collimating the beam and carefully aligning all the apertures and slits for the beam passage. Such background electrons are produced mainly by electrons scattered by the beam at the edges of the spectrometer slits and gas cell apertures and can be a large source of error at zero degree observation. The

beam collimation and all the aperture and slit alignments were diagnosed by measuring charge currents at each part of the beam passage as shown in Fig. 16. Strong background was produced by the beam collimator before the gas cell differential region so that the beam current at the collimator was reduced by blocking the uncollimated beam with the most downstream 4-jaw slit just before the chamber (see Fig. 13). In addition, some positive voltage (~ 300 Volts) was applied at the collimator to absorb any stray background electrons. The measured currents at all the other apertures and slits were observed to be very small, typically smaller than 0.1% of the beam current measured at the Faraday cup. The Rydberg analyzer was in place just for the first half of this work (This had been installed for the study of the field ionized high- n Rydberg electron), and then was replaced by a short nozzle. The alignment and collimation were further checked by applying some voltages at the small electro-static deflector just before the chamber as shown in Fig. 16. This was originally installed for the adjustment of the electron beam from an electron gun.

This beam-induced electron background was directly determined by taking an electron spectrum without gas in the target cell. Around the BEe peak and K Auger electrons, this background could be reduced to less than a few percent of the true counts and was subtracted with negligible error. However, for projectile velocities higher than 1.5 MeV/u the background was sometimes observed to be considerable as compared to K -Auger electron yields. This considerable background turned out to be from the collimator contamination due to the deposition of the carbon-oxide materials which apparently originated from the diffusion pump oil. But an exact reason for this buildup remains unknown.

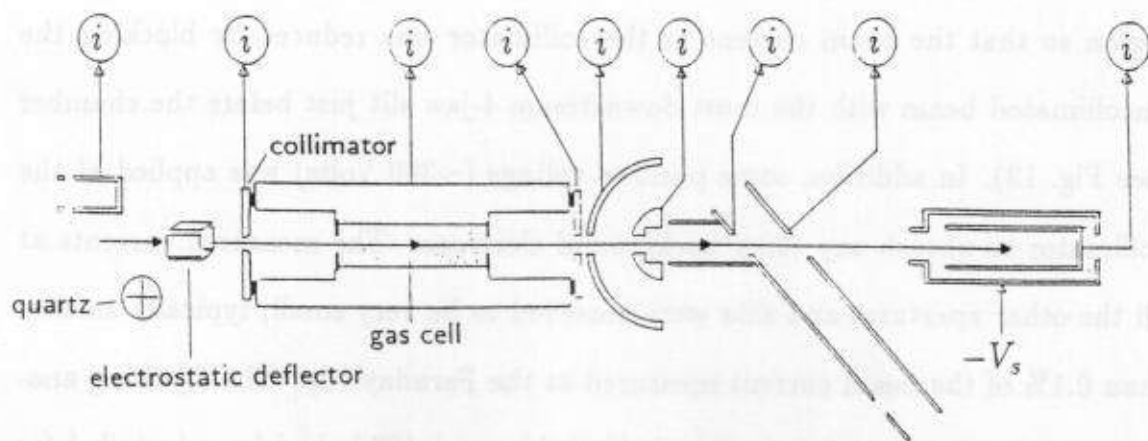


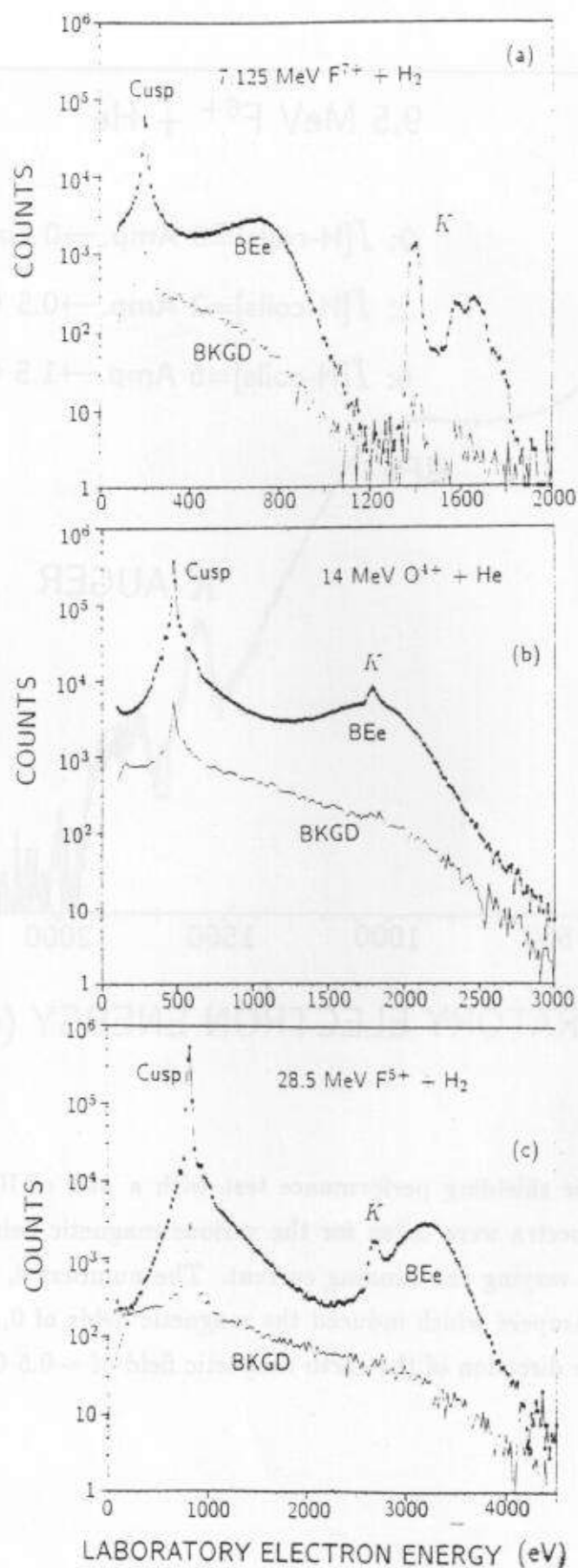
FIGURE 16. Beam passage diagnosis through the target gas cell and spectrometer. The beam passage can be carefully checked by measuring currents at all the apertures.

In Fig. 17, a typical beam-induced background is compared to true electrons produced in the typical ion-atom collisions of this work. As will be discussed in the next sections, the background subtraction error will be accounted for in the electron production cross section measurements. In the measurements of the BEE production cross sections, the beam-induced background is straightforwardly subtracted with small error. However, in the measurements of the *KLL* Auger production cross sections, a spectrum for the *K* Auger region (see horizontal arrows in Fig. 17) is obtained and then both BEE and beam-induced electron background are subtracted together by finding a polynomial fit to the wings of the *K* Auger spectra.

The residual magnetic field inside the μ -metal shield was observed to be 20–40 mGauss depending on the position. A possible uncertainty in the electron yield measurements, due to this magnetic field, was tested by installing a pair of Helmholtz coils around the scattering chamber. It was found that the field has negligible effect for the electrons whose laboratory energies are larger than ~ 200 eV. These results are illustrated in Fig. 18.

In Fig. 19, some sample spectra of the state-resolved Auger electrons are displayed for the various collision systems of interest in this dissertation. All the line identifications, their state production mechanisms, and their production cross sections will be discussed in Chapters V, VI, and VII, after studying the BEE in an extended order in the next Chapter.

FIGURE 17. Comparison between the truly collisionally produced electrons and the beam-induced background electrons in the overall electron spectra.



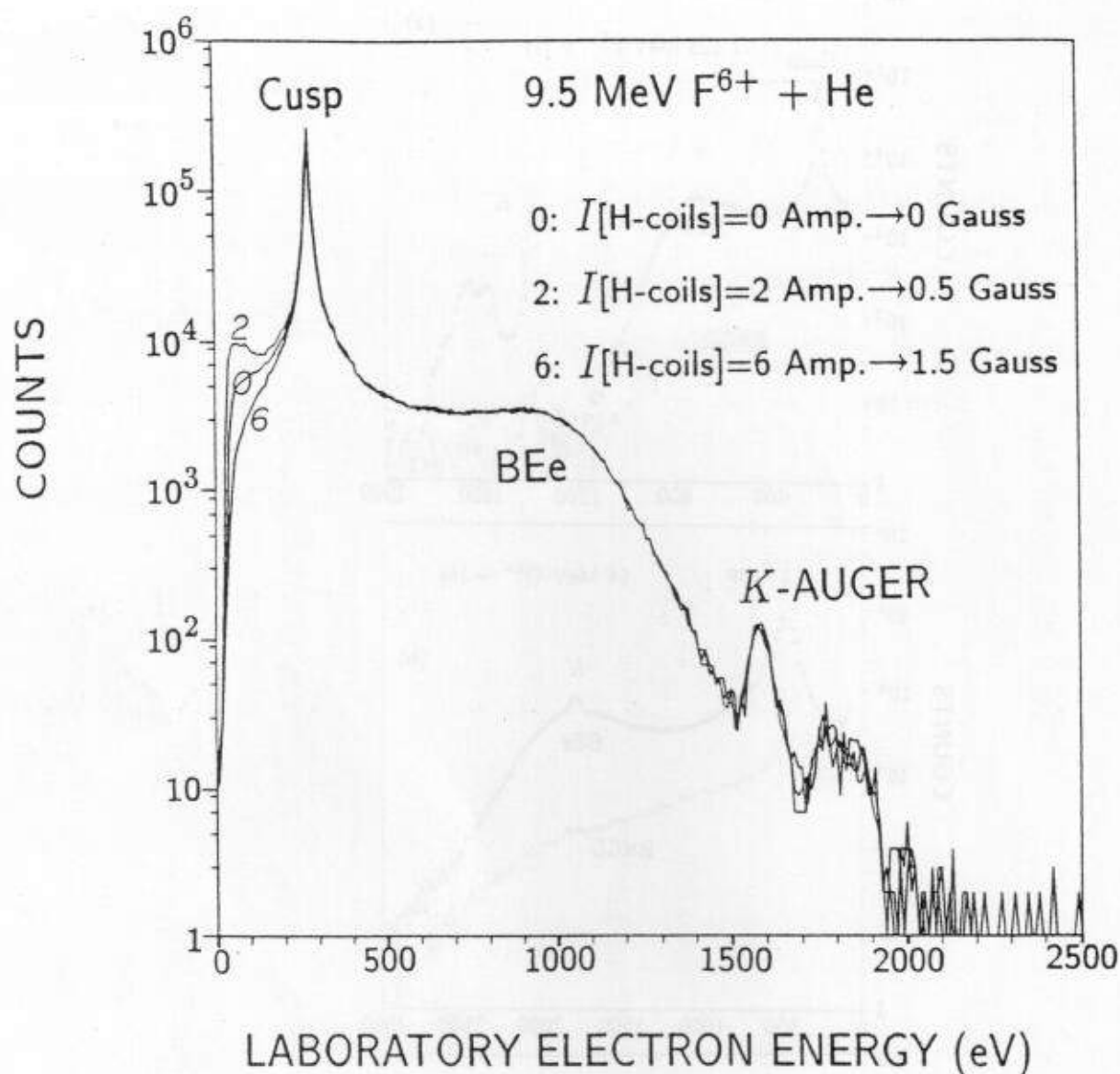
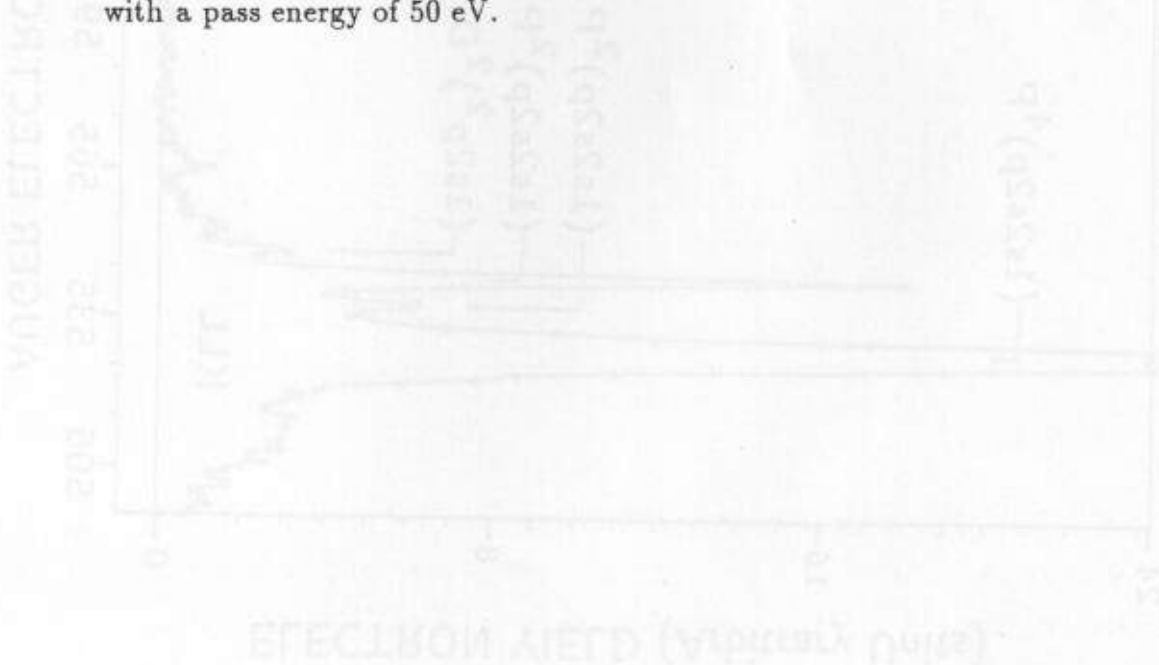
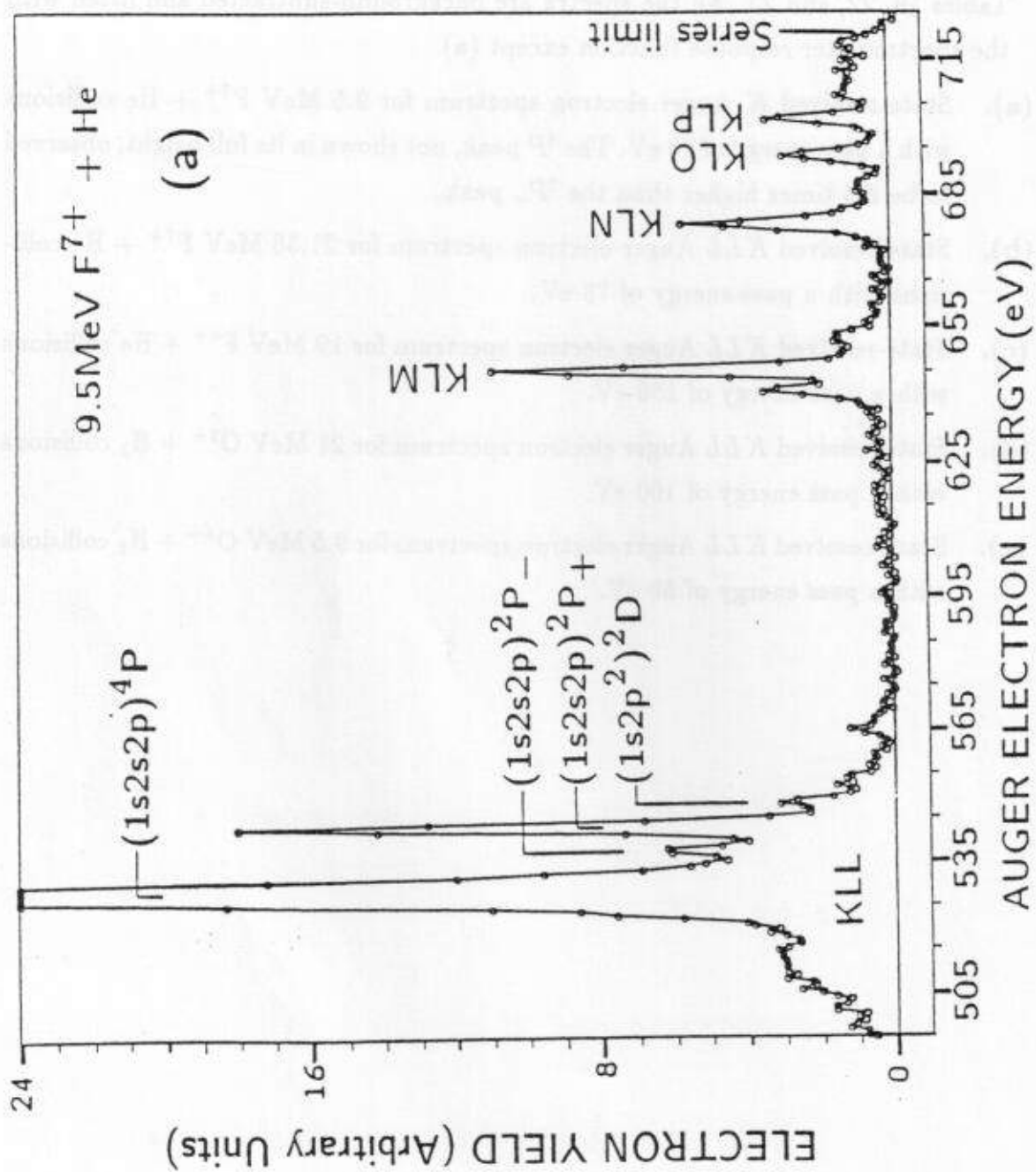


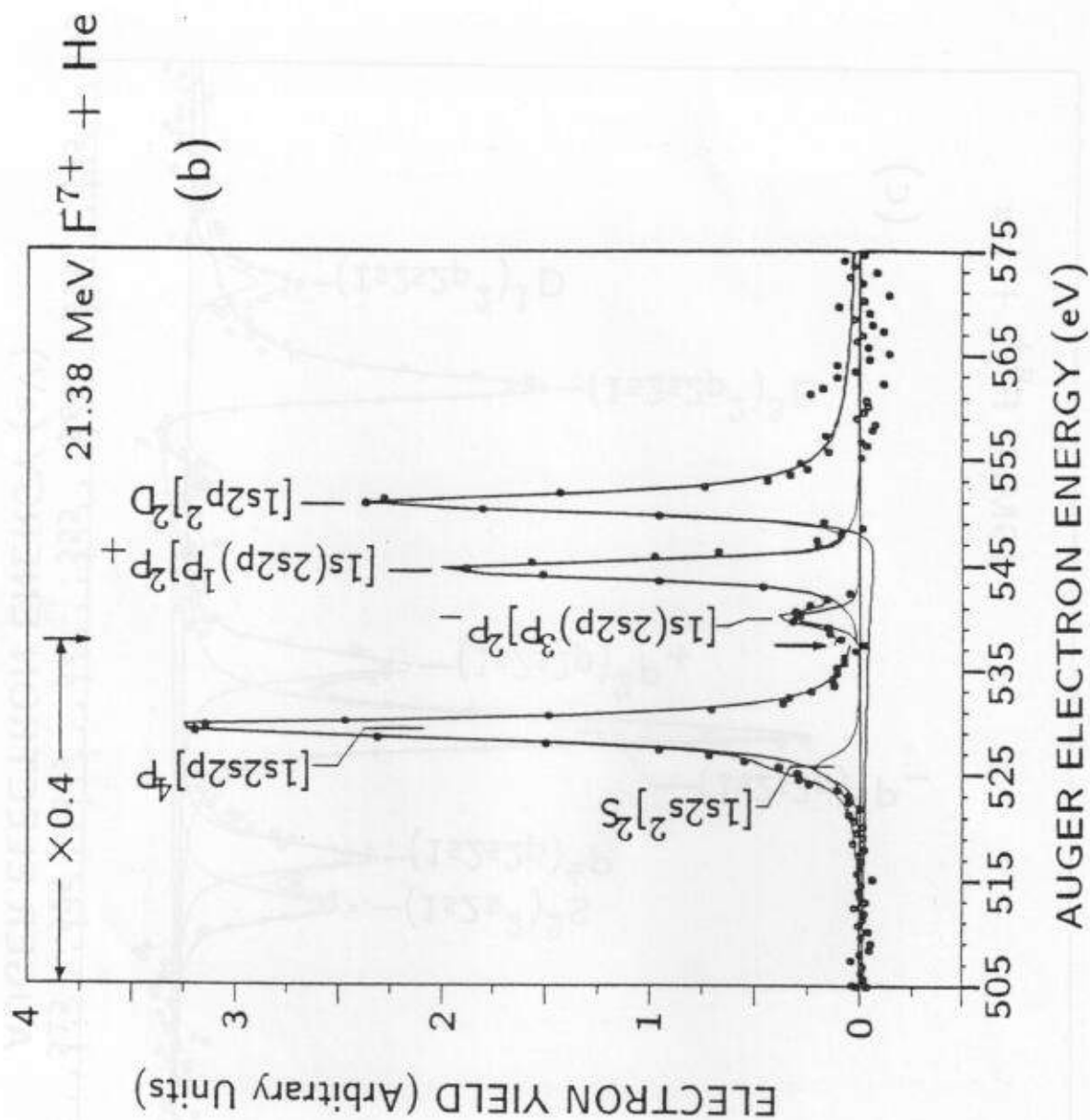
FIGURE 18. Magnetic shielding performance test with a pair of Helmholtz coils. Several electron spectra were taken for the various magnetic fields which were obtained by simply varying the running current. The numbers 0, 2, and 6 refer to the currents in Ampere which induced the magnetic fields of 0, 0.5, and 1.5 Gauss to the opposite direction of the earth magnetic field of ~ 0.5 Gauss.

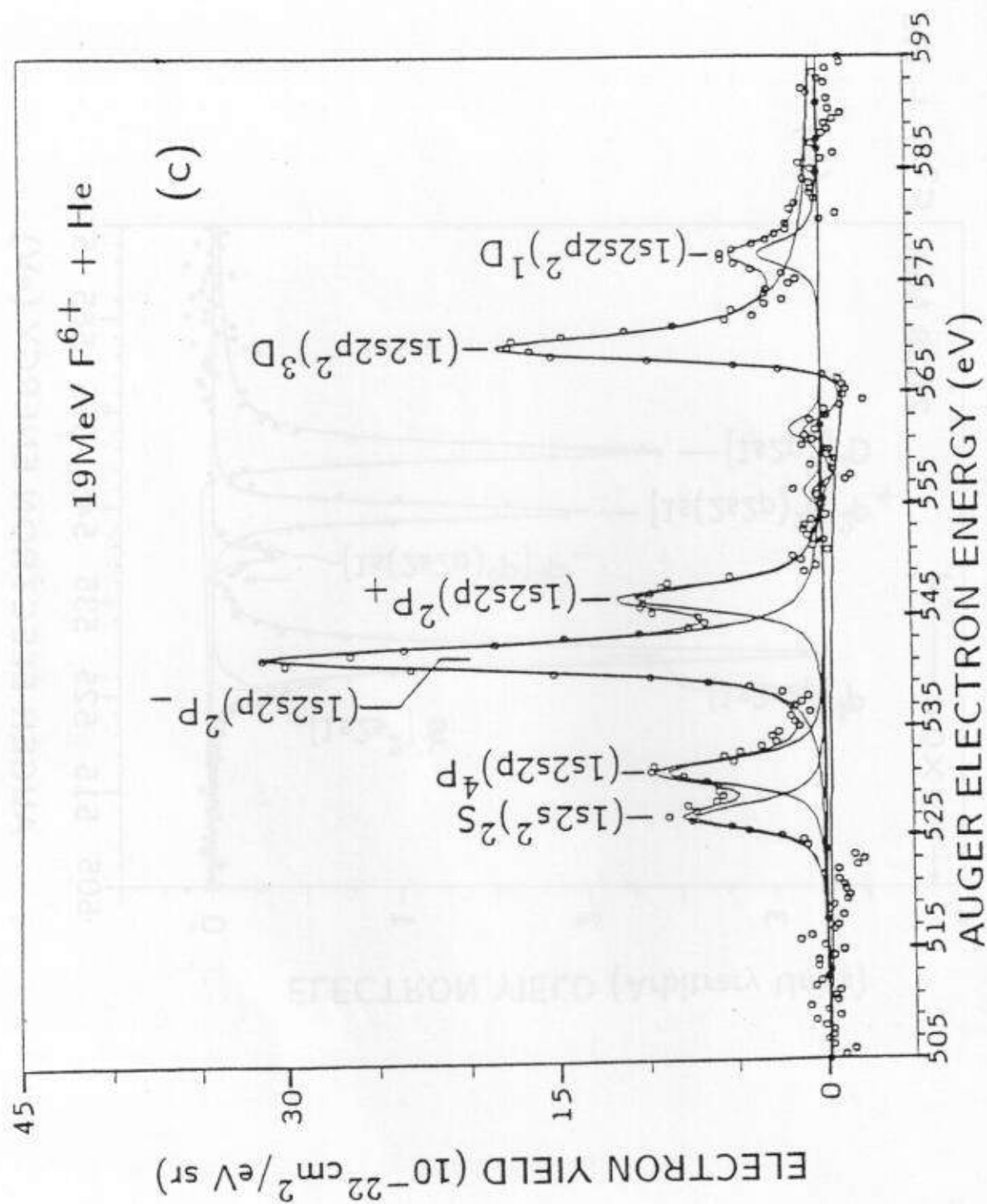
FIGURE 19. Sample of high-resolution projectile *K* or *KLL* Auger electron spectra for the various collision systems. For the Auger line identification see Tables 19, 22, and 23. All the spectra are background-subtracted and fitted with the spectrometer response function except (a).

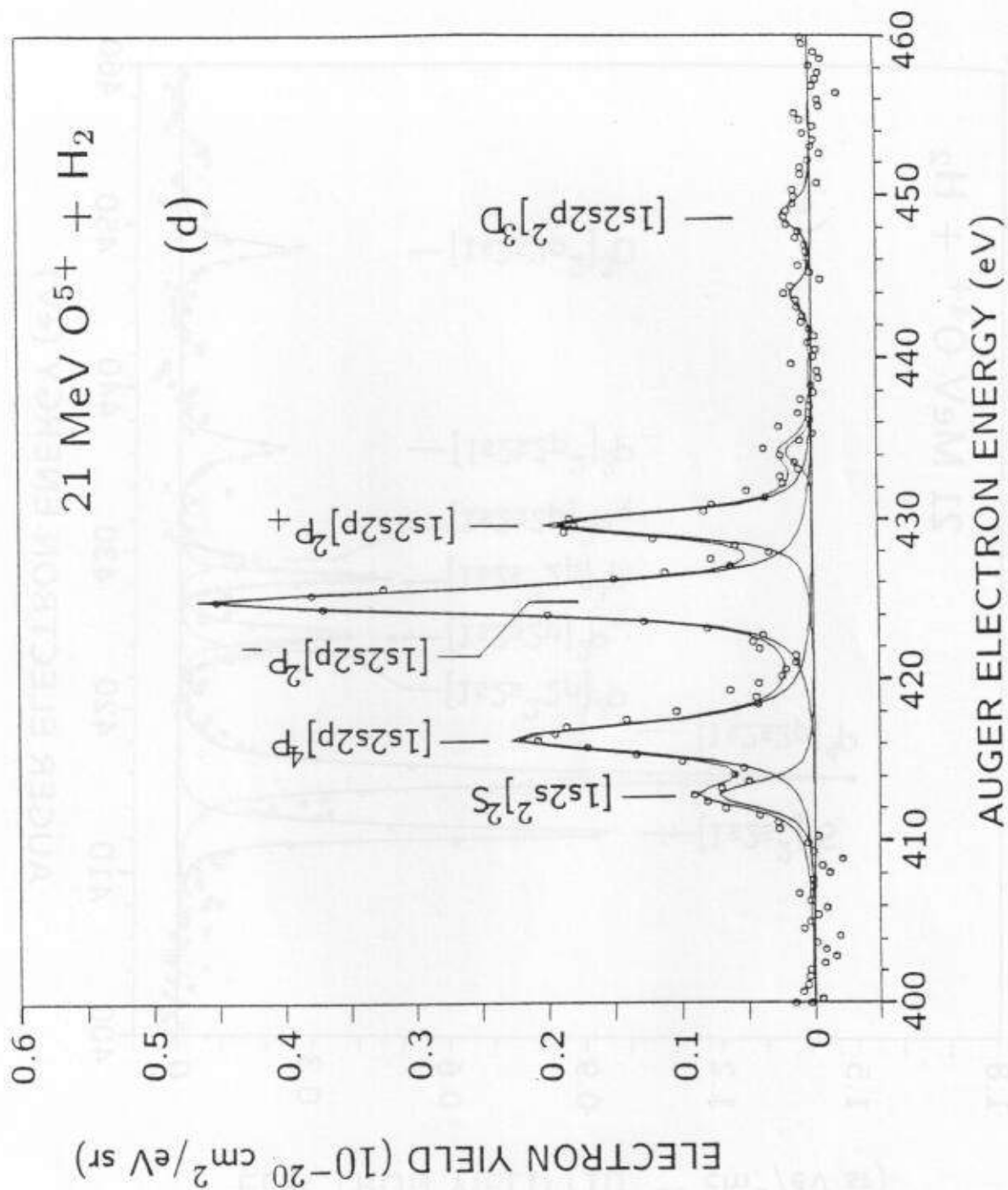
- (a). State-resolved *K* Auger electron spectrum for 9.5 MeV $F^{7+} + He$ collisions with a pass energy of 75 eV. The 4P peak, not shown in its full height, observed to be 8.5 times higher than the $^2P_+$ peak.
- (b). State-resolved *KLL* Auger electron spectrum for 21.38 MeV $F^{7+} + He$ collisions with a pass energy of 75 eV.
- (c). State-resolved *KLL* Auger electron spectrum for 19 MeV $F^{6+} + He$ collisions with a pass energy of 150 eV.
- (d). State-resolved *KLL* Auger electron spectrum for 21 MeV $O^{5+} + H_2$ collisions with a pass energy of 100 eV.
- (e). State-resolved *KLL* Auger electron spectrum for 9.5 MeV $O^{4+} + H_2$ collisions with a pass energy of 50 eV.

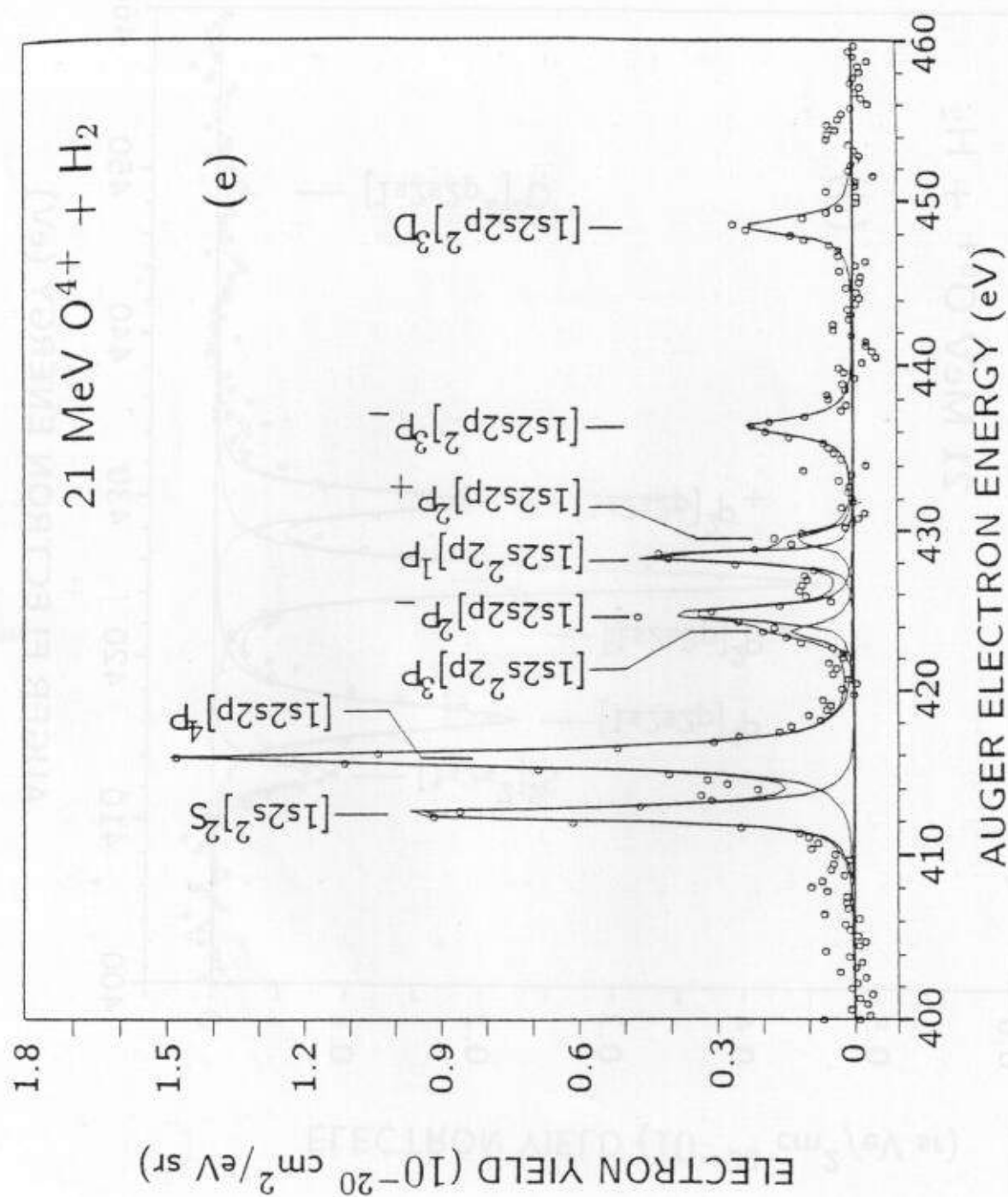












IV. ZERO-DEGREE BINARY-ENCOUNTER ELECTRONS

A. Background and Motivation

In collisions of fast projectiles with light targets, which are of interest in this dissertation, the projectile K -Auger electrons are accompanied by high intensity binary encounter electrons^{31,53,54} (BEE), which are target electrons ionized through direct, hard collisions with energetic projectiles, giving rise to a broad energy distribution. Fig. 20 shows two sample spectra of electrons, observed at zero degrees, in collisions of 0.5 and 1.5 MeV/u F^{9+} with He. For the higher energies of projectiles, K -Auger electrons are located around the strong BEE peak. [see also Fig. 17-(b) and (c)].

Based on classical two-body collision dynamics for heavy ion impact on a *free* electron, the energy of the recoiling electron can be shown to equal $4t\cos^2\theta_{Lab}$ and is known as the BEE peak energy.^{53,54}, where the cusp electron energy t is given by Eq. (4) and θ_{Lab} is the laboratory electron observation angle with respect to the beam direction. Thus for zero-degree measurements ($\theta_{Lab} = 0^\circ$) the BEE peak energy should be at $4t$. In the case of the *quasifree* target electrons of He or H_2 , the BEE peak energy can be expected to be at $4t$ or predicted to be slightly smaller than $4t$ when considering the binding energy of the target electron. In addition, the BEE distribution could be understood to be the Compton profile of the target electron(s) with its centroid velocity to be approximately $4t$. However, all these simple predictions did not work with the measured BEE energy distribution. So, we needed more theoretical and systematic studies. This was the starting point and motivation of the BEE studies.

The production of BEE has been studied using H and He projectiles,⁵⁵⁻⁶² however, to my knowledge, only a few measurements using heavy ion projectiles

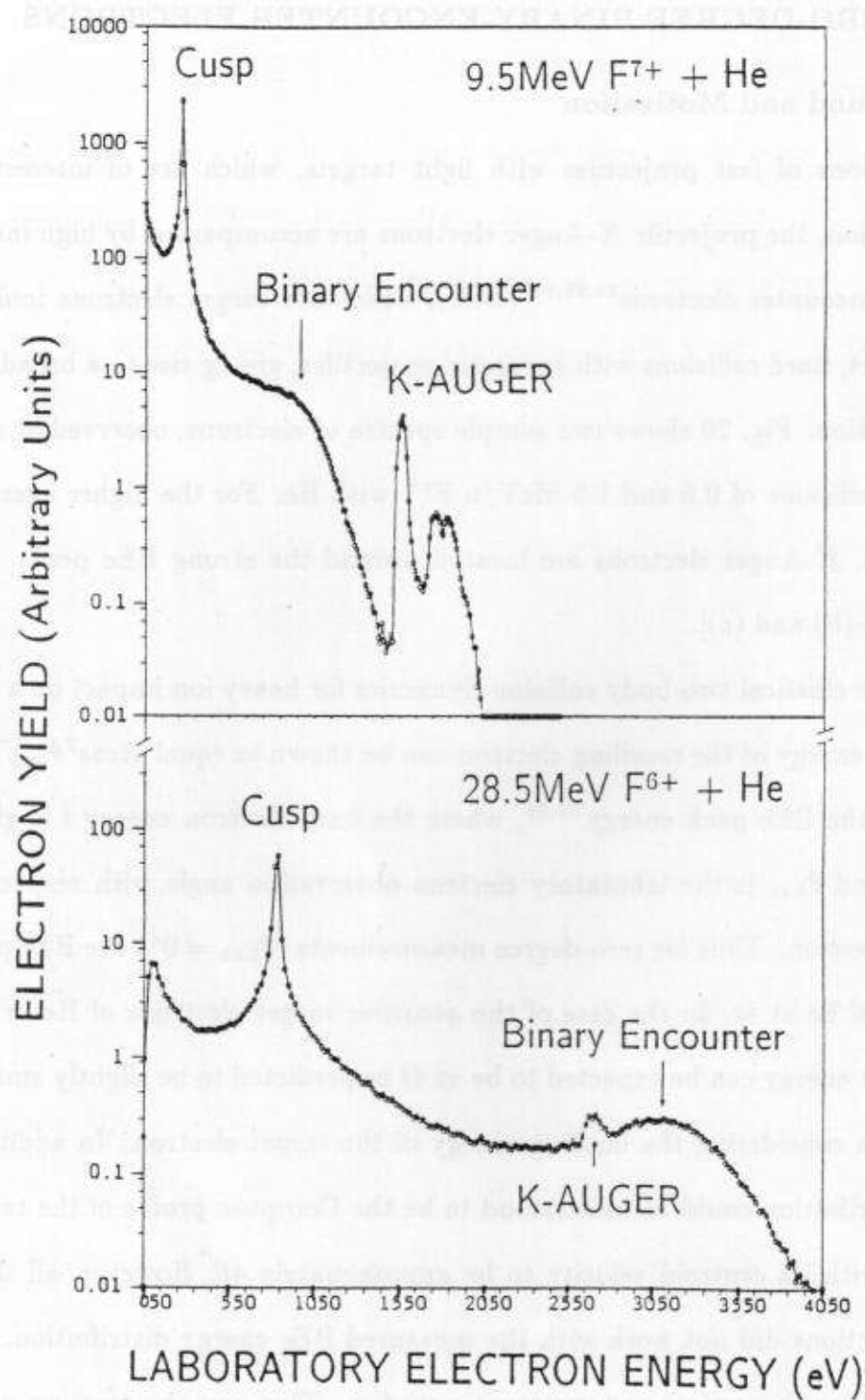


FIGURE 20. Overall electron spectra for two different collision systems. *K* Auger electrons are superimposed over the binary-encounter electrons depending on the projectile beam energy (see also Fig. 17).

have been reported^{31,63} and none at zero degrees. A detailed understanding of BEe can be useful in the study of characteristic *K*-Auger electron spectra in heavy ion-atom collisions, since BEe production is often the dominant component of such spectra and can interfere with the coherent Auger electrons, as for example, in resonant transfer excitation (RTEA).^{29,30} Thus, it is important to have a good quantitative model of BEe production, that can give the correct projectile E_p and Z_p dependences, as well as a good description of projectile screening^{54,64,65} and target electron binding effects.

In this chapter, the production of binary encounter electrons is studied at zero degrees with respect to the beam direction in energetic 1–2 MeV/u collisions of *bare* and highly-charged ions with H_2 and He targets. First, by utilizing bare projectiles we eliminate complications due to possible screening effects,^{54,64} and by using two electron targets we focus on the BEe production for only the *K*-shell. At the rather high collision energies involved in this study, the impulse approximation²⁸ (IA) as well as the plane-wave Born approximation⁴¹ (PWBA) should provide a good description of BEe production. Thus, by measuring double differential cross sections (DDCS) of electron production, in both electron energy and solid angle, we can provide a stringent test of both the IA and PWBA treatments of energetic ion-atom collisions. Secondly, after understanding BEe production with a variety of bare projectiles, the projectile charge q -dependence of the BEe production was also studied. This subject has a more practical application, since all RTE Auger electrons at resonance have the same electron energy as the BEe peak.

In particular, I have developed an IA model in which BEe production at zero degrees can be viewed from the projectile frame, essentially as 180° Rutherford scattering of a “quasifree” target electron by the projectile ion. Upon integrating the Rutherford cross section over the incoming electron’s momentum distribution

due to its orbital motion around the target nucleus (Compton profile) and correctly accounting for its binding energy, it is found that the predicted DDCS are in excellent agreement with the experimental data, particularly in the case of the H_2 targets, over the whole range of collision energies and projectile species studied here. The PWBA DDCS are also found to be in overall agreement with the results of IA calculations and experiments for H_2 targets. However, the BEE peak, observed to be shifted towards lower electron energies (see Fig. 22) from $4t$, is in better agreement with my IA formula than with the PWBA.

Based on the excellent systematic agreement between the IA and the measured DDCS for projectiles ranging from protons to F^{9+} , it was decided that my IA formula for BEE production could be used to provide a direct and accurate *in situ* absolute efficiency normalization (calibration) of our electron spectrometer in the electron energy range of 1–5 keV. This eliminates the extrapolation of the efficiency derived from the normalization to known Ne target K -Auger electron cross sections^{66,67} (Auger energy about 0.8 keV) produced by proton impact.

In addition, BEE studies of this kind lay the foundation for the investigation of more complicated multi-electron ion-atom collision systems⁶⁵ and possibly provide an alternative way (other than the more direct but difficult electron-ion crossed beam experiments) to study multi-electron ion-electron scattering.

The measurements were carried out using a tandem 45° parallel plate electron spectrometer which is described in Chapter II. The BEE spectra were obtained with 2.8% FWHM energy resolution without any electron energy retardation. The acceptance angles were estimated, using the geometrical factors of the spectrometer, to be 1.07° perpendicular to the dispersion plane and 0.16° in the dispersion plane as shown in Table 4. The gas cell was doubly differentially pumped so that the chamber pressure could be maintained below 0.01 mTorr at typical gas

cell pressures of 40 mTorr as mentioned in Table 3. The projectile beam, which was collected in a shielded Faraday cup with voltage suppression to insure proper beam integration, was used to normalize the electron count for each electron energy channel. Partial charge neutralization of the projectile beam due to electron capture in passing through the target gas, which could give rise to erroneous beam integration, was found to be negligible for the collision systems studied here. In one case using the 19 MeV $F^{9+} + He$ capture cross section from Ref. 69, the gas cell length of 10 cm, and a target gas pressure of 40 mTorr, the capture probability is 7%. Neutralization from such capture would change the integrated current by less than 1%.

The binary encounter electrons were recorded under single collision conditions which were found to be valid for target gas pressures less than 80 mTorr in a 10 cm long gas cell. As shown in Fig. 21, the pressure dependence of the BEE yield was tested at 9 different pressures between 0 (background) and 80 mTorr for 19 MeV F^{6+} on H_2 . The yield was found to be linear with pressure confirming the correctness of the beam integration and single collision conditions. All other BEE data were taken at pressures of 0, 20, and 40 mTorr and were also found to be linear with pressure.

Considerable care was taken in reducing the beam-induced background by carefully collimating the beam. Such a background is produced mainly by electrons scattered by the beam at the edges of the spectrometer slits and gas cell apertures and can be a large source of error at zero degree observation. This beam-induced electron background was directly determined by taking an electron spectrum without gas in the target cell. Around the BEE peak, this background could be reduced to less than a few percent of the true counts and was subtracted with small error.

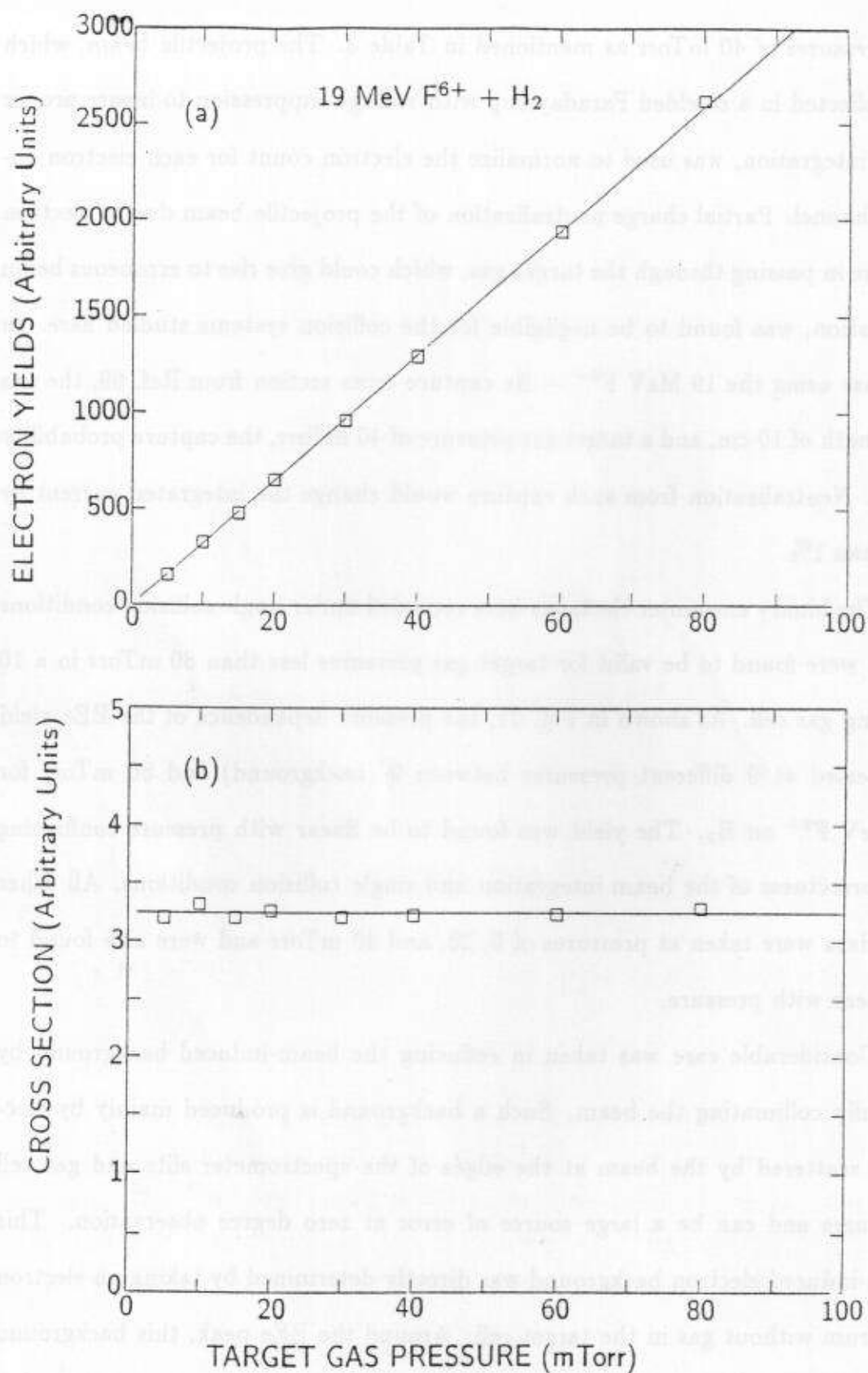


FIGURE 21. Target pressure dependence of the binary encounter electron production. (a); electron yield versus pressure, and (b); cross section versus pressure. Both figures show good single collision conditions.

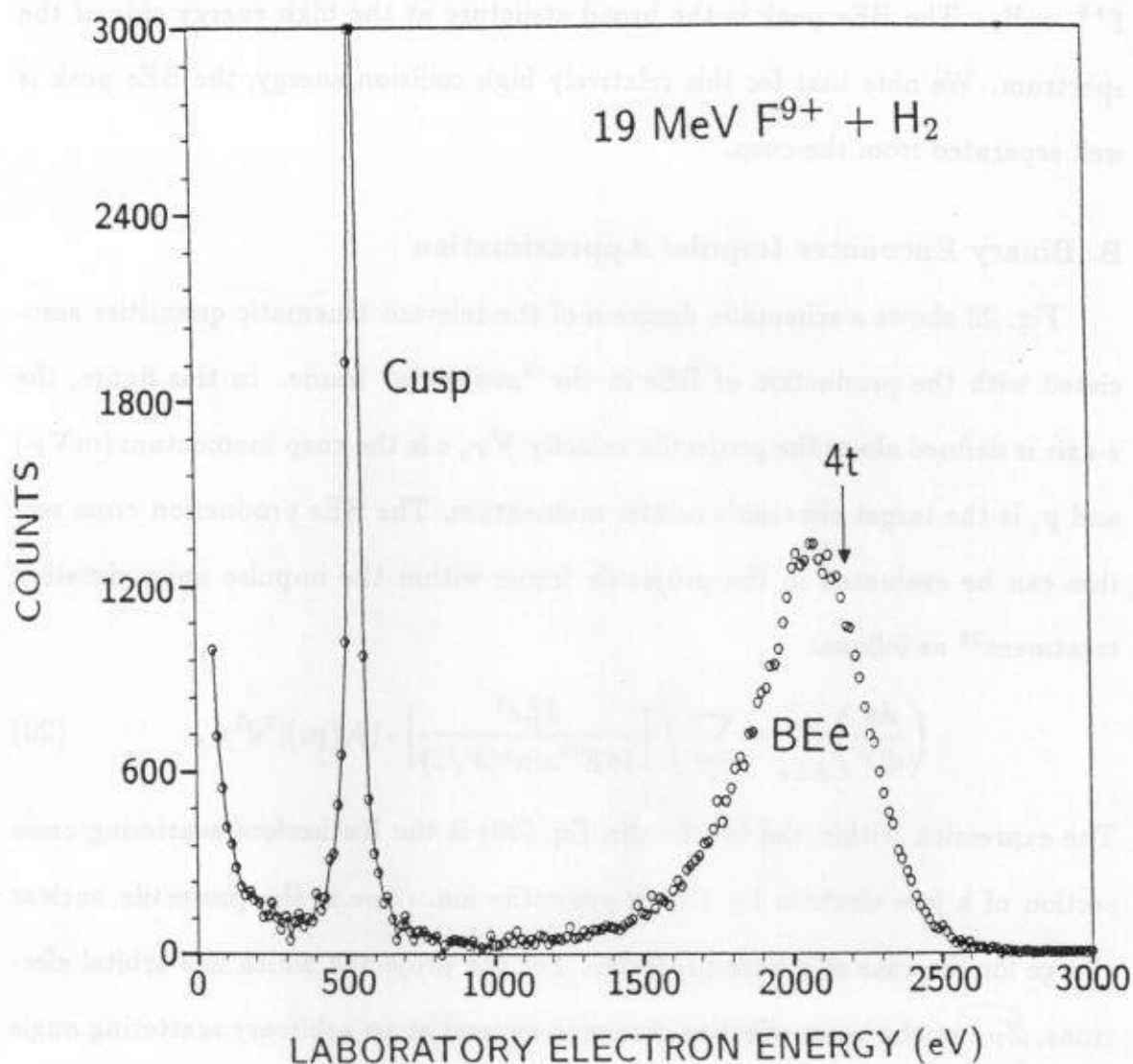


FIGURE 22. Electron energy spectrum for collisions of 19 MeV $F^{9+} + H_2$ observed at zero degrees showing the cusp and binary encounter peaks. Beam-induced background electrons have been subtracted (see text). The cusp, not shown in its full height, at energy t is about 5.5 times higher than the binary encounter peak. The maximum of the binary encounter peak appears at an energy slightly lower than $4t$ (arrow).

Fig. 22 shows a representative electron spectrum for a collision of 19 MeV $F^{9+} + H_2$. The BEe peak is the broad structure at the high energy side of the spectrum. We note that for this relatively high collision energy, the BEe peak is well separated from the cusp.

B. Binary Encounter Impulse Approximation

Fig. 23 shows a schematic diagram of the relevant kinematic quantities associated with the production of BEe in the "projectile" frame. In this figure, the z -axis is defined along the projectile velocity V_P , s is the cusp momentum (mV_P) and p_i is the target electron's orbital momentum. The BEe production cross section can be evaluated in the projectile frame within the impulse approximation treatment²⁸ as follows:

$$\left(\frac{d\sigma}{d\Omega'}\right)_{BEe} = \sum_i \int \left[\frac{Z_{Pe}^2 e^4}{16E'^2 \sin^4(\theta'/2)} \right] \cdot |\psi_i(\mathbf{p}_i)|^2 d^3p_i, \quad (20)$$

The expression within the brackets in Eq. (20) is the Rutherford scattering cross section of a free electron by a bare projectile ion. Z_{Pe} is the projectile nuclear charge for the case of a bare projectile. For the projectile which has orbital electrons, Z_{Pe} might be an effective charge in general at an arbitrary scattering angle θ' . For the zero-degree BEe measurement, the electron scattering angle is $\theta' = 180^\circ$ in the projectile frame. The target electron momentum wave function is given by $\psi_i(\mathbf{p}_i)$ where the subscript i refers to the i -th target electron. E' is the electron energy in the projectile frame.

Including the target ionization energy E_I , from energy conservation considerations, E' is assumed to be expressed as:

$$\begin{aligned} E' &= (s + p_i)^2 / 2m - E_I \\ &= (s^2 + 2sp_{iz} + p_{iz}^2 + p_{iy}^2 + p_{ix}^2) / 2m - E_I. \end{aligned} \quad (21)$$

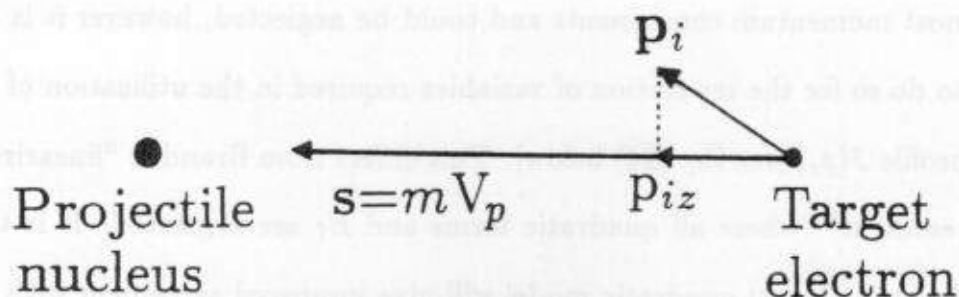


FIGURE 23. Schematic diagram of the kinematics of a target electron in a binary encounter collision with a projectile as seen from the projectile frame. $s \equiv mV_p$ is the cusp momentum, where m is the electron mass and $-V_p$ is the projectile velocity. p_i and p_{iz} are the target electron's orbital momentum and its component along the beam-axis (z -axis), respectively. In this reference frame the target electrons undergo 180° Rutherford scattering from the projectile nucleus and give rise to the BEE observed at 0° in the laboratory frame.

The component of \mathbf{p}_i perpendicular to the cusp momentum \mathbf{s} is neglected, since $(p_{iz}/s)^2 \ll 1$ and $(p_{iy}/s)^2 \ll 1$ for fast collisions. For example, in 1 MeV/u projectile ion impact, $(p_{iz}/s)^2 \simeq .03$ and $.07$ for the most probable value of \mathbf{p}_i set equal to p_{iz} for H_2 and He targets, respectively. We note that $(p_{iz}/s)^2$ is also small for most momentum components and could be neglected, however it is not necessary to do so for the separation of variables required in the utilization of the Compton profile $J(p_z)$ [see Eq. (24) below]. This differs from Brandt's "linearized" RTE-IA treatment²⁸ where all quadratic terms and E_I are neglected. It is thus expected that the present quadratic model will give improved agreement with the observed BEe spectrum at the low energy wing of the BEe peak, where the large momentum components play an increasingly important role. This effect will be more pronounced for atoms with broader Compton profiles, as in the case of He as compared to H_2 .

Defining the cusp energy $t \equiv s^2/2m$, the reduced momentum $r \equiv p_{iz}/s$, and the reduced ionization energy $\lambda \equiv E_I/t$, the electron energy E' is given within the approximation above by:

$$E' = t[(1+r)^2 - \lambda]. \quad (22)$$

Introducing the Compton profile $J(p_z)$ and using Eq. (22), one obtains

$$\left(\frac{d\sigma}{d\Omega'} \right)_{\text{BEe}} = \int \frac{Z_P^2 e^4 s J(p_z)}{32t^3 [(1+r)^2 - \lambda]^2 (1+r)} dE', \quad (23)$$

where

$$J(p_z) = \sum_i \int \int dp_{iz} dp_{iy} |\psi_i(\mathbf{p}_i)|^2. \quad (24)$$

Experimentally determined⁶⁹ Compton profiles were used for both H_2 and He target electrons in the ground state. The experimental Compton profile for He target electrons showed an excellent agreement with the calculated Hartree-Fock

Compton profile in Ref. 70. Thus, the integrand in Eq. (23) is the DDCS for BEE production at 180° in the projectile frame. Therefore,

$$\left(\frac{d^2\sigma}{dE'd\Omega'} \right)_{BEE} = \frac{\sqrt{2}Z_P^2 J(p_z) a_0^2}{32\epsilon_0 t^{2.5} [(1+r)^2 - \lambda]^2 (1+r)}, \quad (25)$$

where t and p_z are now in atomic units, and a_0 and ϵ_0 are the Bohr radius and the atomic unit of energy. This expression can also be written in terms of the Rutherford cross section as

$$\left(\frac{d^2\sigma}{dE'd\Omega'} \right)_{BEE} = \left(\frac{d\sigma}{d\Omega'} \right)_{Rutherford} \cdot \frac{J(p_z)}{V_P + p_z/m}. \quad (25-1)$$

In order to compare with theory, the experimental DDCS and electron energies are transformed from the laboratory to the projectile frame, using:^{4,61}

$$\left(\frac{d^2\sigma}{dE'd\Omega'} \right)_{BEE} = \left(\frac{d^2\sigma}{dEd\Omega} \right)_{BEE}^{Lab} \sqrt{\frac{E}{E_L}} \quad (26)$$

and for $\theta' = 180^\circ$

$$E' = (\sqrt{E_L} - \sqrt{t})^2, \quad (27)$$

E_L being the laboratory electron energy.

C. Data Analysis and Spectrometer Efficiency Normalization

C-1. Determination of the cusp energy t

The cusp energy t , required in Eqs. (25) and (27), was determined experimentally by directly measuring its value in the electron spectrum. This determination of t has been found to be a convenient and reliable way⁷¹ of measuring the actual projectile velocities to within 0.1%, particularly for highly charged ions obtained by post-stripping projectile ions of a lower charge state, a process which results in a small but observable energy loss of the beam as it traverses the stripper foil

TABLE 5

Measured cusp energies t and observed energy shifts $\Delta E_L \equiv 4t - E_L^{maz}$ (see text), for various projectile and target species. E_P is the projectile energy determined from the accelerator calibration, t_0 is the cusp energy derived from E_P , and E_L^{maz} is the laboratory electron energy at the maximum of the BEe peak. Experimental uncertainty on t is about ± 2 eV and on ΔE_L about ± 8 eV.

Projectile	E_P (MeV/u)	t_0 (eV)	t (eV)	$\Delta E_L[\text{H}_2]$ (eV)	$\Delta E_L[\text{He}]$ (eV)
F^{9+}	1.00	549	545	96	186
	1.25	686	682	94	178
	1.50	823	820	93	174
	1.75	960	957	92	171
	2.00	1097	1097	92	169
O^{8+}	1.50	823	820	93	—
N^{7+}	1.50	823	823	93	—
C^{6+}	1.50	823	823	93	—
H^+	$\sim 1.5^a)$	$\sim 820^a)$	$800^b)$	37	82
	2.00	1097	$1085^b)$	19	68

^{a)} Projectile energy was only approximately known.

^{b)} 1.7% larger values of t were required in the IA and PWBA calculations in order to get agreement with data.

($\sim 10 \mu\text{g}/\text{cm}^2$). The experimentally determined values of t are listed in Table 5 together with t_0 , the cusp energy derived from E_P as determined by the accelerator calibration.

C-2. Determination of the DDCS and the spectrometer efficiency

The experimental DDCS for electron production in ion-atom collisions, in general, can be obtained from the following well-known expression:^{62,73}

$$\left(\frac{d^2\sigma}{dE d\Omega} \right)_{exp}^{Lab} = \frac{Z}{N \cdot n \cdot l \cdot \Delta\Omega \cdot E_L^0 \cdot \eta(E_L)}, \quad (28)$$

where Z and N are respectively the number of electrons and projectiles counted per electron energy, n is the target number density, l is the length of the gas cell, $\Delta\Omega$ is the effective solid angle evaluated by Eq. (18), ΔE_L^0 is spectrometer acceptance energy at electron energy E_L , and $\eta(E_L)$ is the overall spectrometer efficiency.

The efficiency $\eta(E_L)$ is the product of the spectrometer transmission, the channeltron detection efficiency, and other possible factors. Channeltron detection efficiencies have been found to range,⁷⁴⁻⁷⁶ depending on the experimental setup, from 20% to 100% over the 1-5 keV electron energy range of interest in this study. In view of these difficulties, $\eta(E_L)$ is determined using our measured electron yields [see Eq. (28)] and the calculated IA-DDCS [see Eqs. (25) and (26)], at the BEe peak, at each collision energy of the $\text{F}^{9+} + \text{H}_2$ system. The values of $\eta(E_L)$ determined by this method are given in Fig. 24. Also shown in Fig. 24 is the value of $\eta(E_L \approx 800 \text{ eV})$ determined from the measured 3 MeV $\text{H}^+ + \text{Ne}$ K-Auger yields normalized to the published⁶⁶ cross section. In view of the simple nature of the BEe process, we have selected and used the BEe-IA normalization to test the systematics of BEe production given below.

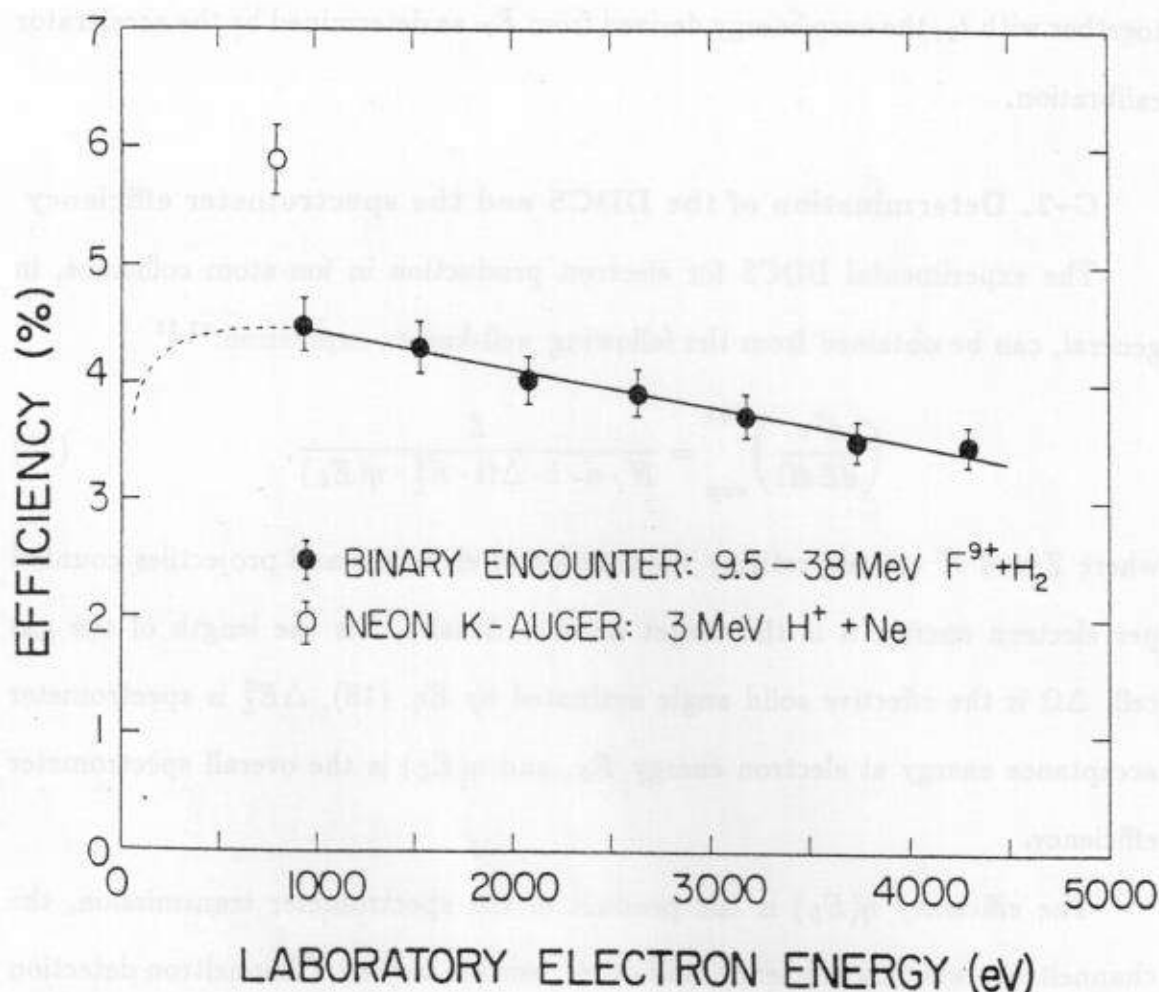


FIGURE 24. Overall absolute spectrometer efficiency $\eta(E_L)$ plotted as a function of the laboratory electron energy E_L . The solid line was interpolated using the data points (solid circles) obtained by normalizing the $F^{9+} + H_2$ BEE yields to the IA calculation (see text). The dashed line was extrapolated using the results of Ref. 76. The open circle is the efficiency measured using the known Ne target K-Auger cross section⁶⁶ at $E_L \approx 800$ eV for 3 MeV $H^+ + Ne$ collisions. The error bars are calculated from statistics alone. The Ne K-Auger data have an overall absolute uncertainty of 20 %.⁶⁶

D. Results and Discussion with Bare Ions

Fig. 25 shows the projectile frame DDCS for collisions of F^{9+} with H_2 and He for three different collision energies. Only the electron yields whose laboratory energies are greater than the cusp electron energy (see Fig. 22) are transformed into the projectile frame, since electrons whose laboratory energies are smaller than the cusp energy are not included in the IA model. The spectrum reflects primarily the underlying Compton profile of the target electrons. We compare these data to the the IA model [see Eq. (25)] (solid line) and the PWBA calculation (dashed line).

The overall agreement between the data and the IA is good except in the very low electron energy region, corresponding to electrons with p_{iz} nearly equal and opposite to the cusp momentum, s , for which the impulse approximation approaches the limit of its validity. The combination of the Compton profile and the E'^{-2} energy dependence of the Rutherford cross section results in an electron energy distribution asymmetrically skewed to lower electron energies. The binding energy of the target electron further shifts the energy distribution to even lower energies. These shifts are more pronounced in He than in H_2 targets due to the broader Compton profile and the larger binding energy of He. Therefore, as seen in Fig. 25, the BEe peak is not found at t in the projectile frame ($4t$ in the laboratory frame), as it would if it arose from collisions with truly free electrons (see the vertical arrows in Figs. 22 and 25).

The origin of the BEe energy shift and its asymmetry is investigated in more detail in Fig. 26, where we compare four different calculations with our measurements. The dot-dashed line is the Compton profile⁶⁹ for either H_2 or He targets centered at $(t - E_I)$ in the projectile frame. The solid line is the IA calculation with $E_I = 15.5$ and 24.5 eV for the H_2 and He targets, respectively.

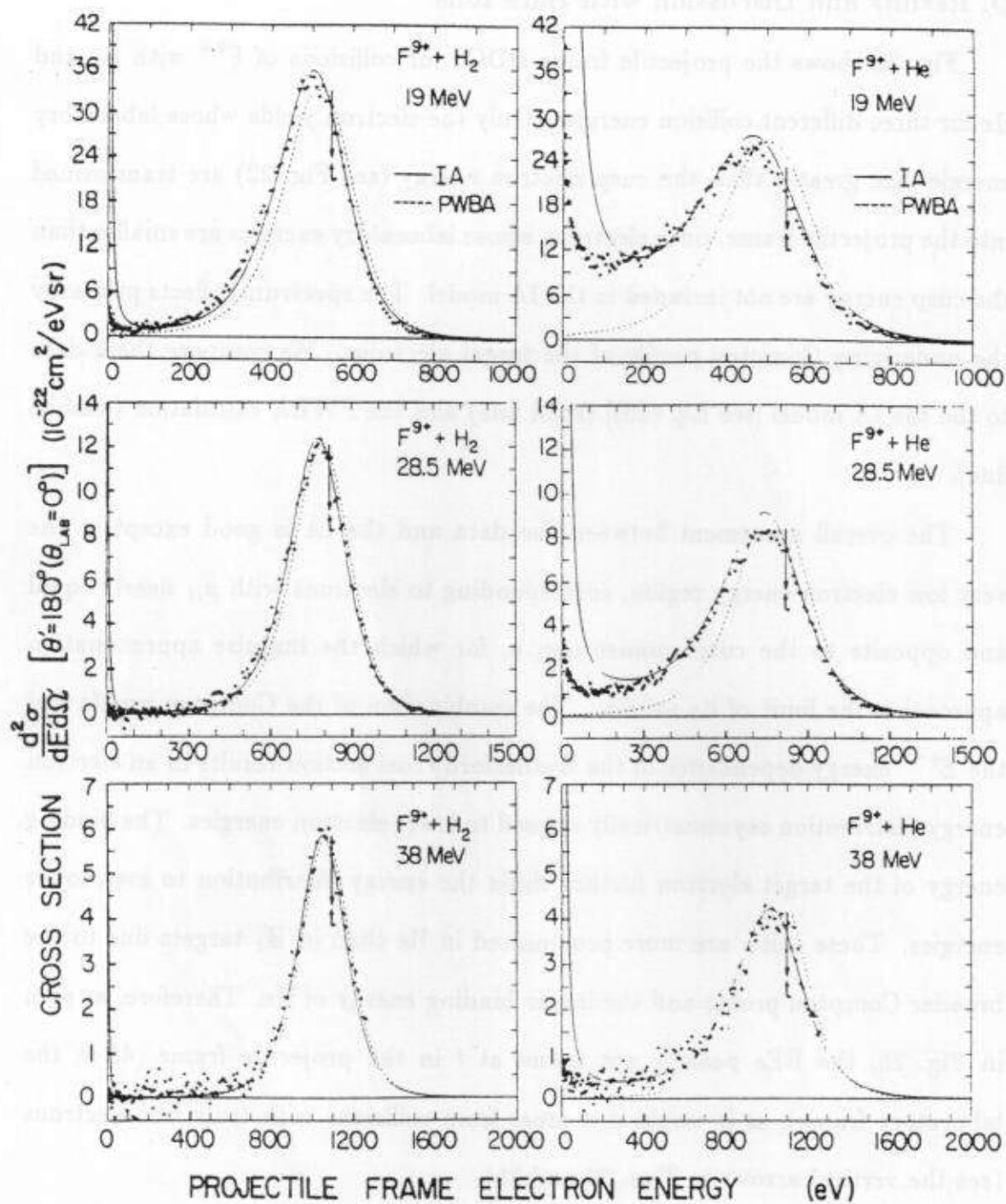
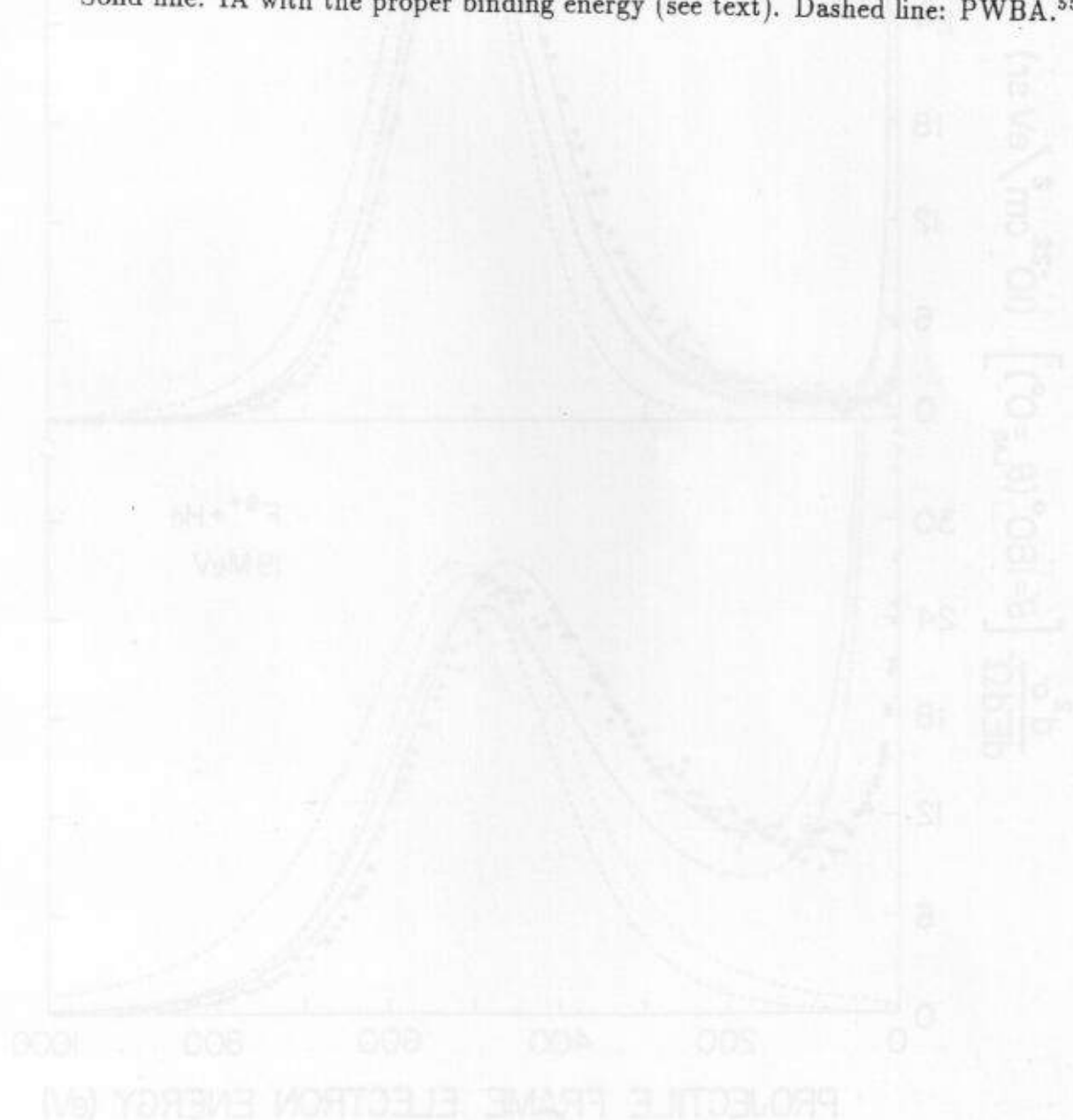
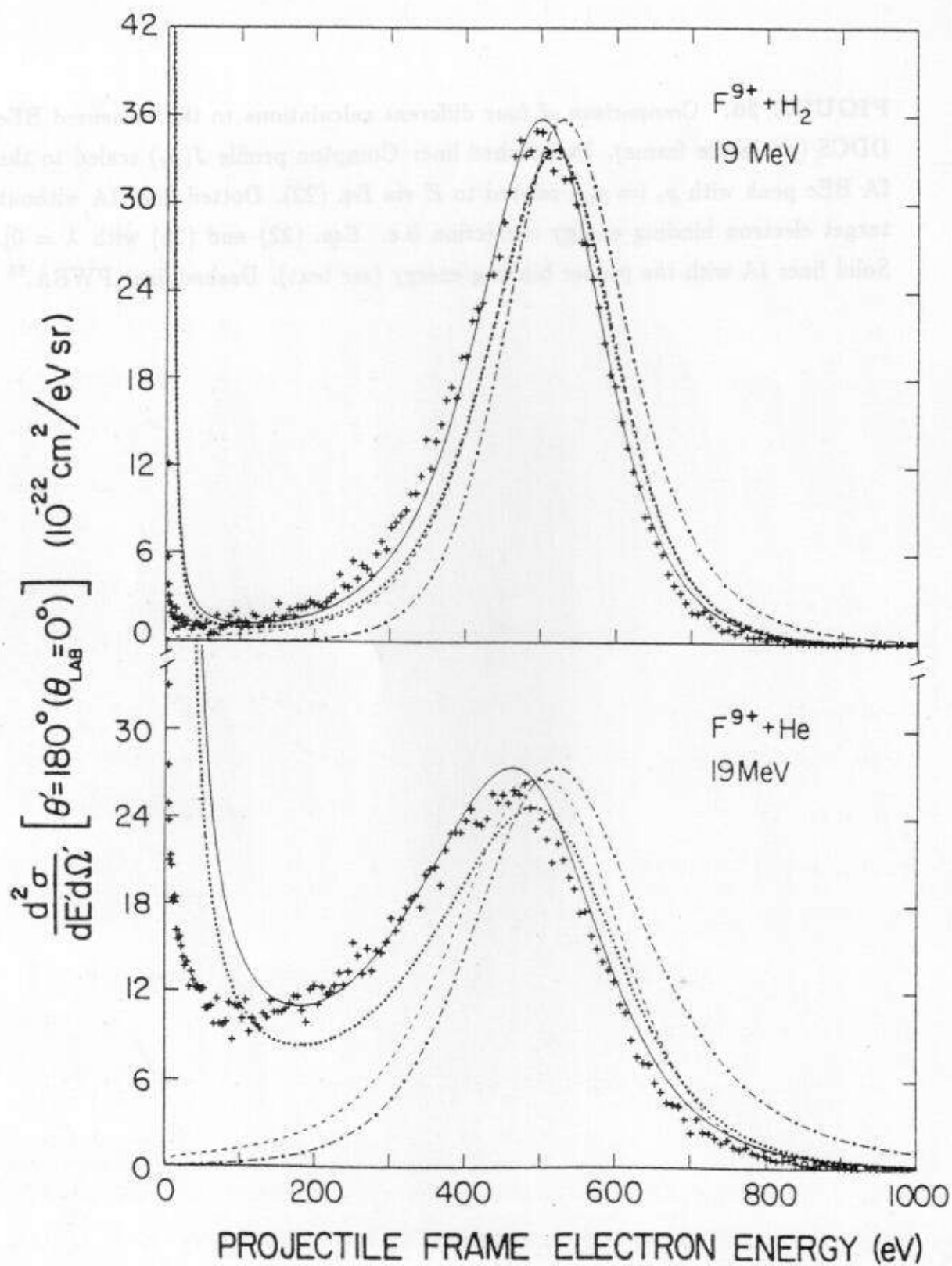


FIGURE 25. BBe DDCCS (projectile frame) measured at $\theta' = 180^\circ$ ($\theta_{Lab} = 0^\circ$ laboratory frame). Solid lines are the result of the impulse approximation (IA) as given by Eq. (25) in text. Also included for comparison (dashed lines) are the results of a plane-wave Born calculation⁵⁵ (PWBA).

FIGURE 26. Comparison of four different calculations to the measured BBe DDCS (projectile frame). Dot-dashed line: Compton profile $J(p_z)$ scaled to the IA BBe peak with $p_z (= p_{iz})$ related to E via Eq. (22). Dotted line: IA without target electron binding energy correction [i.e. Eqs. (22) and (25) with $\lambda = 0$]. Solid line: IA with the proper binding energy (see text). Dashed line: PWBA.⁵⁵





The dotted line is the IA calculation with $E_I = 0$. The dashed line is the PWBA calculation.⁴¹ As observed, around the BEe peak, the PWBA calculation is seen to give the same result as the IA with $E_I = 0$ for 1–2 MeV/u $F^{9+} + H_2$ collisions. The BEe energy shift below $4t$, defined as $\Delta E_L \equiv 4t - E_L^{max}$, was found to vary between ~ 92 – 96 eV for H_2 and ~ 169 – 186 eV for He targets, in collisions with heavy projectiles (see Table 4 for details). E_L^{max} is the laboratory energy at the maximum of the BEe energy distribution, and was extracted by fitting the data by the IA [see Eq. (25)]. The energy shift ΔE_L becomes smaller at higher projectile energies due to the Rutherford scattering E'^{-2} energy dependence. It is interesting to note that the energy shift for protons was smaller than that for the heavy projectiles and could not be fully accounted for, by either the IA or the PWBA treatments, for reasons not yet understood.

The PWBA DDCS were obtained by integrating the analytic expression given by Rudd and Macek⁴¹ over the momentum transfer. In this formulation, the initial state of the target is described by hydrogenic $1s$ wave functions with an effective charge equal to the square root of the binding energy in atomic units.⁴¹ This expression, valid for ionization of a target atom by protons, was generalized to treat other bare ions by multiplying the proton results by Z_P^2 . In Fig. 27 we compare results from 1.5 MeV/u H^+ on H_2 and He. Included as an insert is a comparison of the data for 1.5 MeV/u H^+ and F^{9+} on He. The dashed line is the H^+ data multiplied by Z_P^2 ($=81$). As seen, the Z_P^2 scaling works well only around the BEe peak. The same Z_P^2 scaling trend was observed for the 2 MeV/u data.

We see that the agreement between the data and the PWBA is also good around the BEe peak for F^{9+} collisions with H_2 , but becomes worse for collisions with He (see Fig. 25). In Fig. 25 the energy shift of the BEe peak is not as well accounted for by the PWBA as it is by the IA model.

FIGURE 27. BEe DDCS (laboratory frame) measured for 1.5 MeV $H^+ + H_2$ and He collisions. Solid line: full IA. Dashed lines: PWBA.⁵⁵ Insert: Comparison of 1.5 MeV/u DDCS (same units) for H^+ and $F^{9+} + He$, where the dot-dashed line is the H^+ data multiplied by $Z_p^2 (=81)$.

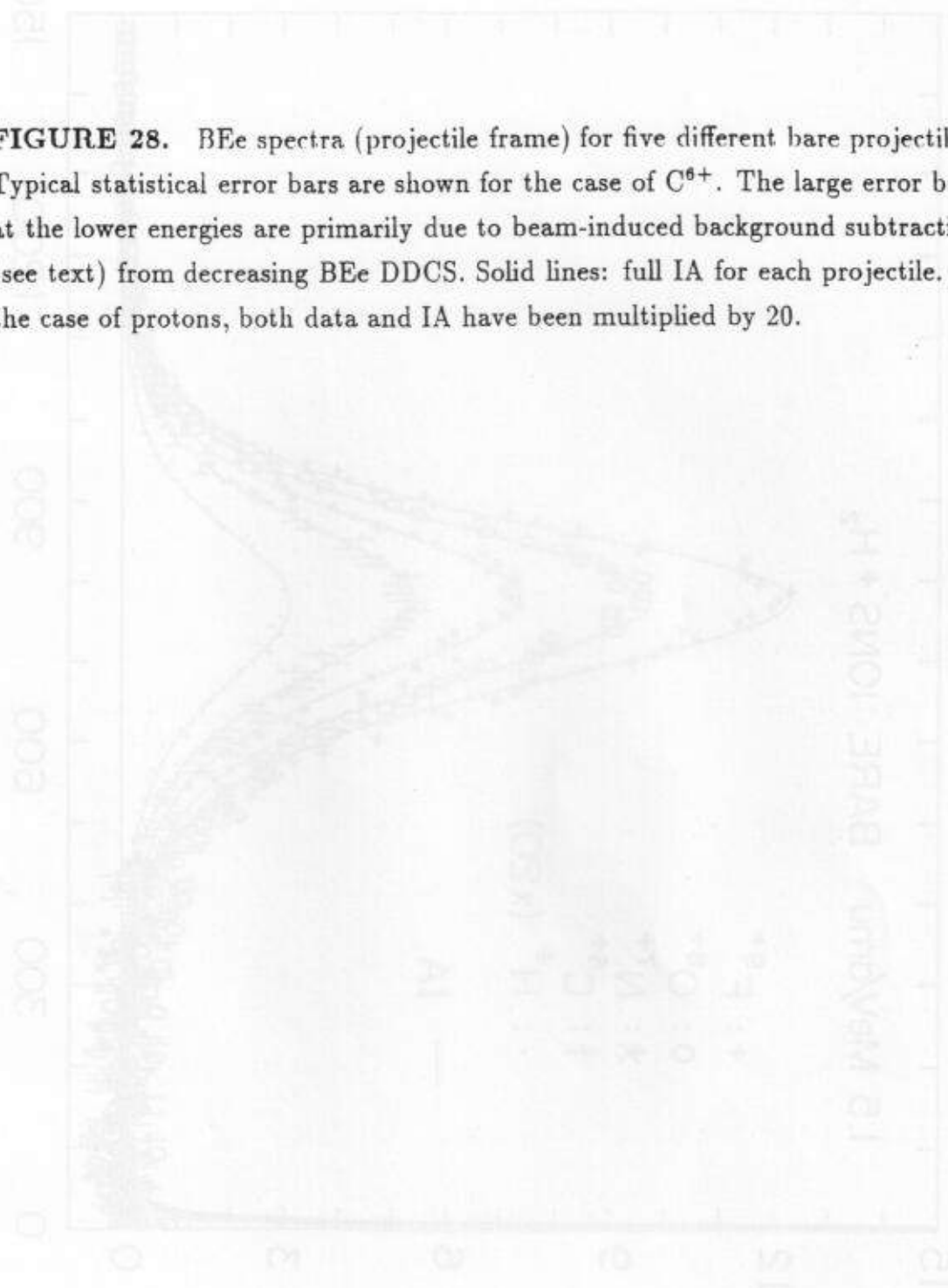
Nevertheless, both IA and PWBA give similar results once the DDCS are integrated over the range of the BEe peak.

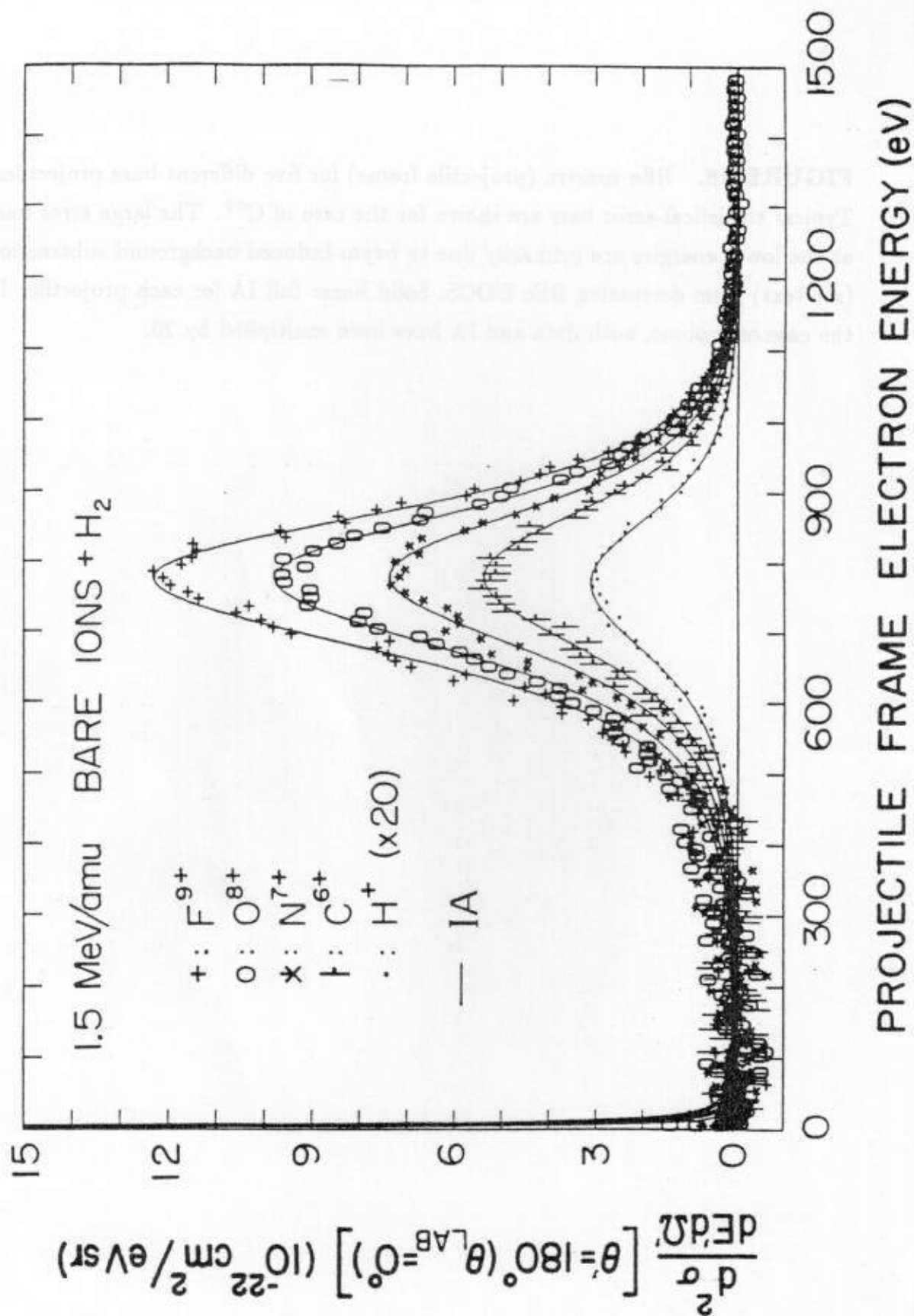
In order to test the Z_P dependence of the BEe production more systematically, various bare ions, F^{9+} , O^{8+} , N^{7+} , and C^{6+} , as well as protons were used as projectiles in collisions with H_2 targets at 1.5 MeV/u. The BEe DDCS for each projectile is compared to the full IA (solid lines) in Fig. 28. The absolute single differential cross section $d\sigma/d\Omega'$ at $\theta' = 180^\circ$ ($\theta_{Lab} = 0^\circ$) was extracted for each projectile by fitting the experimental DDCS with the IA and then integrating over the BEe peak. The resulting cross sections divided by Z_P^2 are plotted in Fig. 29 together with the results of the IA. Shown also are the data and IA results for 2 MeV/u F^{9+} and $H^+ + H_2$ collisions. The Z_P^2 dependence of the BEe production is thus confirmed over this range of Z_P .

In Fig. 30, we compare theoretical and experimental DDCS evaluated at $E = E_L^{max}$ for F^{9+} on H_2 and He for various projectile energies. As discussed earlier, the experimental DDCS have been normalized to the IA DDCS at E_L^{max} for each E_P for $F^{9+} + H_2$. It is seen that the He data show a similar projectile energy dependence as the H_2 data. The extracted exponential fit to the projectile energy dependence shown in Fig. 30 was found to be $\sim E_P^{-2.6}$ for H_2 and $\sim E_P^{-2.7}$ for He targets, respectively, with 5% uncertainty. As seen from Eq. (25), an $E_P^{-2.5}$ dependence is predicted in the limit where λ and $r \rightarrow 0$.

Finally, we consider the possibility of electron capture and its effect on the BEe DDCS. Total capture for these collision systems is quite large (e.g. $\sim 5-0.3 \times 10^{-18}$ cm² for 1-2 MeV/u $F^{9+} + He$),⁶⁸ however, the impact parameter relationship between capture and BEe production processes has yet to be established. In any event, any effect of capture on the BEe DDCS would manifest itself as a deviation from the observed Z_P^2 scaling, since capture at these collision energies

FIGURE 28. BEe spectra (projectile frame) for five different bare projectiles. Typical statistical error bars are shown for the case of C^{6+} . The large error bars at the lower energies are primarily due to beam-induced background subtraction (see text) from decreasing BEe DDCS. Solid lines: full IA for each projectile. In the case of protons, both data and IA have been multiplied by 20.





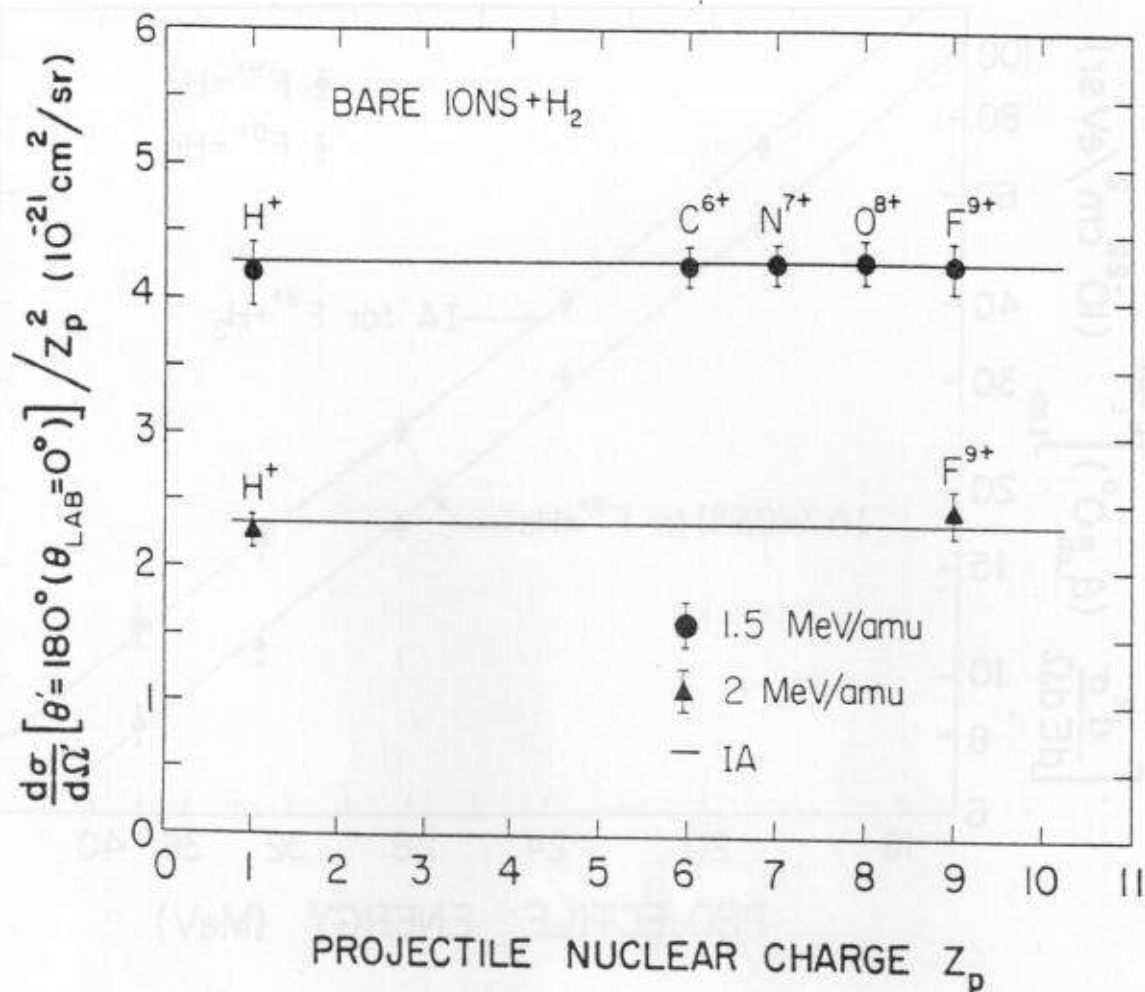


FIGURE 29. Projectile charge (Z_p) dependence of BEE single differential cross sections (projectile frame). Data: solid circles (1.5 MeV/u) and solid triangles (2 MeV/u). Solid lines: full IA. Errors are due primarily to statistics and normalization.

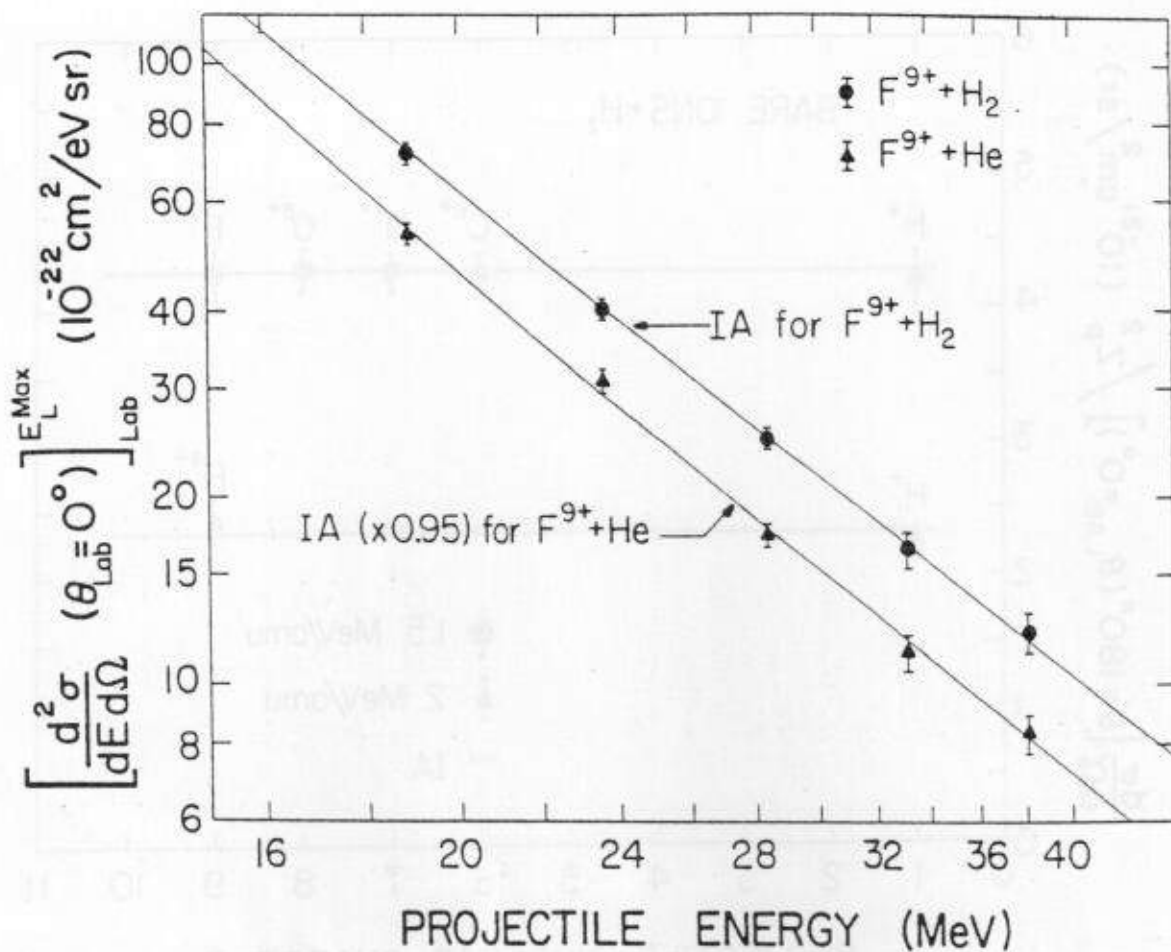


FIGURE 30. Projectile energy dependence of BEE DDCCS (laboratory frame) for $F^{9+} + H_2$ and He collisions. Solid lines: full IA. Solid circles and triangles: Measured DDCCS (at $E_L = E_L^{max}$) for H_2 and He targets, respectively. Errors are due mainly to statistics. The $F^{9+} + H_2$ data have been previously normalized to the IA to determine the spectrometer efficiency shown in Fig. 24 (see text).

is known^{68,77-79} to vary as $\sim Z_P^3$. The strong confirmation of the Z_P^2 scaling of the BEe DDCS, as shown in Fig. 29, suggests that capture can be neglected in the collision systems studied here. A similar argument can also be made about the E_P dependence of capture^{78,79} ($\sim E_P^{-4.5}$) compared to that of BEe production ($\sim E_P^{-2.6}$).

E. Projectile q -Dependence

The projectile charge state dependence of the BEe production at 0° was also studied for collisions of 19 and 28.5 MeV F^{q+} with H_2 and He targets. The charge state q was varied from 3 to 9 for 19 MeV and 5 to 9 for 28.5 MeV projectiles. Previous measurements of BEe production, performed at non-zero observation angles,^{31,59} showed that the addition of electrons to a bare projectile acted to screen the nuclear charge of the projectile, giving rise to a net effective charge Z_P^* , which depended on the ejected laboratory electron energy E_L ,^{36,54,80} and thus influenced the overall BEe production.

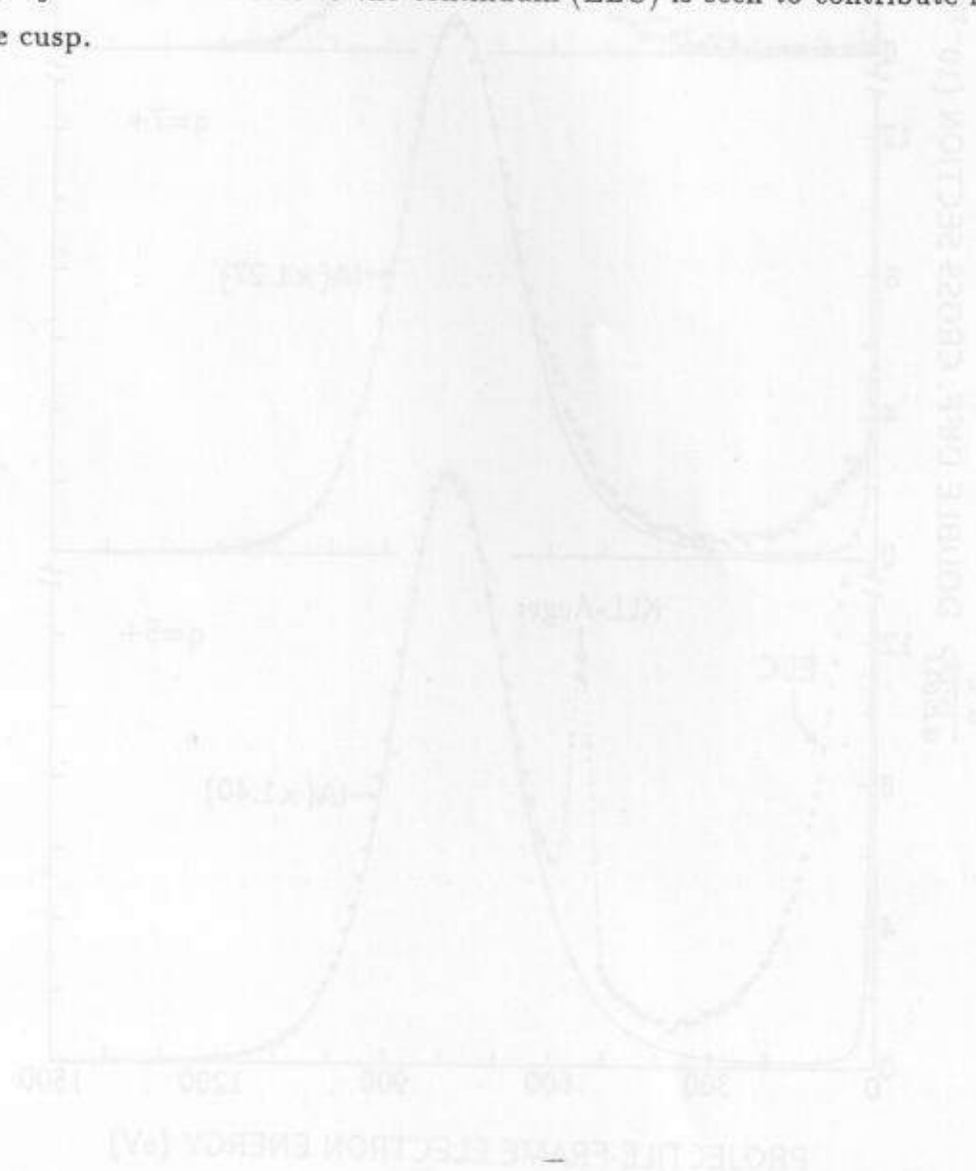
Basic screening ideas dictate that processes occurring outside the electron cloud surrounding the projectile nucleus should be screened to some extent, while processes occurring well within the cloud should experience negligible screening. A more quantitative screening model based on this idea was developed by Toburen *et al*⁸¹ using the Massey criterion: $R_{ad} = V_P / \Delta E_T$ (all quantities in atomic units) relating ΔE_T , the energy transferred between the impinging ion and the ionized electron, to an adiabatic interaction distance R_{ad} , where V_P is the projectile velocity and $\Delta E_T = E_L + E_I$, E_I is the ionization energy of the target electron. If R_{ad} is found to be smaller than the average radius, R , of the projectile electron of interest, no screening is expected. Alternatively, if $R_{ad} > R$ then the projectile electrons should be expected to provide effective screening. In this model, Z_P^* was

always found to be smaller than or equal to the projectile nuclear charge Z_P . Fair agreement with available (non-zero degree) BEe experimental data was found.⁸¹

For the collision systems investigated here, 19 and 28.5 MeV $F^{q+} + \text{He}$ or H_2 and $\theta_{Lab} = 0^\circ$, $\Delta E_T \approx 4t$ around the BEe peak corresponding to $R_{ad} \approx 0.08$ and 0.06 a.u. for 19 and 28.5 MeV collisions, respectively. Thus, $R_{ad} < R_K = 1/9$ a.u., R_K being the K -shell radius of the fluorine ion and therefore negligible screening is expected, i.e. $Z_P^* = Z_P$. This result is also consistent with the IA approach to BEe production mentioned previously. Rutherford electron scattering through 180° (0° laboratory observation) corresponds to impact parameters between the scattered electron and the projectile nucleus that are essentially zero, i.e. close-encounter collisions well within R_K for which minimal screening can be expected. Even if screening effects were important in such 0° measurements, this model would predict that BEe production should decrease with decreasing q [as verified in the case of non-zero angle observation measurements in Ref. 29]. In our present zero degree measurements, the opposite q -dependence was observed. BEe production was found to increase steadily with each electron added to the projectile giving rise to a net *anti-screening* effect totally unpredicted by the above screening model.

The enhancement of the BEe peak can be directly observed in Fig. 31, as the number of projectile electrons is increased. The solid lines are the calculated IA-DDCS [see Eq. (25)] for *bare* projectiles ($Z_P^* = 9$ for all q as discussed above) scaled to the experimental BEe spectra near and above the BEe peak energy by multiplying by the scaling factors shown within parentheses in Fig. 31. The ratios of the BEe DDCS for F^{q+} ($q=3-9$) to that of F^{9+} were determined using the scaling factors shown in Fig. 31. These are plotted in Fig. 32 for the various collision systems investigated. The enhancement of the BEe DDCS with increasing number of projectile electrons, is clearly observed. Similar enhancements were

FIGURE 31. Data: Measured BEE spectra (projectile frame) for collisions of 28.5 MeV $F^{(9,7,5)+}$ with H_2 . Solid lines: IA calculation for bare F^{9+} BEE production scaled to data by multiplying by numbers in parentheses. We note that electrons with zero kinetic energy in the projectile frame correspond to the cusp electrons. For F^{5+} BEE production, the observed *KLL*-Auger electrons result from projectile *K*-shell ionization and/or excitation followed by autoionization. The projectile electron loss to the continuum (ELC) is seen to contribute mainly to the cusp.



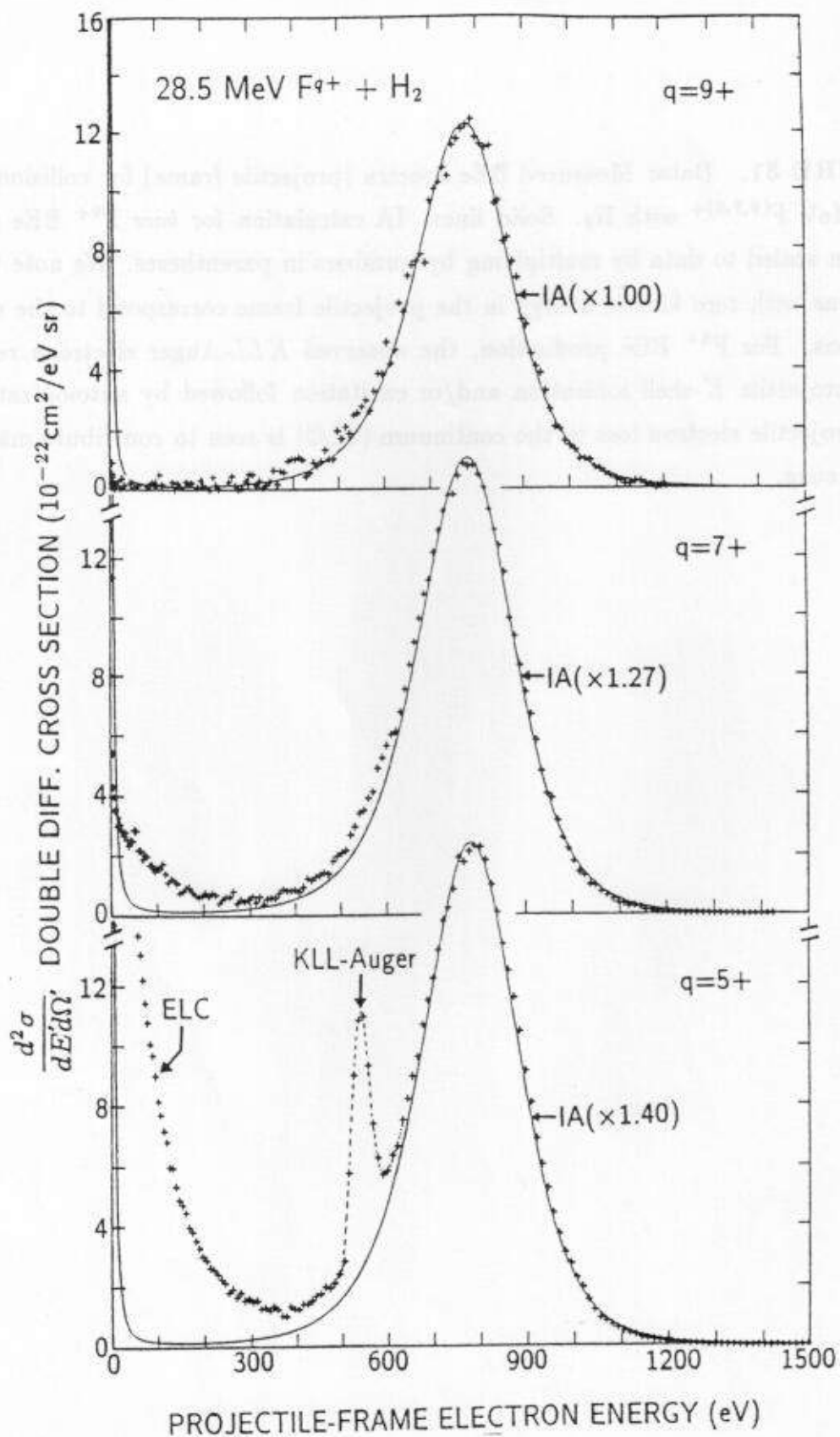
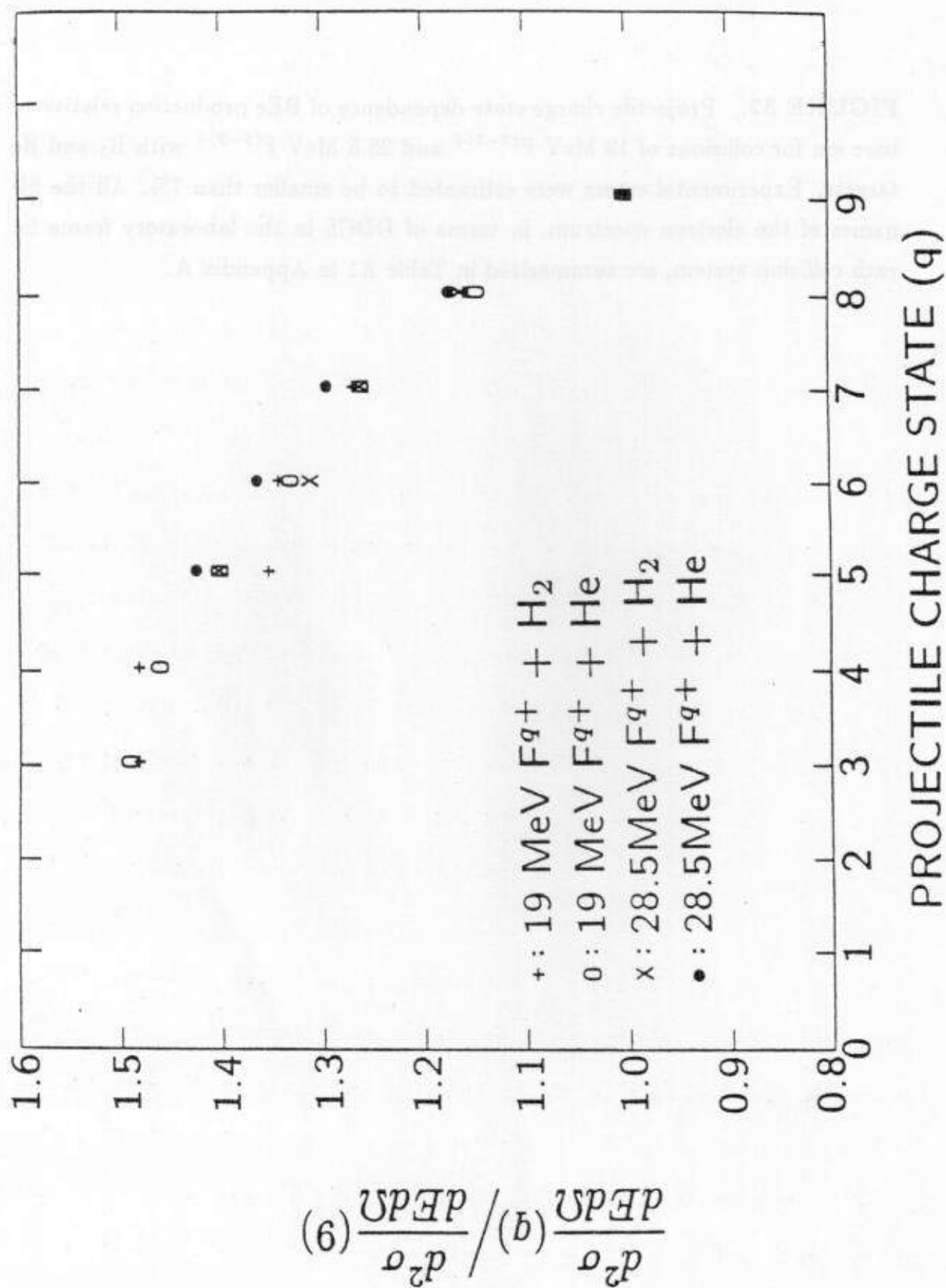


FIGURE 32. Projectile charge state dependence of BEE production relative to bare ion for collisions of 19 MeV $F^{(3-9)+}$ and 28.5 MeV $F^{(5-9)+}$ with H_2 and He targets. Experimental errors were estimated to be smaller than 7%. All the file names of the electron spectrum, in terms of DDOS in the laboratory frame for each collision system, are summarized in Table A1 in Appendix A.





also observed between 1.5 MeV/u O^{8+} and O^{4+} ; N^{7+} and N^{3+} ; and C^{6+} and C^{3+} in collisions with a H_2 target (not shown in figures). Several plausible mechanisms that could give rise to such an enhancement are considered next.

Binary encounters between a tightly bound projectile K -shell electron and a target electron might contribute to the BEe peak, but such a contribution is expected within the IA model to be small, down by a factor of Z_P^{-2} to at most a few percent of the ion nucleus-electron interaction. Similarly, projectile electron ionization (ELC—electron loss to continuum) also contributes to the BEe peak, but negligibly in the vicinity of the BEe peak for the present fast ion-atom collisions, since the cusp and the BEe peak are well separated (see Fig. 12). This was independently confirmed in coincidence measurements for collisions of 9.5 MeV $F^{9+} + H_2$ in which BEe produced by pure target ionization were directly determined.⁸¹ This was accomplished by counting the number of BEe emitted at zero degrees in coincidence with the projectile ion of unaltered q . The BEe production by pure target ionization showed almost the same q -dependence as that found in the present measurements shown in Fig. 32. Thus, any projectile charge changing collision is seen to be effectively eliminated as the cause of the anomalous q -dependence.

The observed enhancement could also be viewed as a net suppression of BEe yields, the suppression increasing with increasing projectile q due to $\sim q^3$ dependence of total electron capture.^{68,77-79} It should be pointed out, however, that the BEe study using the bare projectiles in the previous section demonstrated that the observed Z_P^2 dependence agreed very well with the IA and PWBA (plane-wave Born approximation) calculations for collisions of 1.5 MeV/u F^{9+} , O^{8+} , N^{7+} , C^{6+} and H^+ with H_2 targets. If electron capture considerably affected the BEe production for these fast bare projectiles, some deviation from the Z_P^2 dependence would be observed.

Finally, another possible mechanism for this enhancement is one in which a secondary electron scattering occurs as a cooperative action of the projectile electrons with their nucleus. In such a process, the projectile electrons alter the trajectory of the BEE during the binary encounter collision. In this classical picture, a target electron is scattered by the projectile nucleus at some angle other than 180° and then deflected by a collision with a projectile electron to produce a net 180° scattering event. This enhancement would primarily come from small impact parameter scattering between the target electron and the projectile nucleus.

During the writing of this dissertation three theoretical papers^{83,84} have been written on the anomalous q -dependence of BEE and demonstrated that the anomalous cross section is obtained directly from a screened Coulomb model for back angle electron scattering. This will be discussed in the Chapter of conclusions.

V. ZERO-DEGREE AUGER CROSS SECTION ANALYSIS

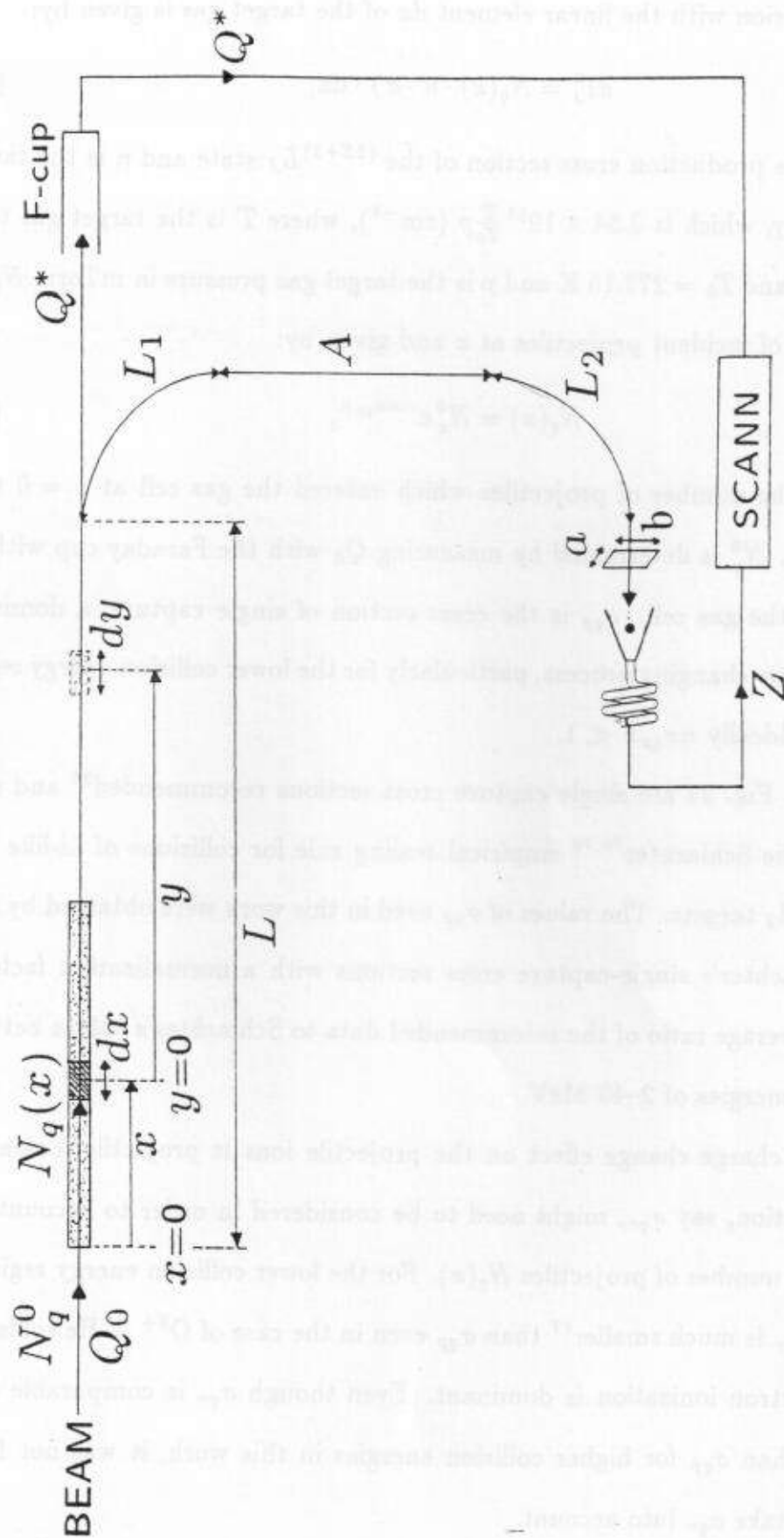
A detailed analysis of *state-resolved* (state-selective) Auger electron production measurements at $\theta=0^\circ$ is carried out. In particular, a large portion of this chapter is dedicated to the discussion of cross section determinations for the metastable $1s2s2p^4P$ state. Extensive attention has been paid by both theorists and experimentalists to the study of the lifetime and production cross section for the 4P state. This state has been observed in the present work and has revealed a variety of different atomic collision processes, for example, projectile $1s \rightarrow 2p$ excitation by target electrons (eeE)¹². In general, when a collisionally produced, excited state of the projectile has a long lifetime compared to the time period for the projectile to pass the collision region of the gas cell, this lifetime should be properly accounted ^{for} in the determination of cross sections. In addition, when Auger production cross sections are measured for an ion-atom collision process, any other dominant process, for example, electron capture should be taken into account. For instance, in collisions of 0.25 MeV/u F^{6+} with He targets of areal density of 40 mTorr \times 10 cm, a strong beam neutralization after passing these gas targets was observed. These projectile charge neutralization effects should be considered. //

A. Differential Cross Sections and Effective Solid Angle Calculation

In this section, I will present the formula developed for the analysis of the double differential cross sections (DDCS) for zero degree Auger production cross sections. The approach is to derive a formula which includes the effects of 1). an extended gas target region, 2). the charge neutralization of the beam, and 3). the lifetime of the intermediate projectile Auger state. e/

As seen in Fig. 33, dI_J^0 , the number of projectiles excited into the $(2S+1)L_J$

FIGURE 33. A schematic diagram for the measurement of the Auger production cross sections. x is the distance from the gas cell entrance to the target source element dx and y is the distance from dx to the Auger-decaying source element dy for a metastable state of a moving projectile. For a prompt state of a moving projectile or for an excited state of a stationary target, dx is the Auger electron production source i.e., $y = 0$ in this case. L is the distance from the entrance of the gas cell to the entrance of the spectrometer. L_1 and L_2 are the parabolic path lengths of the electron trajectory in the analyzing field of the first and second analyzer, respectively. A is the distance between the exit of the first analyzer and the entrance of the second analyzer. $B = A + L_1 + L_2$ is defined. a and b are the width and length of the exit slit of the second spectrometer. All the geometrical factors are listed in Tables 2 and 4. Z , number of electrons for each charge Q^* is counted and recorded by the spectrum acquisition program SCANN.



state by a collision with the linear element dx of the target gas is given by:

$$dI_J^0 = N_q(x) \cdot n \cdot \sigma_J \cdot dx, \quad (29)$$

where σ_J is the production cross section of the $(2S+1)L_J$ state and n is the target number density, which is $3.54 \times 10^{13} \frac{T}{T_0} p$ (cm^{-3}), where T is the target gas temperature in K and $T_0 = 273.15$ K and p is the target gas pressure in mTorr. $N_q(x)$ is the number of incident projectiles at x and given by:

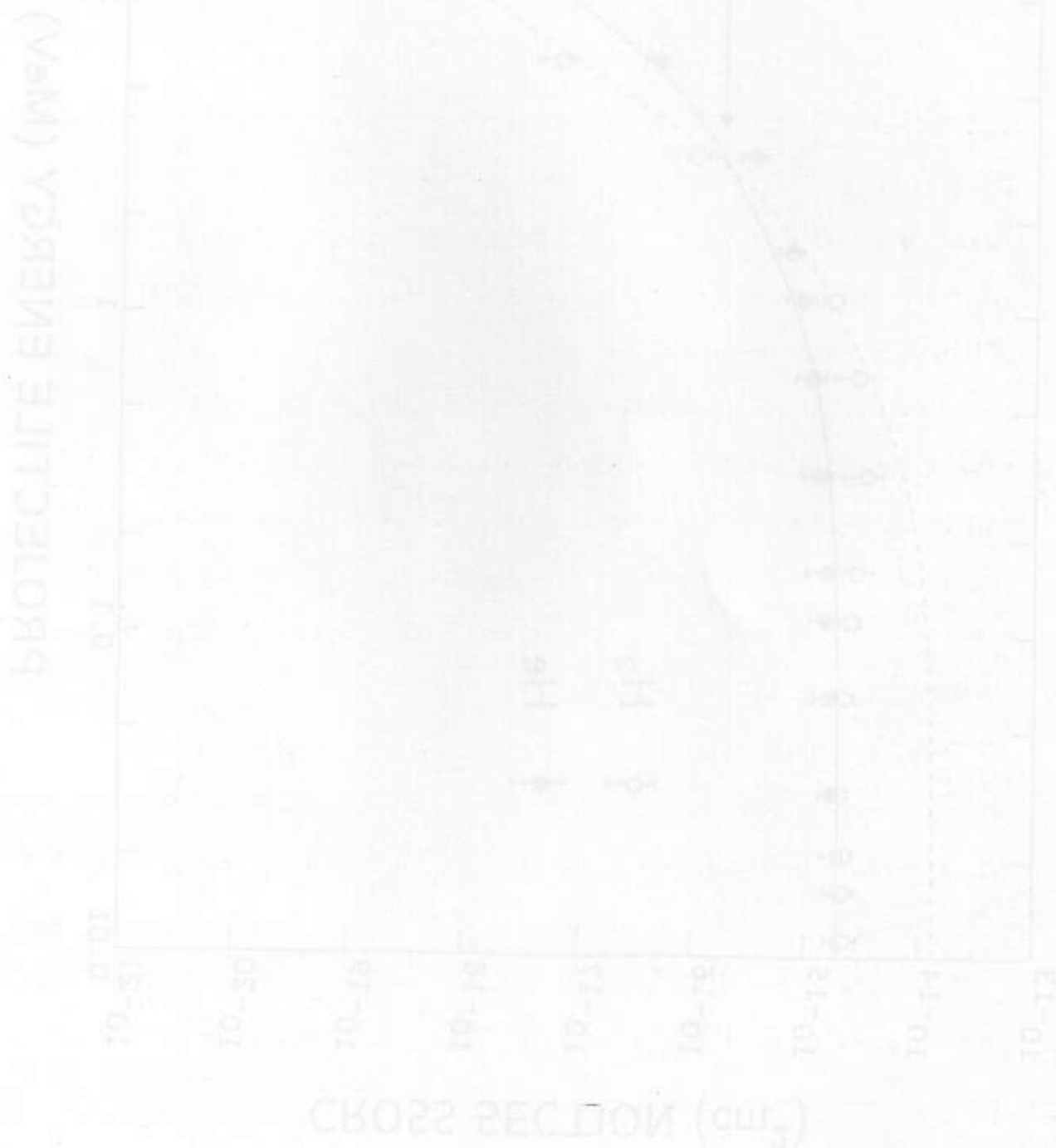
$$N_q(x) = N_q^0 e^{-n\sigma_{qp}x}, \quad (30)$$

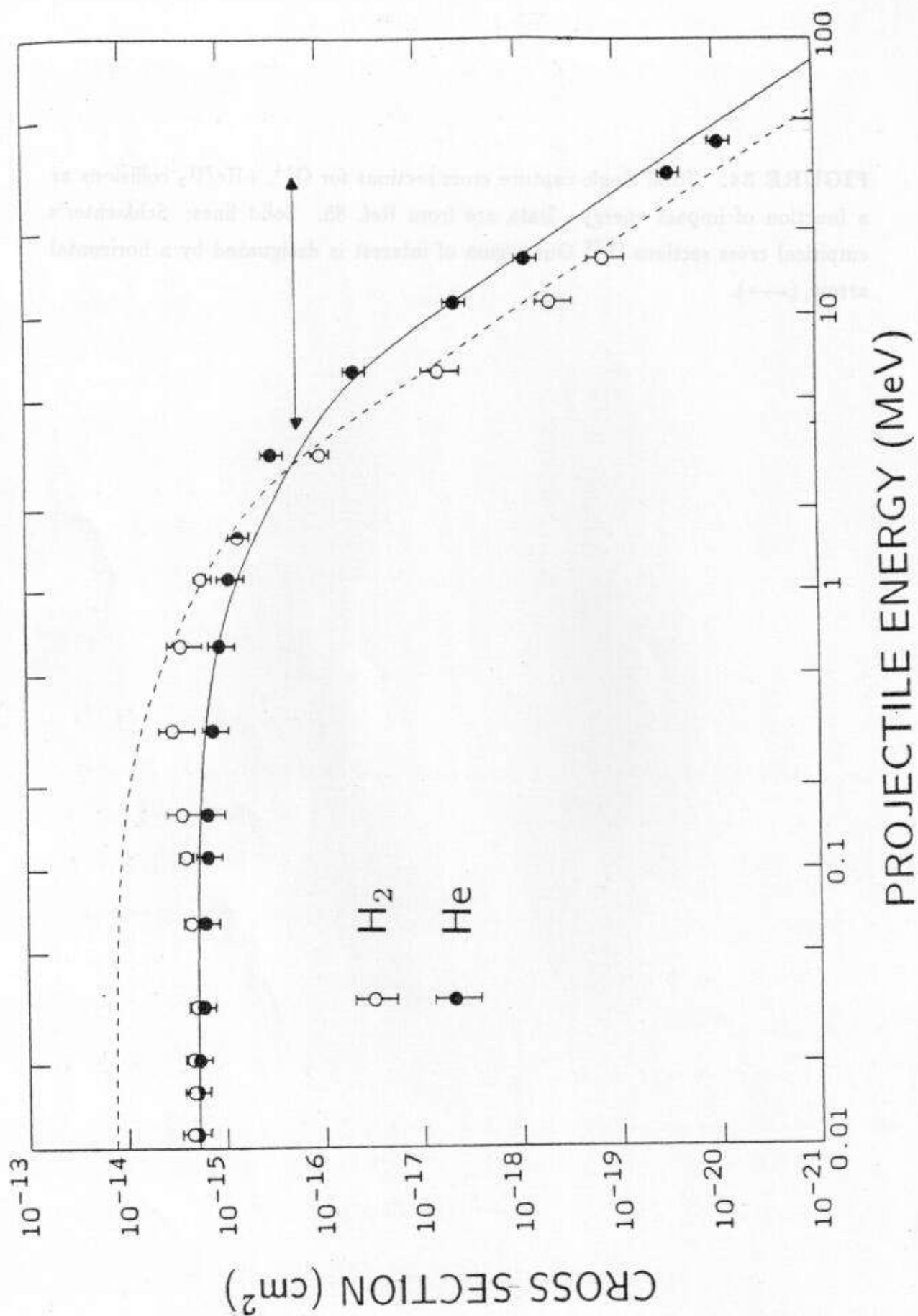
where N_q^0 is the number of projectiles which entered the gas cell at $x = 0$ with charge state q . N_q^0 is determined by measuring Q_0 with the Faraday cup without target gas in the gas cell. σ_{qp} is the cross section of single capture, a dominant projectile charge changing process, particularly for the lower collision energy region of this work. Ideally $n\sigma_{qp}x \ll 1$.

Shown in Fig. 34 are single capture cross sections recommended⁸⁵ and evaluated using the Schlachter^{78,79} empirical scaling rule for collisions of Li-like O^{5+} with He and H_2 targets. The values of σ_{qp} used in this work were obtained by multiplying Schlachter's single-capture cross sections with a normalization factor,⁸⁶ which is an average ratio of the recommended data to Schlachter's values between the collision energies of 2–40 MeV.

Another charge change effect on the projectile ions is projectile ionization. The cross section, say σ_{qr} , might need to be considered in order to account correctly for the number of projectiles $N_q(x)$. For the lower collision energy region of this study, σ_{qr} is much smaller⁸⁷ than σ_{qp} even in the case of $\text{O}^{5+} + \text{He}$ collisions, where $2s$ electron ionization is dominant. Even though σ_{qr} is comparable to or even larger than σ_{qp} for higher collision energies in this work, it was not found necessary to take σ_{qr} into account.

FIGURE 34. Total single capture cross sections for $O^{5+} + He/H_2$ collisions as a function of impact energy. Data are from Ref. 85. Solid lines: Schlachter's empirical cross sections.^{78,79} Our region of interest is designated by a horizontal arrow, (\longleftrightarrow).





If the $(2S+1)L_J$ state has a long lifetime (i.e., *metastable* state), it is necessary to take into account the deexcitation behavior along the projectile trajectory in front of the spectrometer entrance. Shown in Table 6 is a list of lifetime τ and Auger yield ξ of the various Auger states of interest in this study. Definitely the metastable states, $1s2s2p^4P_J$ have a long lifetime compared to the other states which are so called "prompt" states.

After time t following excitation of the metastable state, the number of the excited states which are left is:

$$dI_J(t) = dI_J^0 \cdot e^{-t/\tau_J}, \quad (31)$$

where τ_J is the lifetime of the J -state. Since $t = y/V_p$ and defining $V_p\tau_J \equiv \lambda_J$, $dI_J(t)$ is now expressed as a function of y :

$$dI_J(y) = dI_J^0 \cdot e^{-y/\lambda_J}, \quad (32)$$

which is the number of remaining excited states at y .

In order to illustrate all the effects described so far, variations of $N_q(x)$ for given target gas pressures and $dI_J(y)$ particularly for metastable $1s2s2p^4P_J$ states are shown in Fig. 35 together with the pure geometrical solid angle $\Delta\Omega(y)$ [see Eq. (36) below with $x=0$]. For the prompt states $dI_J = dI_J^0$ and $dI_J(y \neq 0) = 0$, i.e., the collision region is itself the linear emission source of the Auger electrons for the collision energies in this work. As discussed, σ_{qp} , n , and τ_J are important factors for cross section measurements at zero degrees.

The number of decayed projectile ions in the excited J -state, dZ_J^0 , resulting in radiative and Auger decay for the moving source element dy located at y is given by

$$dZ_J^0 = - \sum_k \frac{1}{k!} \frac{\partial^k (dI_J(y))}{\partial y^k} (dy)^k. \quad (33)$$

TABLE 6

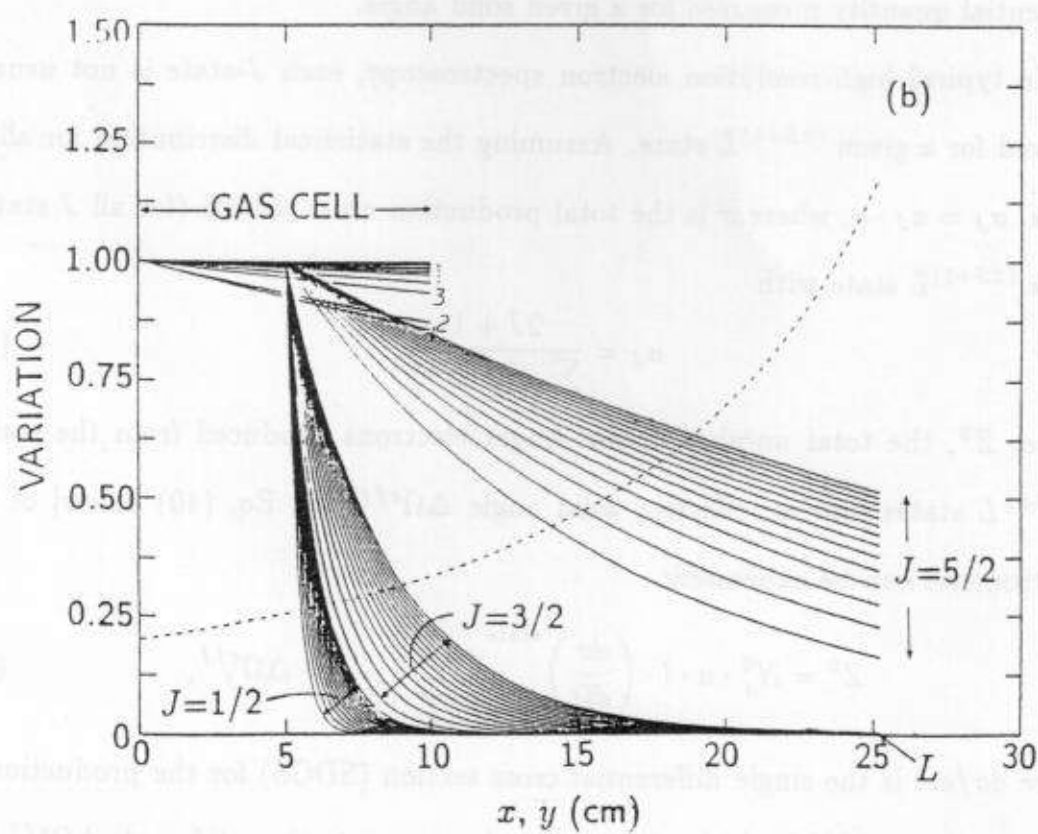
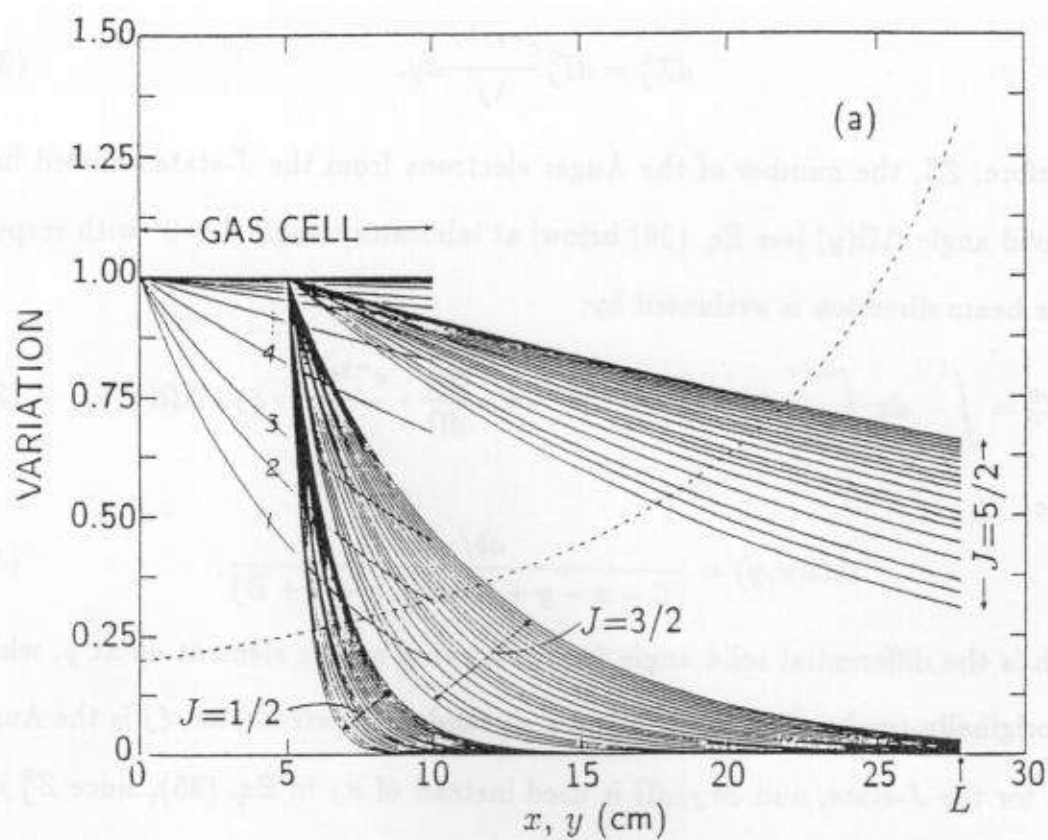
Lifetimes τ and Auger yields ξ , of interest in this work, for various doubly excited states of $(1s2l2l')$ of Li-like O^{5+} and F^{6+} ions and of $(1s2s2p^2)^3,1D$ state of Be-like O^{4+} and F^{5+} ions. $\xi = \sum_J a_J \cdot \xi_J$ is J -averaged value for all the prompt states. For $[1s2s2p]^4P_J$ metastable states, ξ_J for each J -state is shown and thus $\xi=0.8947$ and 0.7932 for O^{5+} and F^{6+} ions, respectively, are estimated. For a given $[1s(2s2p)^3P)]^2P^-$ or $[1s(2s2p)^1P)]^2P^+$ state in this Table, τ_J and ξ_J for each J -value are found to be very nearly the same⁹¹ with only a few % difference for different J -states, and $\xi = \sum_J a_J \cdot \xi_J$ and $\tau = \sum_J a_J \cdot \tau_J$ are J -averaged (statistically weighted) values. τ for prompt states were evaluated by $\tau = (\Gamma_A + \Gamma_X)^{-1}$, where Γ_A and Γ_X are Auger and x-ray transition rates found in the specified references. Typical lifetimes of autoionizing prompt states can be deduced from the Auger line widths of about 0.1 eV as follows:

$$\tau = \frac{\hbar}{\Gamma} = \frac{6.58 \times 10^{-16} \text{ eV} \cdot \text{sec}}{0.1 \text{ eV}} \approx 10^{-14} \text{ sec}$$

TABLE 6: Lifetimes and Auger yields

state	ion	τ (nsec)	ξ or ξ_J	Reference
$[1s2s^2]^2S$	O^{5+}	1.49×10^{-5}	1.000	Ref. 88
	F^{6+}	1.25×10^{-5}	0.9971	Ref. 89
$[1s2s2p]^4P_{1/2}$	O^{5+}	0.91	0.967	Ref. 90
	F^{6+}	0.57	0.928	Ref. 90
$[1s2s2p]^4P_{3/2}$	O^{5+}	3.34	0.701	Ref. 90
	F^{6+}	1.84	0.416	Ref. 90
$[1s2s2p]^4P_{5/2}$	O^{5+}	27.67	0.9998	Ref. 90
	F^{6+}	15.90	0.9997	Ref. 90
$[1s(2s2p)^3P]^2P_-$	O^{5+}	9.44×10^{-5}	0.739	Ref. 91
	F^{6+}	8.08×10^{-5}	0.618	Ref. 91
$[1s(2s2p)^1P]^2P_+$	O^{5+}	1.36×10^{-5}	0.996	Ref. 91
	F^{6+}	1.27×10^{-5}	0.993	Ref. 91
$[1s2p^2]^2D$	O^{5+}			
	F^{6+}	0.97×10^{-5}	0.9785	Ref. 88
$[(1s2s)^3S2p^2]^3D$	O^{4+}		0.899	Ref. 9
	F^{5+}	3.96×10^{-5}	0.89	Ref. 13/88
$[(1s2s)^1S2p^2]^1D$	O^{4+}		0.409	Ref. 9
	F^{5+}	2.29×10^{-5}	0.50	Ref. 13/88

FIGURE 35. Variations of projectile flux, the number of $1s2s2p^4P_J$ states, and the pure geometrical solid angle along the beam direction for (a); 4–32 MeV $O^{5+} + He$ (40 mTorr) collisions, and for (b); 4.75–35.63 MeV $F^{7+} + He$ (various pressures, see Table 11). The projectile flux variation for each collision energy, $N_q(x)/N_q^0 = e^{-n\sigma_{TP}x}$, which is obtained from Eq. (30), is drawn in the gas cell range of $x=0-10$ cm. The designated numbers to the variation curves correspond to the order of the projectile energies in Tables 7 and 11. The decay curve of the 4P_J states for each J and each projectile energy, e^{-y/λ_J} , which is obtained from Eq. (32), is drawn for the states which are produced at the center of the gas cell. The decay curves from the lowest to highest are given in the order of the collision energies for each J group. Also drawn in the dashed line is the variation of the pure geometrical solid angle $\Delta\Omega(y)$ [see Eq. (36) below with $x = 0$] as a function of y from $y = x = 0$ to $y = L$, spectrometer entrance.



For sufficiently small dy/λ_J and neglecting all the higher terms with $k \geq 2$,

$$dZ_J^0 = dI_J^0 \frac{e^{-y/\lambda_J}}{\lambda_J} dy. \quad (34)$$

Therefore, Z_J^0 , the number of the Auger electrons from the J -state emitted into the solid angle $\Delta\Omega(y)$ [see Eq. (36) below] at laboratory angle $\theta = 0^\circ$ with respect to the beam direction is evaluated by:

$$Z_J^0 = \int_{x=0}^l dx \int_{y=0}^{L-x} dy \cdot N_q^0 \cdot e^{-n\sigma_{qr}x} \cdot n \cdot \frac{d\sigma_J}{d\Omega} \cdot \frac{e^{-y/\lambda_J}}{\lambda_J} \cdot \xi_J \cdot \Delta\Omega(x, y), \quad (35)$$

where

$$\Delta\Omega(x, y) = \frac{ab/\sqrt{2}}{(L-x-y+A)(L-x-y+B)}, \quad (36)$$

which is the differential solid angle for the moving source element dy at y , which was originally produced at x , in the present tandem spectrometer, ξ_J is the Auger yield for the J -state, and $d\sigma_J/d\Omega$ is used instead of σ_J in Eq. (35), since Z_J^0 is a differential quantity measured for a given solid angle.

In typical high-resolution electron spectroscopy, each J -state is not usually resolved for a given $(2S+1)L$ state. Assuming the statistical distribution for all J -states, $\sigma_J = a_J \cdot \sigma$, where σ is the total production cross section (for all J states) of the $(2S+1)L$ state with

$$a_J = \frac{2J+1}{\sum_J (2J+1)}. \quad (37)$$

Hence, Z^0 , the total number of the Auger electrons produced from the source of $2S+1L$ states into an effective solid angle $\Delta\Omega^{eff}$ [see Eq. (40) below] of the spectrometer can be expressed:

$$Z^0 = N_q^0 \cdot n \cdot l \cdot \left(\frac{d\sigma}{d\Omega} \right)^{state} \cdot \sum_J a_J \cdot \xi_J \cdot \Delta\Omega_J^{eff}, \quad (38)$$

where $d\sigma/d\Omega$ is the single differential cross section (SDCS) for the production of the atomic state $2S+1L$ which emits Auger electrons into the solid angle $\Delta\Omega^{eff}$ [see

Eq. (43) below]. Therefore, Z , the number of electrons for each electron energy E at the laboratory angle $\theta = 0^\circ$, can be given by:

$$Z(E) = N_q^0 \cdot n \cdot l \cdot \sum_J a_J \cdot \xi_J \cdot \Delta\Omega_J^{eff} \cdot \eta \cdot \int_{\epsilon=-\infty}^{\epsilon=+\infty} \frac{d^2\sigma}{dE d\Omega}(\epsilon) \cdot f(\epsilon - E) d\epsilon, \quad (39)$$

where $d^2\sigma/dE d\Omega$ is the double differential cross section (DDCS) for the production of any atomic state which can result in electron emission with energy of E at angle θ ($\theta=0^\circ$ in our case), $f(\epsilon - E)$ is a normalized spectrometer response function, η is spectrometer efficiency, in general, a function of the laboratory electron energy E but practically a constant value for the peak range of $f(\epsilon - E)$, and $\Delta\Omega_J^{eff}$ is given by (i). for metastable states:

$$\Delta\Omega_{J-meta}^{eff} = \frac{1}{\lambda_J l} \int_{x=0}^l \int_{y=0}^{L-x} e^{-n\sigma_{rp}x} \cdot \Delta\Omega(x, y) \cdot e^{-y/\lambda_J} dy \cdot dx, \quad (40-1)$$

and by (ii). for prompt states ($\Delta\Omega_J^{eff}$ is J -independent and $y=0$):

$$\Delta\Omega_{prompt}^{eff} = \frac{1}{l} \int_0^l \Delta\Omega(x) \cdot e^{-n\sigma_{rp}x} dx, \quad (40-2)$$

where $\Delta\Omega(x)$ is given by Eq. (36). Therefore, the DDCS for Auger or state production at zero degrees can be determined by detecting the number of Auger electrons Z as follows:^{12,13,14}

$$\frac{d^2\sigma}{dE d\Omega} = \frac{Z(E)}{N_q^0 \cdot n \cdot l \cdot \Delta E \cdot \Delta\Omega^{eff} \cdot \eta}, \quad (41)$$

where ΔE is the electron acceptance energy, which is $\Delta E = E \cdot R$ and is the so-called FWHM of spectrometer response function, $R = 2.8\%$ being the present spectrometer resolution in the case of a non-retarding mode. Z for each electron energy E is counted by stepping E for each accumulated charge Q^* , which is measured by the Faraday cup and preset in the data acquisition program. However,

Q_0 measured by the Faraday cup (FC in Fig. 35) without a gas target should be used for the determination of DDSCS, i.e., $N_q^0 = Q_0/qe$, where qe is the incoming projectile charge. The effective solid angle $\Delta\Omega^{eff}$ (for all J) for Auger or state production measurements will be given and discussed later.

The derivation of Eq (41) from Eq. (39) was done in the ideal case where $f(\epsilon - E)$ is treated as a rectangular-shape delta function located at $\epsilon = E$ with a width of ΔE (i.e., infinite spectrometer resolution.) Eq. (41) has been used as a well-known formula^{72,92,93} in typical electron spectroscopy in ion-atom collision experiments. A simple numerical simulation was carried out where double and single differential cross sections, DDSCS ($\frac{d^2\sigma}{dE d\Omega}$) and SDSCS ($\frac{d\sigma}{d\Omega}$), were evaluated using a theoretical electron spectrum of a group of narrow *KLL* Auger lines (the natural line width is typically of ~ 0.1 eV— see Table 6) and a broad binary encounter electron peak. As a model of the response function of the spectrometer in this simulation, the following Gaussian function was used:

$$f(\epsilon - E) = e^{-K(\epsilon - E)^2} \quad (42),$$

where $K = 4\ln 2/(\Delta E)^2$ in order to make the FWHM $\Delta E = E \cdot R$ and its height = 1.

The *KLL* Auger SDSCS obtained by simulating electron spectra with Eq. (39) and then by summing all DDSCS of Eq. (41) were found to be independent of for values of R smaller than about 10 %. In the case of the BEe, both the simulated DDSCS and SDSCS were nearly independent on the choice of R values smaller than several %. All the simulated SDSCS for *KLL* Auger, and the DDSCS and SDSCS for BEe peak for various R were about 6.5 % larger than the corresponding values of the theoretical *KLL* Auger and BEe spectrum. This may be just due to the fact

of $\int_{-\infty}^{+\infty} f(\epsilon - E) d\epsilon = 1.0644 \cdot \Delta E$ for the chosen spectrometer response function

of Eq. (42).

The effective solid angle $\Delta\Omega^{eff}$ in Eq. (41) for the measurements of state production cross sections is given by [see also Eq. (39)]: (i). for a metastable state;

$$\Delta\Omega_{meta}^{state} = \sum_J a_J \cdot \xi_J \cdot \Delta\Omega_{J-meta}^{eff}, \quad (43-1)$$

while (ii). for a prompt state;

$$\Delta\Omega_{prompt}^{state} = \sum_J a_J \cdot \xi_J \cdot \Delta\Omega_{prompt}^{eff} \equiv \Delta\Omega_{prompt}^{eff} \cdot \xi. \quad (43-2)$$

Since the Auger production cross section, $\sigma[Auger]$, is related to the state production cross section, $\sigma[state]$, by:

$$\sigma[Auger] = \sum_J \xi_J \cdot \sigma_J[state] = \sum_J \xi_J \cdot a_J \cdot \sigma[state] = \xi \cdot \sigma[state], \quad (44)$$

where $\xi = \sum_J a_J \cdot \xi_J$ is the J -averaged Auger yield (assuming a J -statistical distribution as mentioned earlier), any Auger cross section, double or single differential, can be obtained by multiplying the corresponding state production cross section with the appropriate ξ , which are listed in Table 6 for all $(2S+1)L$ states of interest in this work. Therefore, the effective solid angle for the measurements of Auger production cross sections can be given by: (i). for a metastable state;

$$\Delta\Omega_{meta}^{Auger} = \frac{1}{\xi} \cdot \sum_J a_J \cdot \xi_J \cdot \Delta\Omega_{J-meta}^{eff}, \quad (45-1)$$

while (ii). for a prompt state;

$$\Delta\Omega_{prompt}^{Auger} = \Delta\Omega_{prompt}^{eff}, \quad (45-2)$$

which is given by Eq (40-2).

In Eq. (39), the electron absorption effect,^{73,92,93} a post-collision effect, by which Auger electrons (or any other ionized electrons) can be deflected from their

original trajectory (zero degrees in our case) due to elastic collisions or can lose some of their energy due to inelastic collisions with target gas, may need to be accounted for. This can be done, in principle, as follows; In the case of a prompt state, the correction factor of $e^{-n\sigma_a(l-x)}$ should be multiplied by Eq. (40-2) [see Eq. (35) to figure out this factor], where σ_a is the absorption cross section which depends on the laboratory electron energy E . In the case of a metastable state, the correction factor of $e^{-n\sigma_a(l-x-y)}$ should be multiplied by Eq. (40-1) with the condition of $(x+y) < l$.

From Refs. 92 and 93, the experimental absorption coefficient, α , an effective area (cm^2) of collisions for all the target gas in a unit volume (cm^3) at unit pressure (Torr), is found to be approximately 0.4 for He targets and 0.7 for H_2 targets for an electron energy of ~ 1 keV, the lowest laboratory energy of K -Auger electrons at zero degrees for 4 MeV O^{5+} collisions. The absorption cross section σ_a can be obtained by dividing α by $3.22 \times 10^{16} \cdot p(\text{in Torr})$ at 300 K. In the worst case scenario, using these values of α , $p = .04$ Torr, and $l = 10$ cm of gas cell, $\alpha \cdot p \cdot l/2 = \sigma_a \cdot n \cdot l/2$ is estimated as 14% for H_2 and 8% for the He target, respectively. Although these values are not negligible, the absorption effect is not considered for the following reasons:

When the spectrometer efficiency η was obtained using binary encounter electron (BEE) production for the collision of 9.5–38 MeV F^{9+} with a H_2 target at 40 mTorr, the electron absorption effect was not taken into account either, since it was assumed that the absorption effect was negligible for 1–4 keV electrons of BEE peak. Therefore, the absorption effect is approximately canceled out in the Auger cross section measurements as long as its target and pressures are the same. For a different target (He) and/or at different pressures this effect can be canceled out with some uncertainty but at most several % even for the worst case

in this study. Therefore, this absorption effect was not taken into account in the present study of 1–3 keV electron spectroscopy with the light targets of H₂ and He, and the uncertainty from this effect can be taken into consideration as an experimental uncertainty. Definitely, for low energy electron spectroscopy with a thick and/or heavy target (e.g., Ne or Ar), the absorption effect will be a very important factor particularly for zero-degree measurements. For example, in the measurement of the Ne *K* Auger electron production cross section for 3 MeV H⁺ + Ne collisions, the absorption coefficient $\alpha = 4$ had to be accounted for. This was done in the spectrometer efficiency normalization using the known⁶⁶ Ne *K* Auger electron production cross section. The normalization results are shown in Fig. 24, and in Fig. A1 in Appendix A.

From Eq. (41), the DDCS for Auger electron production can be expressed in terms of the experimental quantities involved in the cross section measurements as follows:

$$\begin{aligned} \left(\frac{d^2\sigma}{dEd\Omega} \right)^{Auger} &= \frac{Z}{N_q^* \cdot n \cdot l \cdot \Delta E \cdot \Delta\Omega_0 \cdot \eta} \cdot \frac{N_q^*}{N_q^0} \cdot \frac{\Delta\Omega_0}{\Delta\Omega_{eff}} \\ &\equiv \frac{d^2Y}{dEd\Omega} \cdot F_Q \cdot F_\Omega, \end{aligned} \quad (46)$$

where

$$\frac{d^2Y}{dEd\Omega} \equiv \frac{Z}{N_q^* \cdot n \cdot l \cdot \Delta E \cdot \Delta\Omega_0 \cdot \eta} \quad (47)$$

with

$$\Delta\Omega_0 = \frac{ab/\sqrt{2}}{l} \int_0^l \frac{dx}{(L-x+A)(L-x+B)} = \frac{1}{l} \int_0^l \Delta\Omega(x) dx \quad (48)$$

and *Y* stands for the normalized yields for the present experimental set-up. The factor *F_Q* is defined:

$$F_Q \equiv \frac{Q^*}{Q_0} = \frac{N_q^*}{N_q^0}, \quad (49)$$

since $N_q^0 = Q_0/qe$ and $N_q^* = Q^*/qe$. F_Q is measured typically to be 1 except the case of low energy collisions with a thick target (see Tables 7-14). The beam charge neutralization factor F_Q is measured for a given collision system of collision energy and target gas pressure. F_Ω for Auger cross sections is defined:

$$F_\Omega \equiv \frac{\Delta\Omega_0}{\Delta\Omega_{Auger}}, \quad (50)$$

which is an effective solid angle factor for Auger production cross section. $\Delta\Omega_{meta}^{Auger}$ [Eq. (45-1)] or $\Delta\Omega_{prompt}^{Auger}$ [Eq. (45-2)] should be used for the measurements of Auger cross sections from the metastable or prompt state, respectively.

Eq. (47) along with Eq. (48) is the DDCS of Auger electrons from prompt states and BEE from direct target ionization when no appreciable projectile capture is involved. (i.e., $n\sigma_{qp}l \ll 1$). In these cases, both F_Q and F_Ω are 1 and thus $Y = \sigma$ as seen in Eq. (46). Eq. (48), which is identical to Eq. (18), is the pure "geometrical" solid angle for any kind of electron production from the prompt states of either target or projectile line source of the length l at zero-degree observation with the present tandem spectrometer.

Shown in Tables 7-14 are the measured F_Q values and the solid angle factors F_Ω for Auger cross sections, F_Ω^{prompt} and F_Ω^{4P} evaluated for the prompt states and for the metastable $1s2s2p^4P$ state, respectively. These F_Ω factors were calculated for collisions of ~ 0.25 – 2 MeV/amu O^{4+} , O^{5+} , F^{6+} , and F^{7+} with He and H_2 targets of 10 cm length at given pressures. As mentioned earlier, the empirical Schlachter values of σ_{qp} used in the F_Ω calculations are also tabulated. The lifetimes τ and Auger yields ξ and ξ_J for the $1s2s2p^4P_J$ state tabulated in Table 6 were used for this calculation.

TABLES 7-14

are not tabulated.

TABLE 7: $O^{5+} + He$

$E_p(\text{MeV})$	$\sigma_{qp}(\text{cm}^2)$	p (mTorr)	$F_{\Omega}^{\text{prompt}}$	F_{Ω}^{*P}	H_{Ω}^{*P}	F_Q
4	1.27×10^{-16}	40	$2.16^{+.37}_{-.34}$	$1.73^{+.29}_{-.26}$	2.66	0.80
4.75	8.90×10^{-17}		$1.76^{+.23}_{-.22}$	$1.44^{+.18}_{-.17}$	2.24	0.86
5.5	6.25×10^{-17}		$1.50^{+.15}_{-.14}$	$1.25^{+.12}_{-.11}$	1.98	0.93
7	3.05×10^{-17}		$1.23^{+.06}_{-.06}$	$1.05^{+.05}_{-.05}$	1.69	1
8.5	1.50×10^{-17}		$1.11^{+.03}_{-.03}$	$0.98^{+.03}_{-.03}$	1.57	1
10	7.75×10^{-18}		$1.06^{+.01}_{-.01}$	$0.95^{+.01}_{-.01}$	1.54	1
11	5.21×10^{-18}		$1.04^{+.01}_{-.01}$	$0.94^{+.01}_{-.01}$	1.53	1
12	3.62×10^{-18}		$1.03^{+.01}_{-.01}$	$0.94^{+.01}_{-.01}$	1.54	1
14	1.90×10^{-18}		1.01	0.94	1.55	1
16	1.09×10^{-18}		1.01	0.96	1.57	1
17.5	7.49×10^{-19}		1.01	0.97	1.59	1
19	5.31×10^{-19}		1.00	0.97	1.61	1
21	3.49×10^{-19}		1.00	0.98	1.63	1
23	2.39×10^{-19}		1.00	0.99	1.65	1
25	1.69×10^{-19}		1.00	1.00	1.67	1
26.75	1.27×10^{-19}		1.00	1.01	1.69	1
28.5	9.75×10^{-20}		1.00	1.01	1.71	1
30.25	7.60×10^{-20}		1.00	1.02	1.72	1
32	6.01×10^{-20}		1.00	1.03	1.74	1

TABLE 8: $O^{5+} + H_2$

$E_p(\text{MeV})$	$\sigma_{qp}(\text{cm}^2)$	p (mTorr)	$F_{\Omega}^{\text{prompt}}$	F_{Ω}^{*P}	H_{Ω}^{*P}	F_Q
4	4.22×10^{-17}	40	$1.33^{+.15}_{-.14}$	$1.08^{+.12}_{-.11}$	1.68	0.88
5.5	1.12×10^{-17}		$1.08^{+.03}_{-.03}$	$0.91^{+.03}_{-.03}$	1.45	0.99
7	4.09×10^{-18}		$1.03^{+.01}_{-.01}$	$0.89^{+.01}_{-.01}$	1.43	0.99
8.5	1.82×10^{-18}		1.01	0.90	1.45	1
10	9.20×10^{-19}		1.01	0.91	1.47	1
11	6.18×10^{-19}		1.00	0.92	1.49	1
12	4.30×10^{-19}		1.00	0.92	1.50	1
14	2.26×10^{-19}		1.00	0.94	1.54	1
16	1.29×10^{-19}		1.00	0.95	1.56	1
17.5	8.87×10^{-20}		1.00	0.96	1.58	1
19	6.29×10^{-20}		1.00	0.97	1.60	1
21	4.14×10^{-20}		1.00	0.98	1.63	1
23	2.83×10^{-20}		1.00	0.99	1.65	1
25	2.00×10^{-20}		1.00	1.00	1.67	1
26.75	1.51×10^{-20}		1.00	1.01	1.69	1
28.5	1.16×10^{-20}		1.00	1.01	1.70	1
30.25	9.01×10^{-21}		1.00	1.02	1.72	1
32	7.12×10^{-21}		1.00	1.03	1.74	1

TABLE 9: $F^{6+} + He$

$E_p(\text{MeV})$	$\sigma_{qp}(\text{cm}^2)$	p (mTorr)	$F_{\Omega}^{\text{prompt}}$	F_{Ω}^{4P}	H_{Ω}^{4P}	F_Q
4.75	1.73×10^{-16}	40	$2.68^{+.56}_{-.51}$	$1.99^{+.40}_{-.37}$	2.89	0.75
6	1.08×10^{-16}		$1.96^{+.30}_{-.28}$	$1.46^{+.22}_{-.20}$	2.22	0.86
7.125	7.18×10^{-17}		$1.59^{+.18}_{-.16}$	$1.20^{+.13}_{-.12}$	1.89	0.94
9.5	2.99×10^{-17}		$1.22^{+.06}_{-.06}$	$0.95^{+.05}_{-.04}$	1.54	0.99
11.875	1.28×10^{-17}		$1.09^{+.02}_{-.02}$	$0.87^{+.02}_{-.02}$	1.44	1
14.25	6.02×10^{-18}		$1.04^{+.01}_{-.01}$	$0.84^{+.01}_{-.01}$	1.42	1
16.625	3.16×10^{-18}		$1.02^{+.01}_{-.01}$	$0.84^{+.01}_{-.01}$	1.42	1
19	1.81×10^{-18}		1.01	0.85	1.44	1
21.375	1.11×10^{-18}		1.01	0.86	1.46	1
23.75	7.12×10^{-18}		1.01	0.87	1.48	1
26.125	4.78×10^{-19}		1.00	0.88	1.50	1
28.5	3.33×10^{-19}		1.00	0.89	1.52	1
30.875	2.38×10^{-19}		1.00	0.90	1.54	1
33.25	1.75×10^{-19}		1.00	0.91	1.56	1
35.625	1.30×10^{-19}		1.00	0.92	1.57	1
38	9.99×10^{-20}		1.00	0.92	1.59	1

TABLE 10: $F^{6+} + H_2$

$E_p(\text{MeV})$	$\sigma_{qp}(\text{cm}^2)$	p (mTorr)	$F_{\Omega}^{\text{prompt}}$	F_{Ω}^{4P}	H_{Ω}^{4P}	F_Q
4.75	6.92×10^{-17}	40	$1.57^{+.27}_{-.25}$	$1.17^{+.20}_{-.18}$	1.75	0.80
7.125	1.30×10^{-17}		$1.09^{+.04}_{-.04}$	$0.84^{+.03}_{-.03}$	1.33	0.97
9.5	3.89×10^{-18}		$1.03^{+.01}_{-.01}$	$0.82^{+.01}_{-.01}$	1.31	1
11.875	1.53×10^{-18}		1.01	0.81	1.34	1
14.25	7.14×10^{-19}		1.00	0.82	1.37	1
16.625	3.75×10^{-19}		1.00	0.83	1.40	1
19	2.15×10^{-19}		1.00	0.84	1.43	1
20.25	1.65×10^{-19}		1.00	0.85	1.44	1
21.375	1.31×10^{-19}		1.00	0.85	1.45	1
23.75	8.45×10^{-20}		1.00	0.85	1.48	1
26.125	5.67×10^{-20}		1.00	0.88	1.50	1
28.5	3.94×10^{-20}		1.00	0.89	1.52	1
30.875	2.82×10^{-20}		1.00	0.90	1.54	1
33.25	2.07×10^{-20}		1.00	0.91	1.56	1
35.625	1.55×10^{-20}		1.00	0.92	1.57	1
38	1.18×10^{-20}		1.00	0.92	1.59	1

TABLE 11: $F^{7+} + He$

$E_p(\text{MeV})$	$\sigma_{qp}(\text{cm}^2)$	p (mTorr)	$F_{\Omega}^{\text{prompt}}$	F_{Ω}^{*P}	H_{Ω}^{*P}	F_Q
4.75	2.17×10^{-16}	2	$1.08^{+.02}_{-.02}$	$0.85^{+.02}_{-.02}$	1.22	1
7.125	9.67×10^{-17}	5	$1.09^{+.02}_{-.02}$	$0.88^{+.02}_{-.02}$	1.31	1
9.5	4.33×10^{-17}	5	$1.04^{+.01}_{-.01}$	$0.86^{+.01}_{-.01}$	1.31	1
11.875	1.94×10^{-17}	7.5	$1.03^{+.01}_{-.01}$	$0.87^{+.01}_{-.01}$	1.34	1
14.25	9.25×10^{-18}	10	1.02	0.88	1.37	1
16.625	4.86×10^{-18}	15	1.01	0.90	1.40	1
19	2.78×10^{-18}	20	1.01	0.91	1.42	1
21.375	1.70×10^{-18}	30	1.01	0.92	1.45	1
23.75	1.10×10^{-18}	40	1.01	0.94	1.47	1
26.125	7.35×10^{-19}	40	1.01	0.95	1.49	1
28.5	5.11×10^{-19}	40	1.00	0.96	1.50	1
30.875	3.66×10^{-19}	50	1.00	0.97	1.52	1
33.25	2.68×10^{-19}	50	1.00	0.98	1.54	1
35.625	2.01×10^{-19}	50	1.00	0.99	1.55	1

TABLE 12: $F^{7+} + H_2$

$E_p(\text{MeV})$	$\sigma_{qp}(\text{cm}^2)$	p (mTorr)	$F_{\Omega}^{\text{prompt}}$	F_{Ω}^{*P}	H_{Ω}^{*P}	F_Q
4.75	1.04×10^{-16}	4	$1.08^{+.03}_{-.03}$	$0.85^{+.02}_{-.02}$	1.22	1
7.125	1.99×10^{-17}	7.5	$1.03^{+.01}_{-.01}$	$0.83^{+.01}_{-.01}$	1.24	1
9.5	5.98×10^{-18}	20	$1.02^{+.01}_{-.01}$	$0.85^{+.01}_{-.01}$	1.29	1
11.875	2.35×10^{-18}	25	1.01	0.86	1.32	1
14.25	1.10×10^{-18}	40	1.01	0.87	1.36	1
16.625	5.77×10^{-19}	40	1.00	0.89	1.38	1
19	3.30×10^{-19}	40	1.00	0.90	1.41	1
21.375	2.02×10^{-19}	40	1.00	0.92	1.44	1
23.75	1.30×10^{-19}	40	1.00	0.93	1.46	1
26.125	8.72×10^{-20}	40	1.00	0.94	1.48	1
28.5	6.06×10^{-20}	40	1.00	0.96	1.50	1
30.875	4.34×10^{-20}	50	1.00	0.97	1.52	1
33.25	3.18×10^{-20}	50	1.00	0.98	1.54	1
35.625	2.38×10^{-20}	50	1.00	0.99	1.55	1

TABLE 13: $O^{4+} + He$

$E_p(\text{MeV})$	$\sigma_{qp}(\text{cm}^2)$	$p \text{ (mTorr)}$	F_{Ω}^{prompt}	F_{Ω}^{*P}	H_{Ω}^{*P}	F_Q
10	4.17×10^{-18}	20	1.02	0.98	1.46	1
14	1.02×10^{-18}	10	1.00	1.00	1.52	1
17.5	4.02×10^{-19}	15	1.00	1.03	1.56	1
21	1.87×10^{-19}	20	1.00	1.05	1.61	1
25	9.04×10^{-20}	10	1.00	1.07	1.65	1
28.5	5.23×10^{-20}	20	1.00	1.08	1.68	1

TABLE 14: $O^{4+} + H_2$

$E_p(\text{MeV})$	$\sigma_{qp}(\text{cm}^2)$	$p \text{ (mTorr)}$	F_{Ω}^{prompt}	F_{Ω}^{*P}	H_{Ω}^{*P}	F_Q
10	4.94×10^{-19}	20	1.00	0.96	1.45	1
14	1.21×10^{-19}	10	1.00	1.00	1.51	1
17.5	4.76×10^{-20}	15	1.00	1.03	1.56	1
21	2.22×10^{-20}	20	1.00	1.06	1.61	1
25	1.07×10^{-20}	10	1.00	1.07	1.65	1
28.5	6.20×10^{-21}	20	1.00	1.08	1.68	1

B. State-Resolved and Total *KLL* Auger Cross Sections

After transforming the electron energy E and DDCS from the laboratory frame to the projectile rest frame, SDCS for the Auger production cross sections are determined by integrating DDCS for the corresponding electron energy range of the Auger line in an electron spectrum. First, the measured laboratory DDCS and energy E are transformed into the corresponding quantities in the projectile-rest frame as follows:

$$E' = (\sqrt{E} - \sqrt{t})^2 \quad (51)$$

and

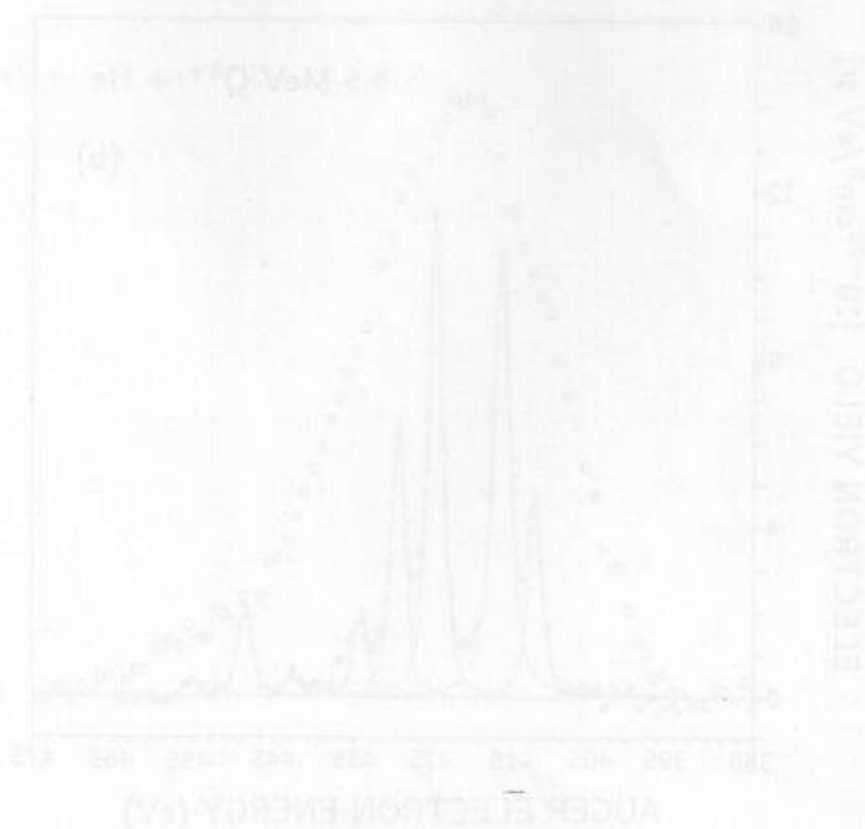
$$\frac{d^2Y}{dE'd\Omega'} = \frac{d^2Y}{dEd\Omega} \cdot \sqrt{\frac{E'}{E}}, \quad (52)$$

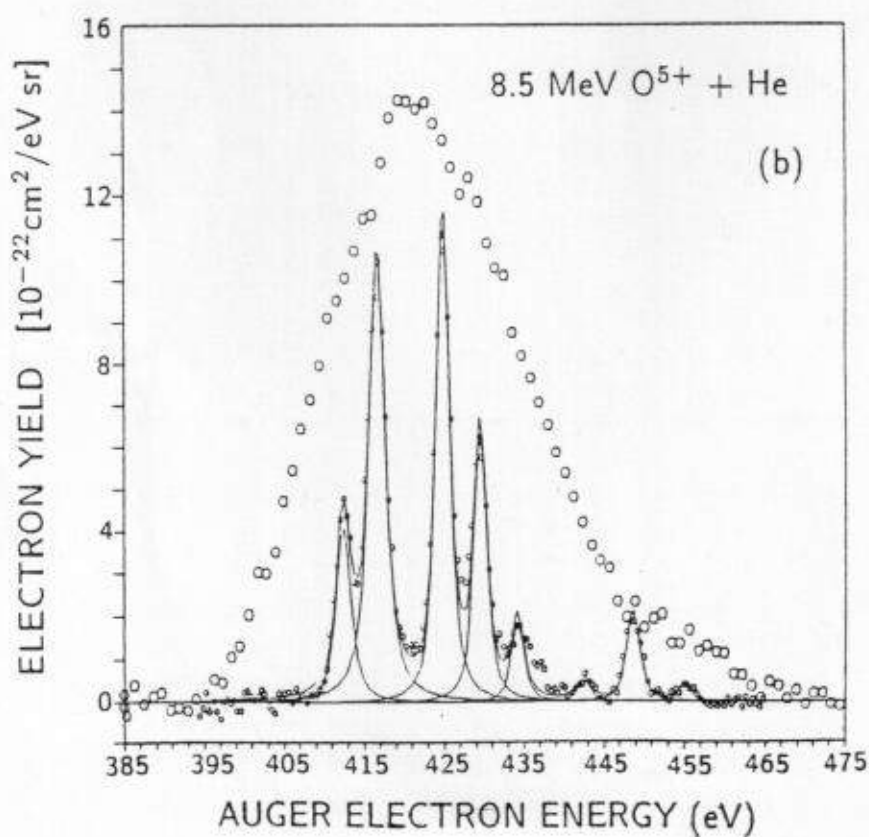
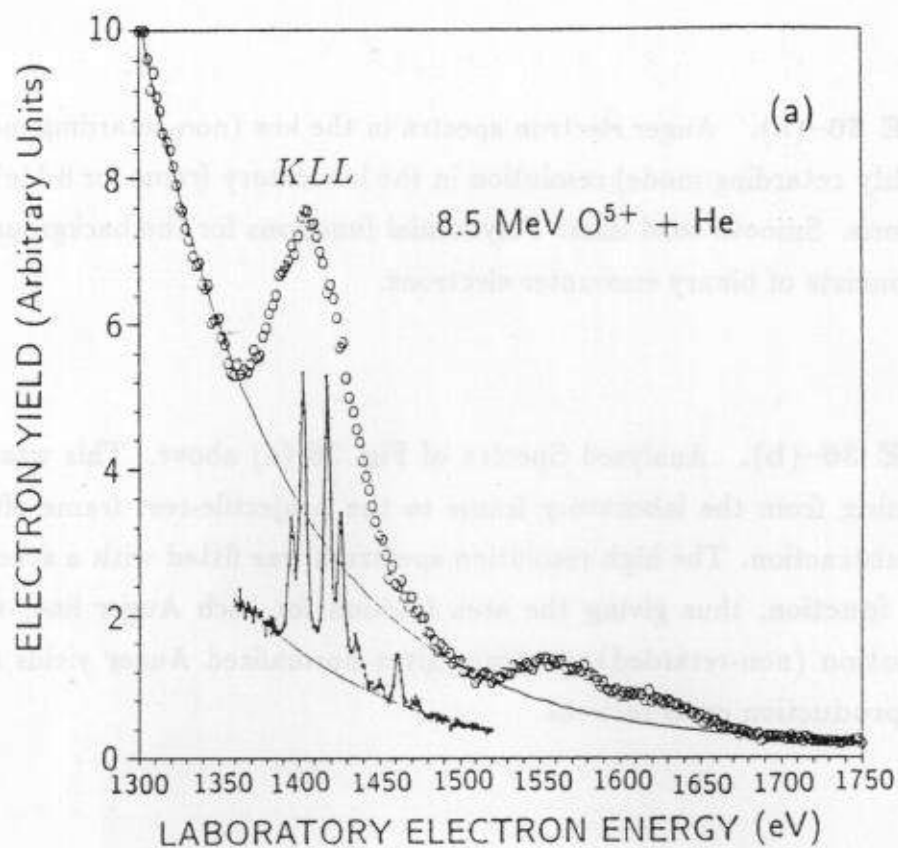
where E' and Ω' refer to electron energy and solid angle in the projectile-rest frame.

An example of the procedure of analysis of the Auger production cross section measurements in this work is as follows: Shown in Fig. 36-(a) are a pair of typical electron spectra with its yields measured in the laboratory frame for 8 MeV $O^{5+} + He$ collisions; one for the *K*-Auger electrons obtained in the non-retarding mode where the electrons are energy-analyzed without any energy retardation, and the other one for *KLL* Auger electrons obtained the in retarding, high-resolution mode where the electron energies are retarded thus increasing the energy resolution. After subtraction of the continuous electron background with a suitable polynomial, the double differential yield (DDY) is determined from the spectrum in the non-retarding mode. The background electrons consist predominantly of the binary encounter electrons (BEE) from the target ionization. Some beam-induced electrons from beam scattering with the apertures of the gas cell and spectrometer also contribute to the background but in small amounts.

FIGURE 36-(a). Auger electron spectra in the low (non-retarding mode) and high (highly retarding mode) resolution in the laboratory frame for 8 MeV $O^{5+} + He$ collisions. Smooth solid lines: Polynomial functions for the background which mainly consists of binary encounter electrons.

FIGURE 36-(b). Analyzed Spectra of Fig. 36-(a) above. This was done by transforming from the laboratory frame to the projectile-rest frame after background subtraction. The high resolution spectrum was fitted with a spectrometer response function, thus giving the area fraction for each Auger line, while the low resolution (non-retarded) spectrum gives normalized Auger yields and thus electron production cross sections.





Shown in Fig. 36-(b) is the low-resolution spectrum without retardation and the high-resolution spectrum with large retardation. Both are background subtracted and transformed to the projectile-rest frame. In particular, the DDY in the low-resolution spectrum is normalized and the area under all the DDY would be the single differential yield (SDY) for *KLL* Auger production. However, the SDY should be corrected to result in SDCS for total *KLL* Auger electron production. These cross sections will be determined as given in Eq. (53) and Eq. (58) below for each prompt or metastable state, and Eq. (60) below for the total *KLL* Auger lines. Solid lines in the high-resolution spectrum are the fitted individual Auger lines with an experimental response function of the spectrometer. The experimental response function has been determined using the 4P Auger line which is strong, particularly, in $F^{7+}(1s2s^3S) + He$ collisions. The shape of the experimental response function is shown Fig. 37.

In the high-resolution spectrum, only the fraction of each Auger line can be obtained rather than the SDCS of the Auger line. Therefore, the SDCS for production of any Auger line from the excited state, $|d\rangle$, can be obtained by a fractional method as follows:

$$\left(\frac{d\sigma}{d\Omega'}\right)_d^{Auger} = (F\Omega)_d \cdot F_Q \cdot f_d \cdot \left(\frac{dY}{d\Omega'}\right)_{KLL}, \quad (53)$$

where f_d is the fraction of d -th Auger line in the high-resolution *KLL* Auger spectrum ($\sum_d f_d = 1$). The f_d for each Auger line in collisions of O^{4+} , O^{5+} , F^{6+} , and F^{7+} with He and H_2 targets were extracted from the fitted high-resolution spectra. $(\frac{dY}{d\Omega'})_{KLL}$ is the normalized SDY of the non-retarding spectrum in the projectile-rest frame which is measured by:

$$\left(\frac{dY}{d\Omega'}\right)_{KLL}^{Auger} = \int_{KLL} \left(\frac{d^2Y}{dE'd\Omega'}\right) dE' \quad (54)$$

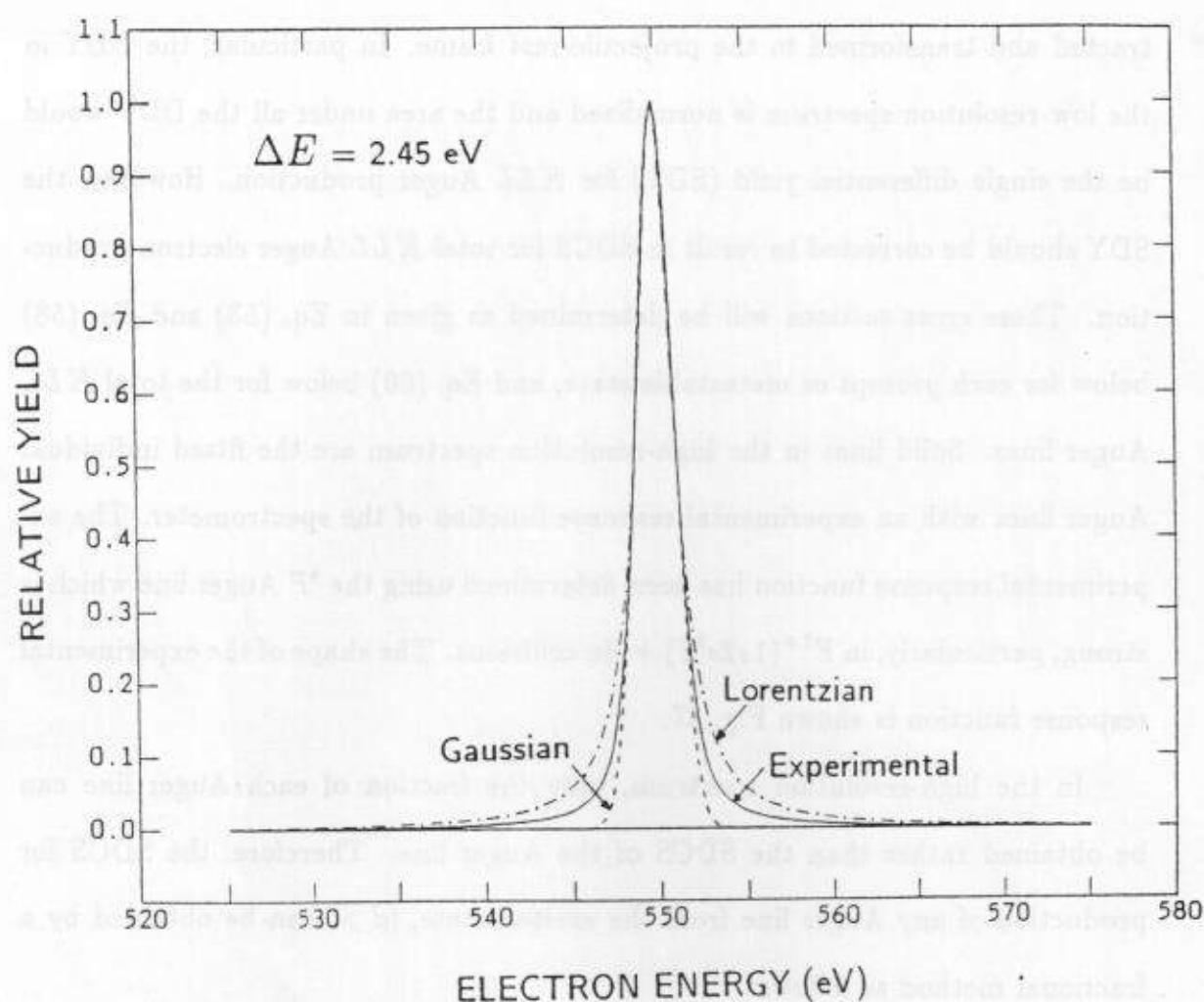


FIGURE 37. Shape of the spectrometer response function for a high-resolution spectrum which was obtained in a highly retarding mode. In the non-retarding mode (low resolution), the response function was observed to have a Gaussian shape [see Fig. 7-(a)].

and these were obtained by measuring K Auger electrons in the non-retarding mode.

The Auger electron production cross section for each *prompt* state was thus obtained by Eq. (53) above. However, in the case of the metastable $1s2s2p\ ^4P$ state, a strong discrepancy was observed between the measured Auger electron yields and the effective solid angle calculation which was done in the previous section of this chapter. In this calculation it was assumed that for a given laboratory electron energy, the spectrometer efficiency of the electron detection is constant regardless of the position of the electron production. This assumption may be valid only for cross section measurements of Auger electrons from the prompt states, where the efficiency is obtained from the binary encounter electrons. This normalization procedure was discussed in the previous Chapter. In the case of measurements of the 4P electrons this assumption is apparently not valid.

This discrepancy is demonstrated in Fig. 38, where the 4P electrons, which are produced inside and outside the gas cell, are separated from each other by applying a voltage to the gas cell assembly. Peak A and B represent the electrons produced outside and inside the gas cell assembly, respectively. If the efficiency is constant, the measured yield ratio of Z_{in} to Z_{out} , which is determined by the effective solid angle for each region, would be 1.6. However, the measured yields ratio was observed to be 0.60. A similar discrepancy was observed for the 4P electron measurements in collisions of 4.75 MeV O^{5+} , 9.5 MeV F^{7+} , and 19 MeV O^{5+} with He targets. These results may indicate the assumption that the overall efficiency for the detection of electrons produced outside the gas cell is much larger (e.g., $1.6/0.6=2.7$ for the case above) than for those produced inside, therefore, it implies that the solid angle calculation for the metastable state is not valid for the region between the gas cell and the entrance of the spectrometer.

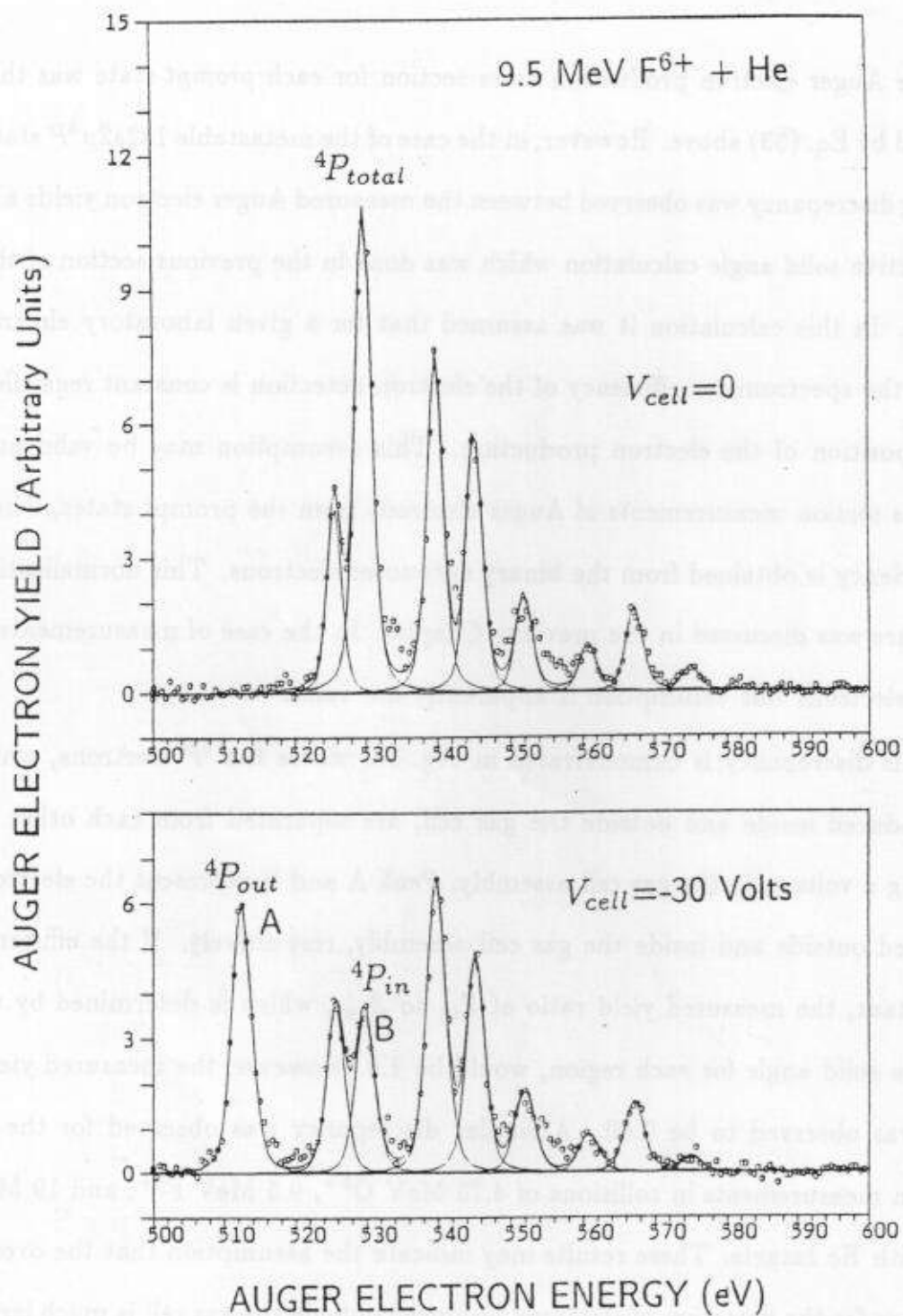


FIGURE 38. Separation of the metastable $1s2s2p^4P$ electron yields produced inside (peak B) and outside (peak A) of the gas cell (see text).

At any rate, since the observed electron yield is proportional to the solid angle and the efficiency, the counting enhancement for the electrons produced outside the region of the gas cell should include any enhancement of the true solid angle and/or the true efficiency for the detection of the 4P electrons produced outside of the gas cell.

Due to this counting problem, only the yield of 4P electrons produced *inside* of the gas cell was used for the cross section measurements, since the spectrometer efficiency was determined by the binary encounter electrons and this efficiency was used for the Auger cross section measurements for all the prompt states. In this way, the complication of 4P electrons emitted outside the gas cell can be ruled out. The SDCS of the 4P electron can be expressed from Eq. (41) as follows:

$$\left(\frac{d\sigma}{d\Omega}\right)_{^4P}^{Auger} = \xi \cdot \left(\frac{d\sigma}{d\Omega}\right)_{^4P}^{state} = \frac{\xi \cdot Z_{^4P}^{in}}{N_q^0 \cdot n \cdot l \cdot \Delta\Omega_{^4P}^{in} \cdot \eta}, \quad (55)$$

where $\Delta\Omega_{^4P}^{in}$ and $Z_{^4P}^{in}$ are the effective solid angles and the measured Auger yields produced inside the gas cell assembly. This can be written and related to Eq. (46) as follows:

$$\begin{aligned} \left(\frac{d\sigma}{d\Omega}\right)_{^4P}^{Auger} &= \frac{Z_{^4P}^{total}}{N_q^* \cdot n \cdot l \cdot \Delta\Omega_0 \cdot \eta} \cdot \frac{N_q^*}{N_q^0} \cdot \left(\xi \frac{\Delta\Omega_0}{\Delta\Omega_{^4P}^{total}}\right) \cdot \frac{\Delta\Omega_{^4P}^{total}}{\Delta\Omega_{^4P}^{in}} \cdot \frac{Z_{^4P}^{in}}{Z_{^4P}^{total}} \\ &\equiv \left(\frac{dY}{d\Omega}\right)_{^4P} \cdot F_Q \cdot F_{^4P} \cdot R_{\Omega} \cdot R_Z, \end{aligned} \quad (56)$$

where F_Q and $F_{^4P}$ are defined in Eqs. (49) and (50), respectively, and R_{Ω} and R_Z are the ratios between the two solid angles and the two electron counts as follows:

$$R_{\Omega} = \frac{\Delta\Omega_{^4P}^{total}}{\Delta\Omega_{^4P}^{in}} \quad (57)$$

and

$$R_Z = \frac{Z_{^4P}^{in}}{Z_{^4P}^{total}}, \quad (58)$$

where $\Delta\Omega_{4P}^{total}$ and Z_{4P}^{total} are the effective solid angles and the measured Auger yields for the total observable decay region prior to the spectrometer entrance. All the $\Delta\Omega$ in Eqs. (45), (46), and (47) refer to the effective solid angle for the 4P state production cross sections and $\Delta\Omega_{4P}^{total}$ is calculated by Eq. (43-1). After transforming the SDY of $(dY/d\Omega)_{4P}$ from the laboratory frame to the projectile-rest frame, the 4P Auger SDCS is given by

$$\left(\frac{d\sigma}{d\Omega'}\right)_{4P}^{Auger} = G_{\Omega}^{4P} \cdot F_Q \cdot f_{4P} \cdot \left(\frac{dY}{d\Omega'}\right)_{KLL}, \quad (59)$$

where

$$G_{\Omega}^{4P} \equiv F_{\Omega}^{4P} \cdot R_{\Omega} \cdot R_Z \equiv H_{\Omega}^{4P} \cdot R_Z. \quad (60)$$

The factor H_{Ω}^{4P} , which is defined as $F_{\Omega}^{4P} \cdot R_{\Omega}$, is easily seen from Eq. (55) to be

$$H_{\Omega}^{4P} = \frac{\Delta\Omega_0}{\Delta\Omega_{4P}^{in}} \cdot \xi_{4P} \quad (61).$$

Thus, H_{Ω}^{4P} is determined by calculating $\Delta\Omega^{in}$ by Eqs. (43-1) and (40-1) with value of the upper limit of the y integration in Eq. (40-1) is taken to be the length of the gas cell and its differential region (see Fig. 35). The values of H_{Ω}^{4P} are included in Tables 7-14.

By comparing Eqs. (59) and (60) with Eq. (53), two more factors should be included in terms of R_{Ω} and R_Z for the Auger cross section estimation of the 4P state than for the prompt states. The product of these two factors is observed to be 0.49-0.54 for collisions of O^{5+} with He/ H_2 . In the recent paper¹² about the 4P cross sections, these two factors were not taken into account and therefore the reported cross sections should be multiplied by these factors resulting in ~ 0.5 times smaller cross sections. The measured factors R_Z vary from 0.41 to 0.30 for the 4P produced in collisions of He- or Li-like 0.30-1.20 MeV/u oxygen and

fluorine projectiles, and 0.30 ± 0.04 for 0.63–1.78 MeV/u O^{4+} collisions which will be discussed later in Chapter VII section B. The different variation of R_Z with different projectile energy and projectile species may be expected. However, for the collision systems in this study R_Z is fairly constant, so the average, 0.32 ± 0.04 , of the measured value will be used for the Auger or state production cross section measurements involved with the 4P state.

The zero-degree SDCS for total KLL Auger electron production is therefore:

$$\begin{aligned} \left(\frac{d\sigma}{d\Omega'} \right)_{KLL}^{Auger} &= \sum_d \left(\frac{d\sigma}{d\Omega'} \right)_d^{Auger} \\ &= F_Q \cdot \left(\frac{dY}{d\Omega'} \right)_{KLL} \cdot \left[f_{4P} \cdot G_{\Omega}^{4P} + \sum_k^{prompt} f_k \cdot (F_{\Omega})_k \right] \\ &= F_Q \cdot \left(\frac{dY}{d\Omega'} \right)_{KLL} \cdot \left[F_{\Omega}^{prompt} - f_{4P} \cdot (F_{\Omega}^{prompt} - G_{\Omega}^{4P}) \right], \end{aligned} \quad (62)$$

where $(F_{\Omega})_k = F_{\Omega}^{prompt}$ and $\sum_k f_k = 1 - f_{4P}$ are used for the case of all the prompt k states.

It may be noted that when the intensity from the metastable 4P state is strong in the KLL Auger spectra, this can affect considerably the determination of total KLL Auger cross sections. In addition, when projectile charge neutralization (capture) is large especially for lower projectile velocities and thick targets, consideration of this effect is crucial in the Auger cross section measurements for both prompt and metastable states. All these effects are, in principle, taken into account through the factors F_{Ω} , F_Q , and G_{Ω} . If these factors are negligible, i.e., neither projectile charge change nor metastable states are involved, then $F_{\Omega} = G_{\Omega}^{4P} = F_Q = 1$, and thus $\left(\frac{d\sigma}{d\Omega'} \right)_{KLL}^{Auger} = \left(\frac{dY}{d\Omega'} \right)_{KLL}$ as expected in Eq. (62).

The KLL Auger cross sections, which were determined by Eq. (62) for all the collision systems studied in this work, are displayed versus the projectile energy in Figs. 39–42. Overall electron-electron interactions of RTE and eeE are

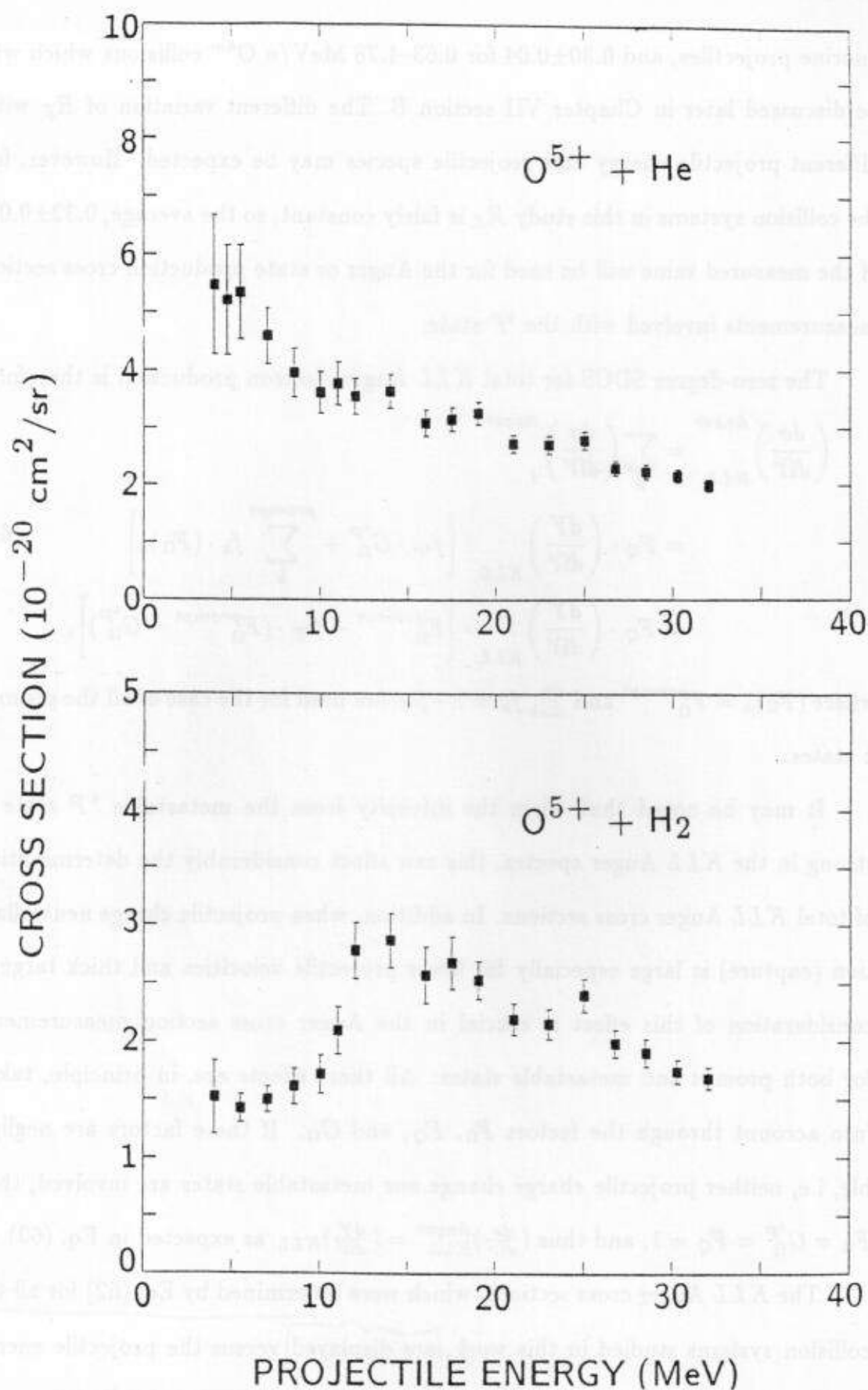


FIGURE 39. *KLL* Auger production cross sections at zero-degrees in collisions of O^{5+} with He and H_2 targets.

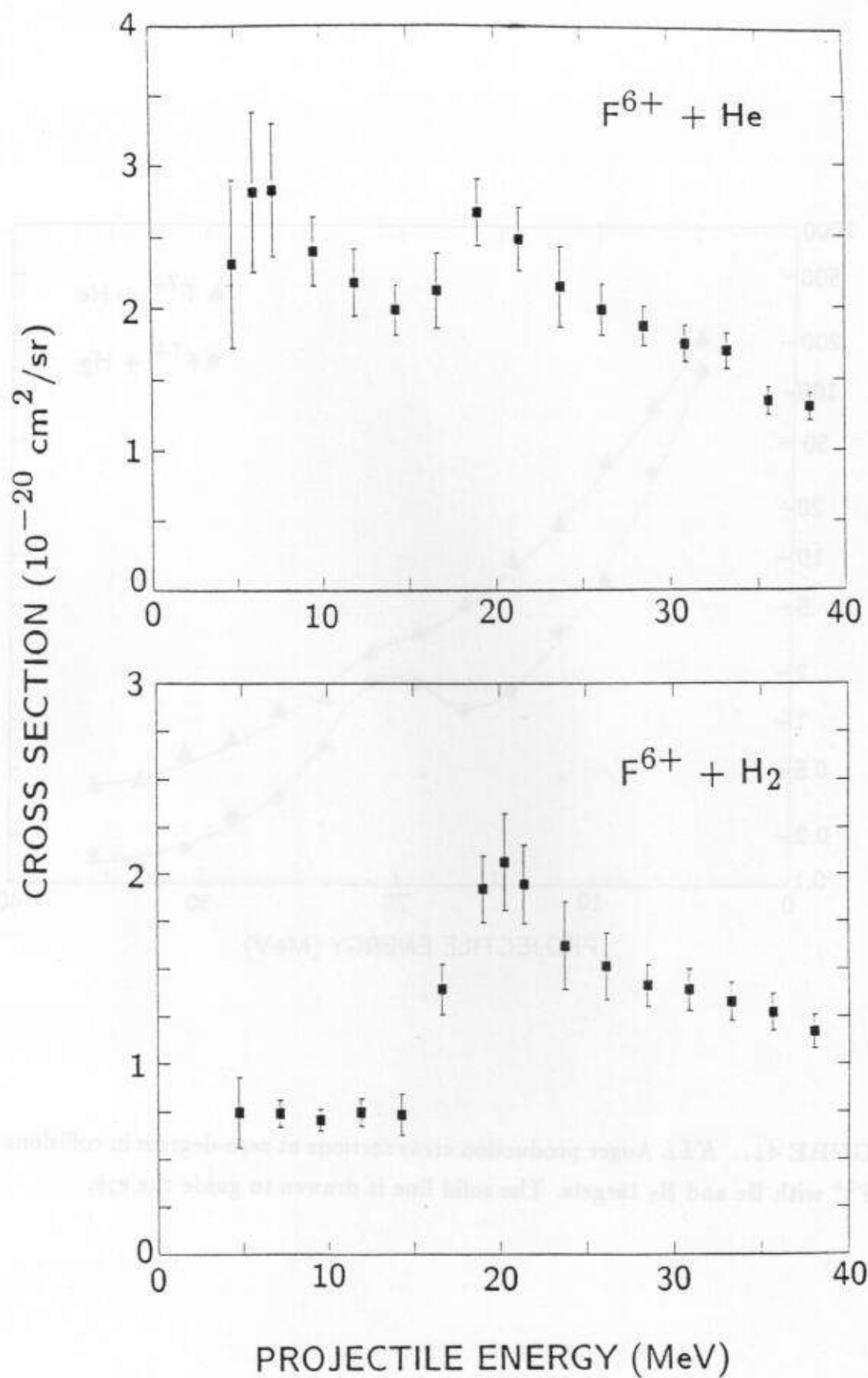


FIGURE 40. *KLL* Auger production cross sections at zero-degrees in collisions of F^{6+} with He and H_2 targets.

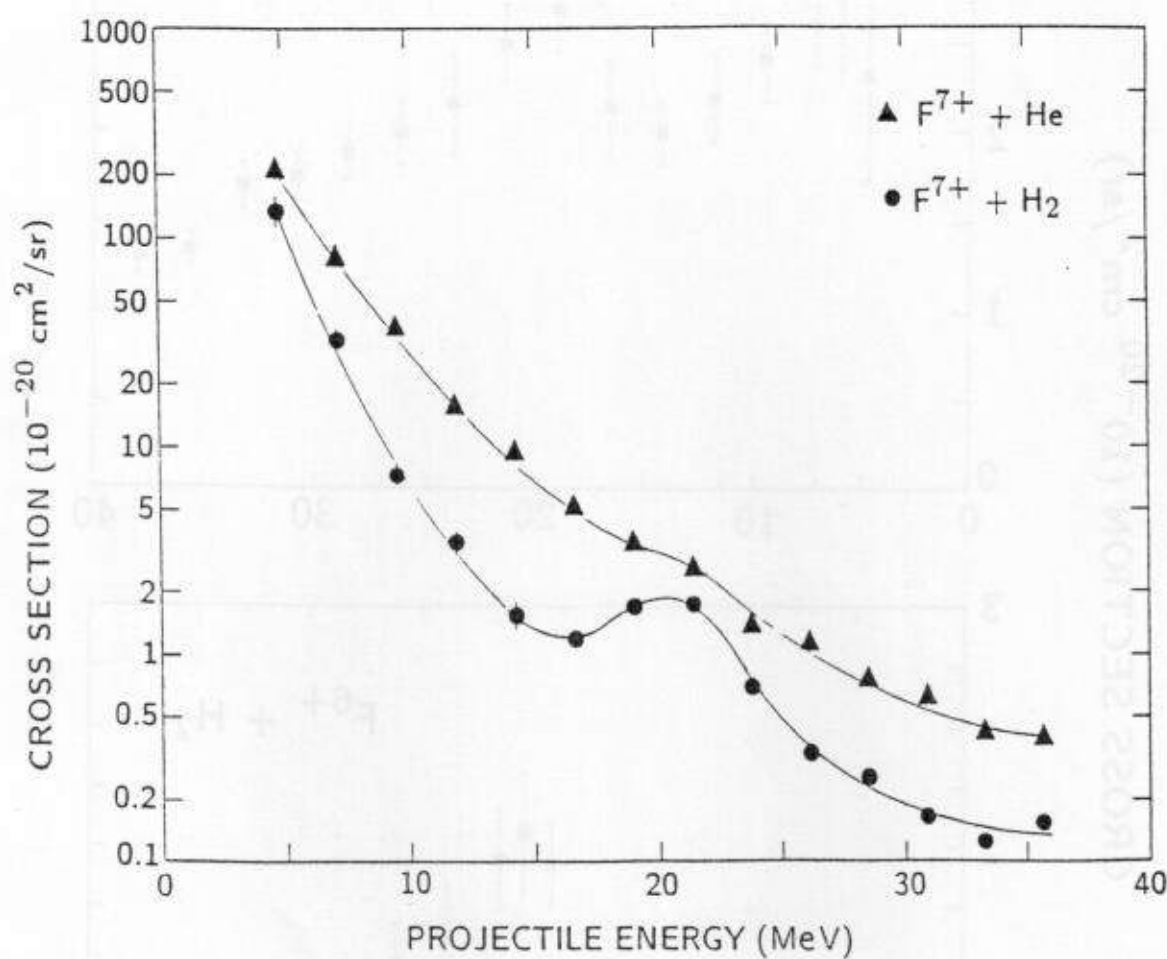


FIGURE 41. *KLL* Auger production cross sections at zero-degrees in collisions of F^{7+} with He and H_2 targets. The solid line is drawn to guide the eye.

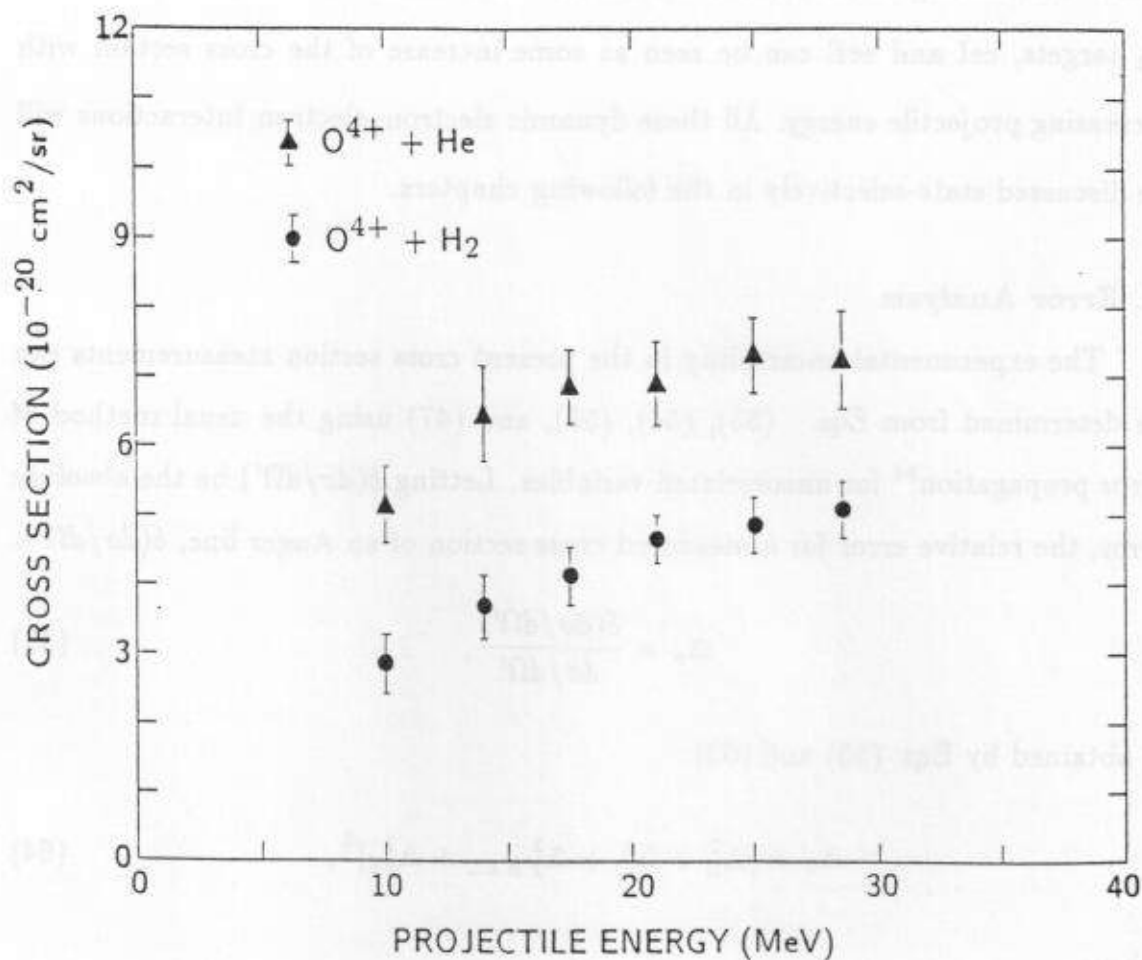


FIGURE 42. *KLL* Auger production cross sections at zero-degrees in collisions of O^{4+} with He and H_2 targets.

well manifested in the case of Li-like O^{5+} and F^{6+} ions colliding with H_2 targets. The RTE contribution for He-like $F^{7+} + H_2$ is also seen in Fig. 41. The eeI is not well distinguished for the Be-like O^{4+} ion cases, however, in the case of H_2 targets, eeI and eeE can be seen as some increase of the cross section with increasing projectile energy. All these dynamic electron-electron Interactions will be discussed state-selectively in the following chapters.

C. Error Analysis

The experimental uncertainty in the present cross section measurements can be determined from Eqs. (53), (54), (59), and (47) using the usual method of error propagation⁹⁴ for uncorrelated variables. Letting $\delta(d\sigma/d\Omega')$ be the absolute error, the relative error for a measured cross section of an Auger line, $\delta(d\sigma/d\Omega')$:

$$\Delta_{\sigma} = \frac{\delta(d\sigma/d\Omega')}{d\sigma/d\Omega'}, \quad (35)$$

is obtained by Eqs. (53) and (63):

$$\Delta_{\sigma} = [\Delta_{\Omega}^2 + \Delta_Q^2 + \Delta_{YKLL}^2 + \Delta_{fd}^2]^{\frac{1}{2}}, \quad (64)$$

where

$$\Delta_{YKLL} = [\Delta_{\eta}^2 + \Delta_{ZKLL}^2 + \Delta_p^2 + \Delta_{Tg}^2]^{\frac{1}{2}} \quad (65)$$

arise from Eq. (47) and the gas cell number density $n = \frac{p}{K_B \cdot T_g}$, K_B and T_g being the Boltzmann's constant and the gas cell temperature, respectively, and

$$\Delta_{fd} = [\Delta_{Zhd}^2 + \Delta_{ZhKLL}^2]^{\frac{1}{2}} \quad (66)$$

and $f_d = Z_d/Z_{KLL}^{high}$, Z_d and Z_{KLL}^{high} being the number of electrons counted for each corresponding Auger line and total KLL -Auger lines in the high-resolution spectrum, respectively. Each of the subscripts in Eqs. (64), (65), and (66) stand for each independently measured variable, i.e., Ω means(\rightarrow) F_{Ω}^{prompt} for prompt

states and the factors of H_{Ω}^{4P} and R_Z for the 4P metastable state, $Q \rightarrow F_Q$, $fd \rightarrow f_d$ for prompt states and f_{4P} for the 4P metastable state; $YKLL \rightarrow (\frac{d\sigma}{d\Omega})_{KLL}$, $ZKLL$ and $ZhKLL$ refer to number of total KLL -Auger electrons in non-retarding mode and high-resolution mode, respectively, Zhd is the number of Auger electrons of the corresponding Auger line in the high-resolution mode, $p \rightarrow$ gas cell pressure, $Tg \rightarrow$ gas cell temperature, and $\eta \rightarrow \eta(E)$ [see Fig. 24]. All Δ 's refer to the relative error as in Eq. (59), i.e., $\Delta_{fd} = \delta(f_d)/f_d$..., and etc.

A detailed error estimation for each variable follows:

- (a). Δ_{Ω} are listed in Tables 7-14 as \pm values, which are estimated by Eq. (45-2) and Eq. (45-1) for the prompt and 4P state, respectively, using uncertainties which come from the error of the recommended electron capture cross sections.⁸⁵ For the 4P state, H_{Ω}^{4P} has approximately the same relative error as F_{Ω}^{4P} and $\sim \pm 13\%$ error of the R_Z factor is also included in Δ_{Ω} .
- (b). Δ_Q is given to be 2% from the uncertainties of the beam currents with and without target gas.
- (c). Δ_{η} is given to be 3.5% because the spectrometer efficiency was obtained for each beam time within this uncertainty (see Fig. 24).
- (d). Δ_p : the accuracy of the target cell pressure was assumed to be better than 1%.
- (e). Δ_{Tg} : the target cell temperature was observed to increase occasionally when a poorly collimated beam hit the gas cell collimator and resulted in some deviation from the room temperature 300 °K which was used as the gas cell temperature in the all cross section measurements. Uncertainty from this possible deviation and the actual room temperature variation from 300 °K is given to be 3%. In a worst case senario, using a thermocouple attached to the gas cell block, the gas cell temperature was observed to increase by 5% after the gas-cell-entrance collimator was hit for a few hours by a high-current high-energy beam which was totally uncollimated. For low energy, low current, or

well-collimated beams (by a 4-jaw slit), this temperature increase by the beam was observed to be negligible.

- (f). Δ_{ZKLL} , Δ_{ZhKLL} , and Δ_{Zhd} were determined by the statistical errors, $\Delta[STAT]$, of the number of the total electrons counted, T , and estimated background electrons (due mainly to binary encounter), B . In addition, a systematic error, $\Delta[BKSB]$, occurred in the process of finding a background polynomial B , was also included as follows:

$$\begin{aligned}\Delta_{\chi} &= (\Delta^2[STAT] + \Delta^2[BKSB])^{\frac{1}{2}} \\ &= \left[\left(\frac{\sqrt{T+B}}{T-B} \right)^2 + \left(\frac{\delta B}{T-B} \right)^2 \right]^{\frac{1}{2}}.\end{aligned}\quad (67)$$

Here, if $\chi \equiv T - B$ is the true number of Auger electrons ($ZKLL$, $ZhKLL$, or Zhd) counted, the first term can be shown to be

$$\Delta[STAT] = \frac{\delta(STAT)}{\chi} = \frac{[(\sqrt{T})^2 + (\sqrt{B})^2]^{\frac{1}{2}}}{\chi} = \frac{\sqrt{T+B}}{T-B}.\quad (68)$$

The standard deviations, \sqrt{T} and \sqrt{B} , for a counted number T and an estimated background number B have been taken as the experimental counting uncertainties, respectively, since it was observed that the typical distribution of electron counts in a raw electron spectrum where the B was estimated showed a good Poission distribution. δB in Eq. (60) is an estimated uncertainty in the determination of the background polynomial B . This uncertainty was only important (5–13 %) when the KLL Auger electrons were distributed around the BEE peak in the non-retarded electron spectrum. In the case of high-resolution spectra, the uncertainty due to the background polynomial determination was observed to be negligible, because the background polynomial showed a good linearity around the KLL-Auger lines.

VI. RESONANT TRANSFER EXCITATION

In the present and following chapters, state-resolved Auger production cross sections are presented to identify the dynamic electron-electron interactions, the main object of this dissertation. In this chapter, resonant-transfer excitation followed by Auger decay (RTEA) is studied as a process of the electron-electron interactions. In the following chapter, electron-electron excitation and electron-electron ionization are presented as other evidences of dynamic electron-electron interactions.

A. Background

Resonant transfer-excitation (RTE)^{95,96} in energetic ion-atom collisions has been studied extensively in recent years.^{9-11,13,14,29,30,96-98} RTE is a two-electron process in which a weakly bound (quasifree) target electron is transferred to a higher orbital ($n \geq 2$) of the projectile and simultaneously excites a projectile electron. The resulting doubly excited state must relax either by radiative (X-ray) decay [RTEX]^{28,96,97} or autoionization (Auger decay) [RTEA].^{9-11,13,14,28-30,98} In the present work, we concentrated on the RTE process of projectile $1s \rightarrow 2l$ excitation *with* capture (transfer) to the $2l$ orbital of the projectile ion.

If the captured electron were truly free, RTEX and RTEA would be equivalent to dielectronic recombination (DR)^{99,100} and resonant excitation-scattering (RES)^{43,100} in electron-ion collisions, respectively. As mentioned in Chapter I, DR is a process of fundamental interest in the high-temperature plasmas of laboratory or astrophysical environments, and, in particular, DR is thought to be an important energy loss mechanism in fusion technology. RES is analogous to the well known resonant scattering in electron-atom collisions.¹⁰¹ Since RES is the other deexcitation channel of the excited state, measurements of RES strengths

(or cross sections) can complement DR cross sections.

The production mechanism of the excited state, $|d\rangle$, is a correlated electron-electron interaction.¹⁷ In energy conservation, DR and RES thus RTE and RTEA are resonant with the electron energy in the ion rest frame, and in angular momentum conservation consideration, they should have an *angular* dependence in their deexcitation processes due to the collisional alignment of the $|d\rangle$ state, which represents the preferential population of the $M_L=0$ magnetic substate.^{29,30,102,103} In addition, since the production channel of the $|d\rangle$ state is just a time-inversed Auger process, the state production cross section or strength can be essentially calculated by the Auger rate between the excited $|d\rangle$ and the initial $|i\rangle$ state.

RTEA and RTE cross sections have been measured and compared with theory,^{28,29,43,104,105} mostly within the impulse approximation²⁸ leading to a good agreement and from which DR or RES cross sections can be extracted. Many RTE experimental studies,^{96,97} in which mostly *K*-shell excitation ($\Delta n \geq 1$ transition) is involved, have been performed for $Z \geq 9$ with multi-state measurements, where the $|d\rangle$ states are not resolved due mainly to low resolution or low efficiency in the x-ray detector. The most stringent tests, to date, of RTE and its associated resonant strength (cross section) have been supplied by state-selective studies^{9,13,14,30} for $Z = 8, 9$ using high-resolution Auger electron spectroscopy.

In the present chapter, I report on RTEA and its RES strength measured at $\theta_{Lab}=0^\circ$ with respect to the projectile beam direction. The RTE states which are clearly identified by the present Auger measurements were O^{4+} , $F^{5+} (1s2s2p^2)^{3,1}D$ and $F^{6+} (1s2p^2)^2D$, $(1s2s2p)^2P_{\pm}$ states. The projectile ions of 0.25–2 MeV/amu Li-like O^{5+} , F^{6+} and He-like F^{7+} were used to form the $^{3,1}D$ and 2D , $^2P_{\pm}$ states, respectively. Both He and H_2 gas targets were used.

In the case of RTE experiments with F^{7+} projectile ions, all possible $1s2l2l'$

$(2S+1)L$ states were searched and their KLL RTEA cross sections were determined for each state as far as their cross sections were measurable in the present work. These state-resolved cross sections showed a good agreement with a theoretical calculation, thus resulting in a complete KLL RTEA measurement. In particular, the RTEA measurement with different L of 2D and $^2P_{\pm}$ RTE states elucidates the recent studies on the angular dependence^{29,30,102,103} of RTE, in which it is shown that the angular differential cross sections of RTEA are determined by total angular momentum L in the L - S coupling scheme.

B. A Theoretical Description

B-1. RTE Impulse Approximation

Within the treatment of the Impulse Approximation of Eq. (1), RTE cross section,²⁸ σ_{RTE} , is given by:

$$\sigma_{RTE}^{gd} = \sum_i \int \sigma_{RC}^{gd} \cdot |\Psi(\mathbf{p}_i)|^2 d^3 p_i, \quad (70)$$

where σ_{RC} is the radiationless (or dielectronic) capture^{9,13,30} cross section for a free electron of momentum \mathbf{p}_i with respect to the incoming projectile. The superscripts gd refer to the atomic state transition from the initial $\langle g|$ to the intermediate $\langle d|$ state, which may be called the "RTE state". In the RTE Auger measurements, the RTEA cross section is thus expressed:

$$\sigma_{RTEA}^{gdf} = \sum_i \int \sigma_{RES}^{gdf} \cdot |\Psi(\mathbf{p}_i)|^2 d^3 p_i, \quad (71)$$

where $\sigma_{RES}^{gdf} = \sigma_{RC}^{gd} \cdot \xi^{df}$ is the cross section of resonant excitation scattering (RES), which is also called resonant excitation (RE). Here the superscripts gdf and df refer to the atomic transition of $\langle g| \rightarrow \langle d| \rightarrow \langle f|$ and $\langle d| \rightarrow \langle f|$, respectively. $\langle f|$ means the final state for the Auger transition and ξ^{df} is the Auger yield

of the corresponding Auger decay channel. For all the RTEA measurements in this dissertation, $\langle g \rangle = \langle f \rangle$, so that all the redundant superscripts have been omitted.

The RTEA process can be shown schematically using Fig. 23 with a He-like or Li-like projectile ion. In the projectile-rest frame, a target electron is incident with an orbital momentum distribution (Compton profile) and is quasi-elastically scattered via the intermediate RTE state. As discussed in the case of the BEe [see Eq. (21)], the electron energy E' in the projectile frame can be expressed:

$$E' = (s^2 + 2sp_{iz} + p_{iz}^2 + p_{ix}^2)/2m - E_I, \quad (72)$$

where the scattering takes places in a collision plane in the totally classical picture of Coulomb scattering. Three cases of the energy E' expression have been considered in the RTE-IA as follows:

(1). case 1;

$$E' = (s^2 + 2sp_{iz})/2m, \quad (73-1)$$

where both quadratic p_{iz}^2 and p_{ix}^2 terms and E_I are neglected,²⁸

(2). case 2;

$$E' = (s^2 + 2sp_{iz})/2m - E_I, \quad (73-2)$$

where both quadratic p_{iz}^2 and p_{ix}^2 terms are neglected,^{8,9,13,30}, and

(3). case 3;

$$E' = (s^2 + 2sp_{iz} + p_{iz}^2)/2m - E_I, \quad (73-3)$$

where only the p_{ix}^2 term is neglected.

The reasonableness of neglecting the p_{ix}^2 term has been discussed in section B of Chapter IV, where case 3 has been used to calculate BEe-DDCS and compared successfully with the experimental data.

Since σ_{RC} , thus, σ_{RES} is dependent on the electron energy E' and E' can be expressed approximately as a function of p_{iz} as in Eq. (73) above, σ_{RTEA} of Eq. (71) is given by:

$$\begin{aligned}\sigma_{RTEA} &= \int \sigma_{RES} \cdot dp_{iz} \sum_i \int \int |\Psi(\mathbf{p}_i)|^2 dp_{iz} dp_{iy} \\ &= \int \sigma_{RES} \cdot dp_z \cdot J(p_z)\end{aligned}\quad (74)$$

where $J(p_z)$ is the Compton profile given by Eq. (24). Using Eq. (73-3) and the delta-function property of σ_{RES} in the electron energy E' , σ_{RTEA} of Eq. (74) is expressed as follows (in the units of $\text{eV}\cdot\text{cm}^2$):

$$\sigma_{RTEA} = \frac{J(Q)}{V_P + Q} \cdot \frac{\Omega_{RES}}{\epsilon_0}, \quad (75)$$

where projectile velocity, V_P , is $V_P = s$ in atomic units and $Q \equiv p_{iz} = p_z$ for identical electrons for He and H_2 targets and in atomic units. $\epsilon_0 = 27.2116$. Q in Eq. (75) is also related to the Auger electron energy E_A between the initial $|g\rangle$ and intermediate $|d\rangle$ states. Therefore,

$$Q = \sqrt{2}(\sqrt{E_A + E_I} - \sqrt{t}), \quad (76)$$

where t is cusp electron energy and all values here are in atomic units. The RES strength Ω_{RES} is defined as

$$\Omega_{RES} = \Delta E_{bin} \cdot \sigma_{RES}, \quad (77)$$

where ΔE_{bin} is the electron energy bin whose size is chosen to be much larger than the total width (transition rate) of the $|d\rangle$ state, which is $\Gamma^d = \Gamma_A^d + \Gamma_x^d$, Γ_A^d and Γ_x^d being the Auger and x-ray rate, respectively. Ω_{RES} is invariant with the ΔE_{bin} and can be determined from the RTEA cross sections as far as the IA is valid.

Theoretically, in the LS -coupling scheme, the Ω_{RES} is given (in cm^2eV) by using the RC strength Ω_{RC} :^{13,29,30,106}

$$\Omega_{RES} = \xi_d \cdot \Omega_{RC} = \xi_d \cdot 2.475 \times 10^{-30} \cdot \frac{(2L_d + 1)(2S_d + 1)}{(2L_i + 1)(2S_i + 1)} \cdot \frac{\Gamma_A(d \rightarrow i)}{E_A}, \quad (78)$$

where $\xi_d = \Gamma_A^d / (\Gamma_A^d + \Gamma_z^d)$ is the Auger yield of the $|d\rangle$ state. E_A is the Auger energy in eV [cf: E_A in a.u. is used in Eq. (76) and Table 15]. L_d , S_d , L_i , and S_i represent the orbital and spin angular momentum quantum numbers of states $|d\rangle$ and $|i\rangle$, respectively. The calculated RC and RES strengths, E_A , Γ_A , and ξ for each $|d\rangle \rightarrow |i\rangle$ transition are listed in Tables 17 and 19 along with our measured RES strengths which will be discussed in the later sections.

For the comparison of the three different treatments of RTE-IA, the σ_{RTEA} and Q relations are deduced, and all the results for the three cases are summarized in Table 15:

Table 15 : Three RTE-IA cases

Case	σ_{RTEA}	$Q(\equiv p_{iz})$	Ref.
IA1	$\frac{J(Q)}{V_p} \cdot \frac{\Omega_{RES}}{\epsilon_0}$	$\frac{E_A - t}{V_p}$	Brandt ²⁸
IA2	$\frac{J(Q)}{V_p} \cdot \frac{\Omega_{RES}}{\epsilon_0}$	$\frac{E_A + E_I - t}{V_p}$	Itoh ⁸
IA3	$\frac{J(Q)}{V_p + Q} \cdot \frac{\Omega_{RES}}{\epsilon_0}$	$\sqrt{2}(\sqrt{E_A + E_I} - \sqrt{t})$	present

In this table IA1, IA2, and IA3 are referred to the cases of (1), (2), and (3) of Eq. (73) above. All RTE studies have used the result of case IA1, where the approximation of Eq. (73-1) is reasonable because high velocity and high Z_P ($Z_P \geq 9$) projectiles were involved. In the RTEA experiments with He^+ , case IA2 was used where the target ionization potential E_I was accounted for.^{8,10} These three IA1, IA2, IA3 cases will be compared with available experimental data later.

B-2. RTE alignment and RTEA interference with BEe

Total RTE cross sections usually have been obtained by multiplying the measured SDSC (typically at 0°) by 4π , assuming *isotropic* emission of the RTE Auger electrons.^{9,13,14,98} Recently an RTEA angular dependence theory including the interference between the BEe and RTE Auger electrons has been formulated²⁹ and confirmed experimentally.¹⁰³

In the classical picture of the RTEA process, RTEA can be treated as an elastic scattering of a quasifree target electron in the projectile frame. In other words, BEe and RTE Auger electrons have the same initial and final state with only different intermediate states resulting in the same elastic scattering. Therefore RTE Auger electrons are expected to interfere with BEe. In addition, the intermediate $(2S+1)L$ RTE state will be populated only in the $M_L=0$ magnetic substate, since the angular momentum of the captured electron must be conserved along the axis of quantization. Therefore, the RTE state is collisionally aligned and thus the induced nonstatistical population of the magnetic substates results in emission-angle dependent Auger or x-ray production. In Ref. 29, within the RTE-IA (IA1 mentioned above), these alignment and interference effects were formulated in terms of the DDSCS of the electron production in electron energy and its emission angle.

Near the resonance energy of the projectiles, evidence of the interference effects was fairly well observed as an asymmetric Fano profile in the measured RTE Auger lines. This profile was predicted by the theoretical DDSCS in Ref. 29. (See also the exhibited Fano profiles at resonance projectile energy in the spectra of Figs. 47, 48, and 51.) However, in zero-degree RTEA measurements, the contribution to the Auger cross section due to the interference effects was found to be smaller than 3% compared to the RTEA cross section.³⁰ This value was estimated for the O^{4+} and $F^{5+} 1s2s2p^2\ ^3,^1D$ RTE states using Eq. (5) in Ref. 29. There-

fore, the small influence from the interference effects was neglected in the present zero-degree RTEA analysis.

The pure RTEA SDCS is expressed as:

$$\frac{d\sigma_{RTEA}}{d\Omega'} = \frac{J(Q)}{V_p + Q} \cdot \frac{\Omega_{RES}}{\epsilon_0} \cdot \frac{W(\theta')}{4\pi}, \quad (79)$$

where

$$W(\theta') = 1 + \sum_{n=1} A_{2n} \cdot P_{2n}(\cos\theta'), \quad (80)$$

where W is the angular distribution factor,¹⁰⁷ θ' is the electron emission angle in the projectile frame, $P_{2n}(\cos\theta')$ are the Legendre polynomials, and A_{2n} is the anisotropy coefficient given in Ref. 107 for the decay from the $L = 0, 1, 2$ states to the $L = 0$ state. For these different L states, the anisotropy coefficients are simply evaluated by using the non-zero magnetic substate population only for $M_L = 0$ as discussed above. Thus, in the following evaluation, the magnetic substate population probability,¹⁰⁷ $Q_{LM_L} = 1$ for $M_L = 0$ and 0 for $M_L \neq 0$:

(a). For $L = 0$ (S state); $W(\theta') = 1$, isotropic.

(b). For $L = 1$ (P state);

$$\begin{aligned} W(\theta') &= 1 + A_2 \cdot P_2(\cos\theta') \\ &= 1 + 2 \frac{Q_{10} - Q_{11}}{Q_{10} + 2Q_{11}} P_2(\cos\theta') \\ &= 1 + 2P_2(\cos\theta') \\ &= 3\cos^2\theta' \end{aligned}$$

(c). For $L = 2$ (D state);

$$\begin{aligned}
 W(\theta') &= 1 + A_2 \cdot P_2(\cos\theta') + A_4 \cdot P_4(\cos\theta') \\
 &= 1 + \frac{10}{7} \frac{Q_{20} + Q_{21} - 2Q_{22}}{Q_{20} + 2Q_{21} + 2Q_{22}} P_2(\cos\theta') + \frac{6}{7} \frac{3Q_{20} - 4Q_{21} + 2Q_{22}}{Q_{20} + 2Q_{21} + 2Q_{22}} P_4(\cos\theta') \\
 &= 1 + \frac{10}{7} P_2(\cos\theta') + \frac{18}{7} P_4(\cos\theta') \\
 &= \dots\dots\dots \\
 &= 5\left(\frac{3}{2}\cos^2\theta' - \frac{1}{2}\right)^2
 \end{aligned}$$

Hence,

$$\frac{W(\theta')}{4\pi} = |Y_{L0}(\theta')|^2, \quad (81)$$

where Y_{L0} is a spherical harmonic and L refers to the angular momentum quantum number of the $|d\rangle$ states of interest.

Therefore, RTEA SDCS is:

$$\frac{d\sigma_{RTEA}^L}{d\Omega'} = \frac{J(Q)}{V_p + Q} \cdot \frac{\Omega_{RES}}{\epsilon_0} \cdot |Y_{L0}(\theta')|^2. \quad (82)$$

Our observation angle is $\theta_{Lab} = 0^\circ$, which corresponds to $\theta = 180^\circ$ in the projectile frame, and thus $|Y_{L0}(\theta' = 180^\circ)|^2$ is simply $(2L + 1)/4\pi$.

In Figs. 43-46 are shown the RTEA-SDCS (at $\theta_{Lab} = 0^\circ$) of the three different IA calculations for the IA1, IA2, and IA3 (see Table 15 above) for four different projectiles of $^3\text{He}^+$, C^{q+} , F^{q+} , and Si^{q+} . The angular factor of Eq. (81) is multiplied for each case of σ_{RTEA} in Table 15. In the case of low Z projectiles, where the cusp energy is comparable to the sum of the Auger electron energy and the ionization potential of the target electron, the IA3 is more reasonable to use than IA1 or IA2. IA2 is very similar to IA3, but some deviation is shown in the high and low projectile energy region as seen in the logarithmic diagrams of Fig. 43-46. Henceforth IA3 is used to calculate RTEA-SDCS, to represent its results with experimental data, and to extract the RES strength Ω_{RES} .

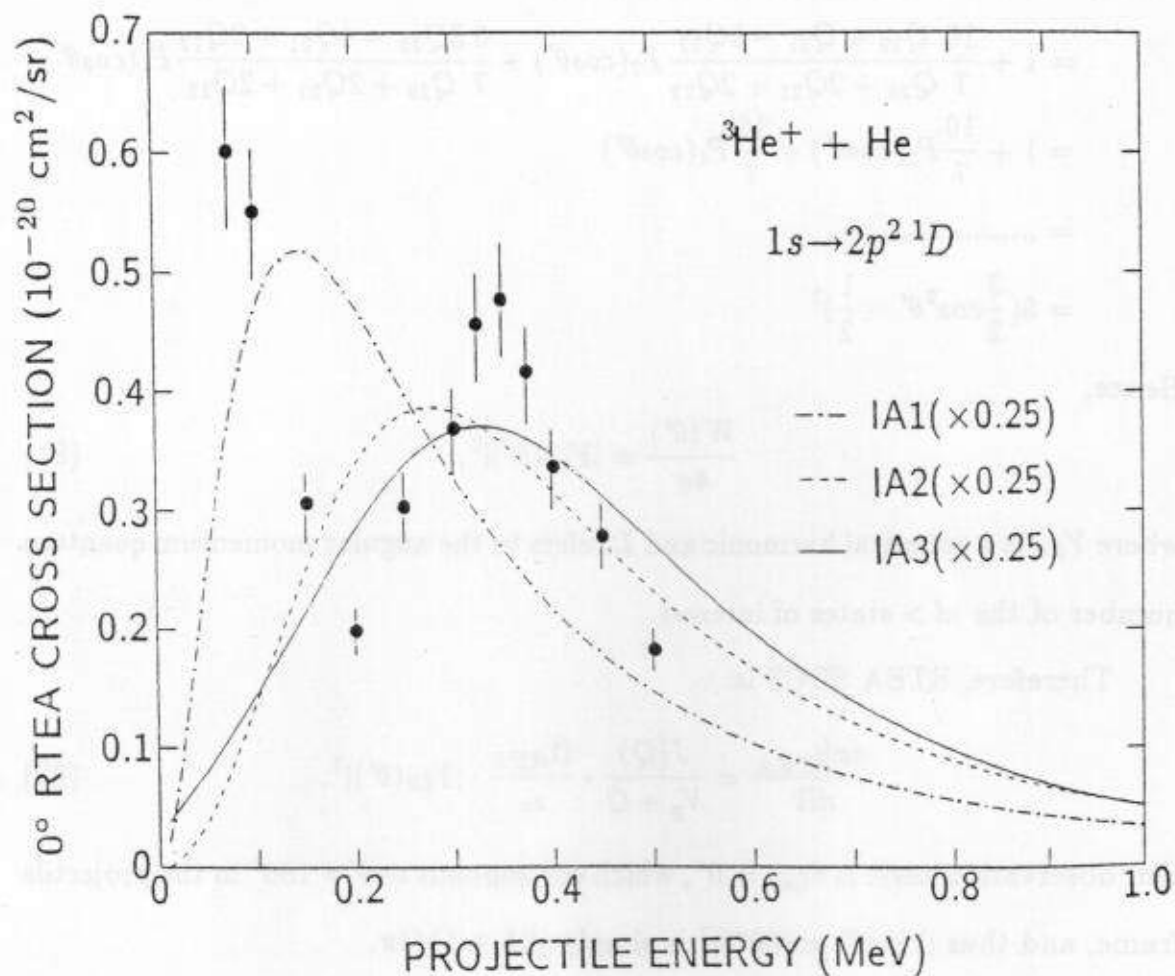


FIGURE 43. RTEA-IA comparison for the $2p^2 \ ^1D$ state produced in $\text{He}^+ + \text{He}$ collisions. The experimental data (solid dots) were taken from Ref. 8. Auger rate Γ_A for this state was taken from Ref. 105.

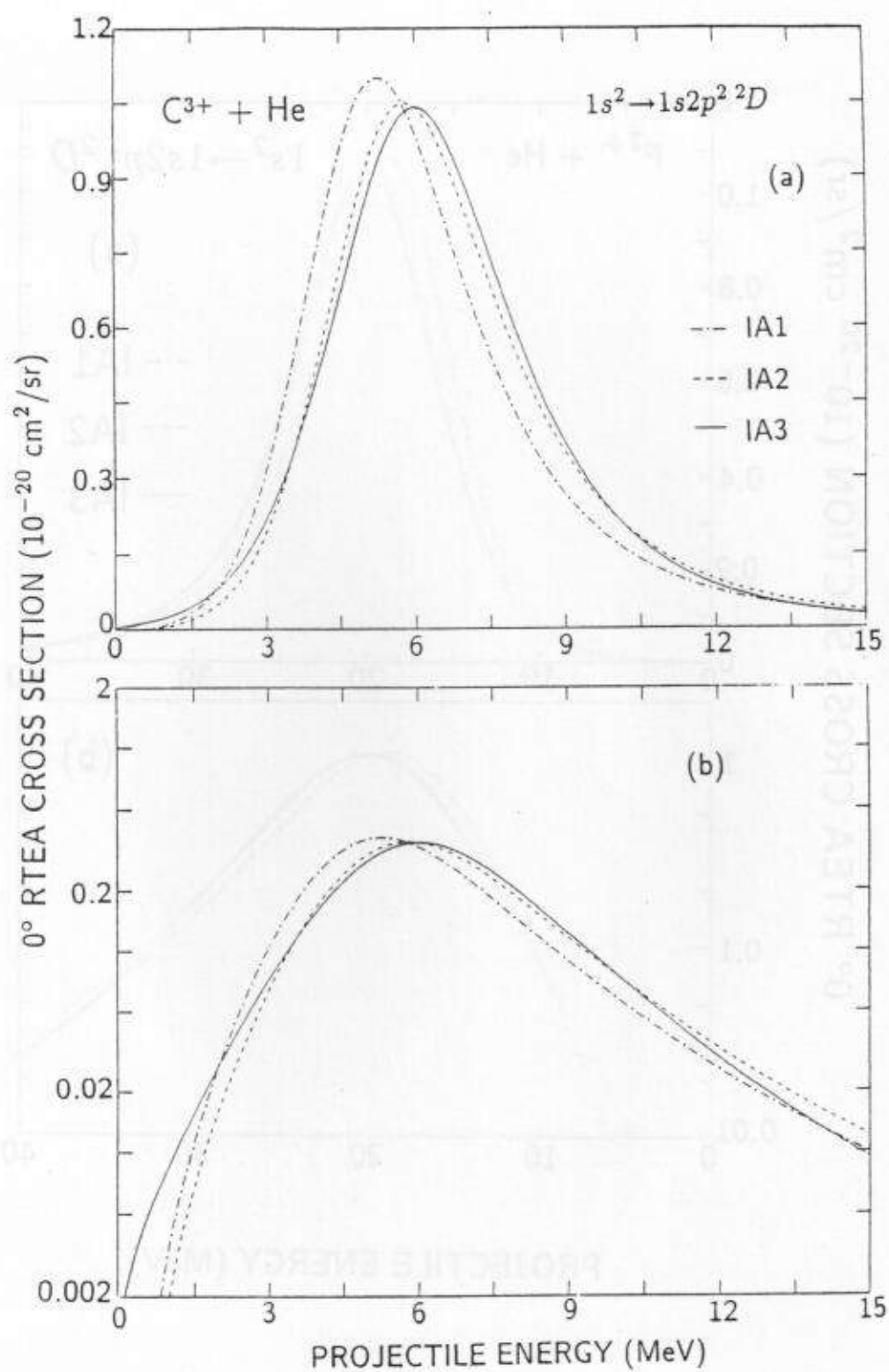


FIGURE 44. RTEA-IA comparison for the $2p^2 \ ^1D$ state produced in $C^{5+} + He$ collisions. (a): in linear scale, and (b): in log scale

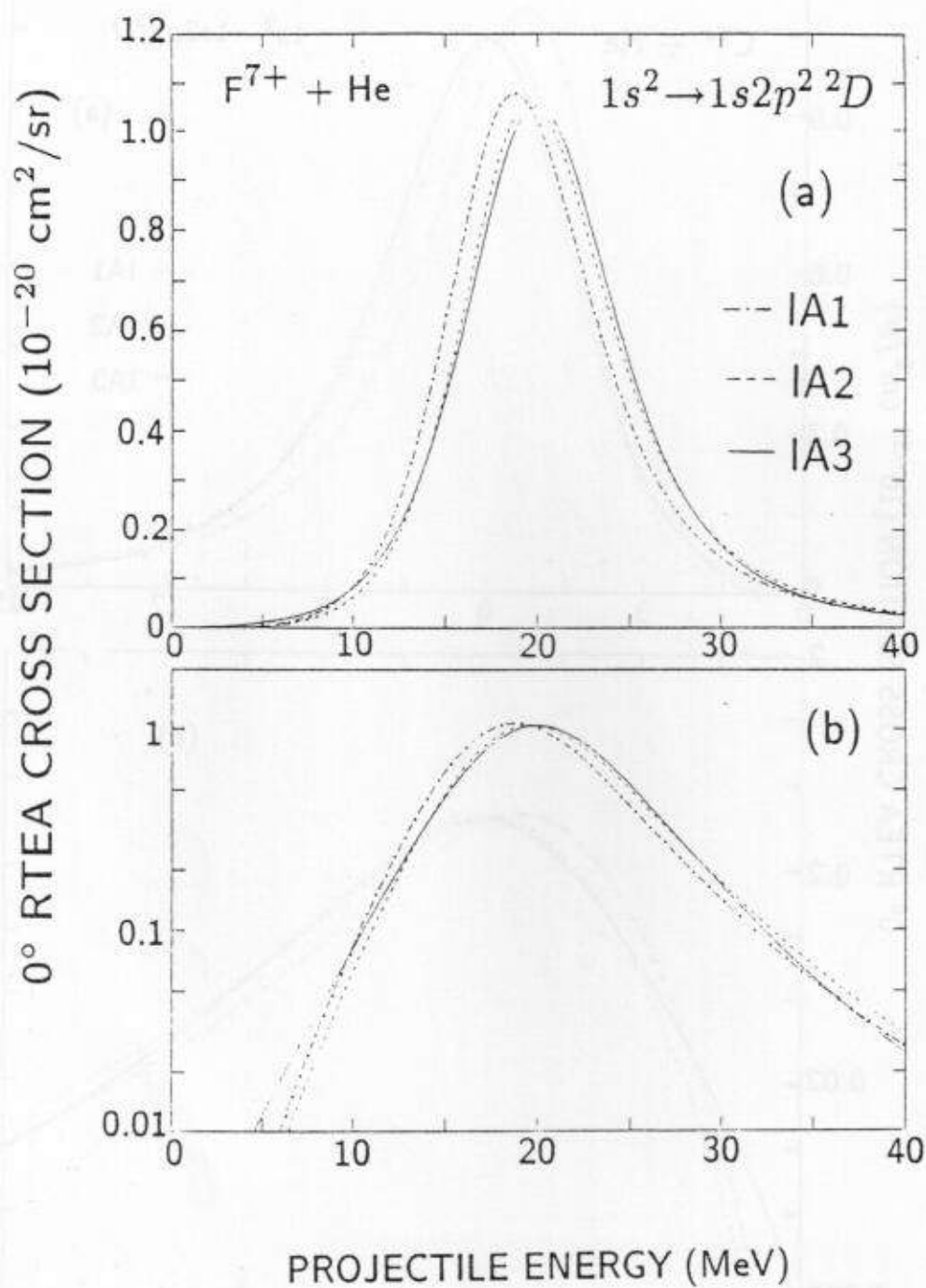


FIGURE 45. RTEA-IA comparison for the $1s2p^2 \ ^2D$ state produced in $F^{7+} + He$ collisions. (a): in linear scale, and (b): in log scale

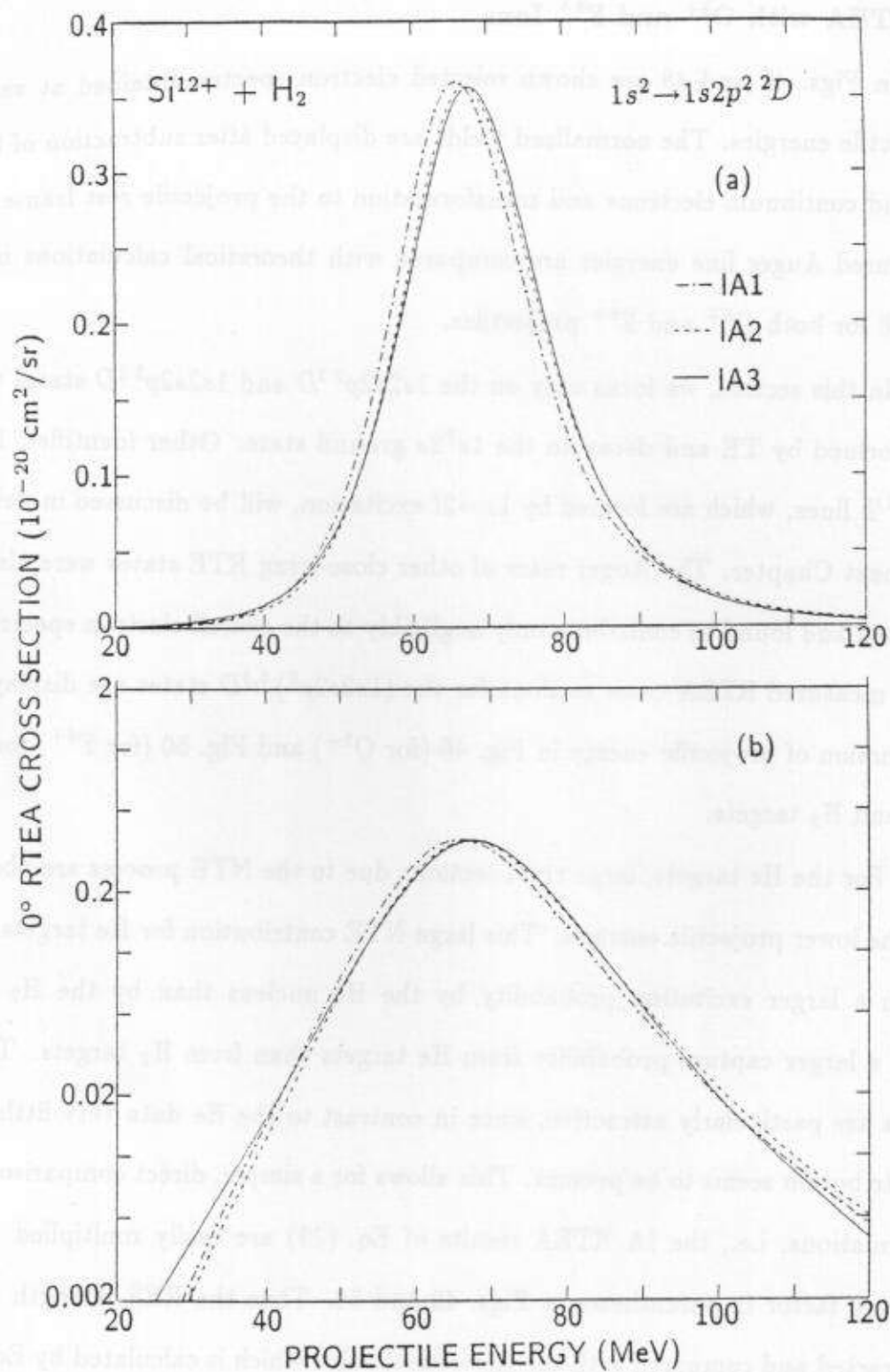


FIGURE 46. RTEA-IA comparison for the $1s2p^2 \ ^2D$ state produced in $\text{Si}^{12+} + \text{He}$ collisions. (a): in linear scale, and (b): in log scale

C. RTEA with O^{5+} and F^{6+} Ions

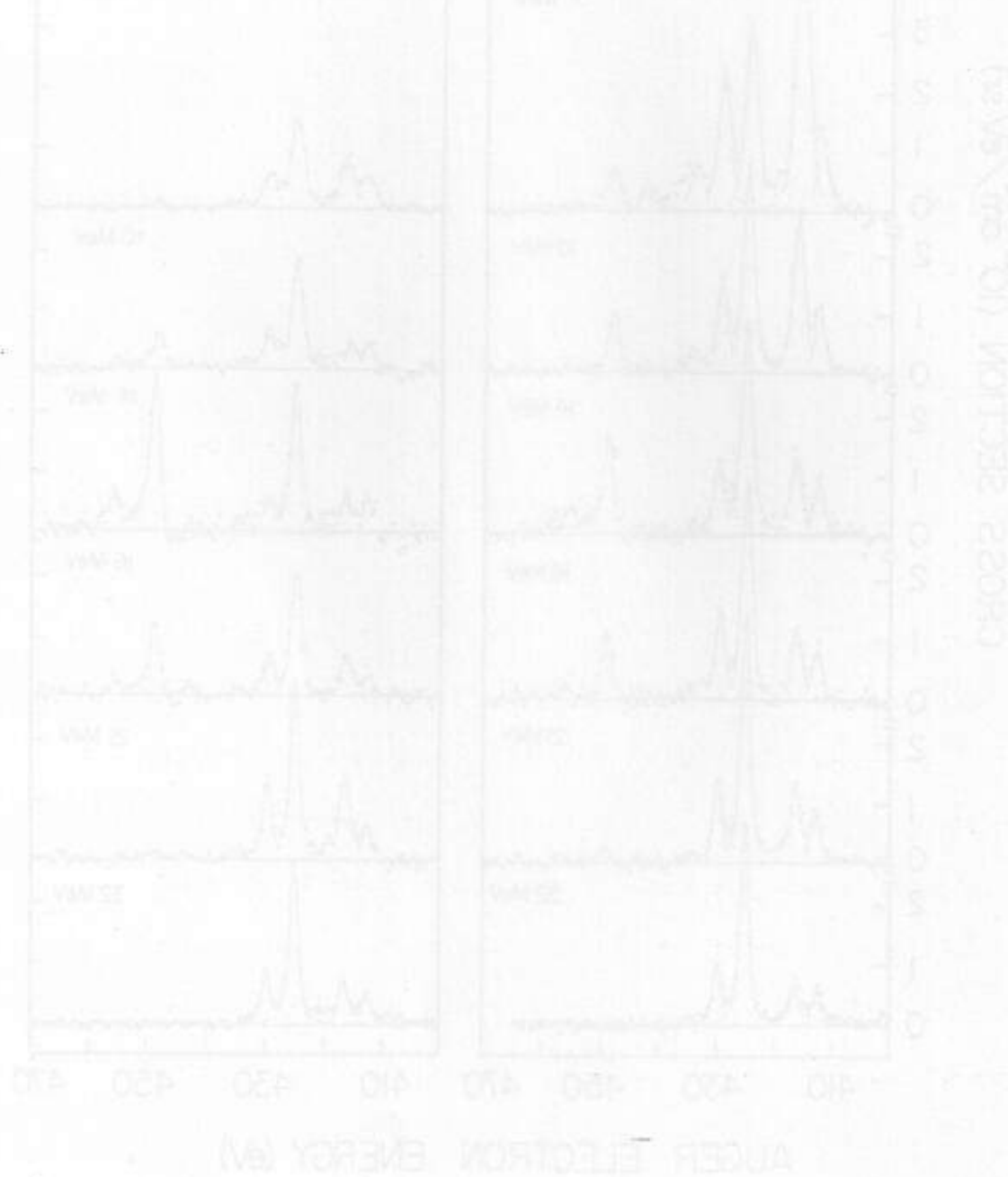
In Figs. 47 and 48 are shown selected electron spectra obtained at various projectile energies. The normalized yields are displayed after subtraction of background continuum electrons and transformation to the projectile rest frame. The measured Auger line energies are compared with theoretical calculations in Table 16 for both O^{5+} and F^{6+} projectiles.

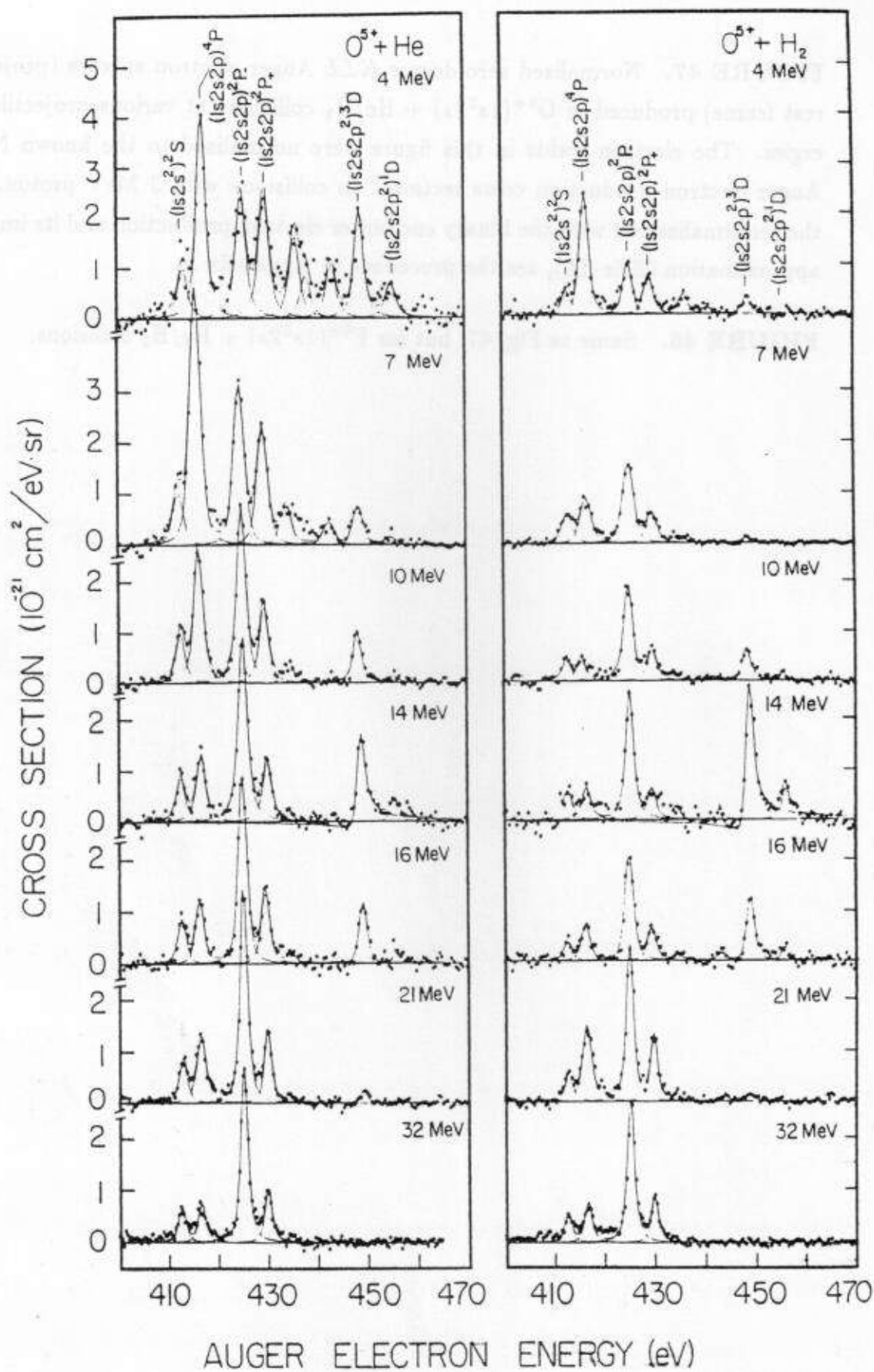
In this section, we focus only on the $1s2s2p^2\ ^3D$ and $1s2s2p^2\ ^1D$ states which are formed by TE and decay to the $1s^22s$ ground state. Other identified $1s2s2l\ (2S+1)L$ lines, which are formed by $1s \rightarrow 2l$ excitation, will be discussed in detail in the next Chapter. The Auger rates of other close-lying RTE states were also calculated and found to contribute only negligibly to the overall electron spectrum.¹³ The measured RTEA cross sections for the $(1s2s2p^2)\ ^{3,1}D$ states are displayed as a function of projectile energy in Fig. 49 (for O^{5+}) and Fig. 50 (for F^{6+}) for both He and H_2 targets.

For the He targets, large cross sections due to the NTE process are observed at the lower projectile energies. This large NTE contribution for He targets result from a larger excitation probability by the He nucleus than by the H_2 nuclei and a larger capture probability from He targets than from H_2 targets. The H_2 data are particularly attractive, since in contrast to the He data very little NTE contribution seems to be present. This allows for a simple, direct comparison with calculations, i.e., the IA RTEA results of Eq. (79) are easily multiplied by the scaling factor in parentheses in Figs. 49 and 50. Thus the RES strength can be extracted and compared with the theoretical value which is calculated by Eq. (78). The theoretical and experimental RES strengths are listed in Table 17 for the $^{3,1}D$ states for both O^{5+} and F^{6+} projectiles. The experimental ratio of $\sigma_{RE}(^3D)$ to $\sigma_{RE}(^1D)$ is thus (4.2 ± 1.1) , while the calculated ratio is 5.4.

FIGURE 47. Normalized zero-degree *KLL* Auger electron spectra (projectile rest frame) produced in $O^{5+}(1s^2 2s) + He/H_2$ collisions at various projectile energies. The electron yields in this figure were normalized to the known Ne *K* Auger electron production cross section⁶⁶ in collisions with 3 MeV proton. For the renormalization with the binary encounter electron production and its impulse approximation (BEe-IA), see the procedure in Appendix A.

FIGURE 48. Same as Fig. 47, but for $F^{6+}(1s^2 2s) + He/H_2$ collisions.





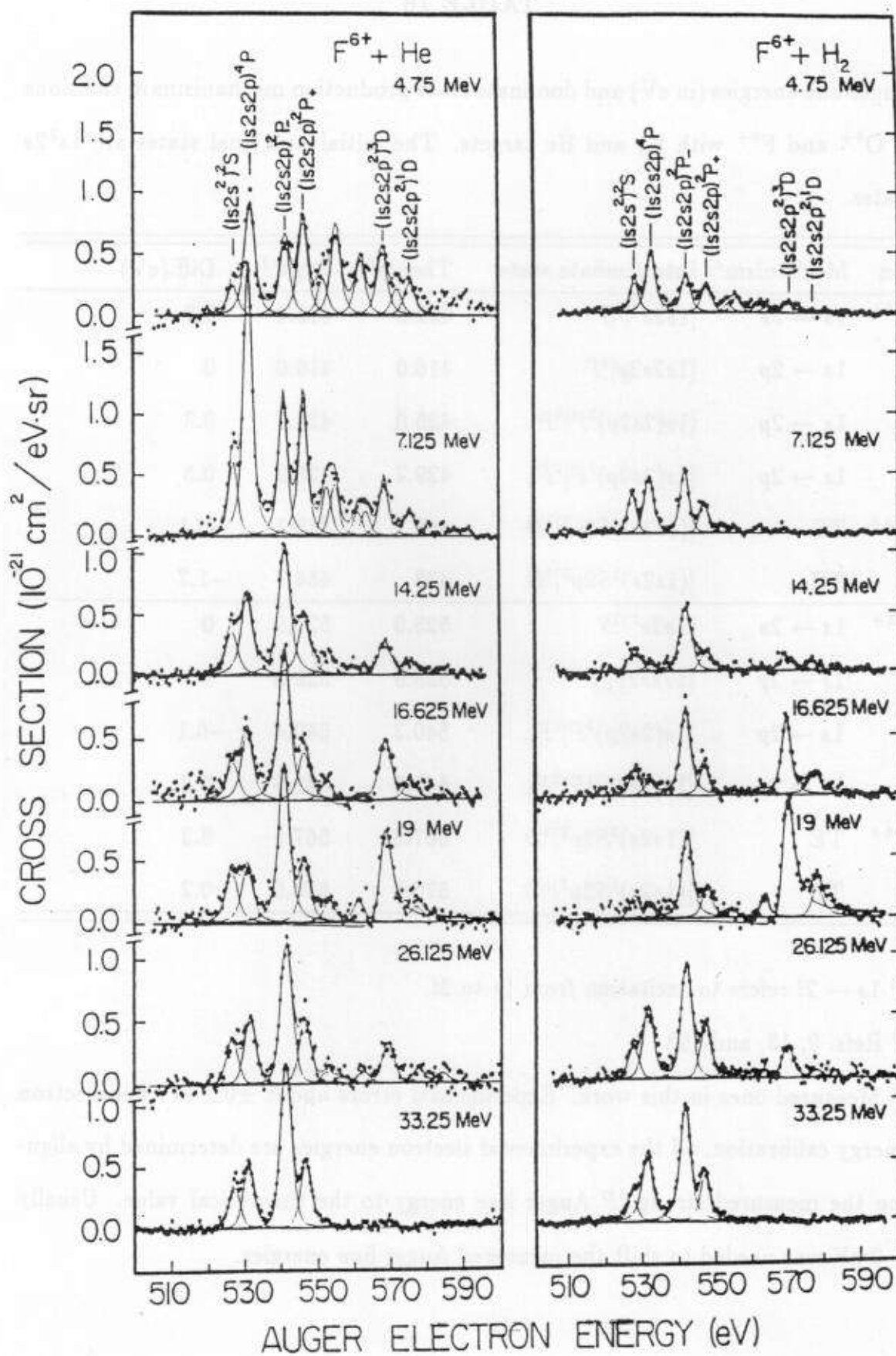


TABLE 16

Auger line energies (in eV) and dominate state production mechanisms in collisions of O^{5+} and F^{6+} with H_2 and He targets. The initial and final states are $1s^2 2s$ states.

Ion	Mechanism ^{a)}	Intermediate state	Theory ^{b)}	Expt ^{c)}	Diff.(eV)
O^{5+}	$1s \rightarrow 2s$	$[1s2s^2]^2S$	412.6	412.4	0.2
	$1s \rightarrow 2p$	$[1s2s2p]^4P$	416.0	416.0	0
	$1s \rightarrow 2p$	$[1s(2s2p)^3P]^2P_-$	425.0	424.7	0.3
	$1s \rightarrow 2p$	$[1s(2s2p)^1P]^2P_+$	429.7	429.2	0.5
O^{4+}	TE	$[(1s2s)^3S2p^2]^3D$	448	448.1	-0.1
	TE	$[(1s2s)^1S2p^2]^1D$	453	454.7	-1.7
F^{5+}	$1s \rightarrow 2s$	$[1s2s^2]^2S$	525.9	525.9	0
	$1s \rightarrow 2p$	$[1s2s2p]^4P$	529.8	529.8	0
	$1s \rightarrow 2p$	$[1s(2s2p)^3P]^2P_-$	540.3	540.4	-0.1
	$1s \rightarrow 2p$	$[1s(2s2p)^1P]^2P_+$	545.6	545.6	0.2
F^{6+}	TE	$[(1s2s)^3S2p^2]^3D$	567.8	567.5	0.3
	TE	$[(1s2s)^1S2p^2]^1D$	576.2	576.0	0.2

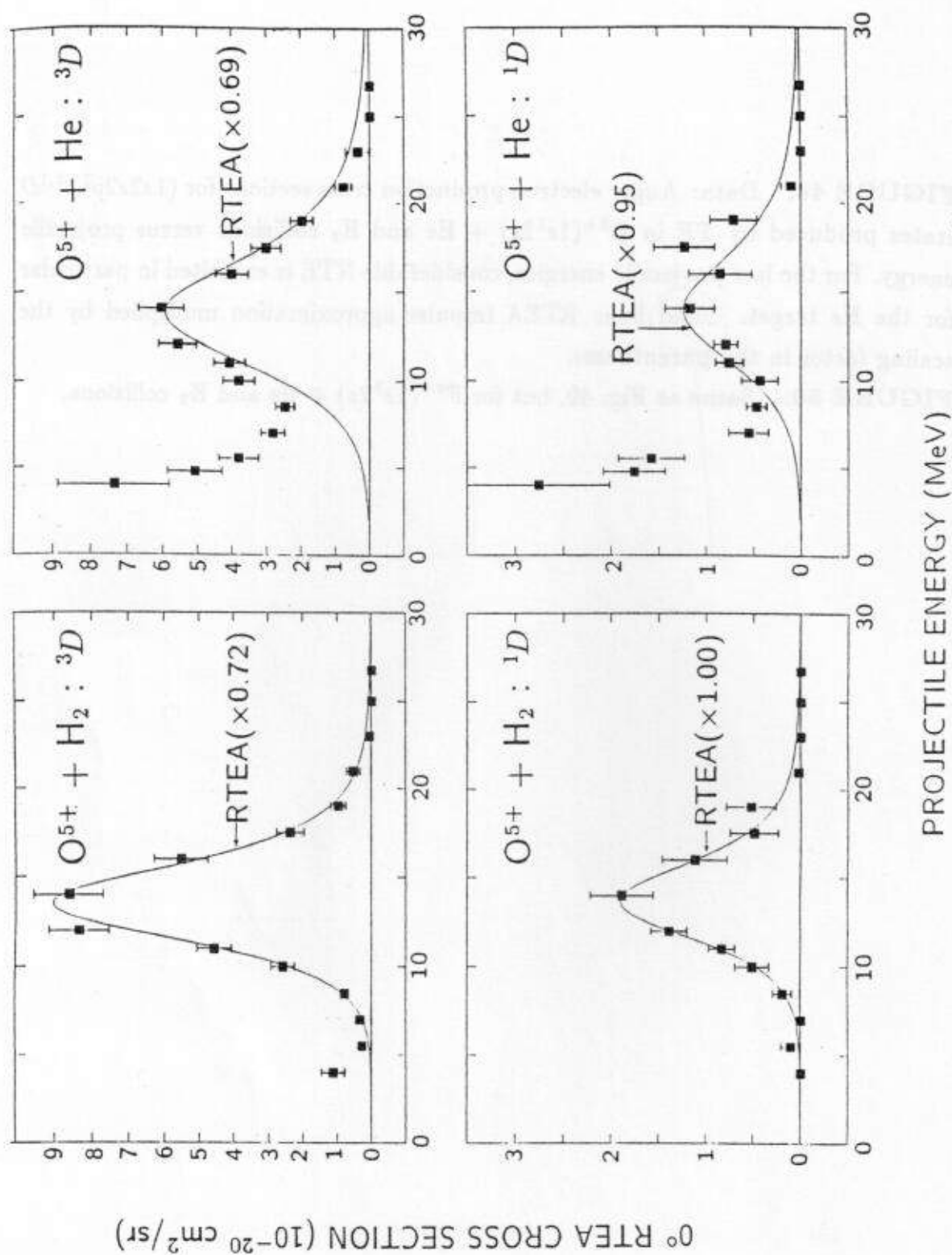
^{a)} $1s \rightarrow 2l$ refers to excitation from $1s$ to $2l$.

^{b)} Refs. 9, 13, and 108.

^{c)} Measured ones in this work. Experimental errors about ± 0.2 eV. For electron energy calibration, all the experimental electron energies are determined by aligning the measured strong 4P Auger line energy to the theoretical value. Usually 1-2 eV was needed to shift the measured Auger line energies.

FIGURE 49. Data: Auger electron production cross sections for $(1s2s2p^2)^3,1D$ states produced by TE in $O^{5+}(1s^22s) + He$ and H_2 collisions versus projectile energy. For the low projectile energies, considerable NTE is exhibited in particular for the He target. Solid line: RTEA impulse approximation multiplied by the scaling factor in the parentheses.

FIGURE 50. Same as Fig. 49, but for $F^{6+}(1s^22s) + He$ and H_2 collisions.



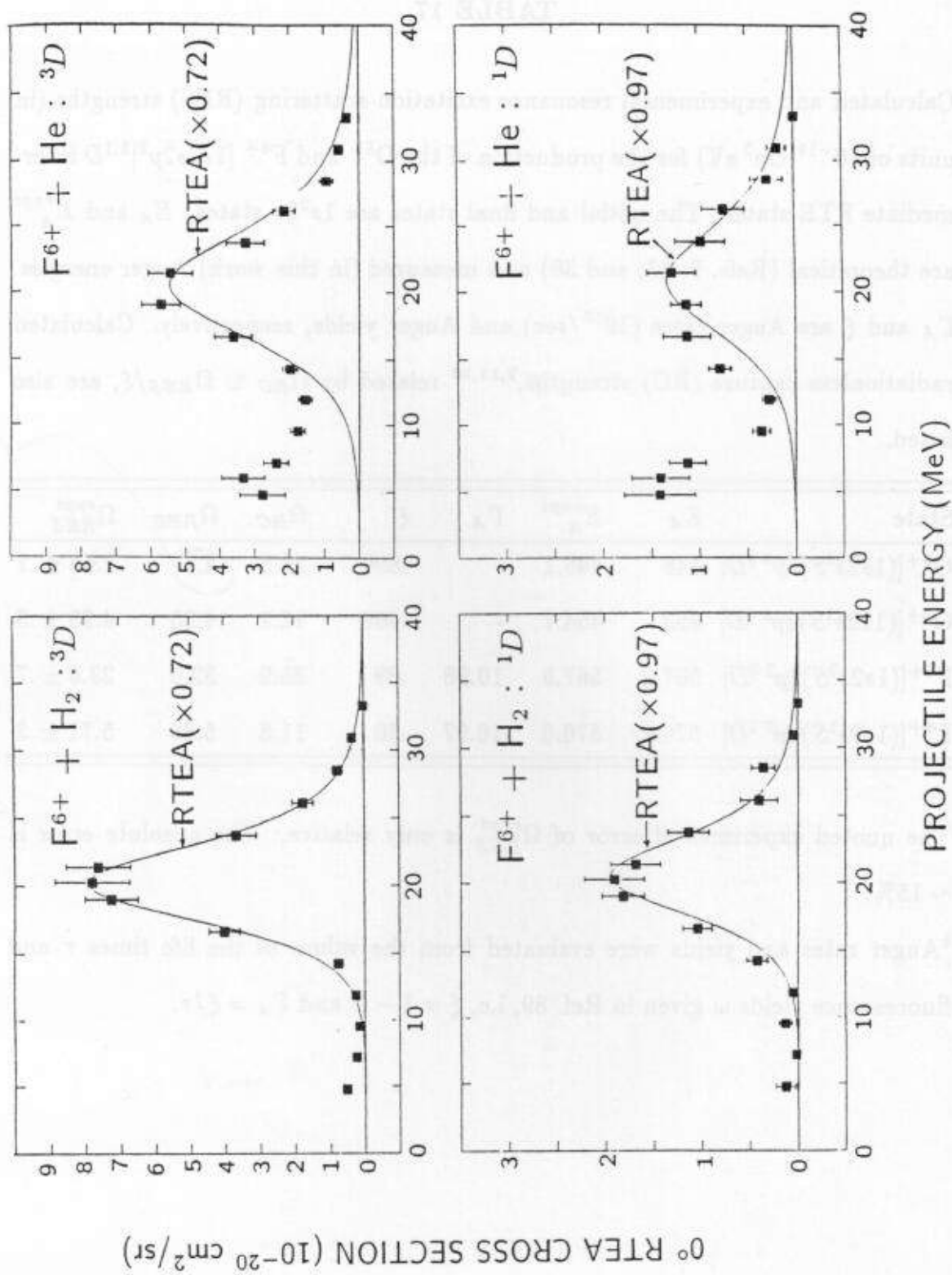


TABLE 17

Calculated and experimental resonance excitation-scattering (RES) strengths (in units of $10^{-19} \text{ cm}^2 \text{ eV}$) for the production of the O^{5+} and $\text{F}^{6+} [1s2s2p^2]^3,1D$ intermediate RTE states. The initial and final states are $1s^22s$ states. E_A and E_A^{expt} are theoretical (Refs. 9, 13, and 30) and measured (in this work) Auger energies. Γ_A and ξ are Auger rates ($10^{13}/\text{sec}$) and Auger yields, respectively. Calculated radiationless capture (RC) strengths,^{9,13,30} related by $\Omega_{RC} \equiv \Omega_{RES}/\xi$, are also listed.

State	E_A	E_A^{expt}	Γ_A	ξ	Ω_{RC}	Ω_{RES}	Ω_{RES}^{expt}
$\text{O}^{5+}[(1s2s^3S)2p^2^3D]$	448	448.1	-	.899	36.3	4.7	$23.5 \pm .7$
$\text{O}^{5+}[(1s2s^1S)2p^2^1D]$	453	454.7	-	.409	12.1	4.95	$4.95 \pm .3$
$\text{F}^{6+}[(1s2s^3S)2p^2^3D]$	567.8	567.5	10.98	.89	35.9	32.0	$23.0 \pm .7$
$\text{F}^{6+}[(1s2s^1S)2p^2^1D]$	576.2	576.0	10.97	.50	11.8	5.89	$5.71 \pm .3$

The quoted experimental error of Ω_{RES}^{expt} is only relative. The absolute error is $\sim 15\%$.

^bAuger rates and yields were evaluated from the values of the life times τ and fluorescence yields ω given in Ref. 89, i.e., $\xi = 1 - \omega$ and $\Gamma_A = \xi/\tau$.

D. RTEA with F^{7+} Ions

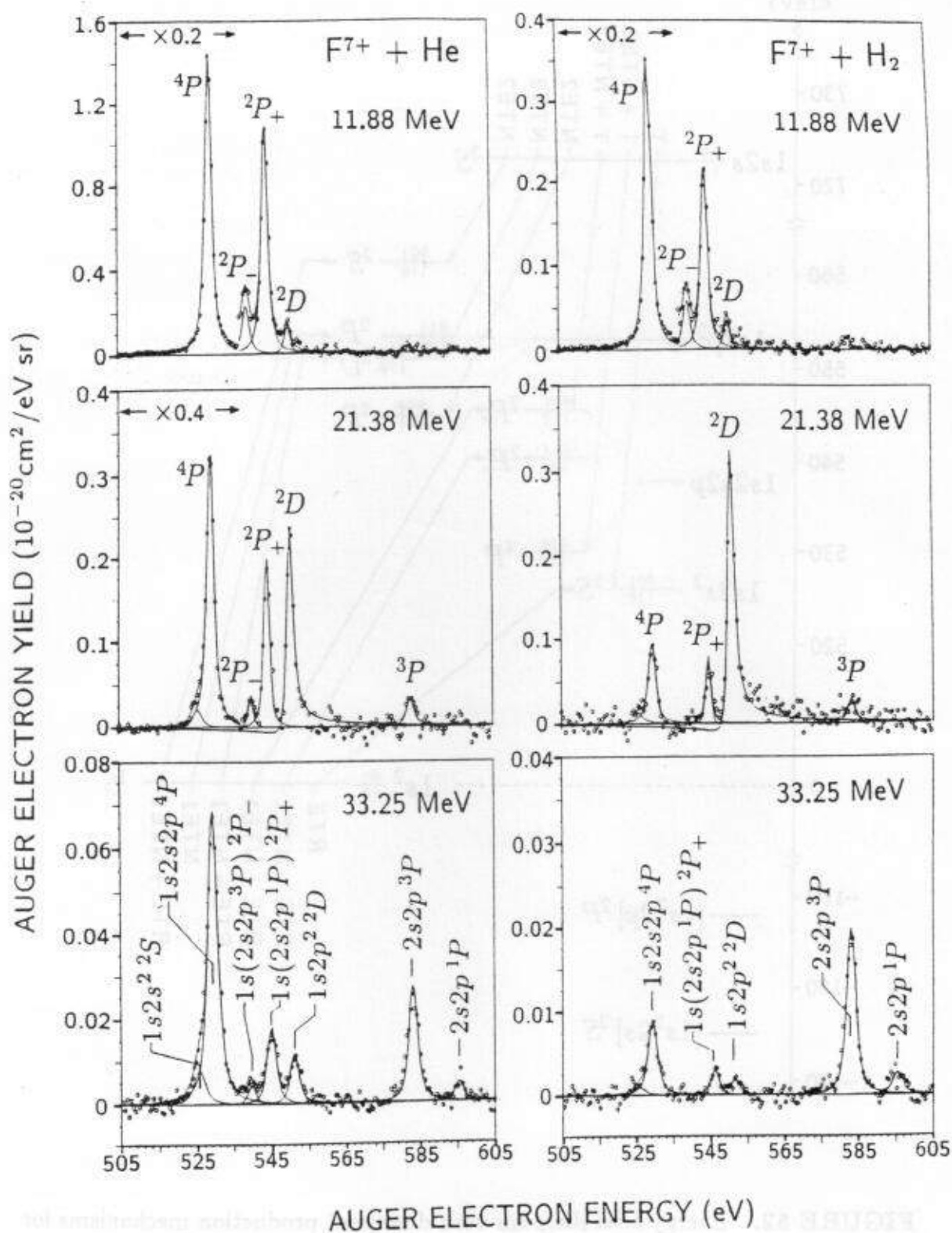
In the production of a He-like F^{7+} beam in the post-stripping foil, long-lived (lifetime = $277 \mu\text{sec}$)¹⁰⁹ metastable $1s2s\ ^3S$ ions are produced as well as $1s^2$ ground state ions. Therefore, the metastable beam fraction¹⁰⁹ must be considered in the cross section analysis. The metastable beam fraction varies from about 5% to 30% depending on the projectile energy. The metastable beam fraction for each projectile energy was taken from Refs. 6 and 109.

In Fig. 51 are shown selected electron spectra obtained at various projectile energies. The normalized double differential yields are displayed after kinematically transforming to the projectile rest frame, and the background electrons arising mainly from the binary encounter scattering have been subtracted. The normalized single differential yields were extracted by fitting the observed lines with Lorentzian or Fano profiles folded with the response function of the electron spectrometer.

The $1s2l2l'\ (^{2S+1})L$ doubly excited states can be produced from both incoming $1s^2\ ^1S$ and $1s2s\ ^3S$ states, and the dominant production mechanisms are illustrated with their energy levels and spin configurations in Fig. 52. It should be noted that RTE from $1s2s\ ^3S$ to $1s2l2l'\ (^{2S+1})L$ states is not energetically allowed. Only from $1s^2\ ^1S$ is RTE possible to some of the $1s2l2l'\ (^{2S+1})L$ states, as long as they have non-negligible Auger rates. Two types of NTE (non-resonant transfer excitation,²⁴ in which the projectile electron is excited by the target nucleus) are possible from both $1s^2\ ^1S$ and $1s2s\ ^3S$ states, and they are denoted hereafter as NTE1 and NTE2, respectively, for the sake of classification. Also shown in Fig. 52 is $2p$ capture [transfer (T)] (and probably np capture followed by cascading to $2p$) channel by the $1s2s\ ^3S$ component beam leading to $1s2s2p\ (^{2S+1})L$ states.

The Auger electron production SDCS from the 2D , $^2P_+$, $^2P_-$,

FIGURE 51. Normalized zero-degree Auger electron spectra (projectile rest frame) produced in $F^{7+}(1s^2\ ^1S, 1s2s\ ^3S) + He$ and H_2 collisions at 3 different projectile energies. The $1s2s2p\ ^4P$ Auger lines, if too large to draw in the given scale, have been reduced by the factors shown in the parentheses (below arrows at 538 eV). The $2s2p\ ^3P$ and 1P produced from $1s2s\ ^3S$ by $1s \rightarrow 2p$ excitation is relatively well pronounced from the background for higher collision energies.



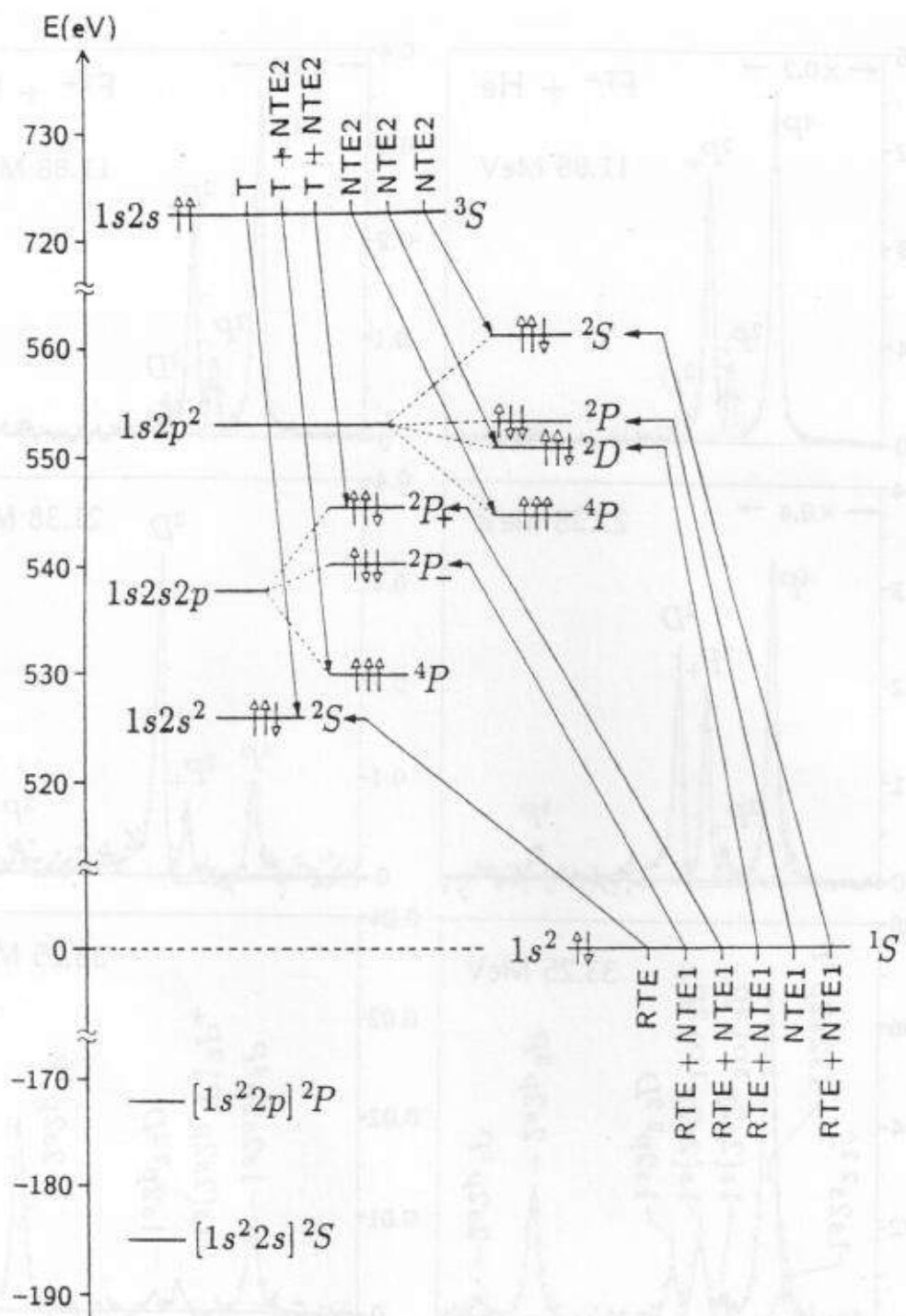


FIGURE 52. Energy level diagram with dominant production mechanisms for the production of $1s2l2l' (^{2S+1}L)$ doubly excited states from F^{7+} ($1s^2 ^1S$) and ($1s2s ^3S$).

and 2S states, (hereafter 2D , $^2P_+$,

$^2P_-$, and 2S denote $1s2p^2\ ^2D$, $[1s(2s2p)^1P]^2P_+$, $[1s(2s2p)^3P]^2P_-$, and $1s2s^2\ ^2S$ state,

respectively) are displayed in Figs. 53 and 54 as a function of projectile energy for

both H_2 and He targets. As seen / Figs. 53 and 54, all these states show strong, / from
considerable, or little RTE signatures depending on the state and target species.

All the estimated theoretical curves in these figures will be discussed later.

In order to extract RTEA cross sections for each state, all the dominant contributions to the formation of each state, which is illustrated in Fig. 52, should be considered as follows: Suppose that the Auger electron count, Z , measured for one of the Auger states can be expressed as;

$$Z = N_0 F_g n l \left[\frac{d\sigma}{d\Omega'} \right]_g \Delta\Omega' \eta + N_0 F_m n l \left[\frac{d\sigma}{d\Omega'} \right]_m \Delta\Omega' \eta, \quad (83)$$

where F_m and F_g are the metastable and ground-state beam fraction, respectively, and $F_m + F_g = 1$. $(d\sigma/d\Omega')_g$ and $(d\sigma/d\Omega')_m$ are the Auger production SDCS due to the metastable and ground-state beam, respectively. Thus Eq. (83) can be expressed as;

$$\frac{d\sigma}{d\Omega'} = F_g \cdot \left[\frac{d\sigma_A}{d\Omega'} \right]_g + F_m \cdot \left[\frac{d\sigma_A}{d\Omega'} \right]_m, \quad (84)$$

where the Auger production SDCS $(d\sigma/d\Omega')$ is given by

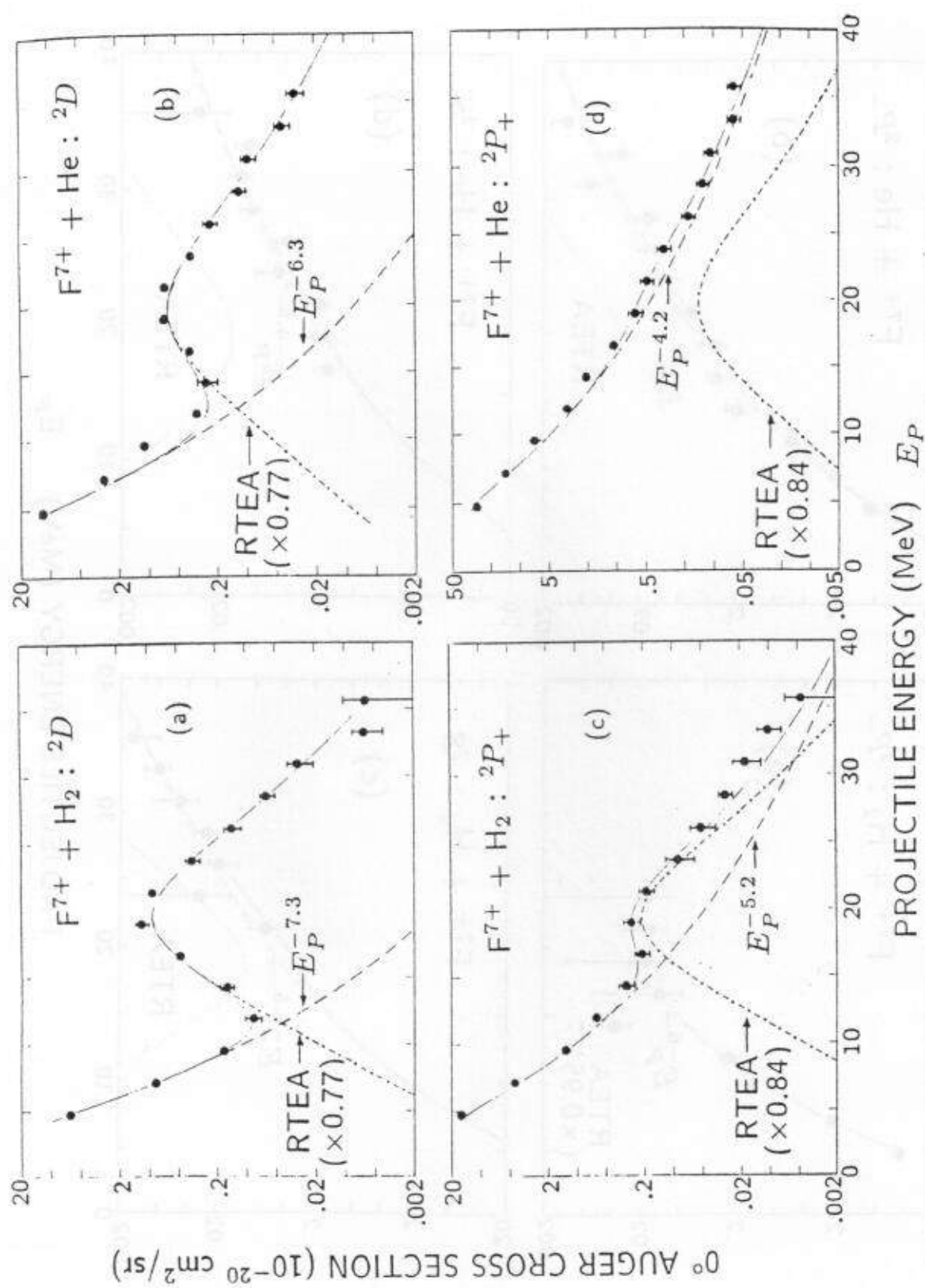
$$\frac{d\sigma}{d\Omega'} = \frac{Z}{N_0 n l \Delta\Omega' \eta}. \quad (85)$$

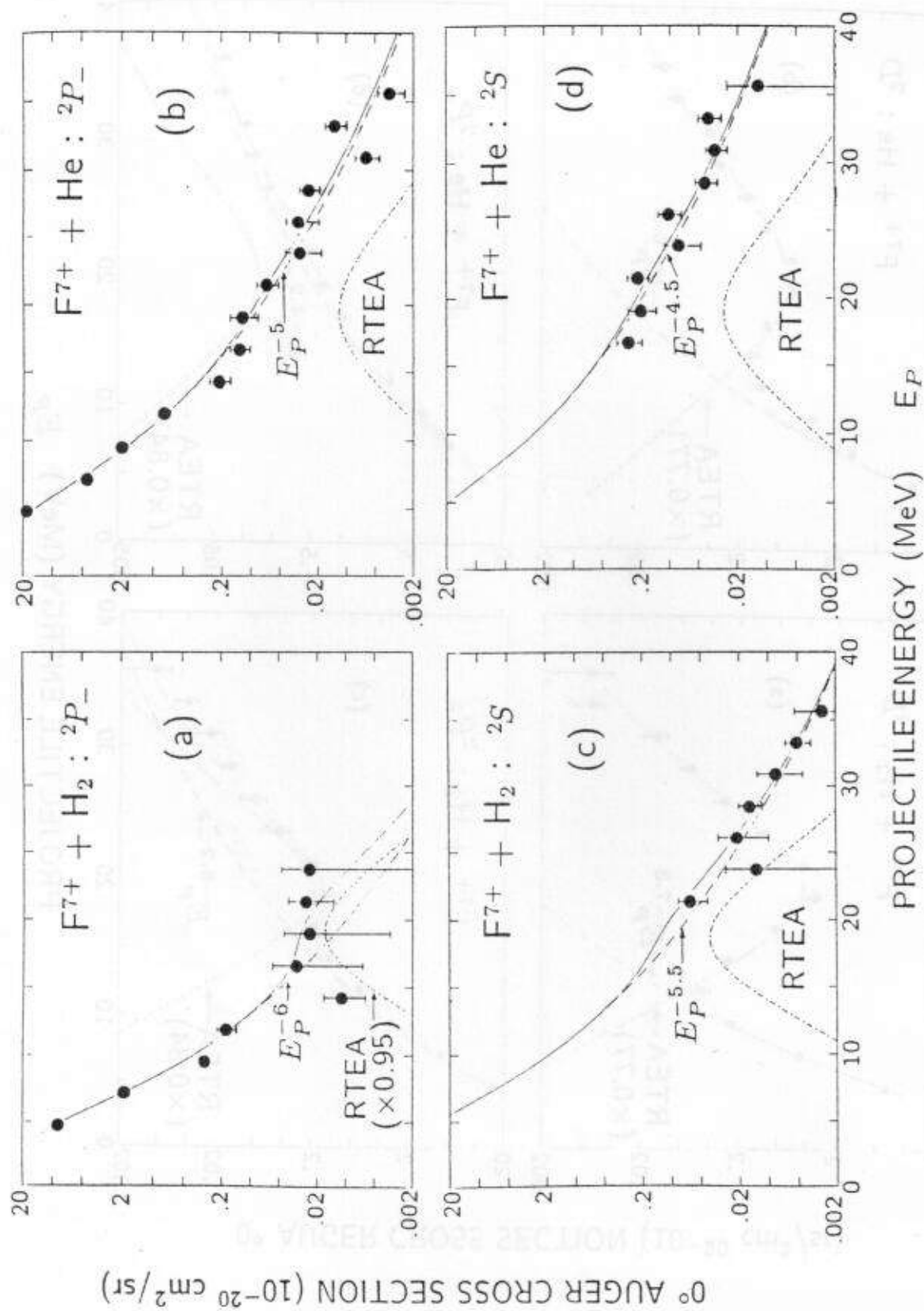
The data presented in Figs. 53 and 54 were evaluated by Eq. (85), and thus these Auger production SDCS are specific for the present F^{7+} beam which consists of the $1s^2$ ground-state and $1s2s^3S$ metastable beam whose fraction was determined previously.^{6,109}

As seen in Fig. 52, the Auger SDCS $(d\sigma/d\Omega')_g$ is produced by RTEA and/or NTE1A, and in same way the Auger SDCS $(d\sigma/d\Omega')_m$ is produced by TA and/or

FIGURE 53. Data: Absolute Auger electron production cross sections from $1s2p^2\ ^2D$ and $1s2s2p^2P_+$ states produced in $F^{7+}(1s^2\ ^1S, 1s2s\ ^3S) + He$ and H_2 collisions versus projectile energy. Solid line in (a) and (b) : sum of RTEA-IA (dot-dashed line) and NTE2A (broken line) contributions. Solid lines in (c) and (d) : sum of RTEA-IA (dot-dashed line) and TA (broken line) contributions (See text).

FIGURE 54. Data: Absolute Auger electron production cross sections from $1s2s2p^2P_-$ and $1s2s^2\ ^2S$ states produced in $F^{7+}(1s^2\ ^1S, 1s2s\ ^3S) + He$ and H_2 collisions versus projectile energy. Solid lines: sum of RTEA-IA (dot-dashed line) and TA and/or NTE2A (broken line) contributions.





NTE2A. The "A" in the acronyms, TA, NTE1A, and NTE2A refers to Auger decay followed by the processes of T (transfer or capture), NTE1, and NTE2, respectively. Therefore, in general, the Auger production SDCS can be given by:

$$\frac{d\sigma}{d\Omega'} = a \frac{d\sigma_{RTEA}}{d\Omega'} + b \frac{d\sigma_{NTE1A}}{d\Omega'} + c \frac{d\sigma_{NTE2A}}{d\Omega'} + d \frac{d\sigma_{TA}}{d\Omega'}, \quad (86)$$

where coefficients, a , b , c , and d are either F_g , F_m , or 0 depending on the state production mechanism. A matrix for these coefficients is shown in Table 18:

TABLE 18

State	$\frac{d\sigma_{RTEA}}{d\Omega'}$	$\frac{d\sigma_{NTE1A}}{d\Omega'}$	$\frac{d\sigma_{NTE2A}}{d\Omega'}$	$\frac{d\sigma_{TA}}{d\Omega'}$
$1s2s^2\ ^2S$	F_g	0	0	F_m
$1s2s2p\ ^4P$	0	0	F_m	F_m
$1s2s2p\ ^2P_-$	F_g	F_g	0	F_m
$1s2s2p\ ^2P_+$	F_g	F_g	F_m	F_m
$1s2p^2\ ^4P$	0	0	F_m	0
$1s2p^2\ ^2D$	F_g	F_g	F_m	0
$1s2p^2\ ^2P$	0	F_g	0	0
$1s2p^2\ ^2S$	F_g	F_g	F_m	0

Before these RTEA cross sections are analyzed, the $1s2s2p^4P$ state is studied first. Shown in Fig. 55 are $1s2s2p^4P$ state production cross sections from the metastable beam component. These cross sections were evaluated by Eq. (86) and Table 18 as follows:

$$\sigma_{4P}^{state} = \left(\frac{d\sigma_T}{d\Omega'} + \frac{d\sigma_{NTE2}}{d\Omega'} \right) \cdot 4\pi = \frac{1}{F_m} \cdot \frac{1}{\xi} \cdot 4\pi \cdot \left(\frac{d\sigma}{d\Omega'} \right)_{4P}^{Auger}, \quad (87)$$

where ξ is the J -averaged Auger yield and $(d\sigma/d\Omega)_{4P}^{Auger}$ is the Auger production SDCS measured in the present work. The total cross sections were obtained by assuming isotropic emission of the Auger electrons from this state. $E_P^{-(4.4 \pm 0.3)}$ and $E_P^{-(5.4 \pm 0.3)}$ dependences of the $1s2s2p^4P$ state production are observed for He and H₂ targets, respectively. The measured E_P dependences were compared to an empirical scaling rule^{78,79} and found to be in fair agreement, even though the scaling rule is for total capture cross sections. In Fig. 55 the results⁶ obtained by high-resolution x-ray spectroscopy at $\theta_{Lab}=90^\circ$ with respect to the beam direction are also given showing a very good agreement between the two independent measurements.

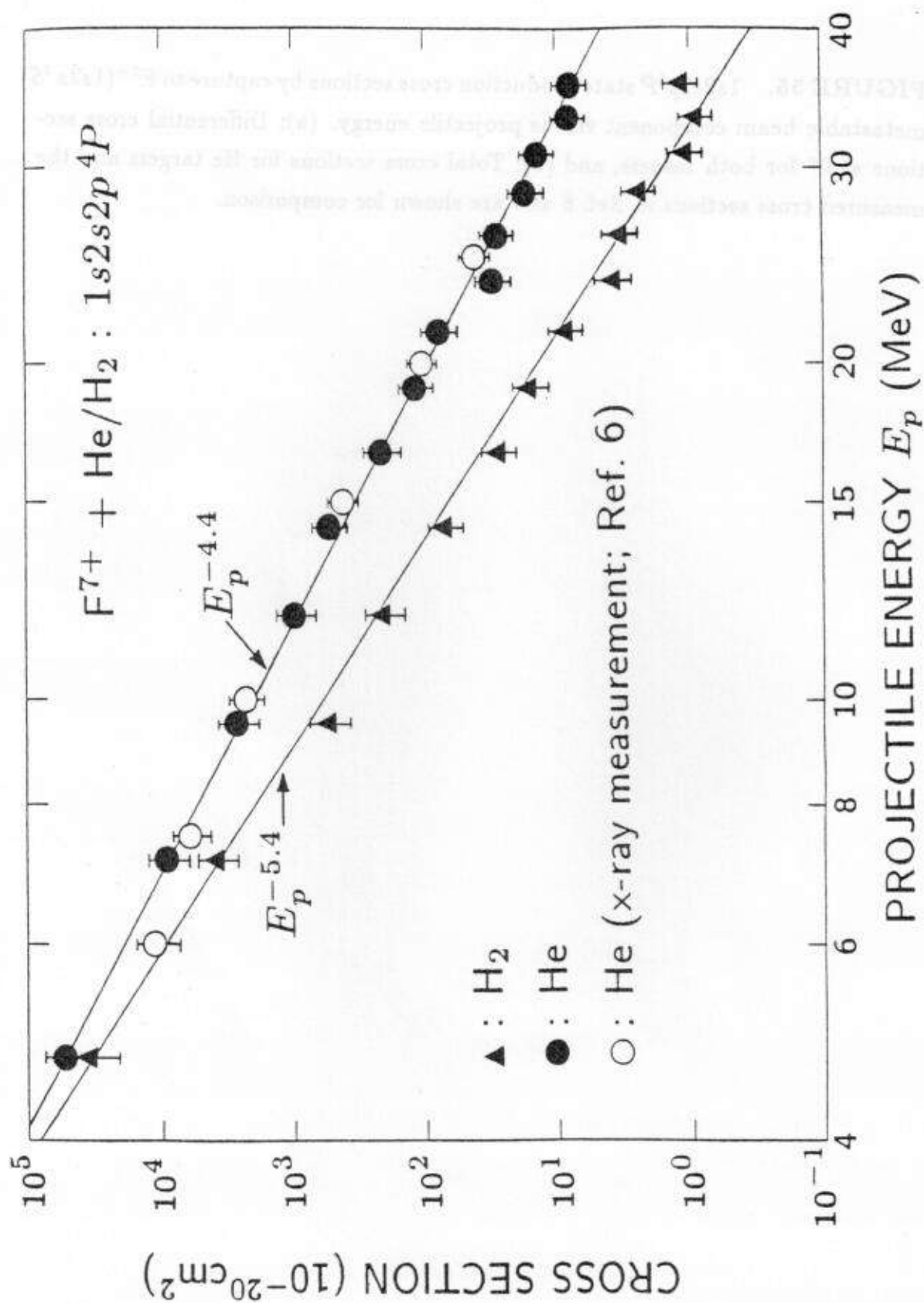
Now the 2D and $^2P_+$ states, which show strong RTE signatures, are studied in detail. Using Eq. (86) and Table 18, the Auger production SDCS can be written as follows: (i). For the 2D state ;

$$\frac{d\sigma_A^D}{d\Omega'} = F_g \cdot \left(\frac{d\sigma_{RTEA}^D}{d\Omega'} + \frac{d\sigma_{NTE1A}^D}{d\Omega'} \right) + F_m \cdot \frac{d\sigma_{NTE2A}^D}{d\Omega'}, \quad (88)$$

where the superscript D refers to the 2D state. (ii). For the $^2P_+$ state;

$$\frac{d\sigma_A^P}{d\Omega'} = F_g \cdot \left(\frac{d\sigma_{RTEA}^P}{d\Omega'} + \frac{d\sigma_{NTE1A}^P}{d\Omega'} \right) + F_m \cdot \left(\frac{d\sigma_{NTE2A}^P}{d\Omega'} + \frac{d\sigma_{TA}^P}{d\Omega'} \right), \quad (89)$$

where σ_{TA} refers to the Auger production cross section due to electron transfer (capture) to the metastable beam component leading to the $^2P_+$ state, [i.e., electron transfer followed by Auger emission (TA)], and the superscript P refers to the



$^2P_+$ state. All the contributing channels to the Auger production, RTEA, NTE1A, NTE2A, and TA are discussed and distinguished from each other as follows:

In the NTE1 and NTE2 processes, $1s \rightarrow 2p$ and $2s \rightarrow 2p$ excitations are involved, respectively. Since the $2s \rightarrow 2p$ excitation cross section is much larger than the $1s \rightarrow 2p$ case, only the small NTE1A contributes to the 2D and 2P Auger SDCS in Eqs. (88) and (89). Furthermore, in the case of a H_2 target, NTE1A cross sections were found to be at most a few % of the maximum RTEA cross section in the RTEA and NTEA measurements for $F^{5+} 1s2s2p^2 \ ^3D$ production in $F^{6+}(1s^22s) + H_2$ collisions (see the previous section). Therefore, practically no NTE1 contributes to the 2D state formation with a H_2 target.

Neglecting the NTE1A contribution, we distinguished and extracted both the RTEA and NTE2A contributions to 2D Auger production in Eq. (88). Here σ_{NTE2A}^D was taken to be proportional to $E_P^{-7.25}$ for H_2 and $E_P^{-6.25}$ for a He target. These E_P dependences appear to be reasonable, when one considers that NTE is qualitatively proportional to the product of the excitation ($2s \rightarrow 2p$ here) and single-capture cross sections. The sum of RTEA and NTE2A contributions is fitted to the data and shown as solid lines in Fig. 53. In the case of a He target, a small NTE1A contribution is observed, but it does not affect extraction of the 2D RTEA contribution. A negligible NTE2A contribution was found to overlap with RTEA cross sections around the RTE peak and higher beam energies for both He and H_2 targets. From the extracted 2D RTEA contribution [see dot-dashed lines in Fig. 53-(a) and -(b)] and using the relationship between σ_{RTEA} and Ω_{RES} [see Eq. (79)], $\Omega_{RES}[^2D]$ was found to be $(35 \pm 2) \times 10^{-19} \text{ cm}^2 \text{ eV}$ for both H_2 and He targets.

In the extraction of the RTEA contribution for $^2P_+$ Auger production, another contribution to the 2P Auger SDCS, which comes from the TA process, must be

accounted for as shown in Eq. (89). Since the TA contribution is dominant for the production of the $^2P_+$ Auger electrons with He targets, as seen in Fig. 53-(d), no appreciable RTE signature is observed. However, in the case of a H_2 target, a significant RTE signature is present [see Fig. 53-(c)]. This is expected when one considers that the $2p$ capture cross section with H_2 is much smaller than that with a He target for higher projectile energies, and that the width and peak of the H_2 Compton profile are about 1.5 times narrower and higher than those of the He Compton profile.

For a H_2 target, the NTE2A contribution is assumed to be much smaller than the TA contribution especially around the RTE peak. Therefore, neglecting both NTE1A and NTE2A contributions (NTE1A contribution was found to be negligible with H_2 target as discussed above) and applying the same $E_p^{-5.5}$ dependence of the TA contribution for $^2P_+$ Auger production as was observed in the 4P state production [see Fig. 55-(a)], the $^2P_+$ RTEA contribution in Eq. (89) was extracted. This result is shown as a dot-dashed line in Fig. 53-(c), and thus, using Eq. (79), $\Omega_{RES}[^2P_+]$ was determined to be $(14 \pm 2) \times 10^{-19} \text{ cm}^2 \text{ eV}$. With this value of $\Omega_{RES}[^2P_+]$, the RTEA contribution is drawn in the case of a He target as shown in Fig. 53-(d).

Similarly, the Auger SDCS from the $[1s(2s2p)^3P]^2P_-$ state also showed an appreciable RTE signature with a H_2 target as shown in Fig. 54-(a), and Ω_{RES} was extracted to be $(1 \pm .3) \times 10^{-19} \text{ cm}^2 \text{ eV}$. In the case of the $1s2s^2^2S$ state, a theoretical RTEA contribution is given in Fig. 54-(d), and no appreciable RTE signature is observed experimentally.

Finally, we compare our measured Ω_{RES} with the theoretical values calculated by Eq. (78) and tabulated in Table 19. As seen in Table 19, only the $1s2p^2^2\dot{D}$ and $[1s(2s2p)^1P]^2P_+$ states have strong RES strengths. This is consistent with

TABLE 19

Calculated and experimental resonance excitation-scattering (RES) strengths (in units of $10^{-19} \text{ cm}^2 \text{ eV}$) for the production of all $F^{6+}[1s2l2l']$ intermediate states. The initial and final states are $1s^2$ states. E_A and E_A^{expt} are theoretical (Refs. 107 and 111) and measured (in this work) Auger energies. Γ_A and ξ are Auger rates ($10^{13}/\text{sec}$) and Auger yields, respectively. Calculated radiationless capture (RC) strengths^{9,13}, related by $\Omega_{RC} \equiv \Omega_{RES}/\xi$, are also listed.

State	E_A	E_A^{expt}	Γ_A	ξ	Ω_{RC}	Ω_{RES}	Ω_{RES}^{expt}
$[1s2s^2]^2S$	525.9	526.1	7.966 ^a	.9971 ^b	7.50	7.48	-
$[1s2s2p]^4P$	529.8	529.8	< .001 ^{c,e}	.8947 ^c	0.00	0.00	-
$[1s(2s2p)^3P]^2P_-$	540.3	540.1	0.579 ^{a,f}	.618 ^{b,g}	1.59	1.10	$1. \pm .3$
$[1s(2s2p)^1P]^2P_+$	545.6	545.2	6.184 ^{a,f}	.9896 ^b	16.8	16.7	14 ± 2
$[1s(2p^2)^3P]^4P$	544.9	-	$\sim .001^d$.9751 ^b	0.01	0.01	-
$[1s(2p^2)^1D]^2D$	551.1	551.2	10.13 ^a	.9785 ^b	45.5	44.5	35 ± 2
$[1s(2p^2)^3P]^2P$	553.1	-	.0085 ^b	.0128 ^b	0.02	0.00	-
$[1s(2p^2)^1S]^2S$	561.2	-	1.23 ^b	.8574 ^b	1.09	0.93	-

Quoted experimental error of Ω_{RES}^{expt} is only relative. Absolute error $\sim 15\%$.

^aRef. 110.

^bAuger rates and yields were evaluated from the values of the life times τ and fluorescence yields ω given in Ref. 89, i.e, $\xi = 1 - \omega$ and $\Gamma_A = \xi/\tau$.

^cRef. 90; ^dRef. 111.

^eAuger rate of $[1s2s2p]^4P$ is about 10^{-5} of $[1s(2s2p)^1P]^2P$ Auger rate (see Ref. 90).

^fAuger rate in Ref. 90 is about 30% larger than this value in Ref. 110.

^gAuger yield in Ref. 90 is about 10% larger than this value in Ref. 89.

VII. ELECTRON-ELECTRON EXCITATION AND IONIZATION

In this chapter, the experimental results of two other kinds of the dynamic electron-electron interactions are discussed. These are electron-electron excitation (eeE) and electron-electron ionization (eeI); the excitation or ionization of the projectile $1s$ electron by a *target electron*.

Considering the extensive efforts required in the experimental studies of electron impact excitation (eIE) or electron impact ionization (eII), where various types of crossed-beam or merged-beam arrangements have been applied,¹¹³ the present studies in fast ion-atom collisions could possibly provide an alternative route for the studies of ion-electron collisions. In particular, such fast ion-atom excitation and ionization could provide presently unavailable information about inner-shell eIE and eII.

A. Electron-Electron Excitation

In energetic ion-atom collisions projectile inner-shell excitation is usually attributed to the Coulomb interaction between the target *nucleus* and the projectile electrons.¹¹³ The projectile energy at threshold for such a direct electron-*nucleus* excitation (enE), K_0^{enE} , is equal to the required electron excitation threshold energy ΔE^{th} . The excitation cross section, σ_{enE} , is expected to scale as $Z_T'^2$, where Z_T' is the effective target nuclear charge,¹¹⁴ and reaches a maximum value at projectile velocities near the velocity of the excited electron. It remains rather constant or decreases very slowly upon further increase of the projectile energy.^{6,114-6}

Projectile inner-shell excitation also can be attributed to the Coulomb interaction between the target *electrons* and the projectile electrons.^{114,117-20} As seen from the projectile frame, the target electrons are impinging on the projectile. For free electrons such an excitation process is known as electron-impact excitation

(eIE). For bound electrons, as in the ion-atom collisions considered here, we refer to this process as electron-electron excitation (eeE). The projectile energy at threshold for eeE is given by:

$$K_0^{eeE} = \frac{M}{m} \Delta E^{th}, \quad (90)$$

where $\frac{M}{m}$ is the ratio of the projectile to electron mass. The cross section, σ_{eeE} , is smaller¹¹⁵ than σ_{enE} by a factor of $1/Z_T'^2$, and is expected to exhibit the sharp threshold behavior of the underlying eIE process. The observed threshold behavior of σ_{eeE} , will be partially washed-out by the target electron's orbital velocity distribution.

By detecting the emitted stabilizing x-rays^{6,115-7} or Auger electrons¹²⁰ with high resolution, information can be gained about the production of these excited projectile states. To date, no experiment has been able to distinguish eeE from enE, although the effects of the target electrons have been included in calculations in the form of an overall screening or antiscreening¹²⁰⁻² of the target nucleus charge.

In this section, I present measurements in which we clearly observe the eeE process. These measurements consist of the observation of projectile $1s \rightarrow 2p$ excitation in energetic 0.25-2 MeV/u collisions of Li-like ($1s^2 2s$) O^{5+} and F^{6+} ions with H_2 and He targets. This was done by taking the state-resolved *KLL* Auger spectra which were shown in Figs. 47 and 48. By using such low- Z targets enE is minimized. For these ions, the $1s \rightarrow 2p$ eIE threshold energy corresponds to an equivalent projectile energy of about 16.3 MeV for O^{5+} and 25.0 MeV for F^{6+} , respectively. These threshold energies were evaluated by using Eq. (91) below and ΔE^{th} which was estimated as follows;

$$\Delta E_{1s \rightarrow 2p}^{th} = E_A(1s2s2p - 1s^2) + E_I(1s^2 2s), \quad (91)$$

where $E_A(1s2s2p-1s^2)$ is the average Auger energy for the $1s2s2p$ to $1s^2$ transition (see Table 19) and $E_I(1s^22s)$ is the ionization potential¹²³ (for the $2s$ electron).

As seen in the 0° high resolution (state-resolved) *KLL* Auger electron spectra of Figs. 47 and 48, four $1s \rightarrow 2l$ excitations are identified. Those are for the $[1s2s^2]^2S$, $[1s(2s2p)^3P]^2P_-$, $[1s(2s2p)^1P]^2P_+$, and $[1s2s2p]^4P$ states. First, I will discuss the production of the 4P state for which the eeE process is best exemplified.

A-1. $1s2s2p^4P$ State Produced by eeE

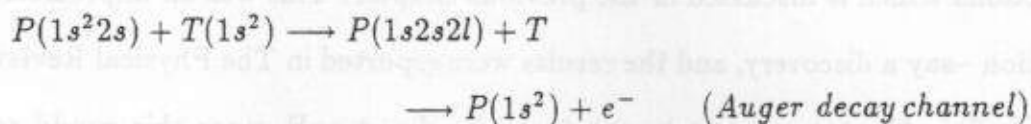
The most surprising observation in this experiment is that a strong $1s2s2p^4P$ state is produced. Motivation of the experiment was the measurement of the RTEA cross sections which is discussed in the previous chapter. This was an unpredicted observation—say a discovery, and the results were reported in *The Physical Review Letters*.¹² This 4P state cannot be produced by direct enE, since this would require a spin-flipping transition not possible for such low- Z ions. However, $1s \rightarrow 2p$ excitation can proceed to the 4P state through eeE by the exchange¹¹⁸ of the projectile electron with the exciting target electron. Thus, for the production of this state at collision energies above K_0^{eeE} , eeE should be distinguishable from enE.

In the present experiment, the production of the O^{5+} and $F^{6+} (1s2s2p)^4P$ states above ~ 0.75 MeV/u was found to increase sharply with projectile energy, particularly for collisions with an H_2 target. The energy dependence of the threshold-like behavior of the measured cross sections could be described quite well by using calculated cross sections for eIE found in the literature, folded by the momentum distribution (Compton profile) of the target electrons. By accounting for the target electrons' "quasifree" nature in this way, we relate eIE, a free-electron-ion collision process to that of eeE, an ion-atom collision process. This is analogous to the impulse approximation treatment of Resonance Transfer

Excitation (RTE), relating dielectronic recombination, another free-electron-ion collision process, to that of RTE occurring in ion-atom collisions.

These 4P results constitute a direct measurement of $1s \rightarrow 2p$ excitation of an ion by an electron, information presently unavailable by existing electron-ion experiments.¹¹⁵ Furthermore, eeE is a part of the more complex 2eTE process recently reported⁹⁸ in energetic $F^{8+} + H_2$ collisions. (More recently the 2eTE data were reevaluated¹⁰² and the 2eTE contribution was estimated to be much smaller than the original⁹⁸ finding.)

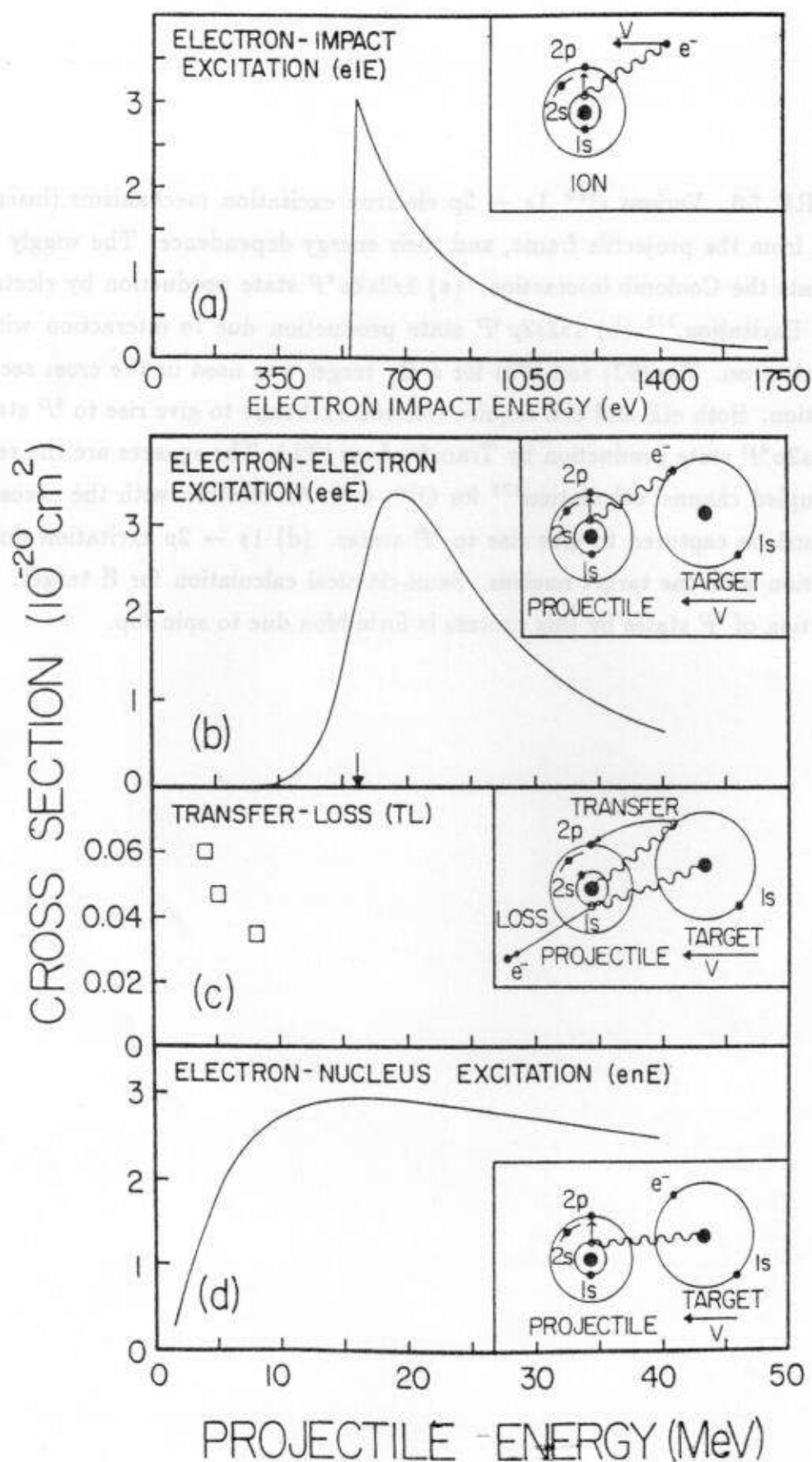
Doubly-excited Li-like $O^{5+}(1s2s2l)$ and $F^{6+}(1s2s2l)$ projectile (P) states were formed in collision with a target T (He or H_2),



The $(1s2s2l)$ autoionizing states can decay by ejecting an Auger electron which was detected with high resolution at 0° with respect to the beam direction. The resulting target state was not determined.

The most likely $1s \rightarrow 2p$ excitation mechanisms resulting in the production of a $1s2s2p$ configuration are shown schematically in Fig. 56, together with their expected energy dependence. In the production of the 4P state, enE [Fig. 56(d)] cannot contribute, since it is forbidden by spin-flip considerations.¹¹⁹ In the case of eeE [Fig. 56(b)], the 4P state can be formed if electron exchange¹¹⁷ is included. Finally, in the case of Transfer-Loss (TL) [Fig. 56(c)], the production of the 4P state requires¹¹⁹ the transfer of a target electron to the $2p$ projectile orbital with the simultaneous loss of a projectile $1s$ electron, resulting in a net $1s \rightarrow 2p$ excitation of the projectile. TL is expected to be less important at high velocities due to the rapid decrease of the capture cross section with increasing projectile energy.

FIGURE 56 Various $O^{5+} 1s \rightarrow 2p$ electron excitation mechanisms (inserts), as seen from the projectile frame, and their energy dependence. The wiggly line represents the Coulomb interaction. (a) $1s2s2p^4P$ state production by electron-impact Excitation.¹²⁵ (b) $1s2s2p^4P$ state production due to interaction with a target electron. Eqs.(92) and (93) for a H_2 target was used in the cross section calculation. Both eIE and eeE require electron exchange to give rise to 4P states. (c) $1s2s2p^4P$ state production by Transfer-Loss (TL). The squares are the result of a coupled channel calculation¹²⁴ for $O^{5+} + H$. An electron with the necessary spin must be captured to give rise to 4P states. (d) $1s \rightarrow 2p$ excitation due to interaction with the target nucleus. Semi-classical calculation for H target. The production of 4P states by this process is forbidden due to spin-flip.

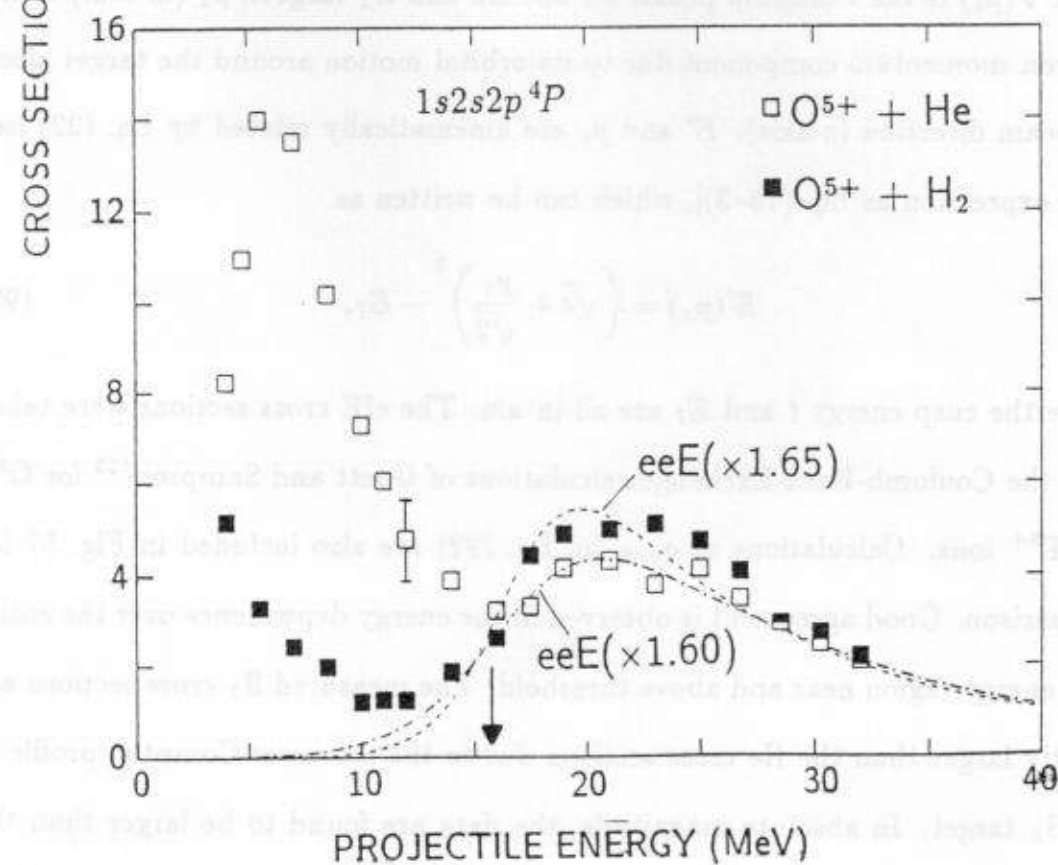
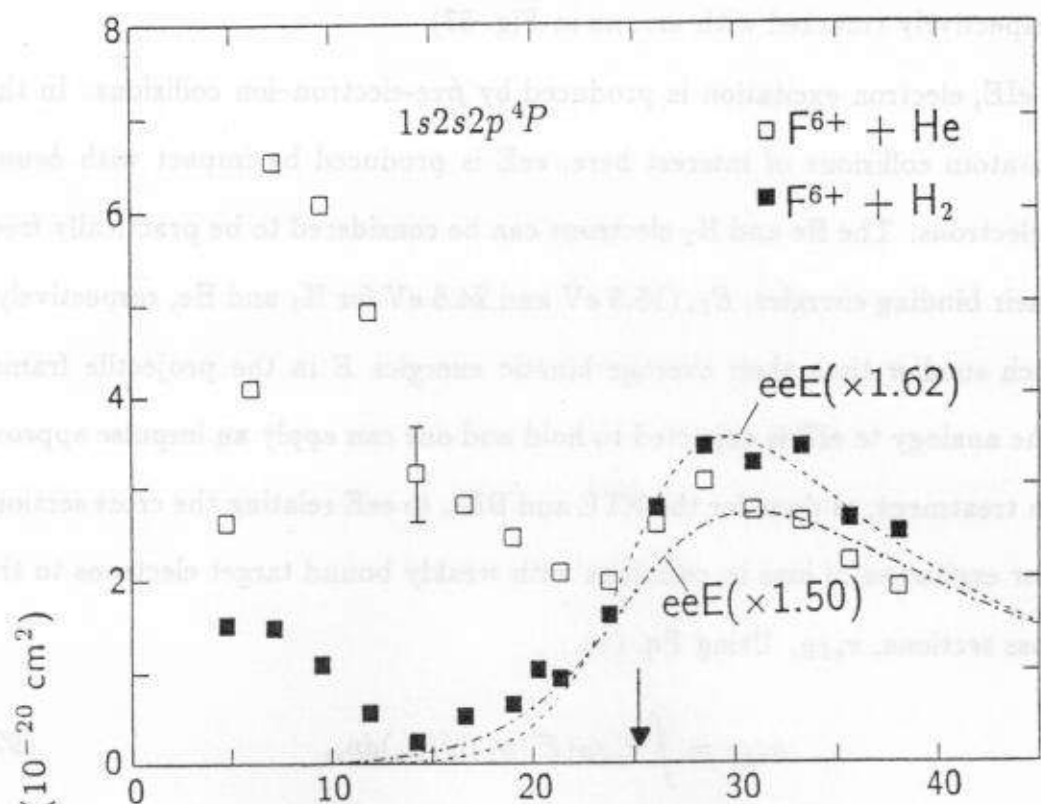


Preliminary calculations¹²⁴ [squares in fig. 56(c)] have shown TL cross sections to be about two orders of magnitude smaller than the measured 4P cross sections. Thus, only eeE remains a likely contributor of the 4P state at energies near and above the threshold projectile energy. Included for comparison [Fig. 56(a)] is the electron-impact excitation process and its dependence on the energy of the impinging free electron.

The 4P state production cross sections are displayed as a function of projectile energy in Fig. 57. The normalized electron yields were converted to production cross sections assuming the unresolved J -sublevels of the 4P state to be statistically populated and using the theoretical Auger yields ξ . In addition, the 4P_J states are metastable, therefore the measured yield depends on their lifetimes. The theoretical lifetimes and Auger yields are listed in Table 5. The lifetime correction has been performed by calculating the effective solid angles in Chapter 5, and the results were tabulated in Tables 6–13 for each collision system. The corrections for this effect were expected to result in an overall change of the measured yields by a factor of at most ~ 0.8 – 1.0 depending on projectile velocity. (See the variation of the solid angle correction factor F_{Ω}^{4P} in Tables 6–13. For a few low projectile energies, this factor was calculated to be quite large due to the projectile charge neutralization effect.) However, as discussed in details in Chapter V section B, electrons produced between the gas cell and the spectrometer entrance were found to be more effectively detected than those produced inside the gas cell. Thus this resulted in the correction factor of 0.4 – 0.55 depending upon projectile velocity (see chapter V section B for more details).

Electron-electron excitation (eeE) should become important at projectile energies close to the threshold energy for eIE. The average $1s \rightarrow 2p$ excitation energy $\Delta E_{1s \rightarrow 2p}^{th}$ is 562 eV and 723 eV for O^{5+} and F^{6+} , respectively, corresponding

FIGURE 57. Data: Cross sections for the production of $1s2s2p^4P$ states by $1s \rightarrow 2p$ projectile excitation in collisions of $F^{6+}(1s^22s)$ and $O^{5+}(1s^22s)$ projectiles with He and H_2 targets versus projectile energy. Calculation: electron-electron excitation (eeE) cross sections using $1s2s2p^4P$ theoretical electron-impact excitation cross sections¹²⁵ folded by the Compton profile of the target [see Eqs. (92) and (93) in text]. i) Dashed lines: Calculated eeE for H_2 targets; ii) Dash-dot lines: Calculated eeE for He targets. Arrows (at 16.3 and 25.0 MeV) mark the projectile energy corresponding to the threshold for $1s \rightarrow 2p$ electron-impact excitation.



to a threshold projectile energy K_0^{eeE} equal to 16.4 and 25.0 MeV for O^{5+} and F^{6+} , respectively (marked with arrows in Fig. 57).

In eIE, electron excitation is produced by *free*-electron-ion collisions. In the fast ion-atom collisions of interest here, eeE is produced by impact with *bound* target electrons. The He and H_2 electrons can be considered to be practically free, since their binding energies, E_I , (15.5 eV and 24.6 eV for H_2 and He, respectively) are much smaller than their average kinetic energies E in the projectile frame. Thus the analogy to eIE is expected to hold and one can apply an impulse approximation treatment, as done for the RTE and BEE, to eeE relating the cross section, σ_{eeE} , for excitation of ions in collisions with weakly bound target electrons to the eIE cross sections, σ_{eIE} . Using Eq. (1),

$$\sigma_{eeE} = \int \sigma_{eIE}(E'(p_z))J(p_z)dp_z, \quad (92)$$

where $J(p_z)$ is the Compton profile for the He and H_2 targets, p_z (in a.u.) is the electron momentum component due to its orbital motion around the target along the beam direction (z -axis). E' and p_z are kinematically related by Eq. (22) [see same expression as Eq. (73-3)], which can be written as

$$E'(p_z) = \left(\sqrt{t} + \frac{p_z}{\sqrt{2}} \right)^2 - E_I, \quad (93)$$

where the cusp energy t and E_I are all in a.u. The eIE cross sections were taken from the Coulomb-Born-Exchange calculations of Goett and Sampson¹²⁵ for O^{5+} and F^{6+} ions. Calculations of σ_{eeE} by Eq. (92) are also included in Fig. 57 for comparison. Good agreement is observed in the energy dependence over the entire high energy region near and above threshold. The measured H_2 cross sections are slightly larger than the He cross sections due to the narrower Compton profile of the H_2 target. In absolute magnitude, the data are found to be larger than the

calculation by a factor of ~ 1.6 for the collision systems studied here. Integration over $J(p_z)$ spreads out the underlying sharp threshold of eIE [Fig. 56(a)].

We finally note that a more complicated two-step three-body interaction, in which the projectile is excited by enE followed by the exchange of the excited $2p$ projectile electron with a target electron, could also give rise to the 4P state. We would expect such a two-step enE process to be much less probable than eeE , particularly at high velocities where the overall interaction time is limited. The eeE process (in the production of the 4P state) involves only two electrons in a one-step mechanism, since the electron exchange is included directly in the antisymmetrization of the wavefunctions involved in calculating¹²⁵ σ_{eIE} . This is borne out by our data where at the higher projectile energies our calculations [Eq. (92)] for eeE seem to be in fair agreement with the data. On the other hand, this two-step enE process could be the main contributor at the lower collision energies, where the calculated TL cross sections¹²⁴ [Fig. 56(c)] were found to be much smaller than experiment. A fully correlated calculation of enE with exchange is difficult and has not been reported to date. More theoretical work is needed before the low energy peak in the cross sections can be fully understood.

In conclusion, we have determined excitation cross sections for producing the $(1s2s2p) ^4P$ state in 0.25 - 2 MeV/u collisions of $O^{5+}(1s^22s)$ and $F^{6+}(1s^22s)$ projectiles with He and H_2 targets. At high collision energies above ~ 0.75 MeV/u, the excitation can be attributed to an interaction between the $1s$ projectile electron and a target electron. This process can be related to impact excitation of ions by free electrons on applying an impulse approximation treatment to projectile excitation by weakly bound target electrons. Strong excitation threshold effects were observed, particularly in the case of H_2 targets. The energy dependence was well described by this model. The absolute magnitude of the measured cross

were smaller
 sections was small than theory by a factor of $\sim 0.6-0.8$ depending on the collision system. By relating ion-atom excitation to electron-impact excitation, ion-atom measurements could possibly provide cross sections for inner-shell electron-impact excitation of ions for which there are presently no measurements.

A-2. Electron-Electron Excitation for Other $1s2s2l$ States

Similar eeE effects were also seen, but to a lesser extent due to the competition from enE, for the production of the $(1s2s2p)^2P_+$ state with H_2 targets.¹²⁶ A theoretical CBE-eIE for all four $1s2s2l$ states is shown with a function of the free electron impact energy E_{eI} in Fig. 58, where E_{eI} is related by $E_{eI} = E(p_z = 0)$ with Eq. (93). In other words, the most probable energy of the incoming target electrons in projectile frame, which corresponds to $E(p_z = 0)$, is $t - E_I$ as expected.

In Figs. 59-62, all the measured state production cross sections for all four $1s2s2l$ states for each collision system are presented. The eeE contributions, which were calculated by IA of Eq. (92) using the CBE-eIE results in Fig. 58, are also included in these figures. Above the excitation threshold (see horizontal arrows), a considerable eeE contribution for the $^2P_+$ state and an appreciable eeE contribution for the $^2P_-$ state are shown in the case of H_2 targets. However, in the case of the He targets, the eeE contribution for the $^2P_{\pm}$ states is not seen, probably due to a strong enE.

The enE cross section for the $^2P_+$ and $^2P_-$ state produced by $1s \rightarrow 2p$ was estimated using a scaled PWBA calculation as follows:

$$\sigma_{enE} = n_A \cdot Z_T^2 \cdot \left[\frac{13.6 \cdot \frac{3}{4}}{\Delta E_{th}} \right]^2 \cdot \sigma_{pH}[1s \rightarrow 2p], \quad (94)$$

where n_A is the number of atoms in target particle, Z_T is atomic number of target nucleus, $\sigma_{pH}[1s \rightarrow 2p]$ is the PWBA $1s \rightarrow 2p$ excitation cross section for the H atom by proton impact as a function of proton velocity v_p .¹²⁷ The cross section σ_{enE} of

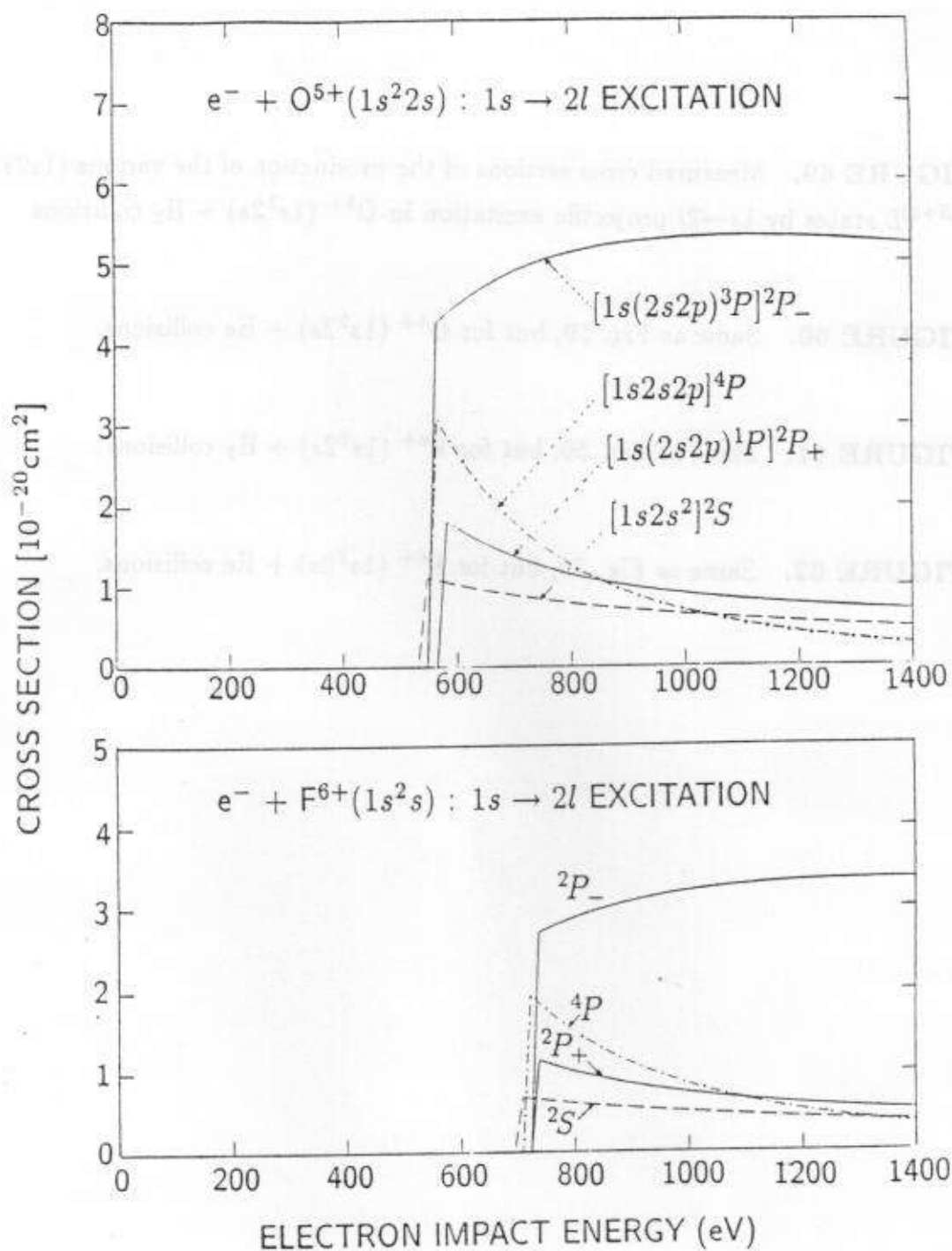


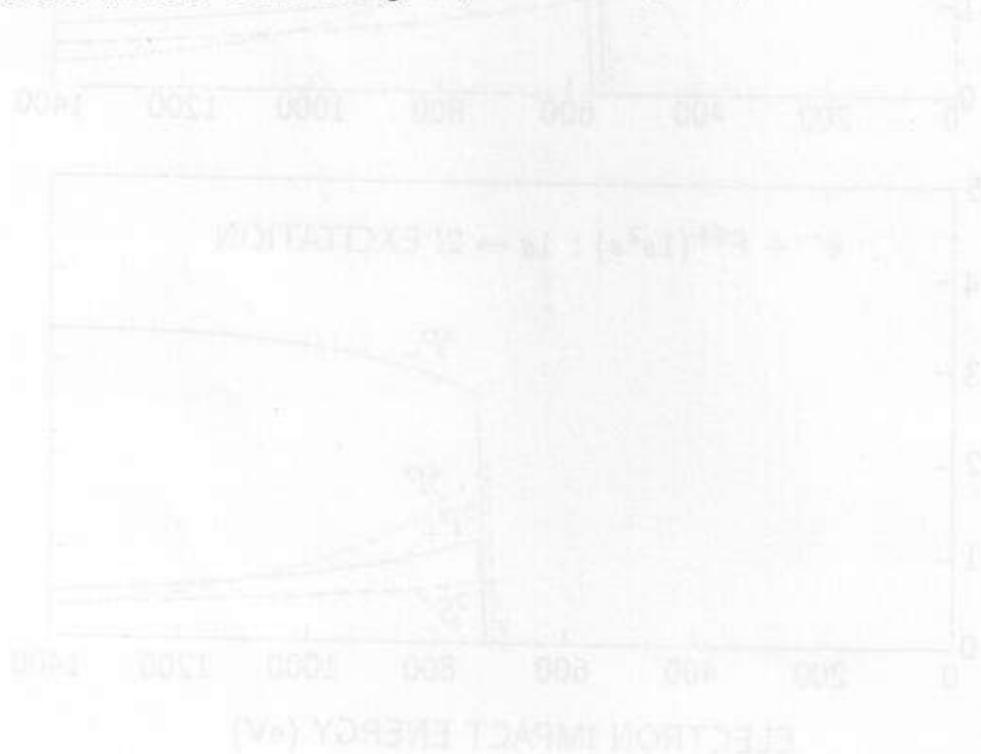
FIGURE 58. Theoretical cross sections of electron impact $1s \rightarrow 2p$ excitation of O^{5+} and F^{6+} ions for the four $1s2s2l$ (^{2S+1}L) states as a function of the electron impact energy.¹²⁵

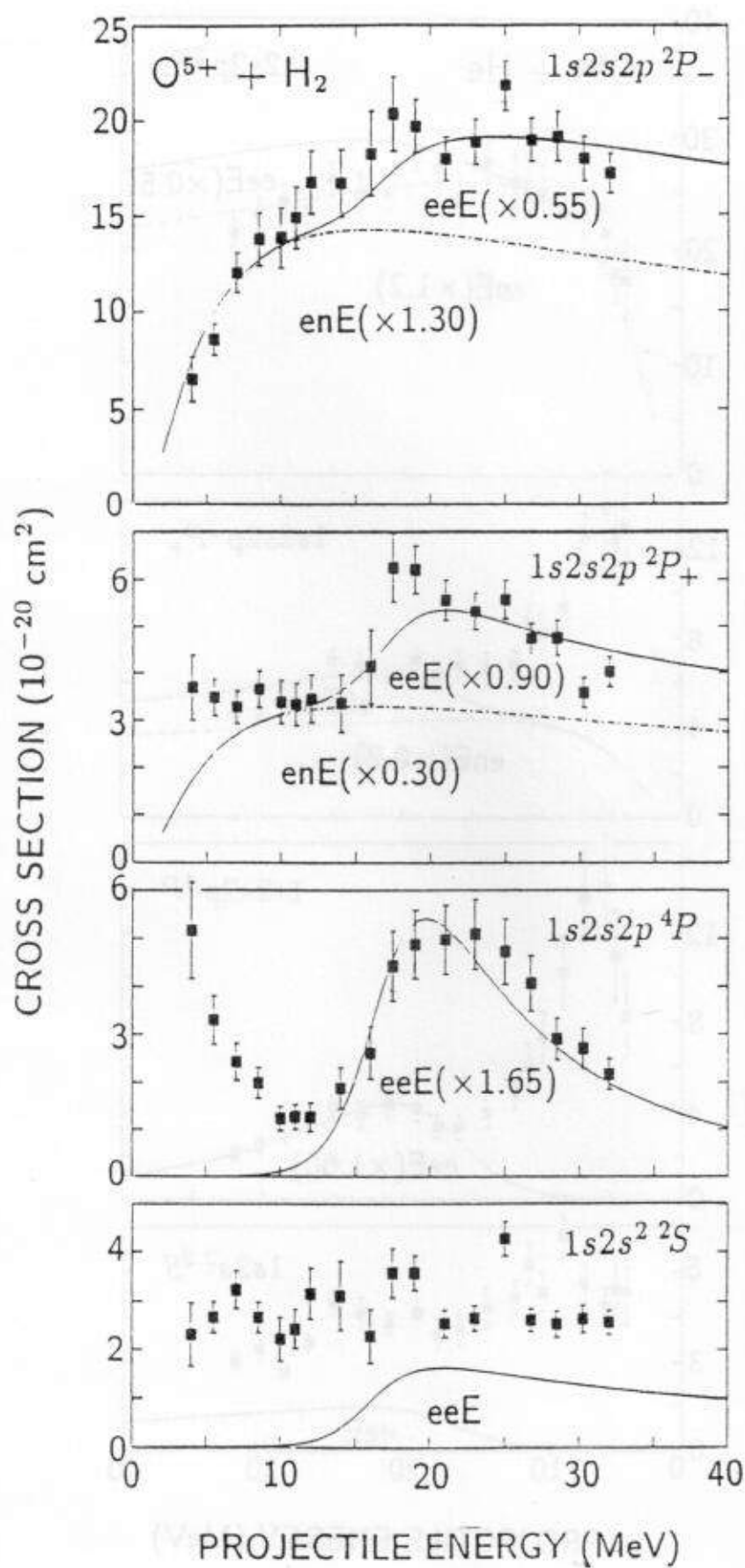
FIGURE 59. Measured cross sections of the production of the various $(1s2s2l)$ $(2S+1)L$ states by $1s \rightarrow 2l$ projectile excitation in $O^{5+} (1s^2 2s) + H_2$ collisions

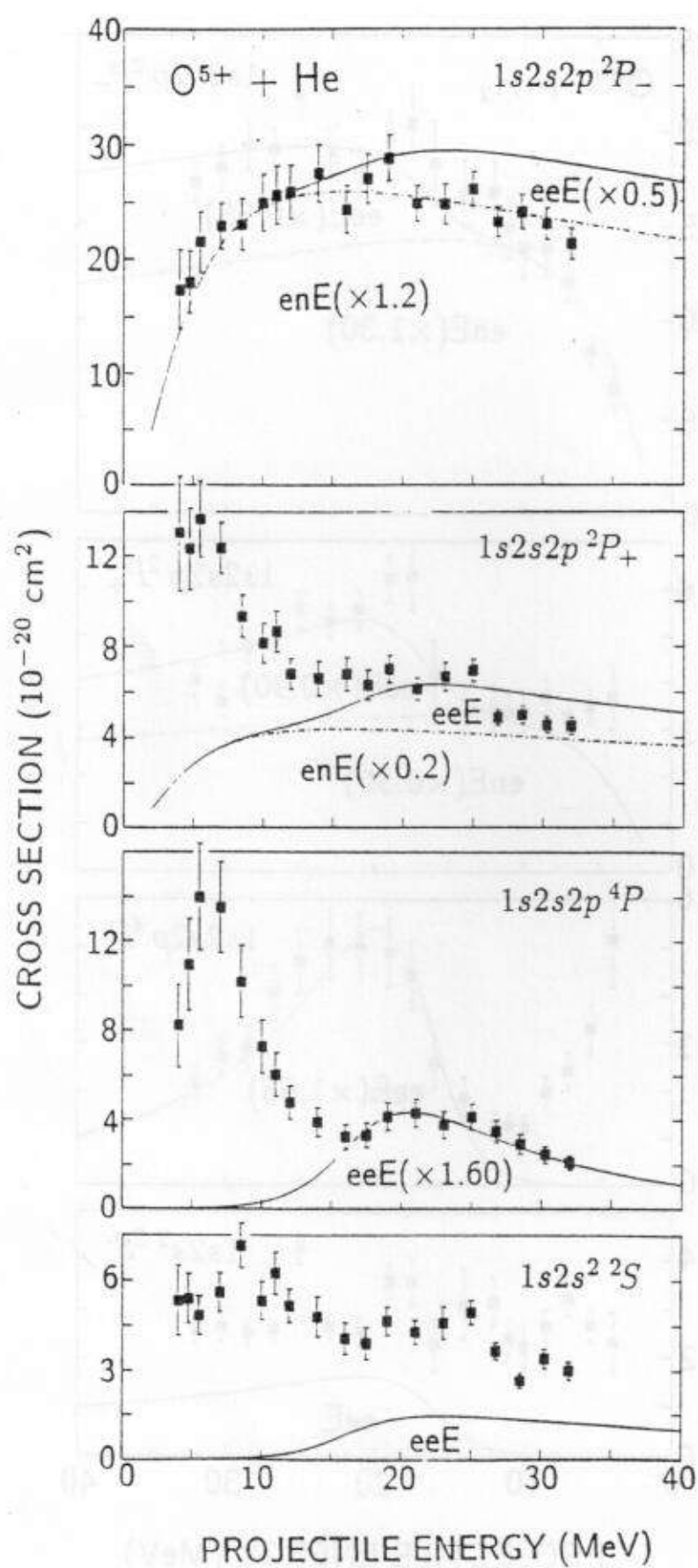
FIGURE 60. Same as Fig. 59, but for $O^{5+} (1s^2 2s) + He$ collisions.

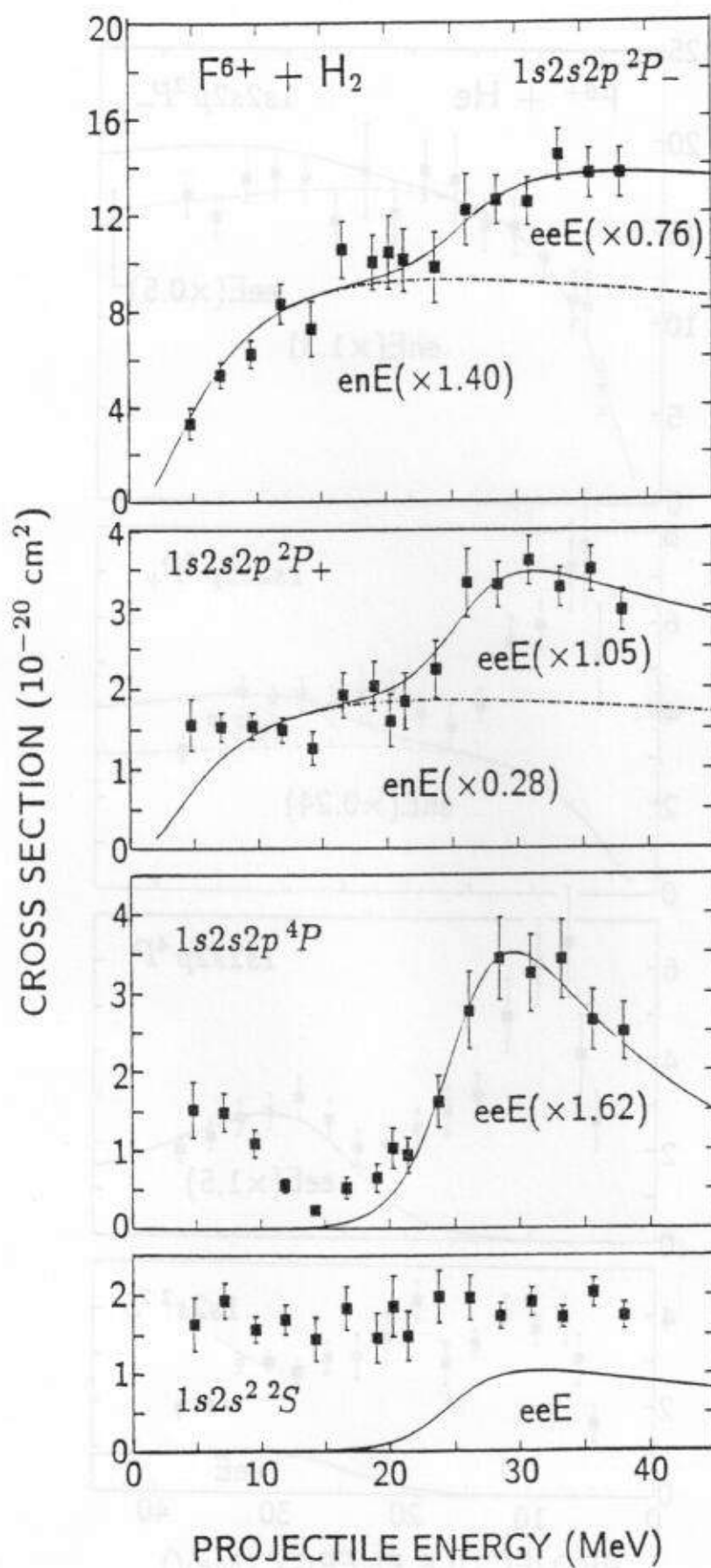
FIGURE 61. Same as Fig. 59, but for $F^{6+} (1s^2 2s) + H_2$ collisions.

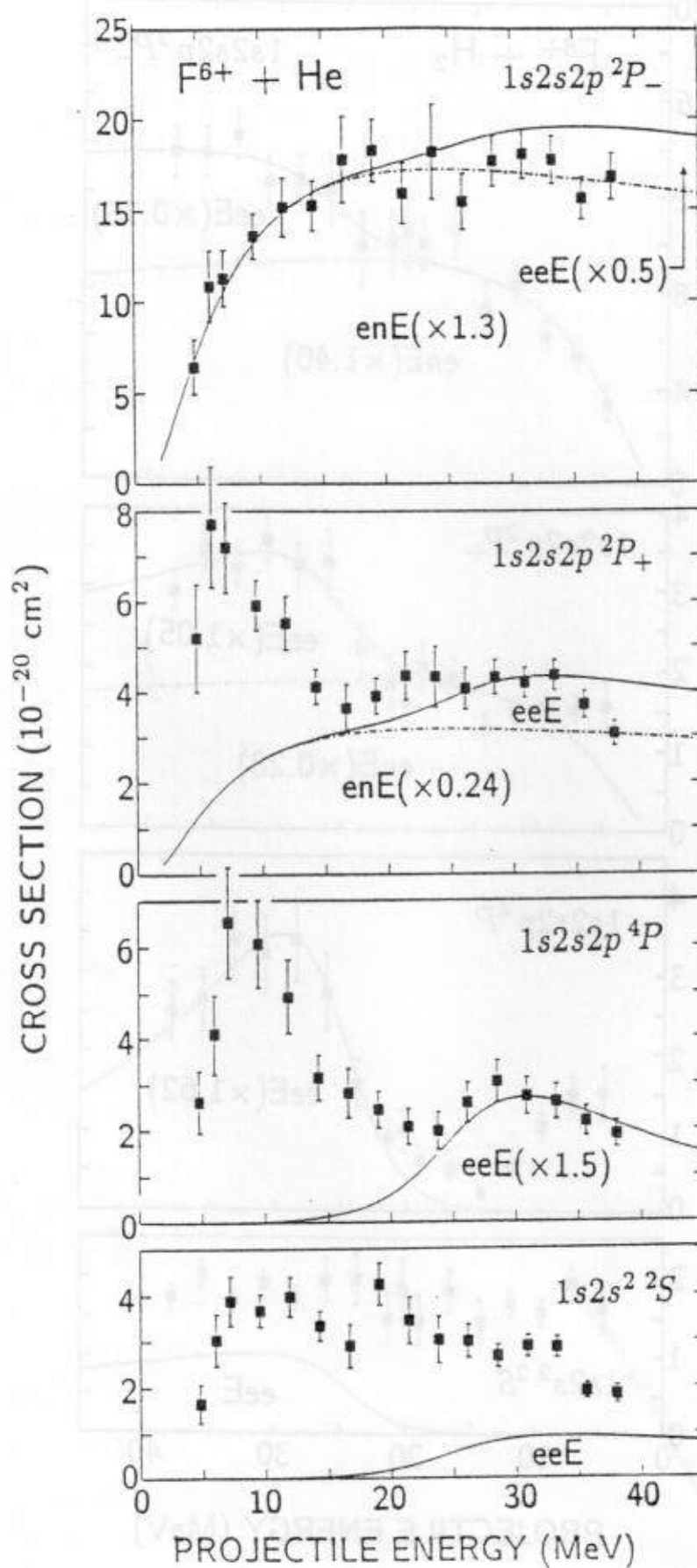
FIGURE 62. Same as Fig. 59, but for $F^{6+} (1s^2 2s) + He$ collisions.











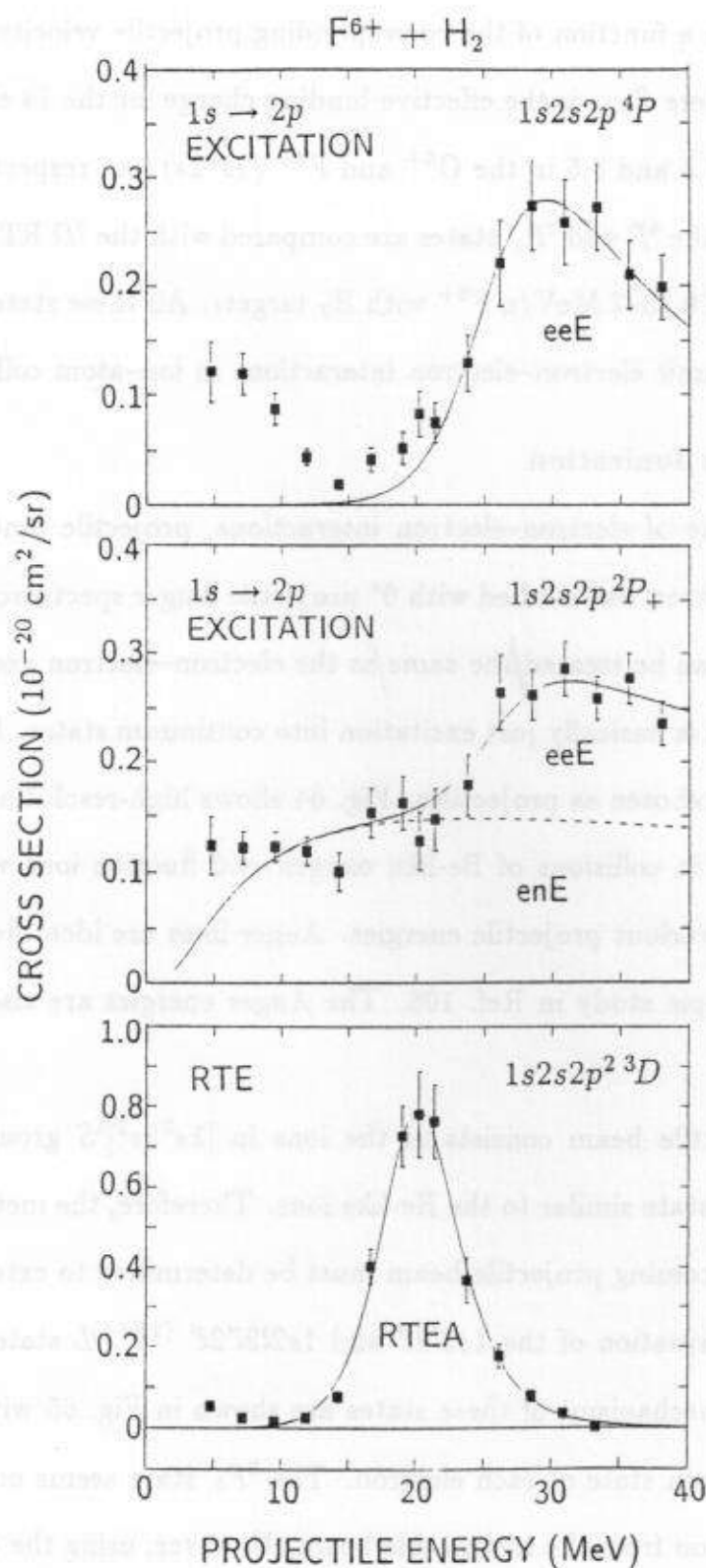


FIGURE 63. Comparison of zero-degree ($d\sigma_{eeE}/d\Omega$) and ($d\sigma_{RTE}/d\Omega$) for collisions of F^{6+} with H_2 targets.

Eq. (94) is now given as a function of the corresponding projectile velocity which is set to be $Z_{eff} \cdot v_p$, where Z_{eff} is the effective binding charge for the 1s electron and is evaluated to be 7.5 and 8.5 in the O^{5+} and F^{6+} ($1s^2 2s$) ion, respectively

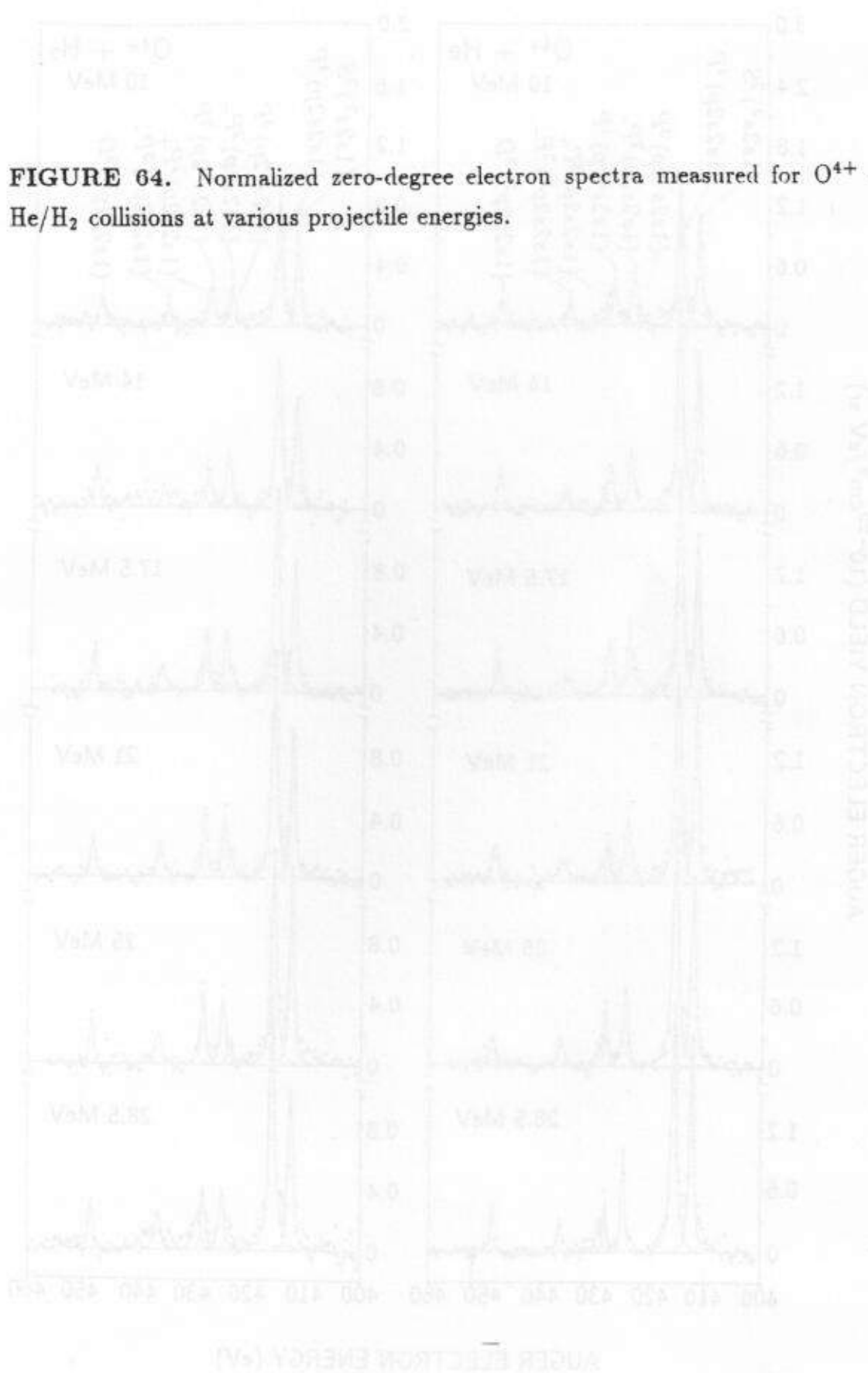
Finally, in Fig. 63, the 4P and $^2P_+$ states are compared with the 3D RTE state produced in collisions of 0.25–2 MeV/u F^{6+} with H_2 targets. All these states show a solid evidence of dynamic electron–electron interactions in ion–atom collisions.

B. Electron–Electron Ionization

As another evidence of electron–electron interactions, projectile inner shell ionization by target electron was studied with 0° projectile Auger spectroscopy. In principle, this process can be treated the same as the electron–electron excitation process, since ionization is basically just excitation into continuum states. For this study Be-like ions were chosen as projectiles. Fig. 64 shows high-resolution *KLL* Auger electron spectra in collisions of Be-like oxygen and fluorine ions with He and H_2 targets for the various projectile energies. Auger lines are identified from the previous spectroscopic study in Ref. 108. The Auger energies are also listed in Table 20.

The Be-like projectile beam consists of the ions in $[1s^2 2s^2]^1S$ ground and $[1s^2 2s 2p]^3P$ metastable state similar to the He-like ions. Therefore, the metastable beam fraction in the incoming projectile beam must be determined to extract the cross sections of the formation of the $1s 2l 2l'$ and $1s 2l 2l' 2l'' (^{2S+1}L)$ states. The dominant production mechanisms of these states are shown in Fig. 65 with their energy levels and the spin state of each electron. The $^2P_+$ state seems not to be produced by 1s ionization from the metastable beam. However, using the concept of the fractional parentage for the configuration,¹²⁸ the $^2P_+$ state is allowed to be formed.

FIGURE 64. Normalized zero-degree electron spectra measured for $O^{4+} + He/H_2$ collisions at various projectile energies.



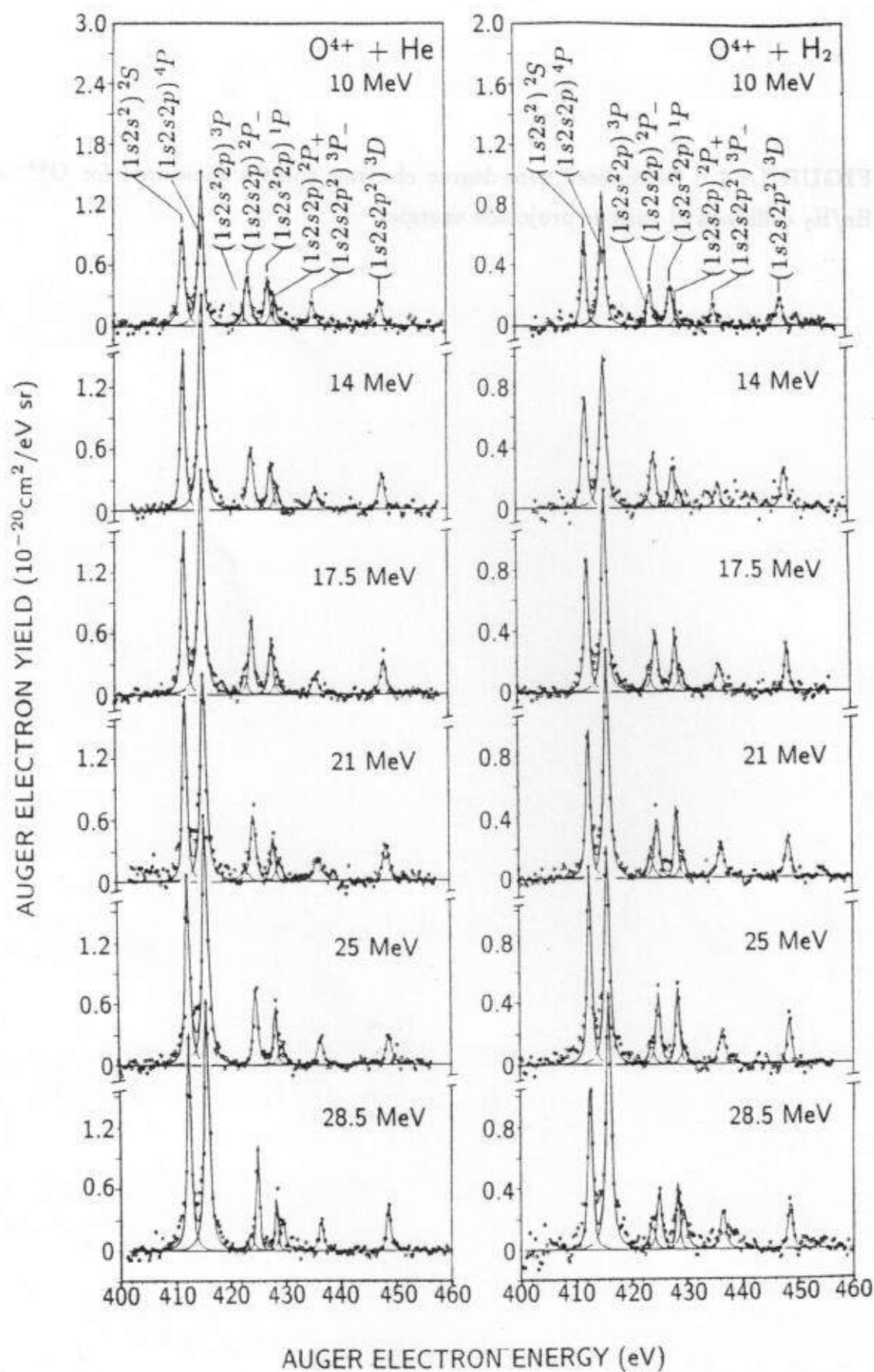


TABLE 20

Theoretical and experimental Auger line energies (in eV) in collisions 10–28.5 MeV O^{4+} ($1s^2 2s^2 {}^1S$ and $1s^2 2s 2p {}^3P$) with H_2 and He targets. Initial states are the 1S ground and 3P metastable states in the incoming beam. Intermediate states are the states collisionally produced. Final states are the deexcited states with Auger emission.

Initial	Intermediate	Final	Theory ^{a)}	Expt ^{b)}	Diff.(eV)
$[1s^2 2s^2] {}^1S$	$[1s 2s^2] {}^2S$	$1s^2$	412.6	412.7	-0.1
$[1s^2 2s 2p] {}^3P$	$[1s 2s 2p] {}^4P$	$1s^2$	416.0	416.0	0.0
$[1s^2 2s^2] {}^1S$	$[1s 2s^2 2p] {}^3P$	$1s^2 2p$	424.2	423.7	0.5
$[1s^2 2s 2p] {}^3P$	$[1s 2s 2p] {}^2P_-$	$1s^2$	425.0	424.9	0.1
$[1s^2 2s^2] {}^1S$	$[1s 2s^2 2p] {}^1P$	$1s^2 2p$	428.5	428.4	0.1
$[1s^2 2s 2p] {}^3P$	$[1s 2s 2p] {}^2P_+$	$1s^2$	429.7	429.5	0.2
$[1s^2 2s 3p] {}^3P$	$[1s 2s 2p^2] {}^3P_-$	$1s^2 2p$	436.4	436.4	0.0
$[1s^2 2s 2p] {}^3P$	$[1s 2s 2p^2] {}^3D$	$1s^2 2s$	448.0	448.2	-0.2

^{a)}Ref. 108

^{b)}Measured ones in this work. Experimental errors about ± 0.2 eV. For electron energy calibration, all the experimental electron energies are determined by aligning the measured strong 4P Auger line energy to the theoretical value. Usually 1–2 eV is needed to shift the measured Auger line energies. The all measured energies are in a good agreement with the measured ones in Ref. 108.

ENERGY (eV)

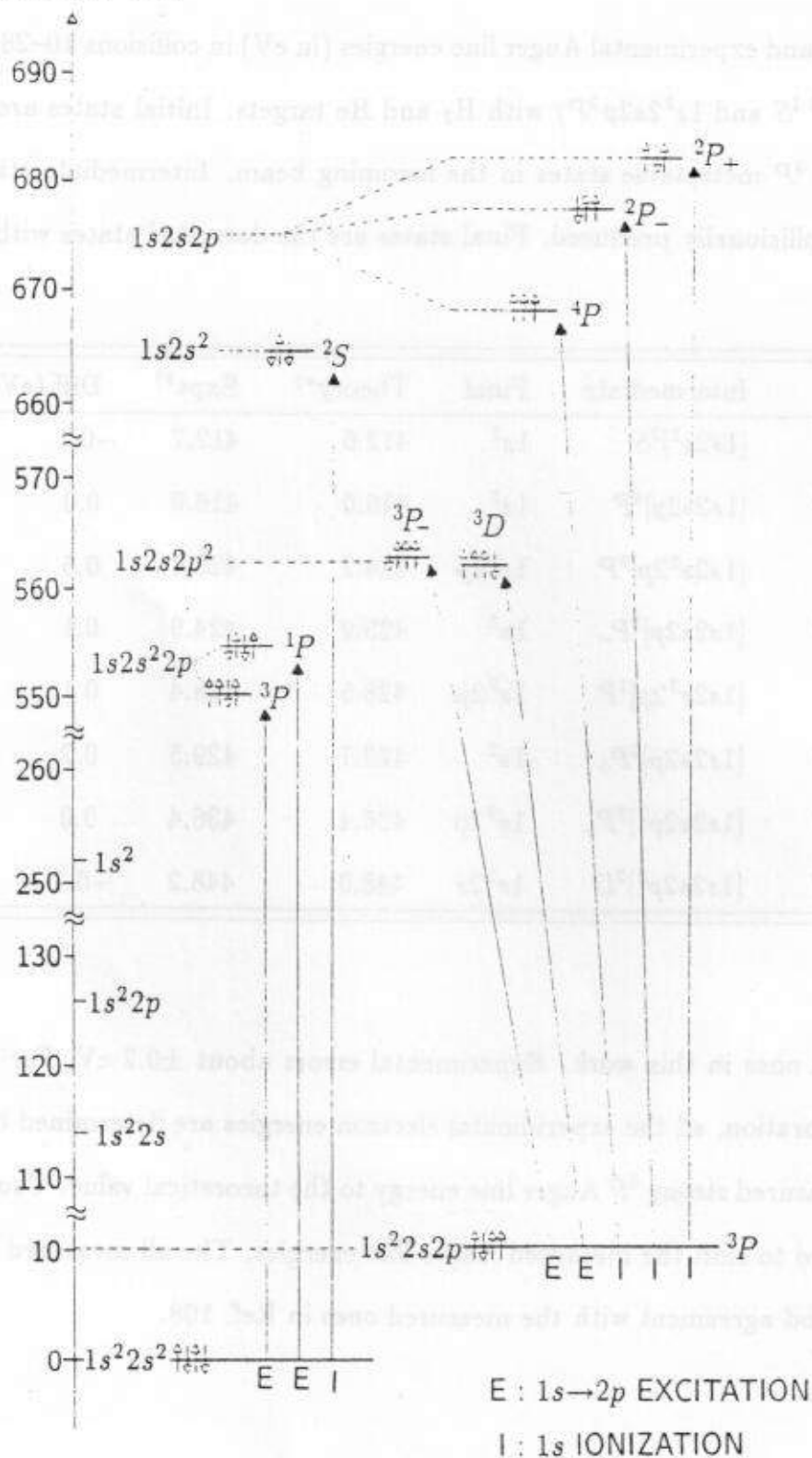


FIGURE 65. State production mechanisms from the $O^{4+}(1s^22s^2, 1s^22s2p^3P)$ to the various $O^{5+}(1s2l2l')$ and $O^{4+}(1s2l2l'2\ell')$ states.

In order to find the metastable beam fraction, Auger electron yields from the 2S , 4P , $^2P_-$, and $^2P_+$ states could be used. However, due to the uncertainty in the solid angle evaluation (see chapter V for details) for 4P electron measurements and the line blending problem for the $^2P_+$ state (see spectra of Fig. 64), 2S and $^2P_-$ electron yields are used to obtain the metastable beam fraction. As shown in Fig. 65, the 2S state is predominantly produced by $1s$ electron ionization in the ground state beam and the 4P and $^2P_-$ states are produced by $1s$ ionization in the metastable beam. Auger yields ξ for these states are well known and contained in Table 5. For the given collision parameters, the measured electron yields at 0° , Z_{1S} and Z_{1P_-} for these three states can be given:

$$Z_{1S} = N_g \cdot n \cdot \sigma_{1S} \cdot \xi_{1S} \cdot \Delta\Omega_{\text{prompt}} \cdot \eta, \quad (95)$$

$$Z_{1P_-} = N_m \cdot n \cdot \sigma_{1P_-} \cdot \xi_{1P_-} \cdot \Delta\Omega_{\text{prompt}} \cdot \eta, \quad (96)$$

where N_g and N_m are the number of the projectile ions in the ground and metastable states, respectively, n is target number density, ξ is the (J -averaged Auger) yield listed in Table 5, and $\Delta\Omega$ is the effective solid angle estimated with Eq. (45-2). σ_{1S} and σ_{1P_-} are the $1s$ electron ionization (K -vacancy production) cross sections resulting in the 2S and $^2P_-$ state, respectively. As shown in Fig. 65, the ionization cross section of *one* $1s$ electron should be approximately the same for both ground and metastable states due to only the small difference in $21/21'$ configuration. Both $1s$ electrons can contribute to the ionization from the ground state forming the 2S state. However, the ionization of only one of *two* $1s$ electrons *from the metastable state can contribute to either a $^2P_-$ and $^2P_+$ or 4P formation.* Hence, the probability of producing a 4P state will be the same as the "sum" of that of the $^2P_-$ and $^2P_+$ states. The state production probability ratio of $^2P_-$ to $^2P_+$ can be found to be 3 using the table of fractional parentage coefficients.¹²⁸

Therefore, the state production probabilities of 2S , 4P , $^2P_-$, and $^2P_+$ will be in the ratio 8:4:3:1 and thus

$$\sigma_{2S} = 2 \cdot \sigma_{4P} = \frac{8}{3} \cdot \sigma_{2P_-} = 8 \cdot \sigma_{2P_+}. \quad (97)$$

Therefore, the measured electron yields for 2S and $^2P_-$ states, expressed in Eqs. (94) and (95), are used to calculate the metastable beam fractions. Using Eqs. (94), (95), and (96), the electron yield ratio of the 2S to $^2P_-$ state is given by

$$\frac{Z_{2S}}{Z_{2P_-}} = \frac{\frac{8}{3} \cdot \xi_{2S}}{\xi_{2P_-}} \cdot \frac{N_g}{N_m}. \quad (98)$$

Therefore, the metastable beam fraction F_m , defined to be $F_m = N_m/N$, where $N = N_m + N_g$, is expressed by

$$F_m = \frac{N_m}{N_m + N_g} = \left[\frac{N_g}{N_m} + 1 \right]^{-1} = \left[\frac{\xi_{2P_-}}{\frac{8}{3} \cdot \xi_{2S}} \cdot \frac{Z_{2S}}{Z_{2P_-}} + 1 \right]^{-1}. \quad (99)$$

Thus, the metastable beam fraction is extracted using the Auger yields ξ 's, (which are from the atomic structure calculations, and the measured Auger electron intensity ratio between the two states. Here we assumed that the collisionally produced states are not aligned, but this assumption has yet to be tested stringently. The measured metastable fractions are found to be 0.61 averaged for both He and H₂ targets for all projectile energies as shown in Fig. 66. These results are consistent with the value of 0.60 ± 0.05 measured for 10 MeV O⁴⁺ + He collisions reported in Ref. 108 and the value of 0.64 measured¹²⁹ in collisions of 3–10 MeV C²⁺ with various gas targets.

From the measured electron yields for the 4P and $^2P_-$ states, the electron counting ratio, R_Z , which is defined by the following relation (see Chapter V section B), is extracted:

$$R_Z = Z_{4P}^{in}/Z_{2P_-}^{total}, \quad (58)$$

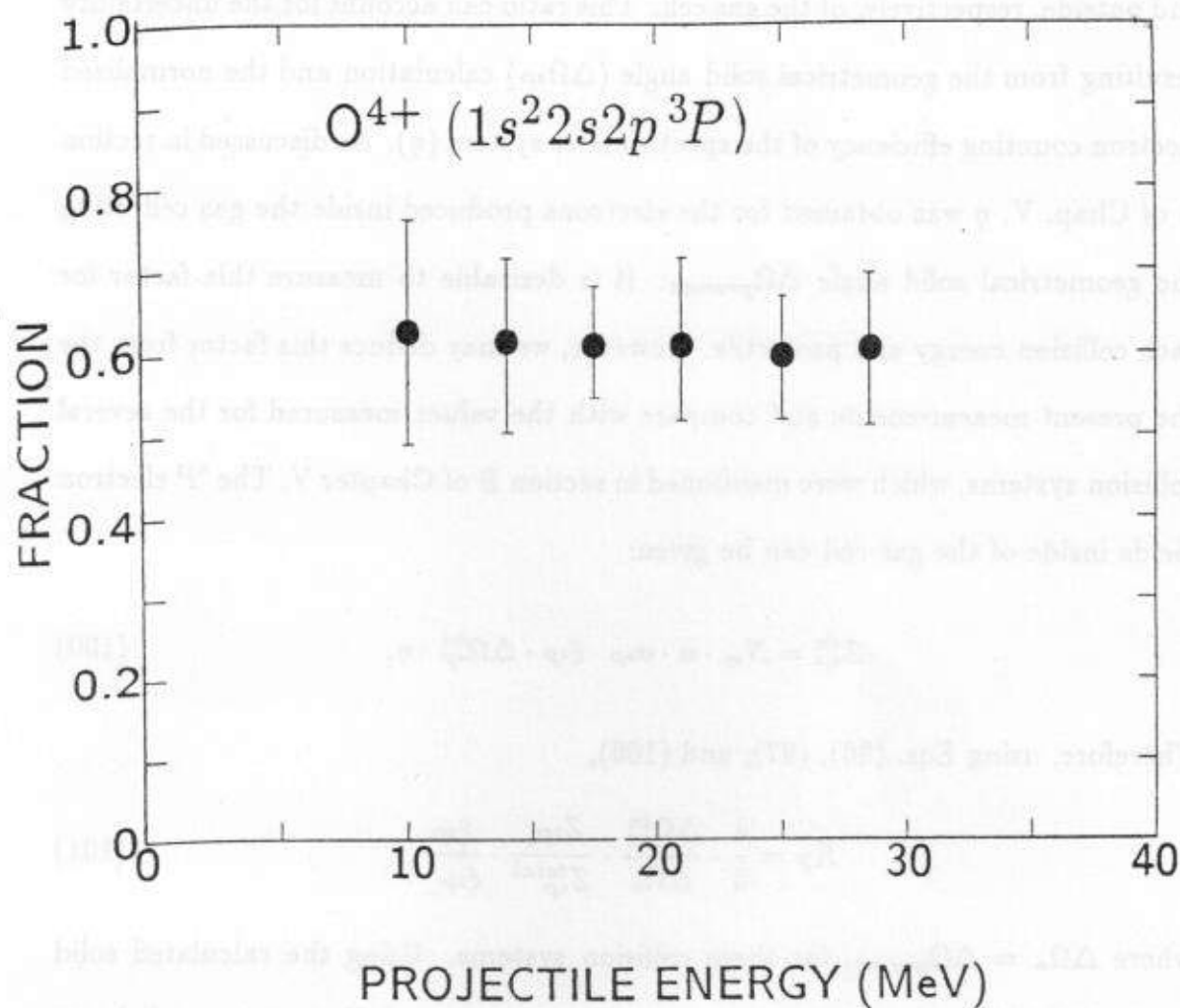


FIGURE 66. Measured $O^{4+}(1s^2 2s 2p)^3P$ metastable beam fractions (see text).

where Z_{4P}^{in} and Z_{4P}^{total} are the measured electron yields which are produced inside and outside, respectively, of the gas cell. This ratio can account for the uncertainty resulting from the geometrical solid angle ($\Delta\Omega_{4P}$) calculation and the normalized electron counting efficiency of the spectrometer system (η). As discussed in section B of Chap. V, η was obtained for the electrons produced inside the gas cell using the geometrical solid angle $\Delta\Omega_{prompt}$. It is desirable to measure this factor for each collision energy and projectile. However, we may deduce this factor from the the present measurements and compare with the values measured for the several collision systems, which were mentioned in section B of Chapter V. The 4P electron yields inside of the gas cell can be given:

$$Z_{4P}^{in} = N_m \cdot n \cdot \sigma_{4P} \cdot \xi_{4P} \cdot \Delta\Omega_{4P}^{in} \cdot \eta. \quad (100)$$

Therefore, using Eqs. (96), (97), and (100),

$$R_Z = \frac{4}{3} \cdot \frac{\Delta\Omega_{4P}^{in}}{\Delta\Omega_o} \cdot \frac{Z_{2P_-}}{Z_{4P}^{total}} \cdot \frac{\xi_{4P}}{\xi_{2P_-}}, \quad (101)$$

where $\Delta\Omega_o = \Delta\Omega_{prompt}$ for these collision systems. Using the calculated solid angle $\Delta\Omega_{4P}^{in}$, R_Z was extracted, averaged for both H_2 and He targets, and shown in Fig. 67 versus projectile energies. No significant variation of the R_Z factor was observed in the given projectile velocity range. Therefore a value of $R_Z = 0.3 \pm 0.05$ can be used to get the cross section of the 4P state production for all projectile energies. This value is reasonably consistent with the observed value of 0.35 in section B of chapter V.

Using the extracted metastable beam fractions, all the state production cross sections for $1s$ ionization and $1s \rightarrow 2p$ excitation can be determined. Here we concentrate on the K -shell ionization. The experimental cross sections for the 2S state were shown in Fig. 68 with the theoretical estimation which will be discussed

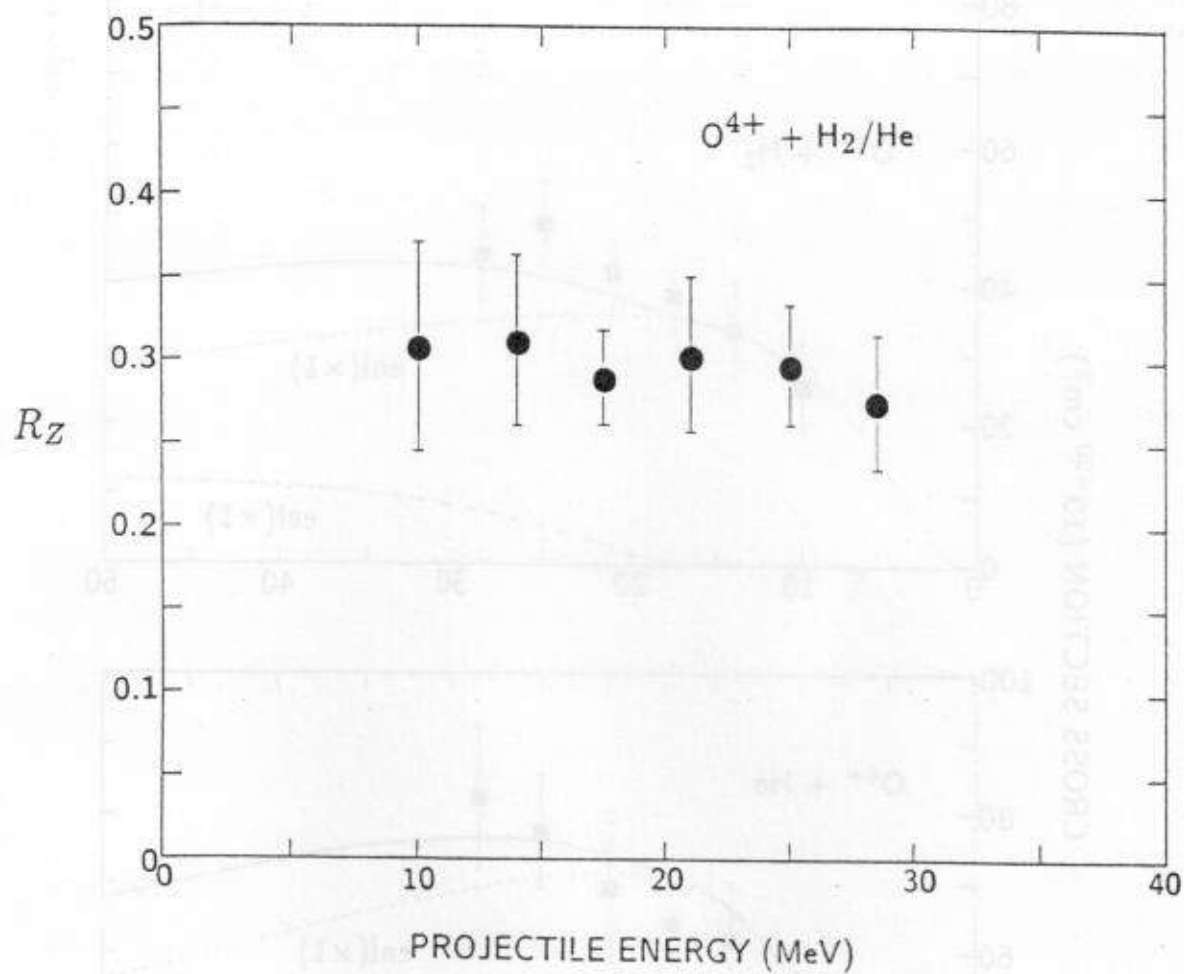


FIGURE 67. Extracted 4P electron yields ratio of inside to total (see text) for $O^{4+} + H_2/He$ collisions.

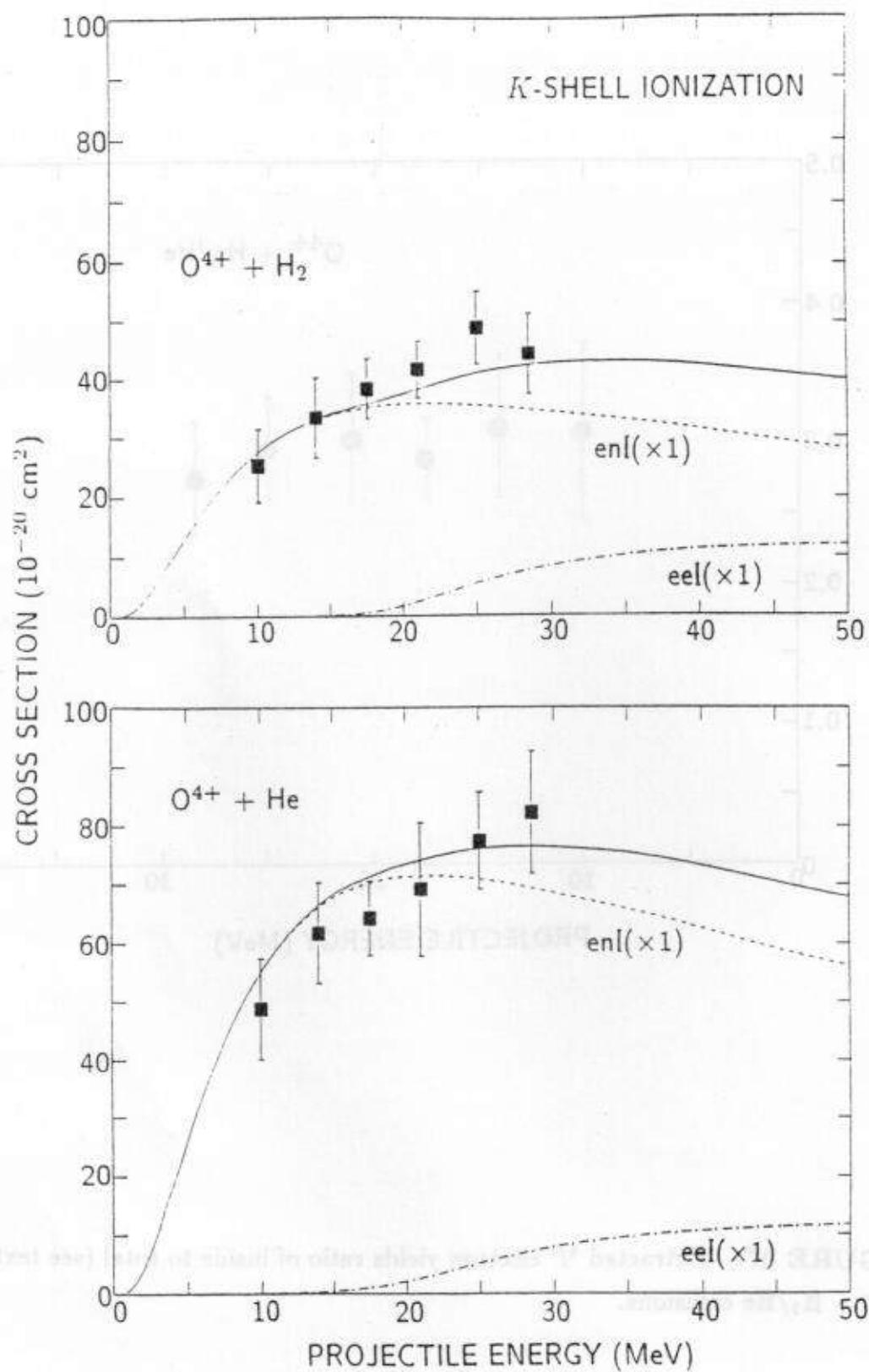


FIGURE 68. *K*-shell ionization cross sections in $O^{4+} + H_2/He$ collisions versus projectile energy

as follows: The strong contribution by the target nucleus is seen and some contribution by the target "electron" is observed at the projectile energies higher than the 1s ionization threshold (see vertical arrow). As an electron-electron interaction or anti-screening effect, this electron-electron ionization could be significant at the high velocity collisions between target electrons and ions.

The cross section for 1s electron ionization by target nucleus, σ_{enI} , for the present multi-electron collision system of $O^{4+} + H_2/He$ is estimated by scaling the PWBA ionization cross sections¹³¹ of $H^+ + H$ collisions as follows:

$$\sigma_{enI} = 2 \cdot n_A \cdot \frac{Z_T^2}{Z_P^4} \cdot \sigma_{pH} \cdot \left[\frac{13.6 \cdot Z_P^2}{I_{1s}} \right]^2 = 2 \cdot n_A \cdot Z_T^2 \cdot \sigma_{pH} \cdot \left[\frac{13.6}{I_{1s}} \right]^2, \quad (102)$$

where 2 comes from the two *K*-shell electrons, n_A is the number of nuclei in a target particle (2 for H_2 and 1 for He), Z_T is the atomic number of the target nucleus, Z_P is the projectile atomic number (here 8 for the oxygen ions), σ_{pH} is the ionization cross sections for $H^+ + H$ collisions which are tabulated as a function of proton velocity $v - P$ in Ref. 131, and I_{1s} is the 1s ionization threshold energy of $O^{4+} (1s^2 2s^2)$, which is estimated fairly accurately as follows:

$$I_{1s} = E_I(1s^2 2s^2) + E_I(1s^2 2s) + E_A^{2S}, \quad (103)$$

where $E_I(1s^2 2s^2)$ and $E_I(1s^2 2s)$ are the ionization potential for the 2s electron ionization and E_A^{2S} the Auger electron energy from the 2S state of the present interest. I_{1s} is thus found to be 664.6 eV for the 1s ionization in $O^{4+} (1s^2 2s^2)$. The cross section σ_{enI} of Eq. (102) is now given as a function of the corresponding projectile velocity which is set to be $Z_{eff} \cdot v_p$, where $Z_{eff} = 7.35$ is the effective binding charge for the 1s electron in the $O^{4+} (1s^2 2s^2)$ ion. The results of σ_{enI} are given by dashed lines in Fig. 68.

The ionization contribution by the target electrons, σ_{eeI} can be calculated by the IA treatment using the electron impact ionization (eII) cross sections, σ_{eII} , as

follows: Using Eq. (1) and the Compton profile for the target electrons,

$$\sigma_{eeI} = \sum_i \int \sigma_{eII} \cdot |\Psi|^2 d^3 p_i = \int \sigma_{eII} \cdot J(p_z) dp_z. \quad (104)$$

In the projectile rest-frame the target electrons are incoming with the orbital velocity distribution (Compton Profile) and the incoming electron energies is expressed by Eq. (24). So, the integration is needed for each projectile energy.

The σ_{eII} is given by using the cross section formula in Ref. 130:

$$\sigma_{eII}(1s, u) = \pi a_0^2 \cdot \left[\frac{1}{Z_{eff}(1s)} \right]^2 \cdot n_{1s} \cdot \sigma_R^H(1s, u), \quad (105)$$

where a_0 is the Bohr radius, $Z_{eff}(1s) = 8 - 0.65$ is the recommended¹³⁰ effective charge (in e unit) of the Be-like ion, n_{1s} is the number electrons in the ion $1s$ shell (here 2), and $\sigma_R^H(1s, u)$ is the reduced eII cross section of a hydrogenic ion given by using Eq. (6) of Ref. 130:

$$\sigma_R^H(1s, u) = \frac{1}{u} \left[1.13 \ln(u) + 3.80 \left(1 - \frac{1}{u} \right) + \left(\frac{-2.00}{u} + \frac{3.80}{u^2} \right) \left(1 - \frac{1}{u} \right) \right], \quad (106)$$

where u is the impact electron energy in the units of the ionization threshold I_{1s} . The results of this σ_{eeI} calculation are shown as dot-dashed lines in Fig. 68. The σ_{enI} and σ_{eeI} was summed (incoherently) and the results are given as solid lines in Fig. 68 leading to a good agreement between the calculation and experiment.

The eel contribution is not well distinguished due to the strong contribution of the enI. As a good candidate, C^{2+} ions can be used to see the more pronounced eel effects. The predicted $1s$ ionization cross section as a function of the projectile energy in $C^{2+} + H_2$ collisions is shown in Fig. 69.

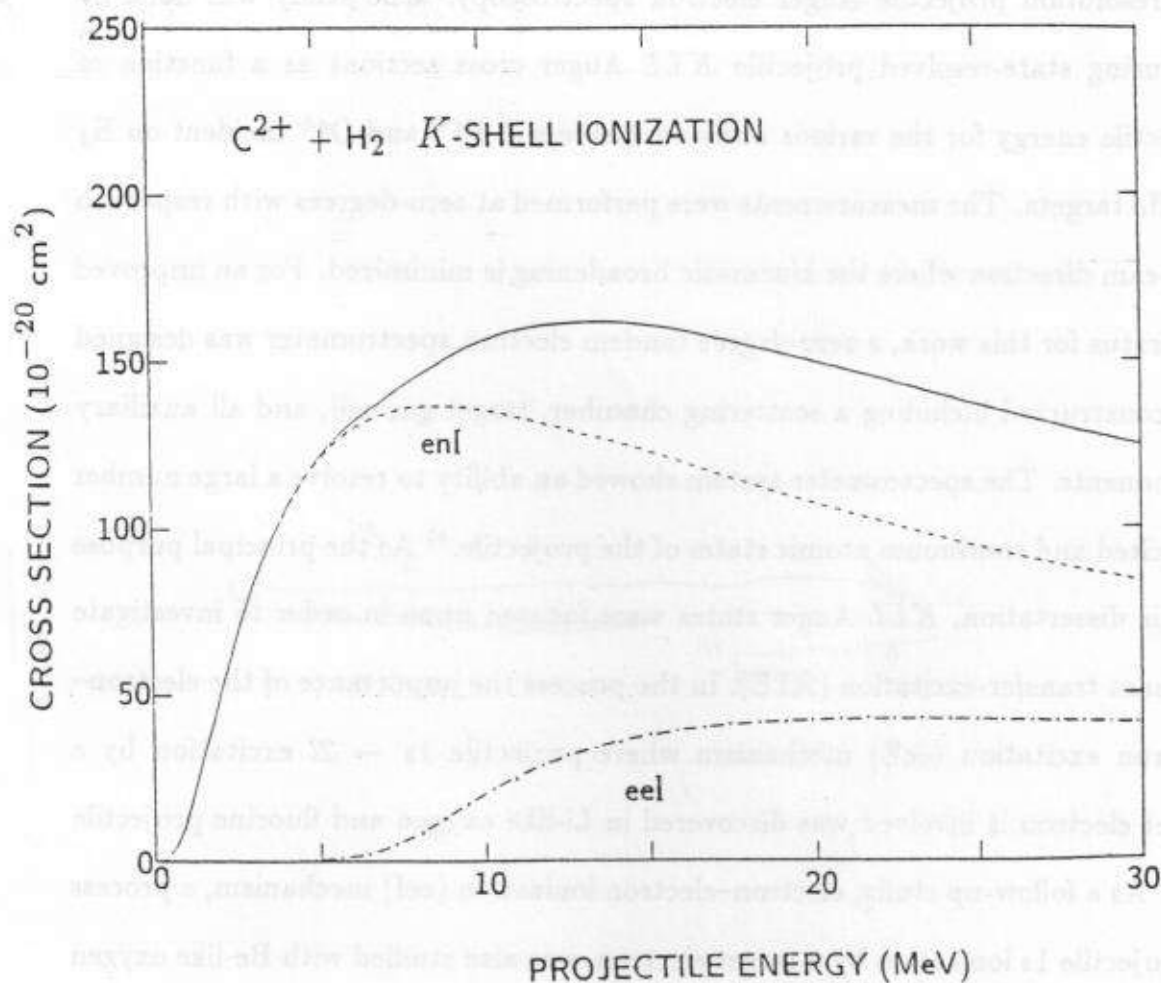


FIGURE 69. K -shell ionization cross sections evaluated by PWBA and CBE calculations in $C^{2+} + H_2$ collisions as a function of projectile energy.

VIII. CONCLUSIONS

Electron-electron interactions in fast ion-atom collisions were studied using high-resolution projectile Auger electron spectroscopy. The study was done by measuring state-resolved projectile *KLL* Auger cross sections as a function of projectile energy for the various collision systems of F^{9+} and O^{7+} incident on H_2 and He targets. The measurements were performed at zero-degrees with respect to the beam direction where the kinematic broadening is minimized. For an improved apparatus for this work, a zero-degree tandem electron spectrometer was designed and constructed including a scattering chamber, target gas cell, and all auxiliary components. The spectrometer system showed an ability to resolve a large number of excited and continuum atomic states of the projectile.⁴⁰ As the principal purpose of this dissertation, *KLL* Auger states were focused upon in order to investigate resonant transfer-excitation (RTE). In the process the importance of the electron-electron excitation (eeE) mechanism where projectile $1s \rightarrow 2l$ excitation by a target electron is involved, was discovered in Li-like oxygen and fluorine projectile ions. As a follow-up study, electron-electron ionization (eeI) mechanism, a process of projectile $1s$ ionization by a target electron, was also studied with Be-like oxygen projectile ions.

Using a high-resolution electron spectrometer and employing various kinds of ion beams from the atomic-physics-dedicated accelerator facility at the J.R. Macdonald Laboratory at KSU, numerous spectroscopic data were obtained in this project and considerable information on state-selective processes was provided. Atomic collision phenomena occurring at the low orbitals of the *highly charged ions* have been under investigation with this "spectroscope". The phenomena were sufficiently attractive, since these could give ample opportunities for a theoretical testing ground and provide some alternative data for free-electron-ion collisions.

In an application aspect, this ion-atom collision information will be important for the studies of high temperature, highly-ionized plasmas such as in thermonuclear fusion and astrophysical environments.

In the frame of an ion projectile, a target particle was simply considered as a bombarding agent. H_2 and He targets were successfully employed to reduce the contribution by the target nucleus in the processes where projectile K -shell excitation or ionization is involved. The role of the quasifree "target electron" in these processes was distinguished from that of the "target nucleus" by treating their contributions incoherently. In the cases of the eeE and eeI , the weakly bound (quasifree) target electron was observed to play the role of the active agent giving rise to the so-called anti-screening effect. Measuring the collision cross sections for the various collision energies, the electron-electron interactions of RTE, eeE , and eeI were distinguished from the NTE, enE , and enI , respectively, whose processes are due to electron-nucleus interactions. The measured cross sections of RTE, eeE , and eeI were compared with available theory, resulting in a good overall agreement. Thus, the cross sections due to the target electrons could provide some collision strengths or cross sections in free-electron-ion collisions.

Theoretically, the impulse approximation (IA) has been successfully applied towards understanding the relationship between the ion-atom and electron-ion collisions as expressed in Eq. (1). For a more profound understanding and for a stringent test of the IA, the binary encounter electrons, which are observed with a strong intensity, were extensively studied resulting in excellent agreement between the measured and calculated double differential cross sections (DDCS). Thus, zero-degree BEE studies have provided a good opportunity for a model treatment of the IA.

The BEE production at zero degrees was studied in 1-2 MeV/u collisions

of bare ions ranging from protons to F^{9+} with H_2 and He targets. At these collision energies the BEe were found to be well separated from the cusp electrons facilitating the determination of their DDCS. A description of the BEe production mechanism within an IA treatment, in which the target electrons undergo a 180° Rutherford scattering by the projectile nucleus in the projectile frame, was found to account for both the position and the shape of the measured BEe DDCS. Attempts to use the known $H^+ + Ne$ K -Auger cross sections to obtain an absolute normalization led to measured DDCS that were consistently lower than the results of the IA by a factor of ~ 0.6 . By normalizing the $F^{9+} + H_2$ data to the IA calculation, we obtained an efficiency curve which reflected the expected electron energy dependence of the detection apparatus (channeltron).

Using this efficiency, good agreement was found between all the BEe data and the full IA calculation, i.e. projectile nuclear charge and energy dependence, as well as target binding energy effects. Calculated BEe DDCS using a PWBA were also compared to our data and the IA model and were found to be in good overall agreement. However, the PWBA calculation did not predict correctly the maximum or the shape of the BEe distribution for the He data.

The good overall systematic agreement of the BEe-IA and our measured BEe-DDCS suggests that the BEe-IA could provide experimentalists with a direct and relatively easy method for an *in situ* efficiency calibration of electron spectrometers at laboratory electron energies larger than about 1 keV. This would be particularly useful in characterizing Auger electron measurements in ion-atom collisions of processes such as RTE, ionization, excitation and capture.

The projectile charge state q -dependence of binary encounter electrons ejected at zero degrees with respect to the beam direction was also studied in fast 19 and 28.5 MeV collisions of F^{q+} with H_2 and He targets with $q = 3 - 9$. The BEe pro-

duction was observed to increase with increasing number of projectile electrons, contrary to the expectations of a previously developed screening model successfully applied to non-zero degree BEe measurements. The observed enhancement could not be readily understood within the impulse approximation model of BEe production. Several plausible mechanisms based on elementary considerations of ionization, capture, or Coulomb focusing by secondary electron scattering were investigated qualitatively, however, none were found to be entirely satisfactory. A quantitative description of screening phenomena for electron-ion scattering at small impact parameters is needed. Angular dependence studies in combination with q -dependence studies of BEe production would be useful in testing such a theory. Further theoretical and experimental work is necessary for a better understanding of this *anomalous* behavior of the zero-degree BEe. Very recently several theoretical calculations^{83,84} were performed and reported leading to a good agreement between the calculations and our measurements.

The extensive studies of the zero-degree BEe gave rise to such an improved IA treatment that the p_z^2 quadratic term is retained and the target ionization potential is included in the expression of the electron energy [see Eq. (22)] in the projectile frame. This improved treatment was also applied consistently to all the electron-electron processes of the RTE, eeE, and eel.

RTE was observed in the formation of O^{4+} , F^{5+} [$1s2s2p^2$]^{3,1} D and F^{6+} [$1s2p^2$]² D , [$1s2s2p$]² P_{\pm} states with 0.25–2 MeV/u Li-like O^{5+} and F^{6+} and He-like F^{7+} projectile ions colliding with He and H_2 targets. The experimental RTEA single differential cross sections (SDCS) measured at $\theta_{lab} = 0^\circ$ as a function of the projectile energy were compared with the calculation of the improved RTEA-IA treatment leading to a good overall agreement. In the RTEA-IA calculation, RTEA angular dependence theory,²⁹ which considers explicitly the alignment of

the RTE states, was also included. Thus, resonant excitation-scattering (RES) strengths for the RTE states were extracted from the measured Auger SDCS using the improved IA formalism, and compared with the theoretical values resulting in a good agreement. As seen in Tables 17 and 19, the experimental values of the RES strength for the strongest RTE states of 3D and 2D were 20–30% smaller than the theoretical values. This could be within experimental and theoretical uncertainties. But, the discrepancy was not exactly understood.

In the case of the RTEA experiment with He-like $F^{7+}(1s^2)$ projectile ions, a complete KLL state-resolved RTEA measurement (see Table 19) was performed. In other words, RTE signatures for all the $8\ 1s2l2l' (^{2S+1})L$ states were searched and their cross sections were compared with the theoretical expectation of RTEA-IA leading to a good agreement between theory and experiment. In particular, the simultaneous agreement for both 2D and $^2P_{\pm}$ states confirms the selection rule (or alignment) for the formation of an RTE state; the $M_L=0$ magnetic substate is preferentially populated in the RTE process.

Some interference between the binary encounter electrons and RTE Auger electrons also has been observed showing a Fano profile in the electron spectra, particularly around the resonance projectile energy. However, the calculated interference for the collision systems investigated was found to be smaller than $\sim 3\%$ for D states.³⁰

As long as the Auger yield ξ in a deexcitation channel is known, and the impulse approximation is valid for an RTE process, zero-degree state-resolved RTEA, thus RES strength measurements can result in the experimental RES cross sections σ_{RES} . Therefore, the dielectronic recombination cross section (σ_{DR}) for any DR channel can be obtained by Eq. (2). For the measurements of RTEA cross sections, an H_2 target would be a good choice, since the NTE contribution was

observed to be practically negligible as seen in the 3D and 1D states (see Figs. 49 and 50).

Now that the theory²⁹ of alignment and interference in the RTEA process is addressed and the improved RTEA-IA formalism is also understood, thanks to the zero-degree BEe studies,^{32,65} Auger rate Γ_A of an RTE state, the most basic atomic parameter in RTEA measurements, could be determined by obtaining an electron spectrum around the resonance projectile energy. The experimental study was initiated by measuring a zero-degree high-resolution electron spectrum in collisions of H-like 20 MeV F^{8+} and 13.5 MeV O^{7+} with H_2 targets.^{133,134} The measured spectrum (DDCS) was normalized to the BEe-IA and compared with the theoretical spectrum which was folded with the known spectrometer response function. Since the x-ray rate Γ_X is calculated to be very small, about 2% of Auger rate Γ_A in the case of F^{7+} , O^{6+} [$2p^2$] 1D RTE state,¹³⁴ the Auger rate was directly extracted from the measured electron spectrum leading to a good agreement between theory and experiment. Some additional studies have been done, however, detailed results or discussions are not included in this dissertation.

The excitation process for producing the $(1s2l2l')^{(2S+1)L}$ states was also investigated in 0.25–2 MeV/u collisions of $O^{5+}(1s^22s)$ and $F^{6+}(1s^22s)$ projectiles with He and H_2 targets. Four excited states; $[1s2s^2]^2S$, $[1s2s2p]^4P$, and $[1s2s2p]^2P_-$, and $[1s2s2p]^2P_+$, which are led by $1s \rightarrow 2l$ excitation, were observed. At high collision energies above ~ 0.75 MeV/u, the cross sections were observed to rise for the cases of the 4P and $^2P_+$ states. This rise can be attributed to an interaction between the $1s$ projectile electron and a target electron [electron–electron excitation (eeE)]. The interaction was also evidenced by the observed onset of the threshold effects, particularly in the case of H_2 targets. This process can be related to impact excitation of ions by free electrons [electron impact excitation (eIE)] on

applying the IA model to projectile excitation by weakly bound target electrons. The projectile energy dependence of the enhanced cross sections by the eeE was well described by this model. Due to the momentum distribution of the target electrons, the sharp threshold effects of eIE were observed to be slightly smoothed out in the case of eeE.

The 4P state was particularly attractive, produced only by the eeE process through the electron exchange interaction. For the formation of the 4P state, $1s \rightarrow 2p$ excitation by target nucleus [electron-nucleus excitation (enE)] is forbidden within a pure LS coupling scheme. In the case of H_2 targets, practically no enE contribution was observed above the threshold energy.

The measurement of the production cross section of the 4P state required a detailed calculation of the effective solid angle of the spectrometer, since this metastable state has a long lifetime and thus decays both inside and after the gas cell. Due to the uncertainty problem of the spectrometer efficiency for the electrons produced after the gas cell, the 4P electrons which are only produced inside of the gas cell were used for the cross section evaluation. The absolute magnitude of the measured cross sections of the 4P state was larger than the theory by a factor of ~ 1.6 for the collision systems studied here. The discrepancy is probably due to the uncertainty in the effective solid angle calculation, including the spectrometer efficiency problem for the metastable state. Possible non-statistical population for the different J -states could be a source of this discrepancy. only s. cell

For other excitation states, eeE was also observed particularly for the $^2P_{\pm}$ state production in the case of H_2 targets. the enE were strongly observed for these states as evaluated by PWBA. Their cross sections seem to add incoherently. ??

By relating ion-atom excitation to electron-impact excitation, ion-atom measurements possibly could provide cross sections for inner-shell electron-impact ex-

citation of ions for which there are presently few measurements.

Finally, studies of electron-electron ionization were also performed for the collision system of Be-like O^{4+} incident on H_2 and He targets. Although the total cross section by eeI is about $1 \times 10^{-19} \text{ cm}^2$ for these collision systems, the eeI contribution is not well pronounced due to the strong enI contribution. As for the case of the F^{7+} beam, the O^{4+} beam has a large amount of a metastable beam component. The state-resolved *KLL* Auger spectroscopy demonstrated an ability of the metastable beam fraction measurement in the case of the Be-like projectile. The measured, large enI cross sections at various projectile energies also showed an excellent agreement with the PWBA calculation. This fact further assures the method of spectrometer efficiency normalization, which was done by the BEe production cross sections at various projectile energies.

Zero-degree projectile Auger spectroscopy has been proved to provide a powerful technique by which one can identify the collisionally-produced Auger states in the projectiles and measure their production cross sections. Traditionally, high-resolution state-selective spectroscopy has been mainly applied to identify an excited atomic state and to measure line profiles and widths. In the present work, however, the spectroscopy has been utilized to measure Auger or state production cross sections.

As J. Briggs pointed out¹⁶ in 1988 "The study of dynamic electron-electron interactions during ion-atom collisions will be a major theme in the ensuing years," this subject has been a challenging task in this dissertation, searching and clarifying the experimental evidences of RTE, eeE, and eeI. Furthermore, the dynamic electron-electron interaction has been quantitatively measured in terms of the collision cross section or strength leading to agreement between theory and experiment. In a recent paper¹³⁴ P. Richard also stressed the dynamic role of the electron in

ion-atom collisions as the "dual personality that *bound* electrons exhibit during excitation and ionization," and he continued that "The free electron has a well defined personality in scattering experiments, however, the normally referred to 'spectator' electrons of an ion or atom can serve in two roles, either to shield the Coulomb field of an exciting nucleus or to actively participate in the excitation or ionization processes."

It would be sufficient to understand thoroughly the dynamic role of the electron in energetic ion-atom collisions.

REFERENCES

1. See for example P. Richard, editor, *Methods of Experimental Physics*, 17 (Academic Press, New York, 1980).
2. B. Crasemann, editor, *Atomic Inner-Shell Processes*, (Academic Press, New York, 1975).
3. C.D. Lin and P. Richard, in *Advances in Atomic and Molecular Physics*, 17, edited by D. Bates and B. Bederson (Academic Press, New York, 1981), pp. 275-353.
4. N. Stolterfoht, *Physics Report* 146 pp 315-424 (1987).
5. M. Tawara, M. Terasawa, P. Richard, T.J. Gray, P. Pepmiller, J. Hall, and J. Newcomb, *Phys. Rev. A* 20, 2340 (1979).
6. M. Terasawa, T.J. Gray, S. Hagmann, J. Hall, J. Newcomb, P. Pepmiller, and P. Richard, *Phys. Rev. A* 27, 2868 (1983).
7. P.L. Pepmiller, P. Richard, J. Newcomb, J. Hall, and T.R. Dillingham, *Phys. Rev. A* 31, 734 (1985).
8. A. Itoh, T.J.M. Zouros, D. Schneider, U. Stettner, W. Zeitz, and N. Stolterfoht, *J. Phys. B* 18, 4581 (1985).
9. J.K. Swenson, Y. Yamazaki, P.D. Miller, H.F. Krause, P.F. Dittner, P.L. Pepmiller, S. Datz, and N. Stolterfoht, *Phys. Rev. Lett.* 57, 3042 (1986).
10. T.J.M. Zouros, D. Schneider, and N. Stolterfoht, *J. Phys. B* 21, L671 (1987).
11. J.M. Anthony, S.M. Shafroth, M. Benhenni, E.N. Strait, T.J.M. Zouros, L.D. Hendrick and D.M. Peterson, *J. de Phys.* 48, C9-301 (1987).
12. T.J.M. Zouros, D.H. Lee, and P. Richard, *Phys. Rev. Lett.* 62, 2261 (1989).
13. T.J.M. Zouros, D.H. Lee, S.L. Varghese, J.M. Sanders, J.L. Shinpaugh, P. Richard, K.R. Karim, and C.P. Bhalla, *Phys. Rev. A* 40, 6246 (1989).
14. B.D. DePaola, R. Parameswaran, and W.J. Axmann, *Phys. Rev. A* 41, 6533 (1990).
15. T.J.M. Zouros, D. Schneider, and N. Stolterfoht, *Phys. Rev. A* 35, 1963 (1987).
16. J. Briggs, in *Electronic and Atomic Collisions*, edited by H.B. Gilbody, W.R. Newell, F.H. Read, and A.C.H. Smith (Elsevier Sciences Publishers B.V. 1988) p.13-20.

17. For a recent review see N. Stolterfoht, in *Electron correlation processes in energetic ion-atom collisions*, edited by M. Ivascu, V. Florescu, and V. Zoran (World Scientific, Singapore 1989) p. 342.
18. J.H. McGuire, Phys. Rev. A **36**, 1114 (1987).
19. "Physics News in 1989," edited by P.F. Schewe, (American Institute of Physics 1989). p 15.
20. For a review on RTE see J.A. Tanis, Nucl. Instrum. & Meth. in Phys. Res. B **40/41**, 70 (1989).
21. R. Hippler, S. Datz, P.D. Miller, P.L. Pepmiller, and P.F. Dittner, Phys. Rev. A **35**, 585 (1987).
22. H.-P. Hülskötter, W.E. Meyerhof, E. Dillard, and N. Guardala, Phys. Rev. Lett. **63**, 1938 (1989).
23. P.L. Pepmiller, P. Richard, J. Newcomb, T.R. Dillingham, J.M. Hall, T.J. Gray, and M. stöckli, IEEE Trans. NS-30 No. 2, 1002 (1983).
24. M. Clark, D. Brandt, J.K. Swenson, and S.M. Shafroth, Phys. Rev. Lett. **54**, 544 (1985).
25. For a recent review see Y. Hahn and K.J. LaGattuta, Phys. Report **166**, 195 (1988).
26. A. Müller, G. Hofmann, K. Tinschert, and E. Salzborn, Phys. Rev. Lett. **61**, 1352 (1988); A. Müller *et al.*, *ibid*, **56**, 127 (1986); P.F. Dittner *et al.*, *ibid*, **51**, 31 (1983); D.A. Knapp *et al.*, *ibid*, **62**, 2104 (1989); R.E. Marrs *et al.*, *ibid*, **60**, 1715 (1988); R. Ali *et al.*, *ibid*, **64**, 633 (1990); G. Kilgus *et al.*, *ibid*, **64**, 737 (1990).
27. D. Brandt, Phys. Rev. A **27**, 1314 (1983).
28. Goldberg and Watson, *Collision theory* Check see Eqs. (11.60b) and (11.40).
29. C.P. Bhalla, Phys. Rev. Lett. **64**, 1103 (1990).
30. T.J.M. Zouros, C.P. Bhalla, D.H. Lee, and P. Richard, Phys. Rev. A **42**, 678 (1990).
31. N. Stolterfoht, D. Schneider, R. Burch, H. Wieman, and J.S. Risley, Phys. Rev. Lett. **33**, 59 (1974).
32. D.H. Lee, P. Richard, T.J.M. Zouros, J.M. Sanders, J.L. Shinpaugh, and H. Hidmi, Phys. Rev. A **41**, 4816 (1990).

33. D.E. Post, in *Atomic and molecular physics of Controlled Thermonuclear Fusion*, edited by C.J. Joachain and D.E. Post (Plenum, New York, 1983); A. Hauer and A.L. Merts, editors, *Atomic Processes in Plasmas*, American Inst. of Phys. conference proceedings **168**; H.P. Summers, Comments At. & Mol. Phys. **21**, 277 (1988).
34. For examples see R. Bartiromo, in *Diagnostics for Fusion Reactor Conditions, Proceedings of the International School of Plasma Physics*, edited by P.E. Stott, D.K. Akulina, G.G. Leotta, E. Sindoni, and C. Wharton (Pergamon Press, New York, 1982); R.K. Janev, Bull. International Atomic Energy Agency **31**, 28 (1989); B.H. Bransden, Nucl. Instr. & Meth. in Phys. Res. **B24/25**, 377 (1987); A.J.H. Nonné, *ibid* **23** 219 (1987).
35. N.J. Peacock and H.P. Summers, Nucl. Instr. & Meth. in Phys. Res. **B23**, 226 (1987); S.M. Younger, *ibid*, **B24/25** 373(1987).
36. J.H. McGuire, N. Stolterfoht, and P.R. Simony, Phys. Rev. **A24**, 97 (1981).
37. A. Itoh, T. Schneider, G. Schiwietz, Z. Roller, H. Platten, G. Nolte, D. Schneider, and N. Stolterfoht, J. Phys. **B16**, 3965 (1983).
38. T.R. Dillingham, Ph. D. thesis, Kansas State University (1983); J.J. Newcomb, *ibid*.
39. A. Itoh, D. Schneider, T. Schneider, T.J.M. Zouros, G. Nolte, G. Schiwietz, Z. Zeitz, and N. Stolterfoht, Phys. Rev. **A31**, 684 (1985).
40. D.H. Lee, T.J.M. Zouros, J.M. Sanders, J.L. Shinpaugh, T.N. Tipping, S.L. Varghese, B.D. DePaola, and P. Richard, Nucl. Instrum. & Meth. in Phys. Res. **B40/41**, 1229 (1989).
41. M.E. Rudd and J.H. Macek, *Case Studies in Atomic Physics* **3**, 47 (1972).
42. D.H. Madison and E. Merzbacher, in *Atomic Inner-Shell Processes*, edited by B. Crasemann (Academic Press, New York, 1975).
43. Y. Hahn, Phys. Rev. **A40**, 2950 (1989).
44. K.D. Sevier, *Low Energy Electron Spectrometry*, 1972.
45. G.D. Yarnold and H.C. Bolton, J. Sci. Instrum. **26**, 38 (1949).
46. G.A. Harrowerm, Rev. Sci. Instrum. **26**, 850 (1955).
47. W. Steckelmacher and M.W. Lucas, J. Phys. E : Sci. Instrum., **12**, 961 (1979).

48. Z. Vager, B. J. Zabransky, D. Schneider, E.P. Kanter, Gu Yuan Zhung and D.S. Gemmell, *Phys. Rev. Lett.* **48**, 592 (1982)
49. G. Schiwietz, D. Schneider and J. Tanis, *Phys. Rev. Lett.* **59**, 1561(1987)
50. K.B. MacAdam and R.G. Rolfes, *Rev. Sci. Inst.* **53**, 592(1982).
51. J.B. Marrion and F.C. Young, *Nuclear Reaction Analysis*, American Elsevier Publishing Co., pp.36-45 (1968).
52. E.A. Kurz, American Laboratory March 1979. and references therein.
53. D.Berényi, in *Proceedings XV Brasov International School on Atomic and Nuclear Heavy Ion Interaction, Poiana Brasov, 1984*, edited by A.L. Berinde, I.A. Dorobantu, V. Zoran, (Central Inst. of Phys., Bucharest, 1986), p. 161.
54. N.Stolterfoht, in *Structure and Collisions of Ions and Atoms*, edited by I.A. Sellin, (Springer-Verlag Press, 1978), pp. 155-199.
55. Refer to equation (18) in M.E. Rudd and J.H. Macek, *Case Studies in Atomic Physics* **3**, 47 (1972).
56. G.N. Ogurtsov, *Rev. Mod. Phys.* **44**, 1 (1972).
57. M.E. Rudd, L.H. Toburen, and N. Stolterfoht, *At. Data and Nucl. Data Tables* **23**, 405 (1979).
58. S.T. Manson, L.H. Toburen, D.H. Madison, and N. Stolterfoht, *Phys. Rev. A* **12**, 60 (1975).
59. L.H. Toburen and W.E. Wilson, *Phys. Rev. A* **19**, 2214 (1979).
60. T.F.M. Bensen and L. Vriens, *Physica* **47**, 307 (1970).
61. F. Drepper and J.S. Briggs, *J. Phys. B* **9**, 2063 (1976).
62. P.D. Fainstein, V.H. Ponce, and R.D. Rivarola, *J. Phys. B* **22**, 1207 (1989).
63. C. Kelbch, R.E. Olson, S. Schmidt, H. Schmidt-Böcking, and S. Hagmann, *J. Phys. B* **22**, 2171 (1989).
64. L.H. Toburen, N. Stolterfoht, P. Ziem, and D. Schneider, *Phys. Rev. A* **24**, 1741 (1981).
65. P. Richard, D.H. Lee, T.J.M. Zouros, J.M. Sanders, and J.L. Shinpaugh, *J. Phys. B.* **23**, L213 (1990).
66. C. W. Woods, R.L. Kauffman, K.A. Jamison, N. Stolterfoht, and P. Richard, *Phys. Rev. A* **13**, 1358 (1976).
67. L.H. Toburen, in *Proceedings of the International Conference on Inner-Shell Ionization Phenomena and Future Applications, Atlanta, Georgia, 1972*, edited

Ne KLL
—

by R.W. Fink, S.T. Manson, J.M. Palms, and P.V. Rao, (National Technical Information Service, U.S. Department of Commerce, Springfield, Va., 1972), p. 979.

68. T.R. Dillingham, J.R. Macdonald, and P. Richard, *Phys. Rev. A* **24**, 1237 (1981).
69. J.S. Lee, *J. Chem. Phys.* **66**, 4906 (1977).
70. F. Biggs, L.B. Mendelsohn, and J.B. Mann, *Atomic Data and Nuclear Data Tables* **16**, 201 (1975).
71. R. Mann, S. Hagmann, and L. Weitzel, *Nucl. Instrum. & Meth. in Phys. Res. B* **34**, 403 (1988).
72. N. Stolterfoht, in *Fundamental Processes in Energetic Atomic Collisions, NATO ASI Series B, Physics*, edited by H.O. Lutz, J.S. Briggs, and H. Kleinpoppen, (Plenum Press, New York, 1983) Vol. **103**, p. 295.
73. L.H. Toburen, *Phys. Rev. A* **3**, 216 (1971).
74. J.P. Macau, J. Jamar, and S. Gardier, *IEEE Trans. Nucl. Sci.* Vol. **NS-23**, No. 6, 2049 (1976).
75. F. Bordoni, *Nucl. Instrum. & Meth.* **97**, 405 (1971).
76. R.L. Arnoldy, P.O. Isaacson, D.F. Gats, and L.W. Choy, *Rev. Sci. Instrum.* **44**, 172 (1973).
77. D. Brandt, *Nuclear Instrum. & Meth.* **214**, 93 (1983).
78. A.S. Schlachter, J.W. Stearns, W.G. Graham, K.H. Berkner, R.V. Pyle, and J.A. Tanis, *Phys. Rev. A* **27**, 3372 (1983).
79. A.S. Schlachter, J.W. Stearns, K.H. Berkner, M.P. Stöckli, W.G. Graham, E.M. Bernstein, M.W. Clark, and J.A. Tanis, in *Electronic and Atomic Collisions* (Abstracts 15th ICPEAC) edited by J. Geddes, H.B. Gilbody, A.E. Kingston, C.J. Latimer, and H.J.R. Walters, (Brighton, United Kingdom, 1987) p. 505.
80. S.T. Manson and L.H. Toburen, *Phys. Rev. Lett.* **46**, 529 (1981).
81. L.H. Toburen, N. Stolterfoht, P. Ziem, and D. Schneider, *Phys. Rev. A* **24**, 1741 (1981).
82. T. Quinteros, private communications and to be published (1990).
83. C.O. Reinhold, D.R. Schultz, and R.E. Olsen, private communications and to be published (1990).

84. R. Shingal, Z. Chen, K.R. Karim, C.D. Lin, and C.P. Bhalla to be published (1990); K. Taulbjerg, to be published (1990).
85. R.K. Janev, R.A. Phaneuf, and H.T. Hunter, *At. Data and Nucl. Data Tables* **40**, 249 (1988).
86. The estimated factor is 1.12 for He target and 0.79 for H₂ target by using the expressions in Ref. 79 for both He and H₂ targets. The formula in Ref. 78 was developed mainly for H₂ target, however the formula in Ref. 79 gives better agreement with the recommended data (Ref. 85) than the formula in Ref. 78.
87. I.S. Dmitriev, V.S. Nikolave, L.N. Fateeva, and Y.A. Teplova, *Sov. Phys.-JEPT* **15**, 11 (1962): single ionization (loss) cross section σ_{qr} for 5.31 MeV O⁵⁺ + He was measured to be 5×10^{-18} cm², which is nearly maximum at this collision energy for this collision system. However, σ_{qr} is not important for the collision energies of this study as will be seen later.
88. K.R. Karim and C.P. Bhalla (private communication).
89. T.W. Tunnell, C. Can, and C.P. Bhalla, *IEEE Trans. Nucl. Sci.* **NS-26**, 1124 (1979)
90. B.F. Davis and K.T. Chung, *Phys. Rev.* **A39**, 3942 (1989) and **A36** 1948 (1987)
91. M.H. Chen and B. Crasemann, *Phys. Rev.* **A27**, 544 (1983).
92. C.E. Normand, *Phys. Rev.* **35**, 1217 (1930).
93. R.B. Brode, *Rev. Mod. Phys.* **5**, 257 (1933).
94. P.R. Bevington, *Data Reduction and Error Analysis for the Physical Sciences* (McGraw-Hill, New York).
95. J.A. Tanis, S.M. Shafroth, J.E. Willis, M. Clark, J. Swenson, E.N. Strait, and J.R. Mowat, *Phys. Rev. Lett.* **47**, 828 (1981).
J.A. Tanis, E.M. Bernstein, W.G. Graham, M. Clark, S.M. Shafroth, B. M. Johnson, K.W. Jones, and M. Meron, *Phys. Rev. Lett.* **49**, 1325 (1982).
96. For reviews on RTE see Ref. 100 and J.A. Tanis, E.M. Bernstein, C.S. Oglesby, W.G. Graham, M.W. Clark, R.H. McFarland, T.J. Morgan, M.P. Stöckli, K.H. Berkner, A.S. Schlachter, J.W. Stearns, B.M. Johnson, K.W. Jones, and M. Meron, *Nucl. Instrum. & Meth. in Physics Research B10/11*, 128 (1985); E.M. Bernstein, M.W. Clark, J.A. Tanis, W.G. Graham, R.H. McFarland, T.J. Morgan, J.R. Mowat, D.W. Mueller, M.P. Stöckli, K.H. Berkner,

- R.J. McDonald, A.S. Schlachter, and J.W. Stearns, Nucl. Instrum. & Meth. in Physics Research B24/25, 232 (1987); R. Schuch, E. Justiniano, M. Schulz, P.H. Mokler, S. Reusch, S. Datz, P.F. Dittner, J.P. Giese, P.D. Miller, H. Schoene, T. Kambara, A. Müller, Z. Stachura, R. Vane, A. Warczak, G. Wintermeyer, in *Proceedings of the XVI International Conference on the Physics of Electronic and Atomic Collisions*, ed. A. Dalgarno, (in press 1990) and references cited therein.
97. J.A. Tanis, E.M. Bernstein, W.G. Graham, M.P. Stöckli, M. Clark, R.H. McFarland, T.J. Morgan, K.H. Berkner, A.S. Schlachter, and J.W. Stearns, Phys. Rev. Lett. 49, 2551 (1984); J.A. Tanis, E.M. Bernstein, M.W. Clark, W.G. Graham, R.H. McFarland, T.J. Morgan, B.M. Johnson, K.W. Jones, and M. Meron, Phys. Rev. A31, 4040 (1985); D.J. McLaughlin and Y. Hahn, Phys. Lett. 112A, 389 (1985); W.G. Graham, E.M. Bernstein, M.W. Clark, J.A. Tanis, R.H. McFarland, T.J. Morgan, and A. Müller, Phys. Rev. A33, 3591 (1986); J.A. Tanis, E.M. Bernstein, M.W. Clark, W.G. Graham, R.H. McFarland, T.J. Morgan, J.R. Mowat, D.W. Mueller, A. Müller, M.P. Stöckli, K.H. Berkner, P. Gohli, R.J. McDonald, A.S. Schlachter, and J.W. Stearns, Phys. Rev. A34, 2543 (1986); W.A. Schönfeldt, P.H. Mokler, D.H.H. Hoffmann, and A. Warczak, Z. Phys. D4, 161 (1986); M. Schulz, E. Justiniano, R. Schuch, P.H. Mokler, and S. Reusch, Phys. Rev. Lett. 58, 1734 (1987); S. Reusch, P.H. Mokler, R. Schuch, E. Justiniano, M. Schulz, A. Müller, and Z. Stachura, Nucl. Instrum. & Meth. in Physics Research B23, 140 (1987); R. Schuch, M. Schulz, E. Justiniano, H. Vogt, S. Reusch, and P.H. Mokler, Nucl. Instrum. & Meth. in Physics Research B23, 140 (1987); E.M. Bernstein, M.W. Clark, J.A. Tanis, W.G. Graham, R.H. McFarland, J.R. Mowat, D.W. Mueller, A. Müller, M.P. Stöckli, K.H. Berkner, R.J. McDonald, A.S. Schlachter, and J.W. Stearns, Nucl. Instrum. & Meth. in Physics Research B23, 154 (1987); D.J. McLaughlin and Y. Hahn, Phys. Rev. A37, 3587 (1988); D.J. McLaughlin and Y. Hahn, Phys. Rev. A38, 531 (1988); M. Schulz, R. Schuch, S. Datz, E.L.B. Justiniano, P.D. Miller, and H. Schöne, Phys. Rev. A38 5454 (1988); C.P. Bhalla and K.R. Karim, Phys. Rev. A39, 6060 (1989); S. Datz, C.R. Vane, P.F. Dittner, J.P. Giese, J. G. del Campo, N.L. Jones, H.F. Krause, P.D. Miller, M. Schulz, H. Schöne and T. M. Rosseel, Phys. Rev. Lett. 63, 742 (1989).
98. A. Itoh, T.J.M. Zouros, D. Schneider, U. Stettner, W. Zeitz, and N. Stolter-

- foht, J. Phys. B18, 4581 (1985); J.K. Swenson, J.M. Anthony, M. Reed, M. Benhenni, S.M. Shafroth, D.M. Peterson and L.D. Hendrik, Nucl. Instrum. & Meth. in Physics Research B24/25, 184 (1987); M. Schulz, J.P. Giese, J.K. Swenson, S. Datz, P.F. Dittner, H.F. Krause, H. Schöne, C.R. Vane, M. Benhenni, and S.M. Shafroth, Phys. Rev. Lett. 62, 1738 (1989);
99. A.M. Burgess, Astrophys. J. 141, 1588 (1965); B.W. Shore, *ibid.* 158, 1205 (1969); Y. Hahn, Adv. At. Mol. Phys. 21, 123 (1985).
100. Y. Hahn, Comments At. & Mol. Phys. 19, No. 2, 99 (1987).
101. P.G. Burke, Adv. At. Mol. Phys. 4, 173 (1968); D.E. Golden, *ibid.* 14, 1 (1978).
102. N.R. Badnell, Phys. Rev. A41, 3555 (1990).
103. M. Benhenni, S.M. Shafroth, J.K. Swenson, M. Schulz, J.P. Giese, H. Schone, C.R. Vane, P.F. Dittner, and S. Datz, submitted to Phys. Rev. Lett. 1990.
104. J.M. Feagin, J.S. Briggs, and T.M. Reeves, J. Phys. B17, 1057 (1984).
105. W. Fritsch and C.D. Lin, Phys. Rev. Lett. 61, 690 (1988).
106. C.P. Bhalla and T.W. Tunnell, J. Quant. Spectrosc. Radiat. Transfer 32, 141 (1984).
107. W. Mehlhorn, Univ. of Aarhus Lecture. Notes (1978).
108. R. Bruch, N. Stolterfoht, S. Datz, P.D. Miller, P.L. Pepmiller, Y. Yamazaki, H.F. Krause, and J.K. Swenson, Phys. Rev. A35, 4114 (1987).
109. T.R. Dillingham, J. Newcomb, J. Hall, P.L. Pepmiller, and P. Richard, Phys. Rev. A29, 3029 (1984).
110. C. Can, T.W. Tunnell, and C.P. Bhalla, J. Elec. Spectroscopy and Related Phenom. 27, 75 (1982).
111. K.T. Chung and B.F. Davis, private communications (1988).
112. E. Träbert, Nucl. Instrum. & Meth. in Phys. Res. B23, 287 (1987).
113. For an excellent review of electron-impact excitation and ionization of ions, see R.A. Phaneuf, in *Atomic Processes in Electron-Ion and Ion-Ion Collisions*, ed. F. Brouillard (Plenum, New York, 1986), p. 117 and references therein.
114. U. Thumm, J.S. Briggs and O. Schöller, J. Phys. B21, 833 (1988).
115. H. Tawara, M. Terasawa, P. Richard, T. J. Gray, P. Pepmiller, J. Hall, and J. Newcomb, Phys. Rev. 20, 2340 (1979).

116. H. Tawara, P. Richard, K.A. Jamison and T. J. Gray, *J. Phys.* B11, L615 (1978)
117. J.R. Macdonald, P. Richard, C.L. Cocke, M. Brown and I.A. Sellin, *Phys. Rev. Lett.* 31, 684 (1973).
118. N.F. Mott and H.S.W. Massey, *The Theory of Atomic Collisions*, 3rd ed., (Oxford University Press 1965), Vol. II, p. 412-424.
119. Y. Hahn, *Phys. Lett.* A119, 293 (1986).
120. N. Stolterfoht, P.D. Miller, H.F. Krause, Y. Yamazaki, J.K. Swenson, R. Bruch, P.F. Dittner, P.L. Pepmiller, and S. Datz, *Nucl. Instrum. & Meth. in Phys. Res.* B24/25, 168 (1987).
121. T.N. Tipping, J.M. Sanders, J. Hall, J.L. Shinpaugh, D.H. Lee, J.H. McGuire, and P. Richard, *Phys. Rev.* A37, 2906 (1988).
122. R. Anholt, *Phys. Lett.* A114, 126 (1986).
123. C.E. Moore, *Atomic Energy Levels*, NSRDS-NBS 35 (U.S. Department of Commerce 1971) Vol. 1 p.58 and 74.
124. Coupled channel calculation for $O^{5+} + H$ (R. Shingal private communication 1989).
125. S.J. Goett and D.H. Sampson, *At. Dat. & Nucl. Dat. Tables* 29, 535 (1983). Fit parameters taken from p. 558; the values used for F^{6+} were interpolated from these tables.
126. T.J.M. Zouros, D.H. Lee and P. Richard, ICPEAC, NY 1989.
127. M.R.C. McDowell and J.P. Coleman, *Introduction to The Theory of Ion-Atom Collisions*, (North-Holland Publishing Co. 1970), p 307-322.
128. C.D.H. Chisholm, A. Dalgarno, and F.R. Innes, in *Advances in Atomic and Molecular Physics*, 5, edited by D.R. Bates and I. Estermann (Academic Press, 1969), pp 297-335. ;J.M. Anthony, private communications (1990).
129. J.M. Anthony, private communications (1990).
130. D.L. Moores, L.B. Golden, and D.H. Sampson, *J. of Phys.* B 13, 385 (1980).
131. T.R. Dillingham, M.S. Thesis, Kansas State University (1977).
132. T.J.M. Zouros *et al.*, *BAPS* 35, 1114 (1990).
133. P. Richard, Proceedings of 15th International Conf. on X-ray and Inner-shell Processes, Knoxville, TN, USA (1990) (AIP Series, edited by T.A. Carrson).

Appendix A. DDCS Normalization

The normalization procedure for the experimental double differential cross sections (DDCS) is described in this Appendix. Initially the spectrometer efficiency was normalized to the known Ne *K* Auger production cross section (see Ref. 66) for the collisions of 3 MeV H⁺ on Ne and the efficiency, say η_{Ne} , was determined. The η_{Ne} was obtained for each beam time and the results are displayed in Fig. A1. The efficiency variation mainly may come from the uncertainty of the optimum channeltron operation voltage (which was to be increased from 2100 eV at beam time 16 to 2300 eV at the last beam time) and setting of the signal processing electronics. The *KLL* Auger production cross section for 9.5 MeV F⁶⁺ + He collisions, which was determined initially using a normalized η_{Ne} value, has been used as a practical standard to obtain the Ne-K-Auger-normalized efficiency η_{Ne} for each beam time.

After finding a more reliable and exact way of the spectrometer efficiency normalization, which was performed using the binary encounter electrons (BEE) at various projectile energies (see section D of Chapter IV), the experimental DDCS are now to be renormalized. The renormalization procedure is as follows: From Eq. (28) in Chapter IV, the DDCS is given by

$$\frac{d^2\sigma}{dE d\Omega} = \frac{Z}{K \cdot \eta(E)}, \quad (A1)$$

where $K = N \cdot n \cdot l \cdot \Delta\Omega \cdot \Delta E$ and $\eta(E)$ can be given by

$$\eta(E) = f(E) \cdot \eta_{Ne}, \quad (A2)$$

where $f(E)$ is the renormalization factor which is in general a function of the electron energy E . From Fig. 24 in Chapter IV and Eq. (A2), $f(E)$ is determined as $f(E) = 5.90\% / \eta(E)$, where 5.9% is the spectrometer efficiency determined using

the Ne K Auger cross sections. $\eta(E)$ is the measured efficiency using BFe peak at various projectile energies of $F^{9+} + H_2$ collisions (see the solid and dashed lines in Fig. 24 of Chapter IV.) The variation of this function with E is assumed to be constant. So, the absolute efficiency $\eta(E)$ is changed by the variation ($\pm 5\%$ —see Fig. A1) of the measured efficiency η_{Ne} , and this small variation is accounted for in the cross section normalization as follows:

Eq. (A1) can be expressed as:

$$\frac{d^2\sigma}{dEd\Omega} = \left(\frac{d^2Y}{dEd\Omega} \right)_{Ne} \cdot \frac{1}{f(E)} = \left(\frac{d^2Y}{dEd\Omega} \right)_0 \cdot \frac{\eta_0}{\eta_{Ne}} \cdot \frac{1}{f(E)}, \quad (A3)$$

where $\left(\frac{d^2Y}{dEd\Omega} \right)_{Ne}$ is η_{Ne} -normalized double differential yields (DDY). $\left(\frac{d^2Y}{dEd\Omega} \right)_0$ is raw DDY which is tentatively normalized with η_0 , evaluated by the data-analyzing program DET, and stored by the DET program. Typically $\eta_0 = 3.67\%$ is used for raw data (spectrum) analysis.

Table A1 shows a list of typical spectrum files of the binary encounter electrons. Measured values of the Ne- K -Auger-normalized efficiency η_{Ne} are also tabulated.

FIGURE A1. Spectrometer efficiency measured for each beam time. The efficiency η_{Ne} was determined measuring the known Ne *K* Auger production cross sections for the collisions of 3 MeV H^+ with Ne targets. The variations of $\pm 5\%$ may come from the settings of the optimum channeltron voltage and electronics used. This variation was accounted for in the measurements of electron production cross sections (see text). The experimental error is about $\pm 3.5\%$ for all data.

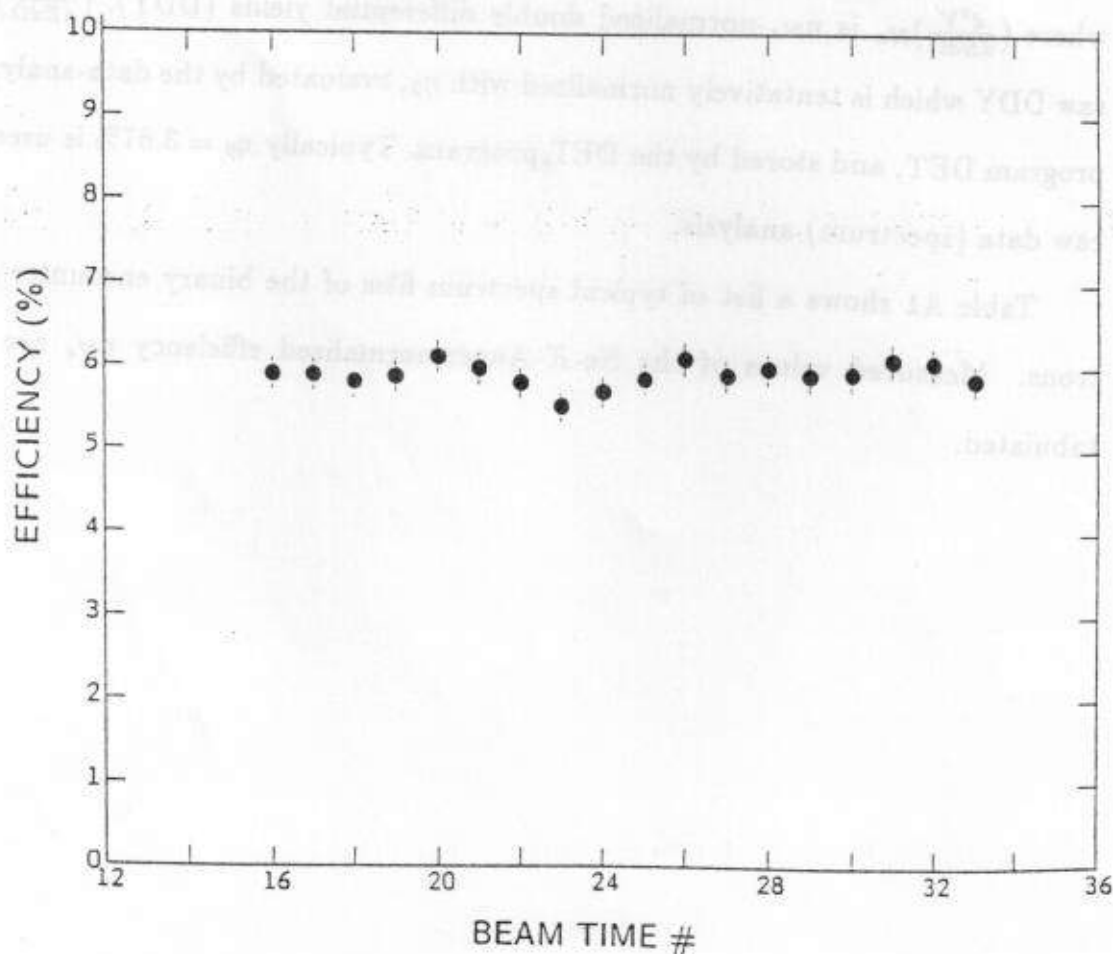


TABLE A1. Spectrum Files of Binary Encounter Electrons

Spectrum files of the double differential cross sections (DDCS) of all electrons which mainly includes cusp continuum and binary encounter electrons (BEE) for the collision systems of 19 MeV $F^{(9-3)+}$ and 28.5 MeV $F^{(9-5)+}$ with H_2 and He targets. The relative BEE distributions as a function of projectile charge state were displayed in Fig. 32 in Chapter IV. E_p is the projectile energy in MeV. DET file name refers to the spectrum file name which contains DDCS in the laboratory frame as a function of the laboratory electron energy E . Also all collision parameters are contained in each spectrum file. Those are target pressure, used efficiency η_0 , projectile charge, and so on. BT No. refers to the beam time number in which the corresponding spectrum was taken. η_{Ne} refers to the Ne-K-Auger-normalized spectrometer efficiency (see text). t is the measured cusp energy in eV, which has the experimental error of $\sim \pm 3$ eV.

E_p (MeV)	F^{q+}	Target	DET file name	BT No.	$\eta_{Ne}(\%)$	$\eta_0(\%)t$ (eV)
19	F^{9+}	H_2	SCAL0320	22	5.81	3.67 546
	F^{8+}		SCAL0314	22	5.81	3.67 546
	F^{7+}		SCAL0313	22	5.81	3.67 546
	F^{6+}		SCAL0310	22	5.81	3.67 548
	F^{5+}		SCAL0815	30	5.91	3.66 549
	F^{4+}		SCAL0873	31	6.10	3.67 550
	F^{3+}		SCAL0882	31	6.10	3.67 551
	F^{9+}	He	SCAL0318	22	5.81	3.67 546
	F^{8+}		SCAL0317	22	5.81	3.67 546
	F^{7+}		SCAL0312	22	5.81	3.67 547
	F^{6+}		SCAL0311	22	5.81	3.67 548
	F^{5+}		SCAL0819	30	5.91	3.66 549
	F^{4+}		SCAL0875	31	6.10	3.67 550
	F^{3+}		SCAL0879	31	6.10	3.67 551
28.5	F^{9+}	H_2	SCAL0525	26	6.10	3.67 820
	F^{8+}		SCAL0533	26	6.10	3.67 818
	F^{7+}		SCAL0534	26	6.10	3.67 820
	F^{6+}		SCAL0420	26	5.70	3.53 826
	F^{5+}		SCAL0542	24	6.10	3.67 824
	F^{9+}	He	SCAL0527	26	6.10	3.67 820
	F^{8+}		SCAL0531	26	6.10	3.67 818
	F^{7+}		SCAL0536	26	6.10	3.67 820
	F^{6+}		SCAL0024	17	5.90	3.67 826
	F^{5+}		SCAL0540	26	6.10	3.67 822

ELECTRON-ELECTRON INTERACTION IN ION-ATOM

COLLISIONS STUDIED BY PROJECTILE

STATE-RESOLVED AUGER ELECTRON SPECTROSCOPY

by

DO-HYUNG LEE

B.S., Seoul National University, 1974

M.S., Seoul National University, 1978

AN ABSTRACT OF A DOCTOR'S DISSERTATION

submitted in partial fulfillment of the
requirements for the degree

DOCTOR OF PHILOSOPHY

Department of Physics

KANSAS STATE UNIVERSITY

Manhattan, Kansas, USA

ABSTRACT

This dissertation addresses the problem of dynamic electron-electron interactions in fast ion-atom collisions using projectile Auger electron spectroscopy. The study was carried out by measuring high-resolution projectile *KLL* Auger electron spectra as a function of projectile energy for the various collision systems of 0.25–2 MeV/u O^{q+} and F^{q+} incident on H_2 and He targets. The electrons were detected in the beam direction, where the kinematic broadening is minimized. A zero-degree tandem electron spectrometer system was developed and showed the versatility of zero-degree measurements of collisionally-produced atomic states. The zero-degree binary encounter electrons (BEE), quasifree target electrons ionized by the projectiles in head-on collisions, were observed as a strong background in the *KLL* Auger electron spectrum. They were studied by treating the target ionization as 180° Rutherford elastic scattering in the projectile frame, and resulted in a validity test of the impulse approximation (IA) and a way to determine the spectrometer efficiency. An anomalous q -dependence, in which the zero-degree BEE yields increase with decreasing projectile charge state (q), was observed. State-resolved *KLL* Auger cross sections were determined by using the BEE normalization and thus the cross sections of the electron-electron interactions such as resonant transfer-excitation (RTE), electron-electron excitation (eeE), and electron-electron ionization (eeI) were determined. Projectile $2l$ capture with $1s \rightarrow 2p$ excitation by the captured target electron was observed as an RTE process with Li-like and He-like projectiles and the measured RTEA (RTE followed by Auger decay) cross sections showed good agreement with an RTE-IA treatment and RTE alignment theory. Projectile $1s \rightarrow 2p$ excitation by a target electron was observed as an eeE process with Li-like projectiles. Projectile $1s$ ionization by a target electron was observed as an eeI process with Be-like projectiles. The measured eeE and eeI cross sections showed threshold effects and are compared with an IA treatment, where electron-impact excitation and ionization cross sections were folded with the momentum distribution (Compton profile) of the target electrons. The extracted electron-electron cross sections can be provided as alternative data to free-electron-ion collisions for processes where K -shell excitation or ionization is involved. Dielectronic recombination (DR) cross sections can be complemented with the RTEA measurement.